Advancing Material Discovery for Selective Adsorption and Catalysis of Toxic Oxo-Anion Pollutants in Aqueous Phase - An Ab-Initio Study

by

Srishti Gupta

A Dissertation Presented in Partial Fulfillment
of the Requirements for the Degree
Doctor of Philosophy

Approved April 2023 by the
Graduate Supervisory Committee:

Christopher Muhich, Chair
Shuguang Deng
Heather Emady
Arunima Singh
Paul Westerhoff

ARIZONA STATE UNIVERSITY

May 2023

ABSTRACT

Anthropogenic processes have increased the concentration of toxic Se, As and N in water. Oxo-anions of these species are poisonous to aquatic and terrestrial life. Current remediation techniques have low selectivity towards their removal. Understanding the chemistry and physics which control oxo-anion adsorption on metal oxide and the catalytic nitrate reduction to inform improved remediation technologies can be done using Density functional theory (DFT) calculations.

The adsorption of selenate, selenite, and arsenate was investigated on the alumina and hematite to inform sorbent design strategies. Adsorption energies were calculated as a function of surface structure, composition, binding motif, and pH within a hybrid implicit-explicit solvation strategy. Correlations between surface property descriptors including water network structure, cationic species identity, and facet and the adsorption energies of the ions show that the surface water network controls the adsorption energy more than any other, including the cationic species of the metal-oxide. Additionally, to achieve selectivity for selenate over sulphate, differences in their electronic structure must be exploited, for example by the reduction of selenate to selenite by Ti^{3+} cations.

Thermochemical or electrochemical reduction pathway to convert NO_3^- to N_2 or NH_3, which are benign or value-added products, respectively are examined over single atom electrocatalysts (SAC) in Cu. The activity and selectivity for nitrate reduction is compared with the competitive hydrogen evolution reaction (HER). Cu suppresses HER but produces toxic NO_2^- because of a high activation barrier for cleaving the second N-O bond. SACs provide secondary sites for reaction and break traditional linear scaling relationships. Ru-SACs selectively produce NH_3 because N-O bond scission is facile, and

the resulting N remains isolated on SAC sites; reacting with H^+ from solvating H_2O to form ammonia. Conversely, Pd-SAC form N_2 because the reduced N^* atoms migrate to the Cu surface, which has a low H availability, allowing N atoms to combine to N_2. This relation between N^* binding preference and reduction product is demonstrated across an array of SAC elements.

Hence, the solvation effects on the surface critically alter the activity of adsorption and catalysis and removal of toxic pollutant can be improved by altering the surface water-network.

This dissertation is dedicated to my parents,

Mr. Sumit Gupta and Mrs. Simi Gupta.

Everything I am and I will be, I owe it all to you.

ACKNOWLEDGMENTS

I would first and foremost like to thank and acknowledge the support I received from my PI, Dr. Christopher Muhich. He taught me not only the complicated concepts of quantum chemistry with patience and ease, but also helped me overcome my biggest fears of sharing my research through writing peer-review articles and giving oral presentations. Thank you for being my guru for the last five years.

I would next like to my committee members – Dr. Shuguang Deng, Dr. Heather Emady, Dr. Arunima Singh and Dr. Paul Westerhoff for helping me reach here today. Thanks to all the graduate students and research scientists from Muhich Research group – Steve Wilson, Tanner Yorgason, Daniel Rivera, Jayni Hashimoto, Obinna Nwokonkwo, Vivienne Pelletier, Ankush Jain, Srashtasrita Das and Dr. Alicia Sandoval, who were always there whenever I got stuck and needed a help running DFT jobs.

I am also grateful to many experimental collaborators– Dr. Paul Westerhoff, Dr. Jaehong Kim, Dr. Haotian Wang, Dr, Julie Zimmerman, Dr. Mike Wong, Dr. Dino Villagran, Dr. Qilin Li, Dr. Kathy James, Dr. Julie M. Goodman, Dr. Susan Korrick, Feng Yang Chen, Zhen-Yu Wu, Reza Nazemi, Xuanhao Wu, Mona Dai, Dr. Carmen Velasco, Dr. Amanday Lounsbury, Dr. Mariana Marcos-Hernandez and Annika Hjelmstad. I learnt a lot about current state of adsorption and reduction technology from your research. I would specifically like to thank Holly Rudel, Emily Briese, Feng Yang Chen, Xuanhao Wu, Elisabeth Thomas and Juliana Levi who are the most wonderful researchers I met through collaborations and CHEGSA/NEWT events. I would also like to thank the undergraduate students I worked with – Anh Ngan Nguyen, Matthew Shaffer, Adam Chismar, Maxon Rubin-Toles and Tracy Flores.

My research would not have been possible without generous funding from National Science Foundation, National Institute of Environmental Health Sciences and U.S. Department of Energy for the projects. Adsorption work was supported by the National Science Foundation Nanosystems Engineering Research Center for Nanotechnology-Enabled Water Treatment (NEWT; Grant ERC-1449500) and by the National Institute of Environmental Health Sciences of the National Institutes of Health under Award Number P42ES030990 as part of the Memcare (Metals Mixtures: Cognitive Aging, Remediation, and Exposure Sources). Catalysis work is also partially based upon work supported by the National Alliance for Water Innovation (NAWI), funded by the U.S. Department of Energy, Energy Efficiency and Renewable Energy Office, Advanced Manufacturing Office under Funding Opportunity Announcement DE-FOA-0001905. Computational work used high-performance supercomputing at ASU and the Extreme Science and Engineering Discovery Environment (XSEDE), supported by NSF (ACI-1548562). I would also like to thank ASU Fulton School of Engineering and GPSA for providing me Engineering Graduate Fellowship, travel grant and mentorship award.

Thank you SEMTE advisory team – Tiffany Wingerson, Lacy Quail, Ya Hu and Christine Quintero, SEMTE IT team especially Gil Speyer and SEMTE business operation team (Tae O'Connor) and NEWT staff – Liz Scroggins, Matt Hotze, Ernest Davis and Christina Crawford for their help.

Finally, I would like to thank my family and friends for their constant support. Thank you, Dr. Sukriti Gupta, and Dr. Karthik Pushpavanam, for being the great role models. Thank you for giving me the push when I needed, and hours of laughter and fun.

TABLE OF CONTENTS

Page

Page

CHAPTER

Page

CHAPTER

Page

CHAPTER

Page

CHAPTER

Page

CHAPTER

LIST OF TABLES

Table Page

LIST OF FIGURES

Figure Page

Figure Page

Figure Page

Figure Page

Figure Page

Figure Page

Figure Page

Figure Page

Figure Page

Figure Page

Figure Page

CHAPTER 1

INTRODUCTION

1.1 Overview

Clean water is a fundamental right necessary for the continued survival of our ecosystem and humanity. Achieving "universal and equitable access to safe and affordable drinking water for all" by 2030 is ranked as the sixth sustainable development global goal.[1] However, the industrial revolution and climate change has led to a scarcity of clean fresh water sources. Currently, 26% of the world's population lacks access to clean drinking water.[2,3]

With the rapid decrease in clean drinking water there is a growing need for affordable and accessible water remediation methods (Target 6.3 and 6.4 of global sustainable goals 2030).[2,3] The removal of anthropogenic contamination from our water resources at affordable costs is a critical barrier to achieving set water remediation global goals.[4] Past and continued mismanagement of industrial manufacturing operations, along with agriculture and mining run off water have led high degrees of water contamination by toxic oxo-anions pollutants like selenate (Se(VI)), selenite (Se(IV)), arsenate (As(V)) and nitrate (NO_3^-).[4-8]

1.1.1 Toxicity of Se and As oxo-anions

Selenium, a metalloid, occurs naturally with sulfur-containing minerals in sedimentary and volcanic rocks.[9] Selenium is an essential micronutrient, important for human health.[10] Insufficient consumption of selenium, less than 55 µg/day, can lead to Keshan disease or Kashin Bech disease which may cause osteoarthritis.[9,11,12] Most of the humans get their selenium requirements from food sources such as nuts, meat, fortified

cereals, beans and lentils.[9] Selenium is also used in industry and agriculture for production of glass, pigments, photovoltaic cells, fertilizers, semiconductor, and electronic devices.[13] The improper disposal of these products can cause selenium to leach into ground waters, and from there enter drinking water sources.[9] Selenium is toxic to humans when it is consumed above the concentration of 140 µg/L or 0.14 ppm from drinking water.[9,10,14] Excessive intake of selenium can cause a range of health problems, including hair loss, nail brittleness, and gastrointestinal disturbances.[12] Long-term exposure to high levels of selenium in water can also lead to more serious health effects such as neurological damage, liver and kidney damage, and an increased risk of certain types of cancer.[15] Figure 1.1(a) shows the distribution of selenium reported by United States Geological Survey.[16] Many areas, especially the Midwest, have much higher concentrations of Se. This can leach into water and increase the health risk to the population living in these regions.

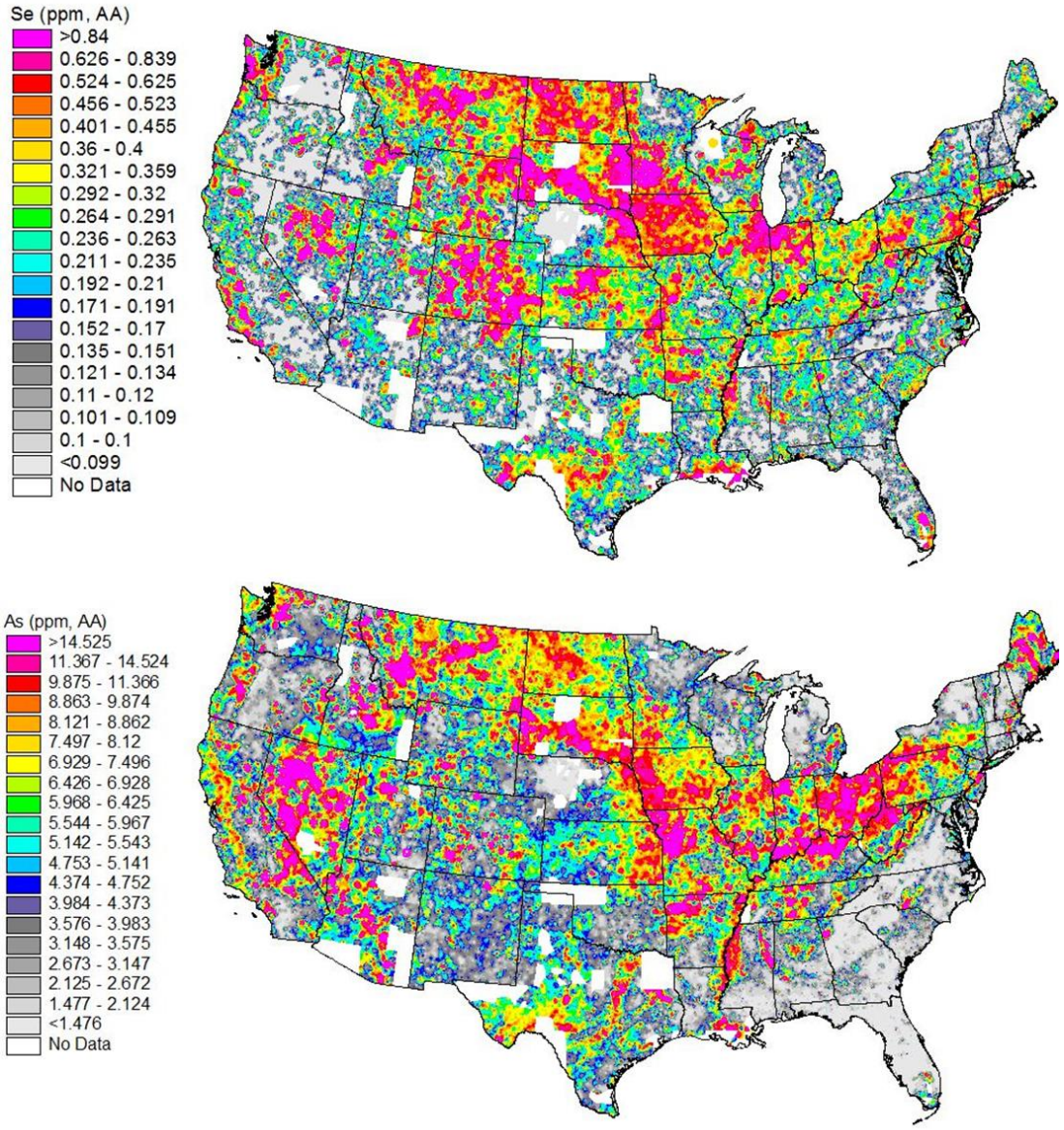

Figure 1.1: Distribution of (a) Selenium and (b) Arsenic in USA reported by The United States Geological Survey and analyzed using Hydride-generation Atomic Absorption Spectrometry method.[16]

Similarly, arsenic is naturally present in soil, minerals, and rocks.[17] It is used in industrial applications like wood preservatives, pesticides and semiconductors. This has led to an increased concentration of arsenic in our drinking water.[8] Consumption of arsenic above 0.08 mg/L can cause abdominal pain, vomiting, diarrhea, and dehydration.[18] Regular consumption of arsenic from drinking water causes chronic health problems such as skin

lesions, respiratory problems, diabetes, and cancer.[8,19] Figure 1.1 shows that arsenic is also present in much higher concentrations across the USA than recommended maximum drinking concentrations (0.01 ppm).[16,19] Therefore, we need to find cost-effective remediation methods to remove both Se and As from drinking water.

Se and As are present in water in their oxo-anion forms – selenate (Se(VI) or Se^{+6}), selenite (Se(IV) or Se^{+4}), arsenate(As(V) or As^{+5}) or arsenide(As(III) or As^{+3}).[20,21] Selenate and selenite are both equally toxic to humans, but selenate is more soluble in water and hence present in larger concentrations in drinking water.[22] Among As oxo-anions, arsenide is more toxic than arsenate as arsenide binds to sulfhydryl (-SH) groups in proteins and enzymes affecting the essential biological processes in the body.[23] Arsenate, however, does not react with the cellular molecules and is less toxic. Arsenide converts to arsenate in aerobic conditions in water and hence higher concentration of arsenate is present in drinking water.[24]

1.1.2 Nitrate toxicity

The Industrial Revolution has increased the use of nitrogen as fertilizers, manure, and sewage treatment.[25,26] Excess nitrate rich chemicals from agricultural lands, refuse dumps, animal feedlots, and septic tanks leach into ground water increasing the concentration of nitrate in our ground water and other water sources.[27,28] Figure 1.2 shows the distribution of nitrate concentration in shallow water and ground water in 2015.[29]

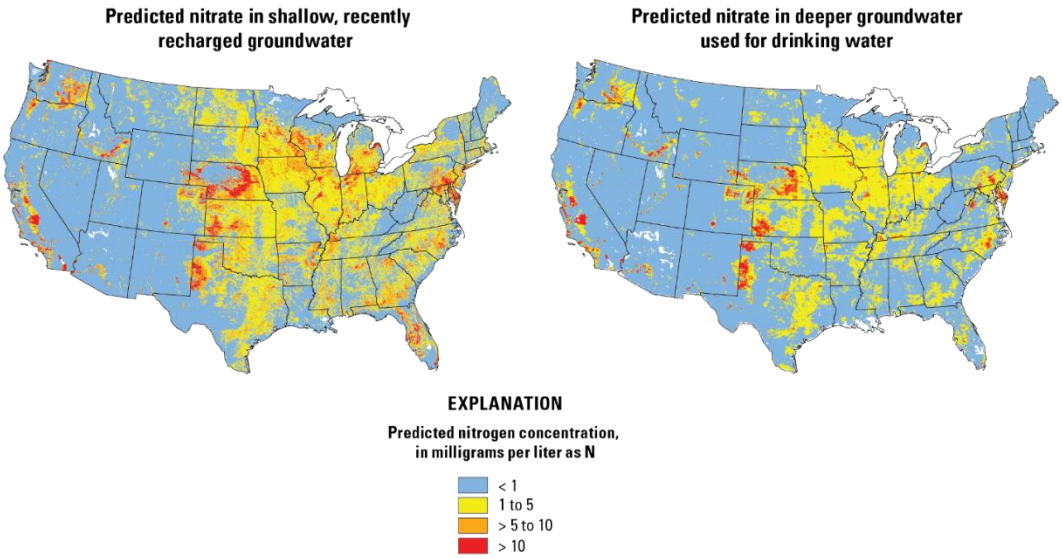

Figure 1.2: Predicted distribution of Nitrate concentration in shallow and deeper U.S. groundwater, reproduced from Desimone et. al. (2015).[29]

The nitrate buildup in water systems routinely exceeds health and safety levels.[7] In 2017, Pennino et. al. found that the Safe Drinking Water Information System reported that over 500 public water systems across the United Stated violated maximum contamination limits of 10 mg nitrate N/L.[30] This affected more than 1,500,000 people across the country.[30] Excess consumption of nitrate is linked to methemologlobinemia, or "blue baby syndrome," where the hemoglobin's ferrous ions turn into ferric ions.[31,32] Infants are most susceptible to methomologlobinemia, which can turn skin to a bluish or gray color and cause more serious health affects like weakness, excess heart rate, fatigue, and dizziness.[31] In adults, increased intake of nitrate is linked to thyroid disease, fatigue, weight gain, hair loss, goiters, and colon cancer.[7,33]

1.2 Technologies to remove toxic oxo-anions

Removal of toxic oxo-anions from water systems is currently done using advanced water treatment technologies such as coagulation and precipitation,[34] ion-exchange membranes,[35] chemical oxidation,[36] biological methods,[6,4,37] and photo-catalysts[4,38]. Coagulation and precipitation is a two-step process to neutralize particles using coagulants like aluminum sulfate, aluminum chloride, ferrous sulfate, ferric chloride, ferric chloride sulfate, hydrated lime, magnesium carbonate, poly-aluminum sulfate chloride and polymerized aluminum-iron blends.[34,39-42] The size of coagulated particles is increased using polymeric materials which precipitate and remove the pollutants in the second step.[34,43,44] Typical ion-exchangers require ion-exchange resins (functionalized porous or gel polymer), zeolites, montmorillonite, or clay to remove toxic oxo-anions.[45] Biological methods of removing oxo-anions like phytoremediation, bioremediation, biosorption, and biofiltration have shown great promise in removing oxo-anions.[23,37,46,47]

These technologies, however, require high start-up costs and are labor and resource intensive. The coagulants and resins required in coagulation and ion-exchange require frequent replacements.[45,48] The membrane technologies still struggle with low permeability, which requires expensive energy usage to maintain pressure across the system, residual sludge and regeneration of resin, and unclogging of membranes.[49,50] Biological process require heavy operation costs to ensure proper growth of microorganisms like maintaining sterile bioreactors, and environmental conditions like pH, temperature, and oxygen concentrations.[24,47,51,52] Therefore, they cannot be used for small-scale operations in remote location or poor communities and are less likely to contribute

towards "universal and equitable access" to clean drinking water. Hence, there is a need to find more affordable and easy-to-use water remediation techniques.

1.2.1 Adsorption of Se and As oxo-anions on metal oxides

Remediation of Se and As oxo-anions by adsorption has been widely accepted as an effective low-cost technology.[53] Adsorption can be used in under-the-sink operations with minimum operational expertise, and hence it is deployable for low-income populations.[53] There is a range of materials which are currently researched as optimal adsorbents to remove Se and As oxo-anions, such as inexpensive metal-oxides, activated carbon, animal biopolymers (e.g. hen eggshell and broiler chicken feathers), chitosan, zero-valent iron, and other miscellaneous adsorbents.[9,14,22,48,54-58] The ideal adsorbent for removal applications in water remediation technology should be inexpensive, abundantly available, effective in near-neutral pH conditions, and have high adsorption capacity.[59] In 2022, Zoroufchi Benis et al. did an extensive review of selenium oxo-anions adsorption on different adsorbents.[53] They found that natural clay minerals and waste materials like eggshells and carbon-based materials have 10 times lower adsorption capacity for selenate and selenite removal (~ 0.3 mg/g adsorbent) compared to metal-oxide based adsorbents.[35,53] A similar observation was made by Canreiro et al. (2021) in their review of the latest trends in adsorption of arsenic oxo-anions.[35]

Hematite (Fe_2O_3) and alumina (Al_2O_3) are naturally occurring, inexpensive adsorbents approved by the EPA for selenium and arsenic oxo-anion removal.[60,61] They are non-toxic, abundant, simple to use, socio-culturally acceptable, and compliant with most local health and safety regulations.[58-60] Moreover, they can be recycled by desorbing captured pollutants through processes like chemical-, electrochemical- or thermal-

regeneration, making them cost effective and environmentally sustainable.[53,58] However, the adsorption capacity of hematite and alumina are dependent on the pH of the solution.[62-65] Selenate, selenite, and arsenate adsorption on alumina and hematite are affected by changing pH conditions (Figure 1.3).[66,67] The adsorption is highest in acidic conditions, with the adsorption capacity dropping by 50% as the pH increases from 4 to 7 for all Se(VI), Se(IV) and As(V).[67-69] This means that double the metal-oxide would be needed for under-the-sink adsorption operations at pH 7, which is ideal for drinking water, compared to pH 4. This limits the usage of hematite and alumina particles for adsorption of selenium and arsenic oxo-anion in real world applications.[70,71]

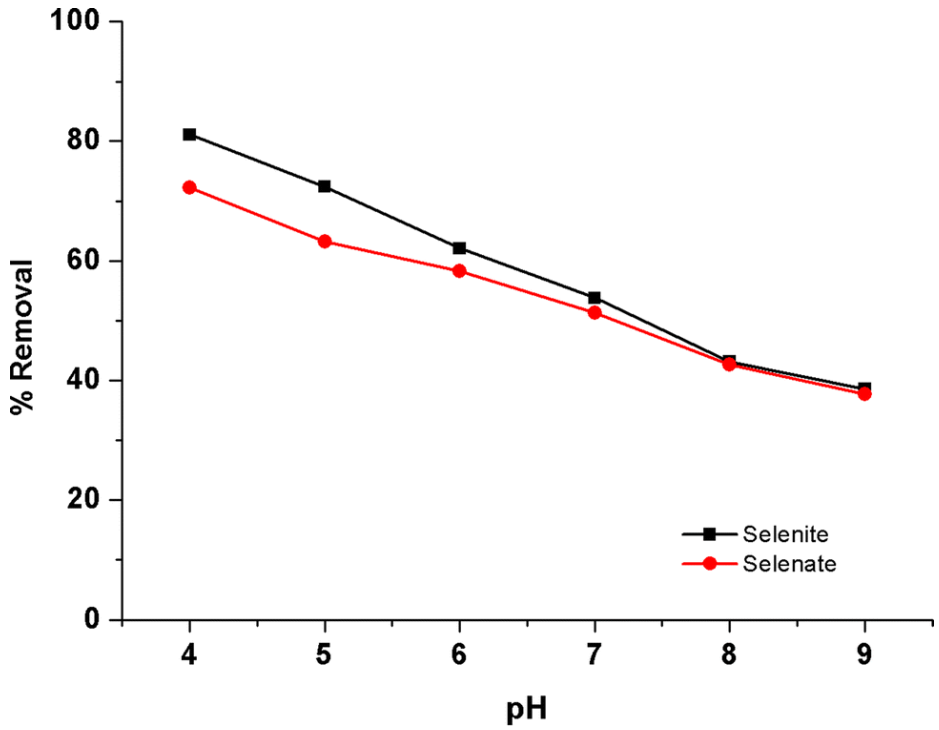

Figure 1.3: pH on selenite and selenate adsorption on mesoporous activated alumina, reproduced from Meher et. al. (2019).[66]

In naturals waters, large concentrations of background oxo-anions (e.g., phosphate, silicate, sulfate) are present that decrease the adsorption of As and Se oxo-anions on alumina and hematite particles.[72-74] The adsorption of 200 µg/L As(V) on alumina dropped

by 37%, 90% and 85% when 500 mg/L of sulphate, 10 mg/L of silicate and 1 mg/L of phosphate, respectively, was present in the solution.[75] The concentrations of competitive species represent the typical concentrations of solutes in the natural water bodies. Similarly, the As(V) adsorption dropped by 10%, 80% and 60% on hematite (Fe_2O_3) surface when sulphate, silicate and phosphate, respectively, were present in the solution.[75] The selenate adsorption on alumina has also shown to drop by 50% upon addition of sulphate in the solution in equal concentration.[76]

Adsorption of Se and As oxo-anions can be improved by modifying the metal-oxide surfaces. Three methods of improving adsorption energies on metal-oxide surfaces are: 1) increasing the number of active sites by increasing surface area to mass ratio,[77] 2) changing the surface structure to increase the binding energy of the target adsorbate,[78] or 3) alter the material composition to increase the binding energy of the target adsorbate.[79] Nanoparticles of metal oxides are employed to reduce the cost of adsorption by increasing the surface area, and thus number of adsorption sites, per mass of the adsorbent.[73,74] However, Villalobos and Pérez-Gallegos determined that surface area alone does not control sorption performance by examining the sorption capacities of chromate anions and lead(II) cations on goethite.[80] They demonstrated that the exposed surface facet has a stronger correlation with sorbent effectiveness than surface area.[81] Lounsbury et al. found that the (012) facet of Fe_2O_3 adsorbs 250-400 µg selenate/m^2 as compared to 90-200 µg/m^2 on the (110) facet.[78] Similarly, the adsorption capacity of As oxo-anions on activated alumina is two to three times higher when impregnated with lanthanum,[79] showing the criticality of adsorbent composition. Engineering inexpensive metal-oxides for selective oxo-anion adsorption

processes would decrease the material quantity needed and produce concentrated effluent that can be used to recycle essential minerals and pave way to create a circular economy.

1.2.2 Catalytic Reduction of Nitrate on Metal Surfaces

Nitrate, on the other hand, is present in a larger concentration in drinking water and needs to be reduced to other N forms like N_2 or NH_3 to maintain the ecological N-cycle.[82] Adsorption leads to production of secondary concentrated stream which involves further steps for cleanup.[83] Remediation on catalytic surfaces via the electrochemical or thermochemical nitrate reduction reaction (NO_3RR) is an emerging technology to convert groundwater nitrate into N_2 or NH_3.[28] It is considered a green alternative against other remediation methods as it does not use chemical reductants, produce biological waste, or a second pollutant stream.[28] Moreover, the electricity or hydrogen required for nitrate reduction can be produced by renewable sources.

Out of the many reduction products, converting NO_3^- into either an innocuous product such as nitrogen gas, N_2, or a commercially reusable product such as NH_3 is of general interest. In 2021, Wang et al. performed a comprehensive review of recent discoveries in the nitrate reduction field to improve the activity and selectivity of the nitrate reduction process.[84] Most metal electrodes had varying degrees of selectivity towards specific products and Turnover Frequency. Pd, Pt, Rd, and Ru have higher selectivity and activity of the NO_3RR over the surface.[85] However, these metals are some of the most expensive elements and cannot be used for affordable usage.[86-88] Also, the nitrate reduction mechanism is suppressed by the hydrogen evolution reaction, which is a critical competitive side reaction occurring over the cathode surface.[89] Nitrate reduction on

inexpensive materials like Cu forms NO_2^-, a toxic compound, which needs to be further removed from the water.[90,91]

Alloying metal surfaces increases the activity and selectivity of the NO_3RR.[88,92] Past studies have tested the NO_3RR on Cu-Ni and Pd-Rd alloys to increase the activity of nitrate reduction.[90,93,94] NO_3RR activity showed a volcanic relationship on alloyed material, where the highest activity was achieved when the 'active sites' were dispersed among the mostly inert metal matrix.[94] However, none of the systems were able to reach the NH_3 production efficiency necessary for commercial use.

In recent years, single atom alloys (SAA) have emerged as a new class of catalysts that can achieve a theoretical limit to atomic utilization and enhance the activity and selectivity of reactions by enabling distinct reaction pathways that were not possible of single metal structures.[95,96] Pd SAA in Cu, Ru SAA in Cu, and Ni SAA in Cu have shown promising results in improving nitrate reduction to a selective product. Moreover, they also show high selectivity to nitrate reduction compared to the HER reaction.[88,95,97-100] Limited information is available to understand how a single atom alloy improves nitrate reduction, or if the limit has been reached in improving the activity and selectivity of nitrate reduction on a single atom catalyst.

However, experimentally determining the properties of material and environmental conditions that improve selectivity for adsorption and reduction via an Edisonian approach is a daunting task because it relies on tedious and expensive testing of material performances on large amounts of perfectly synthesized nanomaterial constructions without a guarantee of success.[74,78] In this dissertation, the adsorption of oxo-anions and the catalytic reduction of nitrate for water remediation processes is investigated using *ab*

initio calculations to determine how material development can be advanced to improve adsorption processes.

1.3 Use of ab Initio Calculations to Understand and Predict Adsorption and Catalysis

Precision *a priori* designs of materials for highly selective water remediation require an understanding of the fundamental mechanisms of the remediation technique at the metal/metal-oxide surface in the presence of solvent. Density functional theory (DFT) has found important application in understanding oxo-anion adsorption and nitrate reduction on heterogeneous surfaces.[71,88,99,101-105] Specifically, DFT methods provide two tools to complement and propel experimental approaches in development of selective materials: 1) the ability to isolate individual cause and effects by focusing on processes at the site of interaction of the studied system; and 2) the use of rapid screening approaches to identify novel sorbent/electrode materials, predicting the most promising candidates that could then be validated experimentally. In the past, quantum methods have been applied primarily for explaining experimentally observed behavior. However, recent advancements in computing power and high accuracy/low computational cost methods are bringing the prediction of novel adsorbents closer to reality.

Two routes to DFT based design of sorbents and catalysts are: 1) brute force materials screening or 2) descriptor identification and materials selection. Due to limitations dictated by system size (<500-1000 atoms) and simulation time scale (either thermodynamic states or a few femto-seconds), the DFT calculation of competitive adsorption and reaction free energies must be completed on a specific material surface facet, with a specific pH, ionic strength, etc.[18-23] Effective screening requires rapid

calculation of adsorption and reduction energies on hundreds to thousands of candidate material compositions and morphologies, which is a complicated and time-consuming process.

The development of adsorption/catalytic descriptors mostly relies on adsorption energy and selectivity derived from the DFT calculations and identification of materials characteristics that correlate with desired performance. For example, Corum and Mason found that strong adsorption of As oxo-anions on Keggin Al-nanoclusters was correlated with large local shape and electronic potential gradients.[106,107] With a suitable and clearly defined descriptor, materials could be screened without detailed DFT calculation and only candidates with most promising properties would be subjected to full DFT calculations (i.e. adsorption energies, Gibbs free energies, spectra calculations, etc.).

Therefore, DFT has a great potential to aid in the discovery of selective oxo-anion adsorbents and catalysts. The key areas that limit its implementation are the size of the model system needed to adequately describe the complex heterogeneous environment and reaction pathways, the development of efficient computational materials screening tools for multi-phase systems, and high-quality experimental validation data. My dissertation focuses on modelling and understanding the fundamental mechanisms of two remediation technologies using DFT: (1) low selectivity of metal-oxides for removal of Se (and As) oxo-anions by adsorption, and (2) low activity or selectivity of electrolytic nitrate reduction reaction on inexpensive metal electrodes. The adsorption energies of species X on adsorbate A us calculated as follows:

$$X_g + A + E_{ads} \leftrightarrow \ X.A$$

Here, X_g is the adsorbate in gas phase, X.A is the adsorbed X species on adsorbate. The E_{ads} (in eV) is the energy required to adsorb one X species on single site of A adsorbate. If E is negative, the adsorption process releases energy, and the reaction is more likely to occur. If the E is positive, the adsorption process requires additional energy, and hence the probability of the event occurring is less. Similarly, the probability of reaction energy occurring, for example A and B combining to form C on the surface, can be calculated using the following equation:

$$A + B + E_{rxn} \leftrightarrow C$$

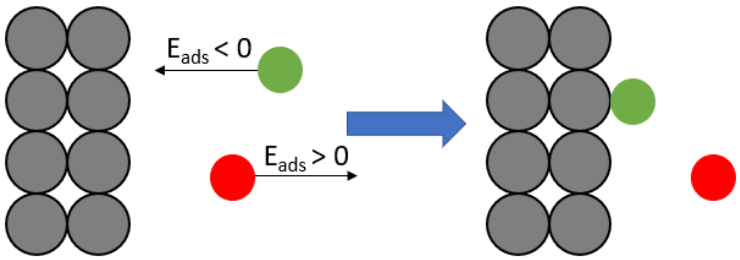

Figure 1.4: The pictorial description of adsorption process controlled by the thermodynamics of the adsorption energy.

These calculations are, however, performed in gas phase. Methods like the hybrid solvent model; computational hydrogen electrode and thermodynamic Hess cycle are employed to capture the role of solvent on metal-oxide and metal surfaces without significantly increasing the computational cost. These models are also compared to the experimental results found in literature. These models are tested for new materials to find more selective surface properties for Selenate adsorption and Nitrate reduction.

1.4 Objectives

The dissertation investigated two remediation technologies adsorption of Se and As oxo-anion on Al_2O_3 and Fe_2O_3 surfaces (Objectives 1.4.1-1.4.3) and electrochemical and

thermochemical nitrate reduction on Cu/Ru metal and single atom in Cu surface (Objectives 1.4.4-1.4.6) using density functional theory. First, I focused on developing a model to study adsorption and catalysis reaction using density functional theory that replicates the experimental results (Objectives 1.4.1 and 1.4.4). The models were used to search for properties and materials that can improve adsorption and catalysis. The objectives are detailed below, and the dissertation addresses each in order.

1.4.1 Understanding the effect of surface properties that controls SeO_4^{2-} adsorption on (012) α-Al_2O_3

The development of new metal-oxide adsorbents is stymied because of the unknown nature of surface factors that affect adsorption energies. Here, my objective was to develop a hybrid solvent model to study the adsorption energies of selenate on the (012) α-Al_2O_3 surface using density functional theory to unravel the physics that controls adsorption. The DFT predicted adsorption energies were used to calculate adsorption isotherms as a function of pH that were compared to experimental isotherm for selenate adsorption on alumina surface found in literature. The control for physical properties like water network, distance between oxo-anion and surface and energy of adsorbing selenate on anhydrous alumina on the adsorption energies was calculated to find the most controlling factor.

1.4.2 Understanding the effect of single atom cationic defect sites in α-Al_2O_3 (012) surface on selenate and sulfate adsorption

In this study, my objective was to isolate the role of cation on the adsorption of selenate in neutral and acidic pH conditions using density functional theory calculations. The cationic affects were investigated by substituting a single cation on the surface of

protonated and neutral (012) Al_2O_3. This enabled isolation of the role of the adsorbent cation from other surface properties like water network change and lattice structure on the adsorption of selenate. The adsorption of selenate on single atom cationic defect sites in α-Al_2O_3 (012) was also compared with sulphate adsorption to find if we can selectively remove selenate from water by changing the cation of metal-oxide surface. The DFT results were finally delineated against nine surface properties by regressing descriptors, alone, in pairs and as orthogonal descriptors developed by principal component analysis.

1.4.3 Adsorption of Se(VI), Se(IV) and As(V) oxo-anions on neutral (012) and (001) hematite surfaces

This work aimed to determine the effect of surface termination and oxo-anion cation on the adsorption on hematite surfaces. Density functional theory calculations were used to determine the water network on [001] and [012] Fe_2O_3 surfaces to determine the number of H_2O and OH molecules and H-bonds on each termination before the adsorption. The adsorption of SeO_4^{2-} was calculated on the two hematite facets to understand the surface water structure on adsorption energy. The adsorption of SeO_4^{2-}, $HSeO_3^-$, $HAsO_4^{2-}$ and $H_2AsO_4^-$ was calculated on the [012] Fe-terminated Fe_2O_3 surface to investigate if cation of oxo-anion affects the adsorption energies on hematite surface.

1.4.4 Electrochemical reduction of NO_3^- towards NH_3 production using dispersed Ru single atom in Cu metal catalyst: an Ab-Initio Study

In this work, density functional theory calculations were performed to examine electrolytic nitrate reduction pathways on Ru in Cu single atom alloy (SAA) catalysts compared to the pure Cu and Ru bulk material. NO_3^- reduction pathways were calculated to NO_2^- and NO, N_2, or NH_3. Specifically, the minimum reaction pathway was mapped for

nitrate reduction to NO_2^-, NO, N_2 and NH_3 on the Cu[111], Ru single atom in Cu[111] and Ru[001] surfaces. The adsorption of ionic species on an electrode was calculated by developing Hess cycle which incorporated pH and potential affects.

1.4.5 Understanding electrochemical vs. thermochemical nitrate reduction on dispersed Pd-single atoms in Cu Metal Catalyst using density functional theory

Here the mechanism of electrochemical and thermochemical nitrate reduction was investigated using Density Functional theory over Pd-single atom alloy dispersed in Cu[111] to understand the differences in two remediation methods on the activity and selectivity of the nitrate reduction. The potential and pH effects are included by considering a Chemical Hydrogen electrode and the protonation energies of aqueous species. The H_2 pressure for thermochemical nitrate reduction is compared to electrochemical potential using Open circuit potential (OCP) based on Nernst equation.

1.4.6 Predicting the activity and selectivity of electrocatalytic and thermochemical nitrate reduction on single atom alloy in Cu surface

In this objective I investigated the nitrate reduction mechanism on nine single atom substitutions in an inexpensive electrode (Cu) to predict the single atoms that have activity and selectivity of NRR towards NH_3 or N_2 using Density functional Theory. The reaction energies and activation barriers on single atom catalysts are also tested against metal properties if the single atoms also follow linear relationship between activation energies and reaction energy as well as adsorption energies and d-band centers, like pure metal surfaces.

1.5 References

1. Nations, U. THE 17 GOALS. https://sdgs.un.org/goals.
2. WHO, U. Progress on Sanitation and Drinking Water: 2015 Update and MDG Assessment; 2015.

3. Progress towards the Sustainable Development Goals; United Nations: High-level political forum on sustainable development, convened under the auspices of the Economic and Social Council, 30 April 2021, 2021; p 27.
4. Alvarez, P. J. J.; Chan, C. K.; Elimelech, M.; Halas, N. J.; Villagran, D., Emerging opportunities for nanotechnology to enhance water security. Nat Nanotechnol 2018, 13 (8), 634-641.
5. Serio, F.; Miglietta, P. P.; Lamastra, L.; Ficocelli, S.; Intini, F.; De Leo, F.; De Donno, A., Groundwater nitrate contamination and agricultural land use: A grey water footprint perspective in Southern Apulia Region (Italy). Science of The Total Environment 2018, 645, 1425-1431.
6. Stefaniak, J.; Dutta, A.; Verbinnen, B.; Shakya, M.; Rene, E. R., Selenium removal from mining and process wastewater: a systematic review of available technologies. Journal of Water Supply: Research and Technology-Aqua 2018, 67 (8), 903-918.
7. Ward, M. H.; Jones, R. R.; Brender, J. D.; de Kok, T. M.; Weyer, P. J.; Nolan, B. T.; Villanueva, C. M.; van Breda, S. G., Drinking Water Nitrate and Human Health: An Updated Review. Int J Environ Res Public Health 2018, 15 (7).
8. Podgorski, J.; Berg, M., Global threat of arsenic in groundwater. Science 2020, 368 (6493), 845-850.
9. Fernández-Martínez, A.; Charlet, L., Selenium environmental cycling and bioavailability: a structural chemist point of view. Reviews in Environmental Science and Bio/Technology 2009, 8 (1), 81-110.
10. Lenz, M.; Lens, P. N., The essential toxin: the changing perception of selenium in environmental sciences. Sci Total Environ 2009, 407 (12), 3620-33.
11. Kaur, N.; Sharma, S.; Kaur, S.; Nayyar, H., Selenium in agriculture: a nutrient or contaminant for crops? Archives of Agronomy and Soil Science 2014, 60 (12), 1593-1624.
12. Olson, O. E., Selenium Toxicity in Animals with Emphasis on Man. Journal of the American College of Toxicology 1986, 5 (1), 45-70.
13. Luoma, S. N.; Presser, T. S., Emerging Opportunities in Management of Selenium Contamination. Environmental Science & Technology 2009, 43 (22), 8483-8487.
14. Santos, S.; Ungureanu, G.; Boaventura, R.; Botelho, C., Selenium contaminated waters: An overview of analytical methods, treatment options and recent advances in sorption methods. Science of The Total Environment 2015, 521-522, 246-260.
15. Davis, T. Z.; Stegelmeier, B. L.; Hall, J. O., Analysis in Horse Hair as a Means of Evaluating Selenium Toxicoses and Long-Term Exposures. Journal of Agricultural and Food Chemistry 2014, 62 (30), 7393-7397.
16. Jeffrey N. Grossman, A. E. G., Peter N. Schweitzer, Paul G. Schruben, National Geochemical Survey database. U.S. Geological Survey: https://mrdata.usgs.gov/, 2008.
17. Distribution of Arsenic in the Environment. In Arsenic: Medical and Biologic Effects of Environmental Pollutants., Pollutants., N. R. C. U. C. o. M. a. B. E. o. E., Ed. National Academies Press (US): Washington (DC), 1977; Vol. 3.
18. Smedley, P. L.; Kinniburgh, D. G., A review of the source, behaviour and distribution of arsenic in natural waters. Applied Geochemistry 2002, 17 (5), 517-568.
19. Ratnaike, R. N., Acute and chronic arsenic toxicity. Postgraduate Medical Journal 2003, 79 (933), 391-396.

20. Ishikawa, S.; Sekine, S.; Miura, N.; Suyama, K.; Arihara, K.; Itoh, M., Removal of selenium and arsenic by animal biopolymers. Biol Trace Elem Res 2004, 102 (1-3), 113-27.
21. Fox, P. M.; LeDuc, D. L.; Hussein, H.; Lin, Z.-q.; Terry, N., Selenium Speciation in Soils and Plants. In Biogeochemistry of Environmentally Important Trace Elements, American Chemical Society: 2002; Vol. 835, pp 339-354.
22. Sharma, V. K.; Sohn, M.; McDonald, T. J., Chapter 8 - Remediation of Selenium in Water: A Review. In Advances in Water Purification Techniques, Ahuja, S., Ed. Elsevier: 2019; pp 203-218.
23. Yamamura, S.; Amachi, S., Microbiology of inorganic arsenic: From metabolism to bioremediation. J Biosci Bioeng 2014, 118 (1), 1-9.
24. Lim, K. T.; Shukor, M. Y.; Wasoh, H., Physical, chemical, and biological methods for the removal of arsenic compounds. Biomed Res Int 2014, 2014, 503784.
25. Kreitler, C. W.; Jones, D. C., Natural Soil Nitrate: The Cause of the Nitrate Contamination of Ground Water in Runnels County, Texasa. Ground Water 1975, 13, 53-62.
26. Spalding, R. F.; Exner, M. E., Occurrence of Nitrate in Groundwater—A Review. Journal of Environmental Quality 1993, 22 (3), 392-402.
27. Health, I. D. o. P. Nitrates In Drinking Water. http://www.idph.state.il.us/envhealth/factsheets/NitrateFS.htm.
28. Garcia-Segura, S.; Lanzarini-Lopes, M.; Hristovski, K.; Westerhoff, P., Electrocatalytic reduction of nitrate: Fundamentals to full-scale water treatment applications. Applied Catalysis B: Environmental 2018, 236, 546-568.
29. DeSimone, L. A.; McMahon, P. B.; Rosen, M. R. The quality of our Nation's waters: Water quality in principal aquifers of the United States, 1991-2010; 1360; Reston, VA, 2015; p 161.
30. Pennino, M. J.; Compton, J. E.; Leibowitz, S. G., Trends in Drinking Water Nitrate Violations Across the United States. Environmental Science & Technology 2017, 51 (22), 13450-13460.
31. Rehman, H. U., Methemoglobinemia. West J Med 2001, 175 (3), 193-196.
32. Knobeloch, L.; Salna, B.; Hogan, A.; Postle, J.; Anderson, H., Blue babies and nitrate-contaminated well water. Environmental Health Perspectives 2000, 108 (7), 675-678.
33. Nitrate and Drinking Water from Private Wells. Centers for Disease Control and Prevention 2015.
34. Bratby, J., Coagulation and Flocculation in Water and Wastewater Treatment – Third Edition. IWA Publishing: 2016.
35. Carneiro, M. A.; Pintor, A. M. A.; Boaventura, R. A. R.; Botelho, C. M. S., Current Trends of Arsenic Adsorption in Continuous Mode: Literature Review and Future Perspectives. Sustainability 2021, 13 (3), 1186.
36. Marinho, B. A.; Cristóvão, R. O.; Boaventura, R. A. R.; Vilar, V. J. P., As(III) and Cr(VI) oxyanion removal from water by advanced oxidation/reduction processes—a review. Environmental Science and Pollution Research 2019, 26 (3), 2203-2227.

37. Song, B.; Tian, Z.; van der Weijden, R. D.; Buisman, C. J. N.; Weijma, J., High-rate biological selenate reduction in a sequencing batch reactor for recovery of hexagonal selenium. Water Research 2021, 193, 116855.
38. Weidner, E.; Ciesielczyk, F., Removal of Hazardous Oxyanions from the Environment Using Metal-Oxide-Based Materials. Materials 2019, 12 (6), 927.
39. Tempio, J. S.; Zatz, J. L., Flocculation effect of xanthan gum in pharmaceutical suspensions. Journal of Pharmaceutical Sciences 1980, 69 (10), 1209-1214.
40. Sancha, A. M., Review of coagulation technology for removal of arsenic: case of Chile. J Health Popul Nutr 2006, 24 (3), 267-72.
41. Staicu, L. C.; van Hullebusch, E. D.; Oturan, M. A.; Ackerson, C. J.; Lens, P. N., Removal of colloidal biogenic selenium from wastewater. Chemosphere 2015, 125, 130-8.
42. Plattes, M.; Bertrand, A.; Schmitt, B.; Sinner, J.; Verstraeten, F.; Welfring, J., Removal of tungsten oxyanions from industrial wastewater by precipitation, coagulation and flocculation processes. J Hazard Mater 2007, 148 (3), 613-5.
43. A., B.; A., S.; N., K.; M.-J., G.; J., J., Surface termination of hematite at environmental oxygen pressures: Experimental surface phase diagram. Phys. Rev. B 2007, 75, 233406.
44. Can, B. Z.; Boncukcuoglu, R.; Yilmaz, A. E.; Fil, B. A., Effect of some operational parameters on the arsenic removal by electrocoagulation using iron electrodes. Journal of Environmental Health Science and Engineering 2014, 12 (1), 95.
45. Fu, Z.-J.; Jiang, S.-K.; Chao, X.-Y.; Zhang, C.-X.; Shi, Q.; Wang, Z.-Y.; Liu, M.-L.; Sun, S.-P., Removing miscellaneous heavy metals by all-in-one ion exchange-nanofiltration membrane. Water Research 2022, 222, 118888.
46. Rahman, K. Z.; Wiessner, A.; Kuschk, P.; van Afferden, M.; Mattusch, J.; Müller, R. A., Removal and fate of arsenic in the rhizosphere of Juncus effusus treating artificial wastewater in laboratory-scale constructed wetlands. Ecological Engineering 2014, 69, 93-105.
47. Borah, S. N.; Sen, S.; Sarma, H.; Pakshirajan, K., Biological Remediation of Selenium in Soil and Water. In Handbook of Assisted and Amendment: Enhanced Sustainable Remediation Technology, 2021; pp 403-421.
48. Perendija, J.; Veličković, Z. S.; Cvijetić, I.; Lević, S.; Marinković, A. D.; Milošević, M.; Onjia, A., Bio-membrane based on modified cellulose, lignin, and tannic acid for cation and oxyanion removal: Experimental and theoretical study. Process Safety and Environmental Protection 2021, 147, 609-625.
49. Ortega, A.; Oliva, I.; Contreras, K. E.; González, I.; Cruz-Díaz, M. R.; Rivero, E. P., Arsenic removal from water by hybrid electro-regenerated anion exchange resin/electrodialysis process. Separation and Purification Technology 2017, 184, 319-326.
50. Zhou, B.-W.; Zhang, H.-Z.; Xu, Z.-L.; Tang, Y.-J., Interfacial polymerization on PES hollow fiber membranes using mixed diamines for nanofiltration removal of salts containing oxyanions and ferric ions. Desalination 2016, 394, 176-184.
51. Cavalca, L.; Corsini, A.; Zaccheo, P.; Andreoni, V.; Muyzer, G., Microbial transformations of arsenic: perspectives for biological removal of arsenic from water. Future Microbiology 2013, 8 (6), 753-768.

52. Katsoyiannis, I. A.; Zouboulis, A. I., Application of biological processes for the removal of arsenic from groundwaters. Water Research 2004, 38 (1), 17-26.
53. Zoroufchi Benis, K.; McPhedran, K. N.; Soltan, J., Selenium removal from water using adsorbents: A critical review. Journal of Hazardous Materials 2022, 424, 127603.
54. Börsig, N.; Scheinost, A. C.; Schild, D.; Neumann, T., Mechanisms of selenium removal by partially oxidized magnetite nanoparticles for wastewater remediation. Applied Geochemistry 2021, 132, 105062.
55. Filippov, L. O.; Silva, L. A.; Pereira, A. M.; Bastos, L. C.; Correia, J. C. G.; Silva, K.; Piçarra, A.; Foucaud, Y., Molecular models of hematite, goethite, kaolinite, and quartz: Surface terminations, ionic interactions, nano topography, and water coordination. Colloids and Surfaces A: Physicochemical and Engineering Aspects 2022, 650, 129585.
56. Ugwuja, C. G.; Bayode, A. A.; Olorunnisola, D.; Unuabonah, E. I., Occurrence and Management of Selenium Oxyanions in Water. In Progress and Prospects in the Management of Oxyanion Polluted Aqua Systems, Oladoja, N. A.; Unuabonah, E. I., Eds. Springer International Publishing: Cham, 2021; pp 103-128.
57. Wang, Z.; Zhang, H.; Ren, J.; Lin, X.; Han, T.; Liu, J.; Li, J., Predicting adsorption ability of adsorbents at arbitrary sites for pollutants using deep transfer learning. npj Computational Materials 2021, 7 (1), 19.
58. Weidner, E.; Ciesielczyk, F. Removal of Hazardous Oxyanions from the Environment Using Metal-Oxide-Based Materials Materials [Online], 2019.
59. Hua, M.; Zhang, S.; Pan, B.; Zhang, W.; Lv, L.; Zhang, Q., Heavy metal removal from water/wastewater by nanosized metal oxides: A review. Journal of Hazardous Materials 2012, 211-212, 317-331.
60. Huang, X.; Hou, X.; Song, F.; Zhao, J.; Zhang, L., Facet-Dependent Cr(VI) Adsorption of Hematite Nanocrystals. Environ Sci Technol 2016, 50 (4), 1964-72.
61. Lin, T.-F.; Wu, J.-K., Adsorption of Arsenite and Arsenate within Activated Alumina Grains: Equilibrium and Kinetics. Water Research 2001, 35 (8), 2049-2057.
62. Gupta, S.; Anh Nguyen, N.; Muhich, C. L., Surface water H-bonding network is key controller of selenate adsorption on [012] α-alumina: An Ab-initio study. Journal of Colloid and Interface Science 2022, 617, 136-146.
63. Ji, Y.; Li, L.; Wang, Y.-t., Selenium removal by activated alumina in batch and continuous-flow reactors. Water Environment Research 2020, 92 (1), 51-59.
64. Su, T.; Guan, X.; Gu, G.; Wang, J., Adsorption characteristics of As(V), Se(IV), and V(V) onto activated alumina: Effects of pH, surface loading, and ionic strength. Journal of Colloid and Interface Science 2008, 326 (2), 347-353.
65. Trussell, R., A. Trussell, AND P. Kreft. SELENIUM REMOVAL FROM GROUND WATER USING ACTIVATED ALUMINA; EPA: 2002.
66. Meher, A. K.; Jadhav, A.; Labhsetwar, N.; Bansiwal, A., Simultaneous removal of selenite and selenate from drinking water using mesoporous activated alumina. Applied Water Science 2019, 10 (1), 10.
67. Peak, D., Adsorption mechanisms of selenium oxyanions at the aluminum oxide/water interface. Journal of Colloid and Interface Science 2006, 303 (2), 337-345.
68. Goldberg, S., Modeling Selenite Adsorption Envelopes on Oxides, Clay Minerals, and Soils using the Triple Layer Model. Soil Science Society of America Journal 2013, 77 (1), 64-71.

69. Xu, T.; Catalano, J. G., Effects of Ionic Strength on Arsenate Adsorption at Aluminum Hydroxide–Water Interfaces. Soil Systems 2018, 2 (1), 1.
70. Guimarães, W. G.; de Lima, G. F.; Duarte, H. A., Comparative DFT study of the oxy(hydr)oxides of iron and aluminum – structural, electronic and surface properties. Surface Science 2021, 708, 121821.
71. He, G.; Zhang, M.; Pan, G., Influence of pH on Initial Concentration Effect of Arsenate Adsorption on TiO2 Surfaces: Thermodynamic, DFT, and EXAFS Interpretations. The Journal of Physical Chemistry C 2009, 113 (52), 21679-21686.
72. Ali, I.; Shrivastava, V., Recent advances in technologies for removal and recovery of selenium from (waste)water: A systematic review. Journal of Environmental Management 2021, 294, 112926.
73. Pincus, L. N.; Rudel, H. E.; Petrović, P. V.; Gupta, S.; Westerhoff, P.; Muhich, C. L.; Zimmerman, J. B., Exploring the Mechanisms of Selectivity for Environmentally Significant Oxo-Anion Removal during Water Treatment: A Review of Common Competing Oxo-Anions and Tools for Quantifying Selective Adsorption. Environmental Science & Technology 2020, 54 (16), 9769-9790.
74. Rudel, H. E.; Lane, M. K. M.; Muhich, C. L.; Zimmerman, J. B., Toward Informed Design of Nanomaterials: A Mechanistic Analysis of Structure–Property–Function Relationships for Faceted Nanoscale Metal Oxides. ACS Nano 2020, 14 (12), 16472-16501.
75. Youngran, J.; Fan, M.; Van Leeuwen, J.; Belczyk, J. F., Effect of competing solutes on arsenic(V) adsorption using iron and aluminum oxides. Journal of Environmental Sciences 2007, 19 (8), 910-919.
76. Yamani, J. S.; Lounsbury, A. W.; Zimmerman, J. B., Adsorption of selenite and selenate by nanocrystalline aluminum oxide, neat and impregnated in chitosan beads. Water Research 2014, 50, 373-381.
77. Yin, Y. B.; Guo, S. J.; Heck, K. N.; Clark, C. A.; Coonrod, C. L.; Wong, M. S., Treating Water by Degrading Oxyanions Using Metallic Nanostructures. Acs Sustain Chem Eng 2018, 6 (9), 11160-11175.
78. Lounsbury, A. W.; Wang, R.; Plata, D. L.; Billmyer, N.; Muhich, C.; Kanie, K.; Sugimoto, T.; Peak, D.; Zimmerman, J. B., Preferential adsorption of selenium oxyanions onto {110} and {012} nano-hematite facets. J Colloid Interface Sci 2019, 537, 465-474.
79. Shi, Q.; Yan, L.; Chan, T.; Jing, C., Arsenic Adsorption on Lanthanum-Impregnated Activated Alumina: Spectroscopic and DFT Study. ACS Applied Materials & Interfaces 2015, 7 (48), 26735-26741.
80. Villalobos, M.; Pérez-Gallegos, A., Goethite surface reactivity: A macroscopic investigation unifying proton, chromate, carbonate, and lead(II) adsorption. J Colloid Interf Sci 2008, 326 (2), 307-323.
81. Villalobos, M.; Cheney, M. A.; Alcaraz-Cienfuegos, J., Goethite surface reactivity: II. A microscopic site-density model that describes its surface area-normalized variability. J Colloid Interf Sci 2009, 336 (2), 412-422.
82. Doane, T. A., The Abiotic Nitrogen Cycle. ACS Earth and Space Chemistry 2017, 1 (7), 411-421.

83. Huno, S. K. M.; Rene, E. R.; van Hullebusch, E. D.; Annachhatre, A. P., Nitrate removal from groundwater: a review of natural and engineered processes. Journal of Water Supply: Research and Technology-Aqua 2018, 67 (8), 885-902.
84. Wang, Z.; Richards, D.; Singh, N., Recent discoveries in the reaction mechanism of heterogeneous electrocatalytic nitrate reduction. Catalysis Science & Technology 2021, 11 (3), 705-725.
85. Li, J.; Zhan, G.; Yang, J.; Quan, F.; Mao, C.; Liu, Y.; Wang, B.; Lei, F.; Li, L.; Chan, A. W. M.; Xu, L.; Shi, Y.; Du, Y.; Hao, W.; Wong, P. K.; Wang, J.; Dou, S.-X.; Zhang, L.; Yu, J. C., Efficient Ammonia Electrosynthesis from Nitrate on Strained Ruthenium Nanoclusters. Journal of the American Chemical Society 2020, 142 (15), 7036-7046.
86. Bishayee, B.; Chatterjee, R. P.; Ruj, B.; Chakrabortty, S.; Nayak, J., Strategic management of nitrate pollution from contaminated water using viable adsorbents: An economic assessment-based review with possible policy suggestions. Journal of Environmental Management 2022, 303, 114081.
87. Carvalho, O. Q.; Marks, R.; Nguyen, H. K. K.; Vitale-Sullivan, M. E.; Martinez, S. C.; Árnadóttir, L.; Stoerzinger, K. A., Role of Electronic Structure on Nitrate Reduction to Ammonium: A Periodic Journey. Journal of the American Chemical Society 2022, 144 (32), 14809-14818.
88. Liu, J.-X.; Richards, D.; Singh, N.; Goldsmith, B. R., Activity and Selectivity Trends in Electrocatalytic Nitrate Reduction on Transition Metals. ACS Catalysis 2019, 9 (8), 7052-7064.
89. Li, Y.; Zhang, L. A.; Qin, Y.; Chu, F.; Kong, Y.; Tao, Y.; Li, Y.; Bu, Y.; Ding, D.; Liu, M., Crystallinity Dependence of Ruthenium Nanocatalyst toward Hydrogen Evolution Reaction. ACS Catalysis 2018, 8 (7), 5714-5720.
90. Hu, T.; Wang, C.; Wang, M.; Li, C. M.; Guo, C., Theoretical Insights into Superior Nitrate Reduction to Ammonia Performance of Copper Catalysts. ACS Catalysis 2021, 11 (23), 14417-14427.
91. Wang, Y.; Qin, X.; Shao, M., First-principles mechanistic study on nitrate reduction reactions on copper surfaces: Effects of crystal facets and pH. Journal of Catalysis 2021, 400, 62-70.
92. Sanchis, I.; Diaz, E.; Pizarro, A. H.; Rodriguez, J. J.; Mohedano, A. F., Nitrate reduction with bimetallic catalysts. A stability-addressed overview. Separation and Purification Technology 2022, 290, 120750.
93. Wang, Z.; Ortiz, E. M.; Goldsmith, B. R.; Singh, N., Comparing electrocatalytic and thermocatalytic conversion of nitrate on platinum–ruthenium alloys. Catalysis Science & Technology 2021, 11 (21), 7098-7109.
94. Wang, Y.; Xu, A.; Wang, Z.; Huang, L.; Li, J.; Li, F.; Wicks, J.; Luo, M.; Nam, D.-H.; Tan, C.-S.; Ding, Y.; Wu, J.; Lum, Y.; Dinh, C.-T.; Sinton, D.; Zheng, G.; Sargent, E. H., Enhanced Nitrate-to-Ammonia Activity on Copper–Nickel Alloys via Tuning of Intermediate Adsorption. Journal of the American Chemical Society 2020, 142 (12), 5702-5708.
95. Li, P.; Jin, Z.; Fang, Z.; Yu, G., A single-site iron catalyst with preoccupied active centers that achieves selective ammonia electrosynthesis from nitrate. Energy & Environmental Science 2021, 14 (6), 3522-3531.

96. Niu, H.; Zhang, Z.; Wang, X.; Wan, X.; Shao, C.; Guo, Y., Theoretical Insights into the Mechanism of Selective Nitrate-to-Ammonia Electroreduction on Single-Atom Catalysts. Advanced Functional Materials 2021, 31 (11), 2008533.
97. Cai, J.; Wei, Y.; Cao, A.; Huang, J.; Jiang, Z.; Lu, S.; Zang, S.-Q., Electrocatalytic nitrate-to-ammonia conversion with ~100% Faradaic efficiency via single-atom alloying. Applied Catalysis B: Environmental 2022, 316, 121683.
98. Chen, F.-Y.; Wu, Z.-Y.; Gupta, S.; Rivera, D. J.; Lambeets, S. V.; Pecaut, S.; Kim, J. Y. T.; Zhu, P.; Finfrock, Y. Z.; Meira, D. M.; King, G.; Gao, G.; Xu, W.; Cullen, D. A.; Zhou, H.; Han, Y.; Perea, D. E.; Muhich, C. L.; Wang, H., Efficient conversion of low-concentration nitrate sources into ammonia on a Ru-dispersed Cu nanowire electrocatalyst. Nature Nanotechnology 2022, 17 (7), 759-767.
99. Calle-Vallejo, F.; Huang, M.; Henry, J. B.; Koper, M. T. M.; Bandarenka, A. S., Theoretical design and experimental implementation of Ag/Au electrodes for the electrochemical reduction of nitrate. Physical Chemistry Chemical Physics 2013, 15 (9), 3196-3202.
100. Gao, Q.; Pillai, H. S.; Huang, Y.; Liu, S.; Mu, Q.; Han, X.; Yan, Z.; Zhou, H.; He, Q.; Xin, H.; Zhu, H., Breaking adsorption-energy scaling limitations of electrocatalytic nitrate reduction on intermetallic CuPd nanocubes by machine-learned insights. Nature Communications 2022, 13 (1), 2338.
101. Wang, S.; Zeng, X.; Lin, J.; Yuan, Z.; Qu, S.; Zhang, B.; Pan, Y.; Chen, N.; Chen, W.; Jia, Y., Molecular Structure of Molybdate Adsorption on Goethite at pH 5–8: A Combined DFT + U, EXAFS, and Ab Initio XANES Study. The Journal of Physical Chemistry C 2021, 125 (40), 22052-22063.
102. Ramadugu, S. K.; Mason, S. E., DFT Study of Antimony(V) Oxyanion Adsorption on α-Al2O3(1$\bar{1}$02). The Journal of Physical Chemistry C 2015, 119 (32), 18149-18159.
103. Nie, X.; Luo, W.; Janik, M. J.; Asthagiri, A., Reaction mechanisms of CO2 electrochemical reduction on Cu(111) determined with density functional theory. Journal of Catalysis 2014, 312, 108-122.
104. Rostamikia, G.; Mendoza, A. J.; Hickner, M. A.; Janik, M. J., First-principles based microkinetic modeling of borohydride oxidation on a Au(111) electrode. Journal of Power Sources 2011, 196 (22), 9228-9237.
105. Kubicki, J. D.; Kwon, K. D.; Paul, K. W.; Sparks, D. L., Surface complex structures modelled with quantum chemical calculations: carbonate, phosphate, sulphate, arsenate and arsenite. European Journal of Soil Science 2007, 58 (4), 932-944.
106. Corum, K. W.; Mason, S. E., Using density functional theory to study shape-reactivity relationships in Keggin Al-nanoclusters. Water Research 2016, 102, 413-420.
107. Sun, W.; Ceder, G., A topological screening heuristic for low-energy, high-index surfaces. Surface Science 2018, 669, 50-56.

CHAPTER 2

RESEARCH METHODS

2.1 Brief review of quantum chemistry and Density Functional Theory (DFT)

I use Density Functional Theory (DFT) to calculate minimum energy configuration for adsorption reactions, as well as meta-stable and transition states of reaction pathways on catalytic surfaces. In this section, I briefly provide the overview of the concepts of quantum chemistry and DFT which are important for understanding and interpreting the results. Cramer[1] and other introductory DFT books are recommended for further reading.

The Schrödinger equation is the fundamental equation in quantum mechanics; it is the "equation of motion" of quantum particles, analogous to Newton's Law for classical particles. The Schrödinger equation states that there exists a Hamiltonian operator (H) which acts upon the wave-function (Ψ) of a chemical system to return the energy of the system (E):

$$H\Psi = E\Psi \qquad eq.\ 2.1$$

Wavefunction, Ψ, an eigenfunction, is by itself uninterpretable and physically unobservable. However, the integral of Ψ with its complex conjugate Ψ^*, $\int \Psi\Psi^* dx$, gives the probability of finding the particle in a region.

$$P(x, x+\delta x) = \ \psi\psi^*\,\delta x \qquad eq.\ 2.2$$

The probability of finding a particle in all space is always equal to 1. Therefore, the constraint on the wavefunction is:

$$P(-\infty,\infty) = \iiint_{-\infty}^{\infty} \psi\psi^* dx\, dydz = <\psi^*|\psi> = 1 \qquad eq.\ 2.3$$

The Hamiltonian operator considers all the energy contribution of the system. For a simple system (i.e., no external electric or magnetic field, heavy elements etc.), the Hamiltonian operator is the summation of kinetic and potential energies of each particle (electrons and nuclei) of the system:

$$H = -\sum_{i}\frac{h^2}{4\pi m_e}\nabla_{\mathrm{i}}^2 - \sum_{k}\frac{h^2}{4\pi m_k}\nabla_{\mathrm{k}}^2 - \sum_{k}\sum_{i}\frac{e^2 Z_k}{r_{ik}} + \sum_{i<j}\frac{e^2}{r_{ij}} + \sum_{k<l}\frac{e^2 Z_k Z_l}{r_{kl}} \quad eq.\ 2.4$$

Table 2.1: Variables in Equation 2.4

i and j	Number of electrons
k and l	Number of nuclei
h	Planks constant
m_e	Mass of electron
m_k	Mass of nucleus
$\nabla_i^2 : \frac{\partial^2}{\partial x_i^2} + \frac{\partial^2}{\partial y_i^2} + \frac{\partial^2}{\partial z_i^2}$	Laplacian operator
e	Charge of electron
Z	Atomic number
r_{ab}	Distance between particle a and b

Table 2.2: Terms in Equation 2.4

$-\sum_{i}\frac{h^2}{4\pi m_e}\nabla_{\mathrm{i}}^2$	Kinetic energy of electron
$-\sum_{k}\frac{h^2}{4\pi m_k}\nabla_{\mathrm{k}}^2$	Kinetic energy of nuclei
$-\sum_{k}\sum_{i}\frac{e^2 Z_k}{r_{ik}}$	The attraction of electron to nuclei
$\sum_{i<j}\frac{e^2}{r_{ij}}$	Interelectronic repulsion
$\sum_{k<l}\frac{e^2 Z_k Z_l}{r_{kl}}$	Internuclear repulsion

It is mathematically possible to calculate an analytical solution to the Schrödinger equation describing the Hydrogen atom; however, this is not the case for systems with more electrons, and it becomes necessary to make simplifying assumptions to reach a solution.

To reduce the number of variables in eq. 2.4, the Born-Oppenheimer Approximation[2] assumes that the nuclei have fixed positions. This assumption is derived from the fact that nuclei are slow moving particles as compared to electrons. Therefore, the electronic Schrödinger equation is:

$$(H_{el} + V_N)\Psi_{el}(q_i; q_k) = E_{el}\Psi_{el}(q_i; q_k) \qquad eq.\ 2.5$$

The H_{el}, the Hamiltonian operator for electronic components, includes the 1st ,3rd and 4th term of eq. 2.4. The 2nd and 5th term are constants, 0 and V_N respectively. The q_i and q_k are independent variables and parameters (nuclear coordinates) of electronic wavefunction. The E_{el} is the 'electronic energy' of the system. The Hartree-product wave function assumes that the electrons do not interact with each other:

$$\Psi_{HP} = \psi_1\psi_2 \ldots . \psi_{\psi_N} \qquad eq.\ 2.6$$

The e-e interactions is added to every electron Hamiltonian (h_i) using the mean-field approximation:

$$V_i\{j\} = \sum_{j \neq i} \frac{p_j}{r_{ij}}\, dr \qquad eq.\ 2.7$$

where p_j is the charge density associated with electron j. Therefore,

$$H = \sum_{1}^{N} h_i = \sum_{1}^{N} \left(-\frac{1}{2}\nabla_i^2 - \sum_{k=1}^{M} \frac{Z_k}{r_{ik}} + V_i\{j\} \right) \qquad eq.\ 2.8$$

The e-e repulsions are doubly counted in Eq. 2.8. Therefore, the final energy is computed as:

$$E = \sum_i \varepsilon_i - \frac{1}{2} \sum_{i \neq j} \iint \frac{|\psi_i|^2 |\psi_j|^2}{r_{ij}} dr_i dr_j \qquad eq.\ 2.9$$

The problem of unknow Ψ, remains, which is required to solve eq. 2.8. An initial guess for the wave function (Ψ_1) for molecular orbitals which are used to construct single-electron h operators. By solving eq. 2.8 and 2.9 we get a new set of wavefunctions (Ψ_2) which can differ from first guess. The new set Ψ_2s' are used in the repeated cycle to solve eq. 2.8 in an iterative 'Self-Consistent Field (SCF)' method until a convergence is achieved and $\Psi_{n+1} \approx \Psi_n$.

For the initial guess wavefunction (Ψ_1), a basis set is constructed by summing a basis function, $\varphi_{\mu,i}$ multiplied by a coefficient ($c_{\mu,i}$). This gives us a wavefunction of each occupied molecular orbital:

$$\psi_i = \sum c_{\mu,i} \varphi_{\mu,i} \qquad eq. 2.10$$

Selecting a correct basic basis set is important for starting any quantum calculations. For molecular simulations, gaussian functions are used as the basis functions, which closely match atomic-like orbitals. For periodic systems, like those used in this study (i.e., crystals, metals and metal oxides and their surfaces), Planewave basis sets are used, which are periodic in nature and are represented by summations of *sines and cosines*. Even though they lose some physicality, they are easy to operate mathematically.

The Variational Principle is used to find ground state energy of the system. The Variational Principle states the ground state energy will always be smaller than or equal to the energy calculated by any wavefunction (Ψ):

$$E_0 \leq \frac{\int \Psi \hat{H} \Psi dx}{\int \Psi \Psi \, dx} = \frac{< \Psi | \hat{H} | \Psi >}{< \Psi | \Psi >} \qquad eq.\ 2.11$$

The coefficients of the basis functions ($c_{\mu,i}$) are determined by minimizing the energy with respect to the free variables (coefficients), i.e., the point where following determinant is zero:

$$\frac{\partial < \epsilon_i >}{\partial \mu} = \frac{\partial}{\partial \mu} \frac{< \sum c_{\mu,i} \varphi_{\mu,i} | \widehat{H_i} | \sum c_{\mu,i} \varphi_{\mu,i} >}{< \sum c_{\mu,i} \varphi_{\mu,i} | \sum c_{\mu,i} \varphi_{\mu,i} >} = 0 \qquad eq. 2.12$$

The energy calculated using variational principal is always higher than the true ground state energy of the system. This is because the energy of electron exchange and correlation is not considered. The exchange energy can be computed by using the Slater Determinant, which includes the spin states of the electron.

$$\Psi_{SD} = \frac{1}{\sqrt{N!}} \begin{bmatrix} \chi_1(1) & \cdots & \chi_N(1) \\ \vdots & \ddots & \vdots \\ \chi_1(N) & \cdots & \chi_N(N) \end{bmatrix} \qquad eq. 2.13$$

$$\chi_n(1) = \Psi_n(1)\alpha(1) \qquad eq. 2.14$$

$\alpha(1)$ is the spin of electron 1 and $\Psi_n(1)$ represent electron 1 in orbital n. Slater Determinant adds the energy required to exchange the electrons from one orbital to another. The electron correlation energy cannot be computed theoretically.

The Hartree-Fock Self-consistent Field method using the slater determinant is used to calculate low energy state minus the electronic correlation energy. However, the Hartree-Fock method is not widely used as:

(1) The computational time used to solve Hartree-Fock SCF methods increases by power function ($f(x) = x^4$) depending upon the number of electrons (x) in the simulation cell. This is because Hartree-Fock Hamiltonian includes 4 electron integral terms.

(2) Because of the mean field theory approximation, Hartree-Fock method cannot calculate electron correlation energy. Advance methods can be used to find it; however, they are very computationally expensive.

This led to the development of other ab-initio methods like Density Functional Theory to find the energy of the system using electron density. DFT is an interpretation of Schrödinger equation in terms of electron probability density (ρ(r)). The early work in Density Functional theory (DFT) can be traced back to early 1920's when Thomas and Fermi.[3] The legitimacy of DFT as a methodology was established by Hohenberg and Kohn in 1964 when they proved two foundational theorems:

(1) The Hohenberg-Kohn Existence theorem[4] which proved the presence of unique ground state density (ρ(r)) corresponding to each external potential (positive charge) (V_{ext}) and Hamiltonian.

(2) The Hohenberg-Kohn Variational Theorem[4] which, similar to MO theory, states that the minimum energy of the system can be calculated by SCF method using:

$$< \Psi|H|\Psi > = E \geq E_0 \qquad eq.\ 2.15$$

Hence, the energy of the system E[ρ(r)] is:

$$E[\rho(r)] = T_{ni}[p(r)] + V_{ne}[\rho(r)] + V_{ee}[\rho(r)] + \Delta T[\rho(r)] + \Delta V_{ee}[\rho(r)] \qquad eq.\ 2.16$$

Table 2.3: Terms in Equation 2.16

$T_{ni}[p(r)]$	Kinetic energy of non-interacting electrons	$\sum_{i}^{N} \langle \chi_i \left\| -\frac{1}{2}\Delta_i^2 \right\| \chi_i \rangle$
$V_{ne}[\rho(r)]$	Nuclear-electron interaction	$-\sum_{i}^{N} \langle \chi_i \left\| \sum_{k}^{nuclie} \frac{Z_k}{\lvert r_i - r_k \rvert} \right\| \chi_i \rangle$
$V_{ee}[\rho(r)]$	Electron-electron repulsion	$\sum_{i}^{N} \langle \chi_i \left\| \frac{1}{2} \int \frac{\rho(r')}{\lvert r_i - r' \rvert} dr' \right\| \chi_i \rangle$
$\Delta T[\rho(r)]$	Correction to kinetic energy deriving the interacting nature of electrons	
$\Delta V_{ee}[\rho(r)]$	All non-classical corrections to electron-electron repulsion energy	

The $\Delta T[\rho(r)]$ and $\Delta V_{ee}[\rho(r)]$ terms of eq. 2.16 are referred to as E_{XC}, or 'exchange-correlation' energy. Unlike HF, which is an approximation, DFT is an exact theory. However, E_{XC} does not have a defined form and is approximated using semi-empirical methods.

Non-classical electron-electron interactions and their kinetic energies are included using exchange-correlation functionals with empirical parameters:

$$E_{XC}[\rho(r)] = \int \rho(r)\varepsilon_{XC}[\rho(r)]dr \qquad eq.\ 2.17$$

Local Density approximation (LDA), Generalized gradient approximation (GGA), Meta-GGA or Hybrid-GGA functionals include exchange correlation energy. LDA, the simplest approximation among the three, assumes that the exchange energy depends only on the local density. Considering only the local value of exchange assumes homogenous electron gas and ignores the gradient change in the density. The gradient corrections are included in GGA exchange functionals as:

$$\varepsilon_{XC}^{GGA}[\rho(r)] = A \times \varepsilon_{XC}^{LDA}[\rho(r)] + B \times \Delta\varepsilon_{XC}\left[\frac{|\nabla\rho(r)|}{\rho^{\frac{4}{3}}(r)}\right] \qquad eq.\ 2.18$$

GGA functionals are developed to fit A and B based on fundamental laws and/or experimental energies. The common GGA functional include PW91, PBE, BLYP. To improve calculations, HF exact exchange is mixed into DFT functional:

$$E_x\big(\rho(r)\big) = (1 - X)E_{x-GGA} + XE_{exact} \qquad eq.\ 2.19$$

The exchange (Hybrid GGA) brings the wavefunction closer to the true minimum energy. However, the cost of the calculation increases from N^3 to N^4 upon hybridizing the exchange energy. Therefore, the choice of Exchange correlation functional is critical before performing any calculation as it affects the computational cost (LDA < GGA < meta-GGA < hybrid-GGA) and chemical accuracy (hybrid-GGA > meta-GGA > GGA > LDA).

Even with GGA or LDA, the N^3 scale has high computational cost. Pseudopotential approximations are employed DFT to evaluate the interactions of the valence states of an atom. By constructing a pseudopotential to match the true potential beyond a specified cut-off radius, the potential inside the cut-off radius can be approximated for simpler computations.[5] The use of crystal symmetry in periodic systems enables the reduction of the number of plane wave basis sets required to represent the electronic charge density. In addition, the minimum number of discrete points required in the simulation cell can be optimized by considering the Brillouin zone and applying the reciprocal space lattice, as prescribed by Bloch's theorem. These techniques are widely used in DFT calculations to accurately describe the electronic structure of materials.[6]

2.2 Computational set-up of metal/metal-oxide interface

I performed DFT studies in this dissertation using a generalized gradient approximation functional (Perdew-Burke Ernzerhof - PBE)[7], and the projected-augmented wave (PAW) method as implemented in the Vienna Ab initio Simulation Program (VASP).[8,9] I used PAW pseudopotentials[10] to reduce the computational cost of the calculations and explicitly describe the 1s orbital of H atoms, 2s and 2p orbitals of O & N atoms, 3s and 3p orbitals of Al & S atoms, and 3d and 4s orbitals of Sc, Ti, V, Cr, Mn, Fe, Co, Ni & Cu atoms, 4s and 4p orbitals of Ga, Se & As atoms, 4d and 5s orbitals of Mo, Ru & Pd atoms, 5s and 5p orbitals of In atom and 6s and 5d orbitals of Pt, Au & W atoms. DFT-D3 correction account for non-local van der Waals (vdW) interactions based on the method of Grimme et. al.[11]

I used periodic boundary calculations to calculate adsorption and reaction pathways using an infinite slab in 2 dimensions separated by vacuum space to represent metal or metal-oxide surfaces. The slabs considered here are more than four atomic layers thick. I used the pymatgen[12,13] surface generator module to generate the metal and metal-oxide interfaces (Figure 2.1).

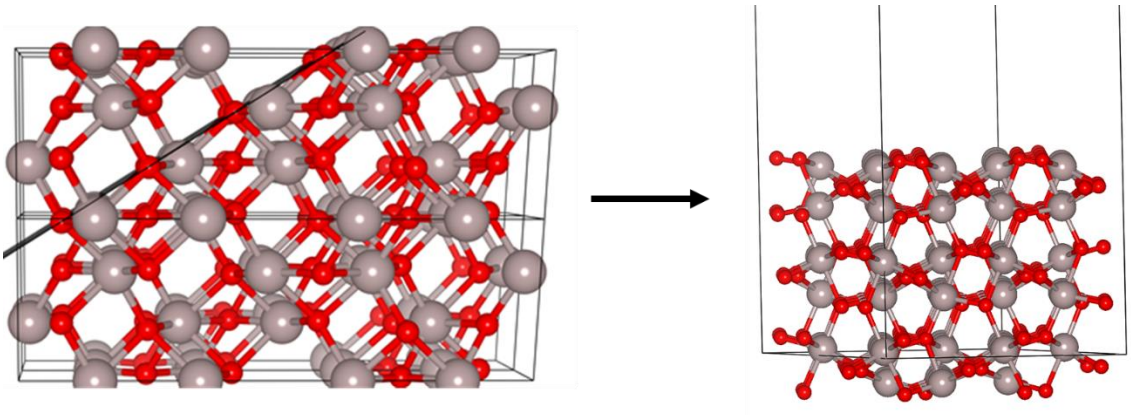

Figure 2.1: [012] Al_2O_3 interface generated using pymatgen[13] surface generator module from α-Al_2O_3 crystal.

The metal and metal-oxide slabs were first relaxed with no constraint to the shape of the simulation cell (only cell volume in constrained). The atoms in the bottom half of the relaxed slab were fixed during reaction and adsorption energy calculations to reduce the computational cost. Moreover, the slab maintained the crystallinity of the metal/metal-oxide nanoparticles, reduced over-relaxation of the atoms compared to molecular models, and provides improved accuracy in the reaction energies.[14] Typically, the reaction energies were calculated on the low surface energy facets of metal and metal oxides which have symmetric surface sites – [012] for Al_2O_3 and Fe_2O_3[15-17] and [111] for Cu and Pd, and [001] Ru surface,[18] However, the adsorption energies of Se and As oxo-anions on [012] and [001] Fe_2O_3 facets with different terminations were calculated in Chapter 5 to understand the role of surface species on adsorption. At least 10 Å vacuum space was added between periodic surface layers. Adsorption energies are calculated on metal and metal-oxide surfaces to confirm that the vacuum space between slabs was enough to reduce spurious interactions between infinite slabs (Figure 2.2). The wave function was constructed from a summation of plane waves and Brillouin zone sampling were performed for each interface until the

energy difference was less than 0.01 eV. The objective specific parameters are detailed in each chapter. Crystal structure representations were obtained using VESTA.[19]

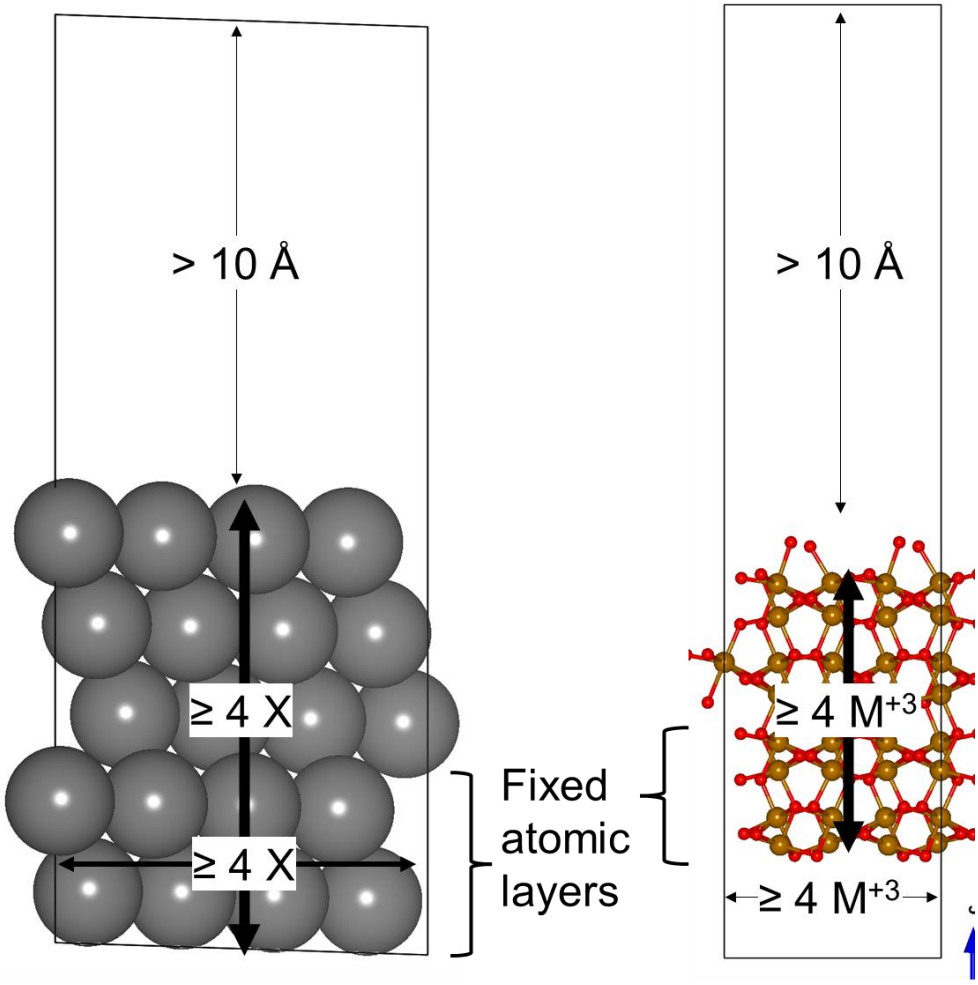

Figure 2.2: Standard periodic simulation cell used to calculate adsorption energies and reaction mechanism on Metal (Cu) (left) and metal-oxide (Fe_2O_3) (right) surfaces.

2.3 Inclusion of Van der Waals force correction in DFT calculations

Density Functional Theory averages the electron density per unit volume. This excludes the influence of van der Waals (vdW) forces or London dispersion forces which are caused by dipoles induced by instantaneous charge fluctuations.[20] Therefore, adsorption energies calculated on metal and metal-oxide surfaces using density functional theory are underestimated. The inclusion of van der Waals forces can be made to the DFT calculations by adding a dispersion correction term (E_{disp}) to a conventional DFT energy E_{tot}^{DFT}.[21]

$$E_{tot}^{DFT-dis} = E_{tot}^{DFT} + E_{disp} \qquad eq.\ 2.20$$

These corrections are achieved by DFT-D3 method of Grimme with zero-damping function,[11] DFT-D3 method with Becke-Johnson damping function,[22] DFT-ulg method,[23] or including nonlocal vdW-DF functionals proposed by Dion et. al.,[24] Lee et. al.,[25] Klimes et. al.[26,27] or Peng et al.[28]

The adsorption energy of selenate on the Fe_2O_3 surface was calculated to find the optimal van der Waals correction to use for the DFT calculations. The average time taken for five electronic steps is multiplied by 50 steps × 250 SCF steps to find the average time taken for structure configuration using a specific method of including the dispersion correction term. The results of adsorption energy vs. time taken are presented in Figure 2.3. As expected, the adsorption energy is less endothermic when dispersion calculations (0.20-0.56 eV) are added to the adsorption energy calculations. The variation in adsorption energy calculated using different methods is much smaller than the differences between adsorption energies for different configurational changes and competitive species. nonlocal vdW-DF functionals which have the least endothermic adsorption energies require 30-40

more hours to run a single simulation. Considering that hundreds of jobs per study are run, this would significantly increase the computational cost without significantly changing the results of my calculations. Therefore, the DFT-D3 method of Grimme with zero-damping function was included in all the surface energy calculations, which is easy to implement and does not increase the computational cost of running the simulations.

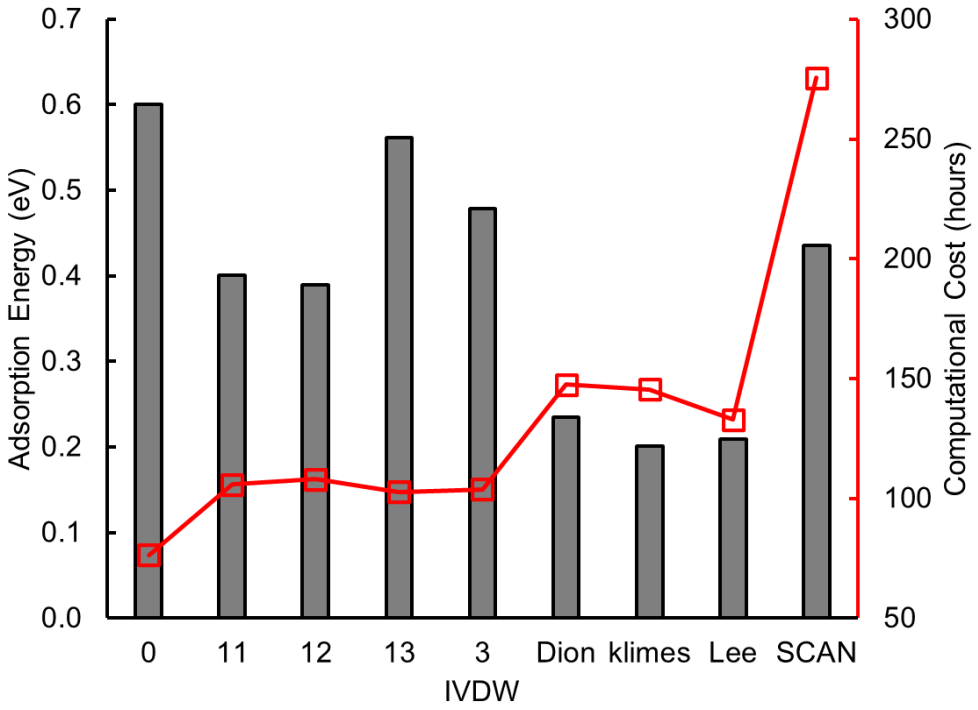

Figure 2.3: Adsorption energy and computational cost of using different Van der Waals force correction in DFT calculations.

2.4 Inclusion of solvent effects for adsorption energy calculations

The method of including solvent effects impacts both prediction quality and computational cost. There are two ways of including solvent effects: (a) filling vacuum space between slabs with explicit water molecules or (b) adding an implicit polarizable continuum dielectric of water solvents[29]. Incorporating water molecules in DFT calculation incurs significant computational expenses. Additionally, the dynamic nature of water

molecules in the solvent phase implies that even minor changes can significantly impact the overall energy of the simulation. Conversely, implicit solvents employ a parameterized methodology to incorporate a continuum model for solvent effects, thereby minimizing the incorporation of solvent atoms in the simulated system. However, with implicit solvent, the short-ranged solvent effects like hydrogen bonding are lost which may be critical for understanding the adsorption mechanism on hydrophilic metal-oxide surfaces.

The cleaved metal-oxygen (M-O) bonds on the metal-oxide surface are substituted with hydroxyl groups upon exposure to an aqueous environment.[30] The surface hydroxyl group protonates or deprotonates based on the pH of the solution and pKa values of surface hydroxyl groups. (Figure 2.4). The presence of the surface hydroxyl groups creates a dense water network comprised of hydrogen bonds that cannot be ignored when calculating adsorption energies. Therefore, to calculate the adsorption energy of oxo-anion on metal-oxide surfaces in chapters 3-5, I have used a Hybrid Solvent Model where only the first highly ordered interfacial water layer is included explicitly. The solvent effects beyond the first layer are considered by including a polarizable continuum dielectric in the vacuum layer. The validity of this model is explained in detail in Chapter 3.

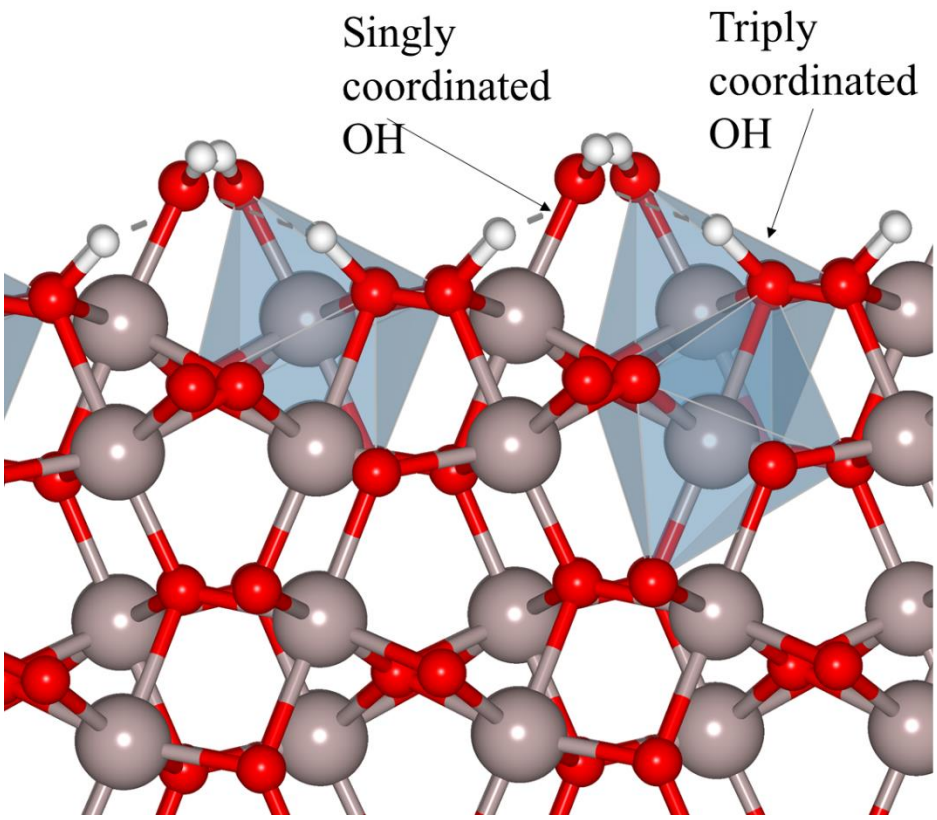

Figure 2.4: Neutral [012] Al_2O_3 surface with dissociated water molecules on the surface.

2.5 Calculating adsorption energies for charged species

Water molecules adsorbed onto metal surfaces form hexagonal or pentagonal clusters, depending on whether the surface is hexagonal closed-packed or non-hcp, respectively.[31] Incorporating these water clusters in DFT calculations would increase computational costs twofold: by expanding the number of initial configurations required to locate the lowest energy state and by increasing the size of the simulation cell. Since the computation of multiple meta-stable states is required to determine the optimum reaction mechanism for calculations performed on metal surfaces, calculating adsorption energies would necessitate a more significant computational expenditure than determining reaction pathways. Additionally, the periodicity over the water clusters would need to be preserved by increasing the simulation cell size from 4×4 to 6×6. As a result, implicit and explicit solvent effects in DFT calculations are currently disregarded in investigations of nitrate reduction mechanisms on metal surfaces. Nonetheless, the solvation energies of adsorbing species are included in the Hess cycle used to determine adsorption energies, which vary as a function of pH.

2.5.1 Inclusion of potential and pH effects at electrode interface

For reactions over electrode surface, the following approach was used to include electrochemical and pH effects in the final reaction energy and saddle point calculations in Chapter 6-8. I calculated the Gibbs free energy for the reaction steps on metal surface electrodes using the computation hydrogen electrode (CHE)[32] to include the voltage effects on Gibbs free energies:

$$G_{H^+} + G_{e^-} = \frac{1}{2} G_{H_2} - eU_{RHE} \qquad eq.\ 2.21$$

where U_{RHE} is applied potential with respect to the relative hydrogen electrode (RHE) and G_{H2} is the free energy of gaseous H_2. The adsorption of aqueous phase charged species are calculated using experimentally calculated solvation energies and pKa values obtained from CRC Handbook of Chemistry and Physics[33]

$$A^- + * \rightarrow A^* + e^- \qquad eq.\ 2.22$$

$$\Delta G_{ads}(A^-) = G_{A^*} + G_{e^-} - G_{A^-} - G_* \qquad eq.\ 2.23$$

$$\Delta G_{ads}(A^-) = G_{A^*} + \left[\frac{1}{2}G_{H_2} - eU_{RHE}\right] - \left[G_{HA} - \Delta G_{sol} - \Delta G_{protonation}\right] - G_* \qquad eq.\ 2.24$$

$\Delta G_{protonation}$ is the free energy of the association of A^- in solution with a proton, and is calculated as

$$\Delta G_{protonation} = G^\circ - 2.303kT(pK_a - pH) \qquad eq.\ 2.25$$

where k is the Boltzmann constant, T is the temperature, and pK_a is the experimental acid dissociation constant of HA[34]. The Hess cycle is explained further in chapter 6.

2.6 References

1. Cramer, C. J., Foundations of Molecular Orbital Theory. In Essentials of Computational Chemistry, Wiley: 2017; Vol. 2nd, pp 125-130.
2. Born, M.; Oppenheimer, R., Zur Quantentheorie der Molekeln. Annalen der Physik 1927, 389 (20), 457-484.
3. Dirac, P. A. M.; Fowler, R. H., Quantum mechanics of many-electron systems. Proceedings of the Royal Society of London. Series A, Containing Papers of a Mathematical and Physical Character 1929, 123 (792), 714-733.
4. Hohenberg, P.; Kohn, W., Inhomogeneous Electron Gas. Physical Review 1964, 136 (3B), B864-B871.
5. Chelikowsky, J. R., 1.01 - Electrons in Semiconductors: Empirical and ab initio Pseudopotential Theories. In Comprehensive Semiconductor Science and Technology, Bhattacharya, P.; Fornari, R.; Kamimura, H., Eds. Elsevier: Amsterdam, 2011; pp 1-41.
6. Monkhorst, H. J.; Pack, J. D., Special points for Brillouin-zone integrations. Phys Rev B 1976, 13 (12), 5188-5192.

7. Perdew, J. P.; Burke, K.; Ernzerhof, M., Generalized gradient approximation made simple. Phys Rev Lett 1996, 77 (18), 3865-3868.
8. Kresse, G.; Furthmuller, J., Efficient iterative schemes for ab initio total-energy calculations using a plane-wave basis set. Phys Rev B 1996, 54 (16), 11169-11186.
9. Kresse, G.; Furthmüller, J., Efficiency of ab-initio total energy calculations for metals and semiconductors using a plane-wave basis set. Computational Materials Science 1996, 6 (1), 15-50.
10. Kresse, G.; Joubert, D., From ultrasoft pseudopotentials to the projector augmented-wave method. Physical Review B 1999, 59 (3), 1758-1775.
11. Grimme, S.; Antony, J.; Ehrlich, S.; Krieg, H., A consistent and accurate ab initio parametrization of density functional dispersion correction (DFT-D) for the 94 elements H-Pu. J Chem Phys 2010, 132 (15), 154104.
12. Sun, W.; Ceder, G., Efficient creation and convergence of surface slabs. Surface Science 2013, 617, 53-59.
13. Tran, R.; Xu, Z.; Radhakrishnan, B.; Winston, D.; Sun, W.; Persson, K. A.; Ong, S. P., Surface energies of elemental crystals. Sci Data 2016, 3, 160080.
14. Paul, K. W.; Kubicki, J. D.; Sparks, D. L., Sulphate adsorption at the Fe (hydr)oxide–H2O interface: comparison of cluster and periodic slab DFT predictions. European Journal of Soil Science 2007, 58 (4), 978-988.
15. Kitayama, M.; Glaeser, A. M., The Wulff Shape of Alumina: III, Undoped Alumina. Journal of the American Ceramic Society 2002, 85 (3), 611-622.
16. Lagauche, M.; Larmier, K.; Jolimaitre, E.; Barthelet, K.; Chizallet, C.; Favergeon, L.; Pijolat, M., Thermodynamic Characterization of the Hydroxyl Group on the γ-Alumina Surface by the Energy Distribution Function. The Journal of Physical Chemistry C 2017, 121 (31), 16770-16782.
17. Jakub, Z.; Kraushofer, F.; Bichler, M.; Balajka, J.; Hulva, J.; Pavelec, J.; Sokolović, I.; Müllner, M.; Setvin, M.; Schmid, M.; Diebold, U.; Blaha, P.; Parkinson, G. S., Partially Dissociated Water Dimers at the Water–Hematite Interface. ACS Energy Letters 2019, 4 (2), 390-396.
18. Grassian, V. H., When Size Really Matters: Size-Dependent Properties and Surface Chemistry of Metal and Metal Oxide Nanoparticles in Gas and Liquid Phase Environments. The Journal of Physical Chemistry C 2008, 112 (47), 18303-18313.
19. Momma, K.; Izumi, F., VESTA 3 for three-dimensional visualization of crystal, volumetric and morphology data. Journal of applied crystallography 2011, 44 (6), 1272-1276.
20. Chiter, F.; Nguyen, V. B.; Tarrat, N.; Benoit, M.; Tang, H.; Lacaze-Dufaure, C., Effect of van der Waals corrections on DFT-computed metallic surface properties. Materials Research Express 2016, 3 (4), 046501.
21. Patra, A.; Bates, J. E.; Sun, J.; Perdew, J. P., Properties of real metallic surfaces: Effects of density functional semilocality and van der Waals nonlocality. Proceedings of the National Academy of Sciences 2017, 114 (44), E9188-E9196.

22. Schröder, H.; Creon, A.; Schwabe, T., Reformulation of the D3(Becke–Johnson) Dispersion Correction without Resorting to Higher than C6 Dispersion Coefficients. Journal of Chemical Theory and Computation 2015, 11 (7), 3163-3170.
23. Kim, H.; Choi, J.-M.; Goddard, W. A., III, Universal Correction of Density Functional Theory to Include London Dispersion (up to Lr, Element 103). The Journal of Physical Chemistry Letters 2012, 3 (3), 360-363.
24. Dion, M.; Rydberg, H.; Schröder, E.; Langreth, D. C.; Lundqvist, B. I., Van der Waals Density Functional for General Geometries. Phys Rev Lett 2004, 92 (24), 246401.
25. Lee, K.; Murray, É. D.; Kong, L.; Lundqvist, B. I.; Langreth, D. C., Higher-accuracy van der Waals density functional. Physical Review B 2010, 82 (8), 081101.
26. Klimeš, J.; Bowler, D. R.; Michaelides, A., Van der Waals density functionals applied to solids. Physical Review B 2011, 83 (19), 195131.
27. Klimeš, J.; Bowler, D. R.; Michaelides, A., Chemical accuracy for the van der Waals density functional. Journal of Physics: Condensed Matter 2010, 22 (2), 022201.
28. Peng, H.; Yang, Z.-H.; Perdew, J. P.; Sun, J., Versatile van der Waals Density Functional Based on a Meta-Generalized Gradient Approximation. Physical Review X 2016, 6 (4), 041005.
29. Mathew, K.; Sundararaman, R.; Letchworth-Weaver, K.; Arias, T. A.; Hennig, R. G., Implicit solvation model for density-functional study of nanocrystal surfaces and reaction pathways. J Chem Phys 2014, 140 (8), 084106.
30. McBriarty, M. E.; von Rudorff, G. F.; Stubbs, J. E.; Eng, P. J.; Blumberger, J.; Rosso, K. M., Dynamic Stabilization of Metal Oxide–Water Interfaces. Journal of the American Chemical Society 2017, 139 (7), 2581-2584.
31. Poissier, A.; Ganeshan, S.; Fernández-Serra, M. V., The role of hydrogen bonding in water–metal interactions. Physical Chemistry Chemical Physics 2011, 13 (8), 3375-3384.
32. Nørskov, J. K.; Rossmeisl, J.; Logadottir, A.; Lindqvist, L.; Kitchin, J. R.; Bligaard, T.; Jónsson, H., Origin of the Overpotential for Oxygen Reduction at a Fuel-Cell Cathode. The Journal of Physical Chemistry B 2004, 108 (46), 17886-17892.
33. Lide, D. R., CRC handbook of chemistry and physics. CRC press: 2004; Vol. 85.
34. Levanov, A. V.; Isaikina, O. Y.; Lunin, V. V., Dissociation constant of nitric acid. Russ. J. Phys. Chem. A 2017, 91 (7), 1221-1228.

CHAPTER 3

SURFACE WATER H-BONDING NETWORK IS KEY CONTROLLER OF SELENATE ADSORPTION ON [012] α-ALUMINA.

3.1 Abstract

Selenate adsorption onto metal oxide surfaces is a cost-effective method to remove the toxin from drinking water systems. However, the low selectivity of metal oxides requires frequent sorbent replacement. The design of selective adsorbents is stymied because the surface factors controlling selenate adsorption remain unknown. We calculate adsorption energies of selenate on the (0 1 2) α-Al_2O_3 surface using density functional theory to unravel the physics that controls adsorption. Our model is validated against experiment by correctly predicting selenate removal efficiency as a function pH. We find that the selenate adsorption energy on the anhydrous α-Al_2O_3 surface is surprisingly anti-correlated with the fully solvated adsorption energy; therefore, the direct interaction between adsorbate and sorbent is eliminated as the controlling mechanism. Rather, the change in number of surface hydrogen bonds after adsorption is the factor most correlated with the adsorption energy ($R^2 > 0.8$); and is thus determined to be the factor controlling selenate adsorption. We find that pH affects adsorption by controlling the number of surface protons available for H-bonding to selenate. This work demonstrates that adsorption prediction should not be made based on gas phase sorption energies and suggests that surface engineering which increases surface protonation may be an effective strategy for increasing selenate sorption.

3.2 Introduction

Selenium (Se) is a reactive non-metal which causes liver and kidney damage after prolonged exposure above 400µg/day.[1,2] The World Health Organization therefore recommends that drinking water contain less than 40 µg/L of total Se,[2] which is present in water as selenate (Se(VI)) and selenite (Se(IV))[3] oxo-anions. While selenite and selenate are both toxic and should be removed from water, selenate (Se(VI)) is more difficult to remove than selenite (Se(IV)) due to its more stable structure, slower reduction rates, lower adsorption on metal-oxides and organic ligand-based composites, and similar structure to its more prevent co-contaminant cousin – sulfate.[4-8] Centralized water treatment facilities decrease Se concentrations to below the exposure limit cost-effectively through processes such as ion-exchange (US \$0.06 m^{-3})[2]; however, such removal of Se concentrations below epidemiological levels is challenging in decentralized systems such as wells and small community water systems, if it is attempted at all. Other physio-chemical and biological treatment processes such as nanofiltration, reverse osmosis, reduction on ferrihydrite, or biological systems are often not economically feasible for use in distributed systems because of high cost and space requirements, low conversions, low efficiency in presence of other ions such as sulfate, phosphate and nitrate etc., fouling, post treatment requirements etc.[8] Under-the-sink adsorptive ion removal provides contaminant removal in distributed water systems while remaining low cost and easy to implement and operate, especially when compared to the reverse osmosis alternative. [9-11]

Aluminum, iron, manganese oxides and hydroxides and organic ligand-based composites are promising adsorbents for removing selenium oxo-anions from soils and water. While organic ligand-based composites such as N,N′-di(3-carboxysalicylidene)-3,4-

diamino-5-hydroxypyrazole have high removal efficiency (up to 95.5% from tap water) for selenite,[12-14] they have not yet been tested for their performance in removing selenate from real wastewater and in presence of other oxo-anions.[15-16] Moreover, they require advanced synthesis procedures and new structures must undergo extensive toxicity tests before their use beyond laboratory scale set-ups.[17] Metal-oxides, on the other hand, are already known to be non-toxic, abundant, simple to use, socio-culturally acceptable, and compliant with most local health and safety regulations; therefore, they are therefore rapidly deployable if they can be made selective.[3,18-22] Moreover, metal oxide adsorbents can be re-cycled by desorbing captured pollutants through processes like chemical-, electrochemical- or thermal-regeneration.[23]

Among candidate sorbents, activated alpha alumina (α-Al_2O_3) removes higher percentages of selenium (99%) than other common adsorbents such as activated carbon (87%) and chitin (49%).[18,24] However, the adsorption of selenate on alumina is strongly controlled by solution pH. At pH ~ 3, 1g/L hydrous alumina particles adsorb approximately 100% of the SeO_4^{2-} from 200 ml of 1.25 mM SeO_4^{2-}.[25] However, the adsorption capacity of alumina decreases with increasing basicity of the solution until pH 9, where the adsorption capacity is approximately 0%. While past literature has extensively documented this trend,[26-28] investigations as to the underlying surface chemistries which give rise to these trends are sparse. This lack of understanding limits rational sorbent design because it is unclear what properties, e.g., materials chemistry, crystal structure or exposed facet, etc., control adsorption, and therefore which properties should be tuned to improve SeO_4^{2+} adsorption.[29-31]

Experimentally unraveling the surface chemistry which enables high adsorption capacity is difficult because many phenomena are interdependent.[21,32] For example, changes in solution pH alter the protonation state of both selenate ($HSeO_4^{1-}$ or SeO_4^{2-} below or above pH 1.7), and the surface hydroxyl groups, (protonated below the ~8-9.6 pH (point of zero charge (PZC) of α-Al_2O_3) and is deprotonated above it)[25]. Additionally, pH is known to change the binding mechanism of selenate on α-Al_2O_3, where it switches between inner or outer sphere configurations.[33,34] Thus although experiments show that adsorption decreases significantly at pH above 7, it has not yet been able to explain why,[18,35,36] due to the extremely challenging nature of isolating individual causes and effects.[7, 37-39] Ab-initio methods, such as Density Functional Theory (DFT), provide a route to understand the fundamental controlling mechanisms of oxo-anion adsorption on metal-oxide surfaces through its ability to examine experimentally non-isolatable or rare cases, and thus delineate the extent to which individual effects and interactions contribute to oxo-anion adsorption.

Pioneering computational studies explored the adsorption of oxo-anions on small molecular clusters of metal oxides (generally monomers or dimers of the crystal formula unit) in order to confirm and understand experimental finding.[40] Adsorption geometries of adsorbate-adsorbent complexes were compared to experimental data such as infrared (IR) vibrational frequencies and extended X-ray absorption fine structure (EXAFS) spectroscopy to understand the nature of chemical and physical bonds between adsorbate and surface.[41-47] They found that the DFT cluster models can accurately predict the first and second shell interatomic distances of oxo-anion adsorbed complexes on metal-(hydr)oxide-H_2O interface.[42] However, molecular clusters inherently ignore long range

order effects such as surface solvation and band structure features such as magnetism, and therefore incorrectly predict adsorption energies and therefore an ability to predict likely structures and sorbent performance.[42,48] Periodic boundary condition slab models overcome the lack of crystalline order of cluster models, where 2D infinite slabs of the metal-oxide crystal represent the surface plane. This reduces over-relaxation of the atoms and provides improved description of the sorbent and thus accuracy in the adsorption energies.[42] Despite recent efforts, periodic models have not yet achieved sufficient accuracy to reproduce experimental adsorption trends, and therefore are not reliable for prediction and trend extraction.

This contribution aims to develop a surface adsorption model which accurately predicts the sorption behavior of selenate on the low energy (012) surface facet of Al_2O_3 as a function of pH, and, using this model, delineate the physics that controls selenate adsorption using DFT calculations. I achieve accurate representation of the surface adsorption through a hybrid explicit/implies solvation model. In depth analysis of these results demonstrate that the H-bonding network of the surface monolayer, not the inherent interaction between selenate and the surface, controls selenate adsorption.

3.3 Computational Methods

3.3.1 First-principle calculations

Density Functional Theory (DFT) calculations were performed using a generalized gradient approximation functional (Perdew-Burke Ernzerhof - PBE)[49], and the projected-augmented wave (PAW) method as implemented in the Vienna Ab initio Simulation Program (VASP).[50,51] PAW pseudopotentials[52] were used to reduce the computational cost

of the calculations and explicitly describe the 1s orbital of hydrogen atoms, 2s and 2p orbitals of oxygen atoms, and 3p, 3d, 4s, and 4p orbitals of aluminum and selenium atoms. Non-local van der Waals (vdW) interactions were accounted for through the DFT-D3 correction, based on the method of Grimme et. al.[53] Implicit water solvent was included using a polarizable continuum model with the water dielectric constant as implemented in the VASPsol module.[54] Adsorption energies were calculated between super cells containing the same number of electrons and atoms, rather than as non-interacting species in separate cells. This last fact was critical in achieving experimental parity. I attribute this finding to the differences in the background compensating jellium charge imposed when charged super cells are used.

The α-Al_2O_3 crystal was represented by a (012) facet slab super cell containing 2×1×3 primitive unit cells (α-$Al_{12}O_{18}$). I chose to investigate the (012) facet because it is a low surface energy facet, the largest constituent (47%) of the gibbsite particles[55,56], and has symmetric adsorption sites[55], simplifying DFT calculations. A 45 Å polarized continuum model implicit solvent filled the space separating the slabs. Such a large space was necessary to remove spurious interactions between atomic layers and any desorbed species in the solution. Desorbed selenate and water species were placed inside the implicit continuum solvent space of the simulation cell with intermolecular distance of at least 6 Å, to minimize Van der Waals interactions but retain solvated behavior (Appendix Figure A.1).

Wave functions were constructed using summations of plane waves with energies up to 500 eV. I found that there is only a 0.001 eV difference in adsorption energies calculated at 500 eV and 600 eV. Atomic geometries and system energies were calculated using a

2×2×1 gamma point centered Monkhorst-Pack k-point mesh, which showed only a 0.0001 eV difference with a 4×4×1 mesh grid. Atomic geometries were relaxed until atomic forces were less than 0.001 eV/Å. The crystal lattice constants obtained (a=b= 4.80Å, c=13.09Å, α=β=90° and γ=120°) match well with experimental results (a=b= 4.76Å, c=12.99Å, α=β=90° and γ=120°)[57].

HSE06 functional[58] calculations were used to validate the PBE results. I found that the HSE06 functional calculated adsorption energy of a SeO_4^{2-} in monodentate configuration on neutral alumina surface was only -0.085 eV more exothermic than the PBE functional. While the difference is non-negligible, it is within the expected error of the methods and do not invalidate the adsorption energy trends observed because the differences in adsorption energy were approximately 10 times higher than the energy differences caused by a change in functional. Thus, the PBE functional was used to perform all the remaining calculations due to its significantly lower computational cost, and the already high cost of including van der Waals, implicit solvent, and the large number of atoms and size of the system. Density of States (DOS) and Crystal Orbital Hamilton Populations (COHP) analysis were performed using vaspkit[59] and LOBSTER[60,61] software respectively. Crystal structure representations were obtained using VESTA.[62]

3.3.2 Hybrid Solvent Method

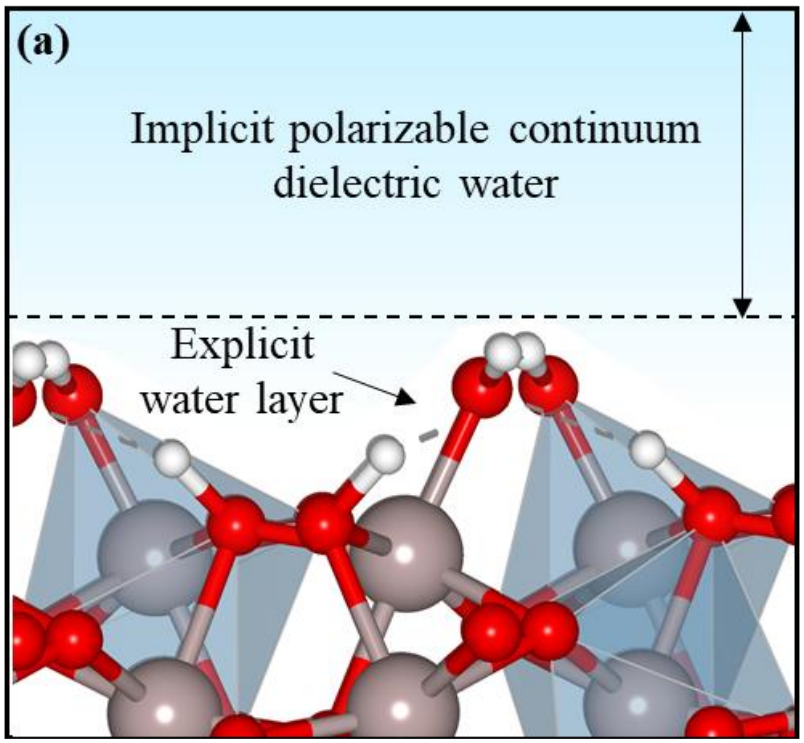

Figure 3.1: Hybrid Solvent Model demonstrating explicit interfacial water and implicit polarizable continuum dielectric. The gray, red, white spheres represent Al, O, H atoms, respectively.

Proper inclusion of solvent interactions with the oxo-anion and metal oxide surface was essential for the accurate calculation of adsorption energies. Incorporating an appropriate solvent distribution at the interface was challenging because it required identification of low energy configuration of highly flexible H-bonding networks. My model, based on micro-solvation concept[63], used one explicit monolayer of water or hydroxyl on the α-Al_2O_3 surface and a coupled polarizable continuum dielectric in the vacuum space to account for solvation beyond first layer (Figure 3.1). This mirrors the experimental X-ray reflectivity findings of Catalano et al. who demonstrated that after the first highly ordered interfacial water layer on the (012) α-Al_2O_3 surface, each addition layer of water decays towards disordered bulk configuration with non-uniform

characteristics.[64.65] I found that the adsorption energy and structure of H_2SeO_4 in monodentate configuration calculated using the HSM model matched that calculated using four explicit water layers which incurred a significantly higher cost, see Appendix Figure A.2. Thus, the HSM model was used in the remainder of this work.

3.3.3 Adsorption energy calculation parameters

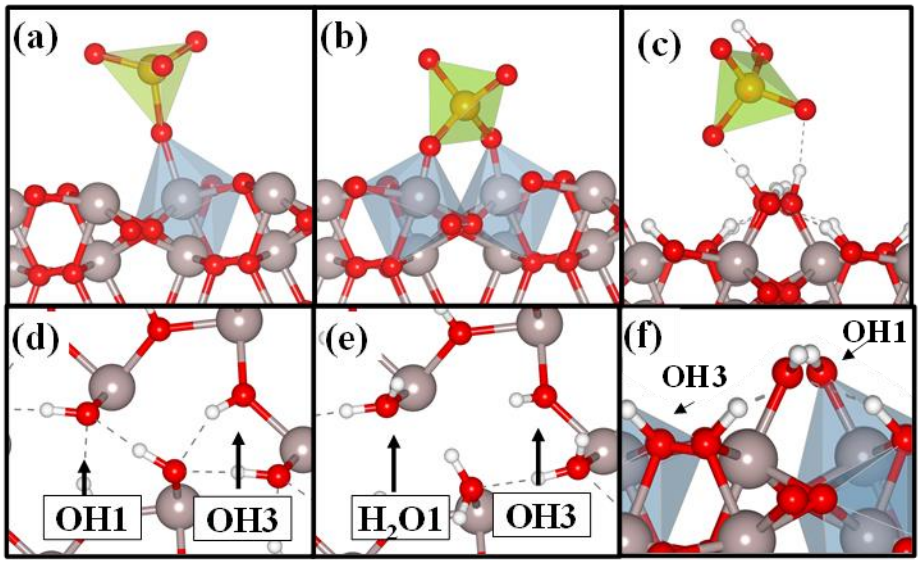

Figure 3.2: Side view of selenate adsorbed in (a) monodentate Monomolecular (MM), (b) bidentate monomolecular (BM) and (c) outer sphere configuration on (012) α-Al_2O_3. Top view of top view of (012) Al_2O_3 surface with dissociated (d) H_2O on neutral Al_2O_3 and (e) H_3O^+ on protonated Al_2O_3. (f) Side view of (012) Al_2O_3 surface with dissociated H_2O. OH1, OH3 and H_2O1 represent singly coordinated OH, triply coordinated OH and single coordinated H_2O, respectively. The grey, yellow, red, white spheres represent Al, Se, O and H atoms, respectively.

I considered both inner and outer sphere adsorption. In inner sphere adsorption the oxo-anion's oxygen atom bonds directly with surface Al atoms, replacing water/hydroxyl groups. I considered seven possible inner sphere monomolecular adsorption configurations for SeO_4^{2-} on (012) α-Al_2O_3 surface, where each bonding oxygen of the oxo-anion replaces one hydroxyl. These configurations included one monodentate (MM), three bidentate (BM) and three tridentate configurations (TM). I also examined two bimolecular configurations

(monodentate bimolecular (MB) and bidentate bimolecular (BB)). In these configurations, two oxygens of the oxo-anion bond to the surface and replace two hydroxyl groups. All the configurations considered are presented in Figure 3.3. I found that all the bimolecular configurations relaxed into mono-molecular configurations (Figure 3.4). Additionally, the tridentate adsorption configurations were highly endothermic. Hence, bimolecular, and tridentate configurations are not further discussed in the paper. In outer sphere adsorption, the oxo-anion does not replace the surface water layers, rather they form H-bonds with the surface water/hydroxyl monolayer. Configurations similar to those described for inner sphere adsorption were constructed for outer-sphere adsorption. For brevity, only the most stable outer-sphere (Outer) configurations are discussed further.

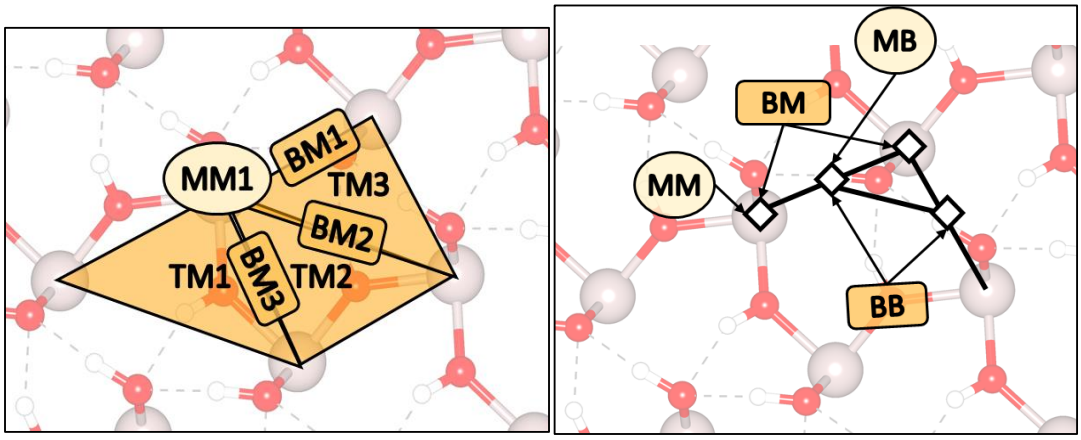

Figure 3.3: (a) Seven possible inner sphere monomolecular adsorption configurations for SeO_4^{2-} on (012) α-Al_2O_3 surface: one monodentate (MM1), three bidentate (BM1, BM2, BM3) and 3 tridentate configurations (TM1, TM2, TM3). (b) Two bimolecular configurations (monodentate bimolecular MB and bidentate bimolecular BB) for SeO_4^{2-} on (012) α-Al_2O_3 surface.

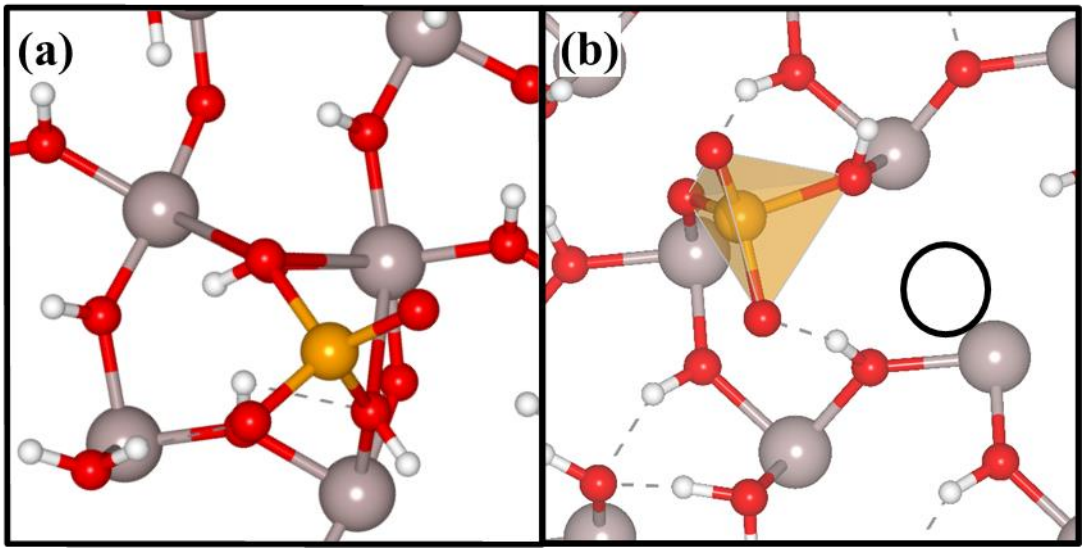

Figure 3.4: The relaxed configuration of $HSeO_4^-$ in Bidentate Bimolecular (BB) configuration above the PZC – (a) before and (b) after the relaxation. The selenate shifts to Bidentate monomolecular (BM) configuration (seen in (b)), with one Al atom with no adsorbed species. The circle in (b) represents the bare site above surface Al. The grey, red, white and orange balls represent Al, O, H and Se atoms respectively.

To delineate the effects of oxo-anion protonation, I included calculations of adsorption energy of selenate in fully (H_2SeO_4), semi ($HSeO_4^-$) and de (SeO_4^{2-}) protonated state in MM, BM and outer-sphere configuration on [012] α-Al_2O_3 surface, even though H_2SeO_4 is a strong acid and not present in aqueous system.[66] The protonation of selenate as a function of pH can be calculated using pKa value of deprotonation of $HSeO_4^-$ from Santos et. al. (2015)[67]:

$$HSeO_4^- \leftrightarrow SeO_4^{-2} \quad pK \sim 1.7 \qquad eq.\ 3.1$$

H_3O^+ molecules were added to the implicit continuum solvent space to account for the protons donated by semi and de- protonated selenate and to maintain a consistent simulation cell between various calculations.

The pH effects on [012] α-Al_2O_3 surfaces were included by altering the protonation of the adsorbed water monolayer. Water molecules dissociatively adsorb on the [012]

Al_2O_3 surface to form singly and triply coordinated hydroxyl groups, labeled OH1 and OH3 respectively[68]. As the pH decreases, the surface adsorbs protons and the previously de-protonated OH1 groups gain a proton re-forming water, while the previously dissociated H^+s' remain on the surface O^{2-} anions, i.e., the OH3 structures remain. The fraction of the protonation and deprotonation of [012] Al_2O_3 surface hydroxyl groups can be calculated using equilibrium and following chemical reactions[68,69]:

$$H_2O1^{+0.5} \leftrightarrow OH1^{-0.5} + H^+ \quad pK \sim 9.9 \qquad eq.\ 3.2$$

$$OH1^{-0.5} \leftrightarrow O^{-0.5} + H^+ \quad pK \sim 11.9 \qquad eq.\ 3.3$$

$$OH3^{+0.5} \leftrightarrow O^{-0.5} + H^+ \quad pK \sim 5.9 \qquad eq.\ 3.4$$

For my calculations, I have considered adsorption of selenate on neutral or protonated surface in all three oxo-anion protonation states and all adsorption configurations. The PZC for [012] α-Al_2O_3 calculated from eq. 3.2-3.4 (figure 3.3(d)) is 7.8, which closely matched the experimentally found PZC of α-Al_2O_3 by Peak (2006).[25] The computational adsorption energy calculations were considered in absence of salt ions present in the solution phase or at the interface. The neutral Al_2O_3 surface has dissociated H_2O (as OH1 and OH3) and protonated surface has H_3O^+ (H_2O1 and OH3) on the surface (figure 3.2 (d) and (e)). Following the studies of She et. al. (2015) and Leung et. at. (2017), I assumed that the configuration with most exothermic adsorption energy corresponds to the experimentally observed species.[41,70] The adsorption energy was calculated using the following equation:

$$\Delta E = E_{ads\_c} - E_{desor_c} \qquad eq.\ 3.5$$

Where $E_{ads\_C} = E_{Al_2O_3.(12-y)OH^-.(n-z)H^+.H_xSeO_4^{2-x}+(2-x)H_3O^+_{aq}+yOH^-.zH^+_{aq}}$ is the energy of the simulated cell containing the adsorbed selenate and $E_{des} =$

$E_{Al_2O_3.12OH^-.nH^+ + H_xSeO_4^{2-x}{}_{aq.} + (2-x)H_3O^+_{aq.}}$ is the energy of simulated cell before adsorption. The variable values (n, x, y) as a function of protonation and adsorption type are listed in Table 3.1.

Table 3.1: Variables affecting adsorption energies as function of pH and type of adsorption.

Variables	Factors affecting the variable		Values
n	Number of H^+ on α-Al_2O_3	Protonated surface	24
		Neutral Surface	12
x	Protonation of selenate	Fully protonated (H_2SeO_4)	2
		Semi protonated ($HSeO_4^-$)	1
		De protonated (SeO_4^{2-})	0
y	Type of adsorption	Bidentate adsorption (BM)	2
		Monodentate Adsorption (MM)	1
		Outer sphere adsorption (outer)	0

3.3.4 Predicted fractionation of adsorbed selenate

I predicted the percentage of selenate ions that will adsorb on Al_2O_3 surface as function of pH using Gibb's free energies of adsorption and equilibrium constants. I assumed that the oxo-anion loses all of its aqueous phase entropy upon adsorption. Therefore, the Gibbs free energy of adsorption is equal to

$$\Delta G_{ads_{n,x}} = \Delta E - T\Delta S \qquad eq.3.6$$

where ΔE is the adsorption energy calculated using eq. 3.5 for respective n and x variables in Table 3.2. The entropy of aqueous $HSeO_4^-$ and SeO_4^{2-} were taken to be 136 J/mol K and 33 J/mol K respectively.[71] I did not calculate the Gibbs free energy of H_2SeO_4 adsorption as it is not present in solution under normal pH conditions. The equilibrium constant is calculated as

$$K_{n,x} = \exp\left(\frac{\Delta G}{RT}\right) = \frac{\alpha}{[H_x SeO_4^{2-x}]_{ini} - \alpha} \qquad eq.3.7$$

Here α is the concentration of $H_x SeO_4^{2-x}$ adsorbed on $[Al_2O_3.12H_2O.(n-12)H^+]$, and $[H_x SeO_4^{2-x}]_{ini}$ is the initial concentration of the different protonated oxo-anion species in aqueous solution and is calculated using pKa value :

$$1.7 = pH + \log\left(\frac{[HSeO_4^-]}{[SeO_4^2 -]}\right) \qquad eq.3.8$$

I assumed an initial total selenate concentration of 1M and that the surface area sufficiently large to accommodate all selenate ions. For the purpose of predicting adsorption, I assumed that the surface was either fully protonated or deprotonated in a fraction equal to the pKa values:

$$5.9 = pH + \log\left(\frac{[Al_3OH]}{[Al_3O]}\right) \qquad eq.3.9$$

$$9.9 = pH + \log\left(\frac{[AlOH_2]}{[AlOH]}\right) \qquad eq.3.10$$

$$11.9 = pH + \log\left(\frac{[AlOH]}{[AlO]}\right) \qquad eq.3.11$$

Combining the fraction of surface protonated sites, deprotonated sites, and various selenate species, the total percent of selenate adsorbed within the limit of infinite Al_2O_3 surface area and non-interacting adsorbates on the alumina surface is:

$$\%\, Se_{ads} = \sum_{n=12,24} \sum_{x=0,1} \alpha \times [H_x SeO_4^{2-x}]_{ini} [Al_2O_3.12H_2O.(n-12)H^+]_{ini} \qquad eq.3.12$$

3.4 Results and Discussion

In this section I first discuss the energy of selenate as a function of oxo-anion adsorption configuration, and surface and oxo-anion protonation. Then, I demonstrate the reliability of adsorption energy as predictor for experimental trends and discuss the effects of structural motif and pH parameters on adsorption. Lastly, I examine the underlying physics controlling selenate adsorption by correlating various physical and chemical parameters of the calculated structures with their adsorption energies.

3.4.1 Selenate adsorption on alumina surface as function of pH

I calcuated the adsorption enenergy of selenate on α-Al_2O_3 as a function of adsorption motif and protonation extent of the selenate and surface. The lowest enregy configuration of each condition is shown in Figure 3.5a and b. Using these adsorption energy and the pK values for protonation/deprotonation of oxo-anion and surface hydroyl groups found in Santos et. al. (2015)[67] and Sung et. al. (2011)[68] respectively, I plotted the fraction of selenate adsorbed, using equation 3.9, as a function of pH, in Figure 3.5c. My precited percent of selenate adsorbed closesly aligned with that experimentally determined selenate adsorption of 1g/L of alumina in 0.01M ionic strength solution.[25] I calculated the adsorption of one selenate oxo-anion per 0.45 nm^2, which corresponds to a loading of ~700 μg selenate/m^2 on α-Al_2O_3. Therefore, I expect that the selenate loadings on Al_2O_3 as a function of pH calculated in Figure 3.5c should hold at least until 700 $\mu g/m^2$.

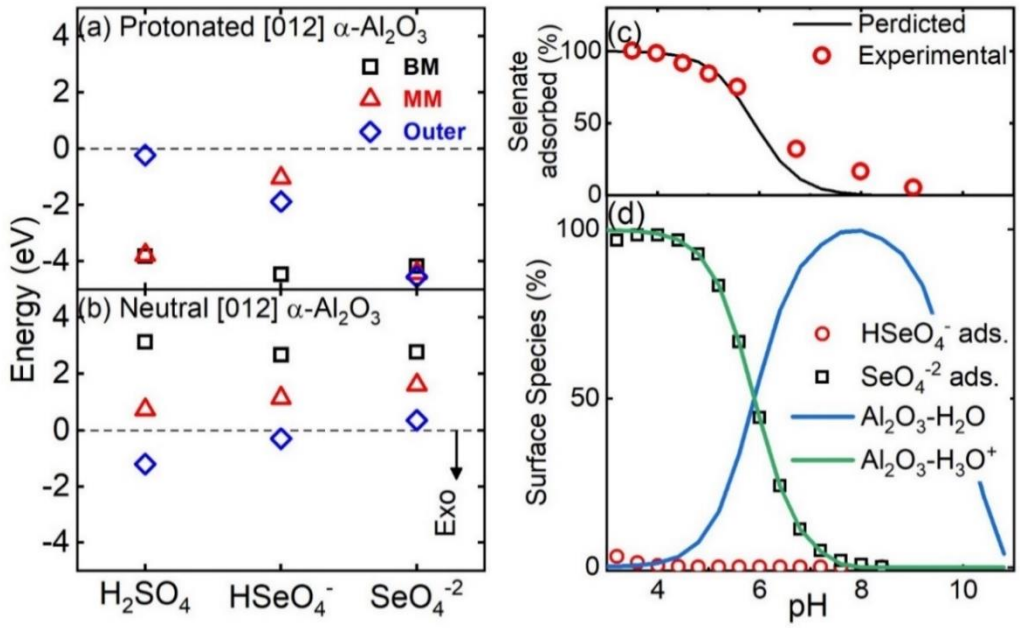

Figure 3.5: (a) and (b) Adsorption energies of selenate on the (012) Al_2O_3 surface as a function of adsorbent configuration, surface protonation and oxo-anion protonation. (c) predicted selenate adsorption as a function of pH compared to experimental selenate removed on 1g/l of alumina at 0.01 M ionic strength (reference[25]). (d) Percentage of surface species (adsorbed selenate and water) on [012] Al_2O_3 as function pH.

Near neutral pH conditions where SeO_4^{2-} dominates (pH > 4), outer-sphere adsorption was the most stable (exothermic) configuration on both the protonated and neutral surfaces. Therefore, selenate is expected to adsorb in outer-sphere configuration, with higher adsorption extents at protonated surface sites. While there was only a slight difference in adsorption energy of deprotonated selenate in different configurations, 0.38 eV between outer-sphere to bidentate configuration, the probability of adsorption occuring in monodentate and bidentate configuration was calcuated to be 0.004 and 3.74×10^{-7} times less likely than the outer-sphere configuration at room temperature respectively from the Boltzmann equation. The predicted preference for outer sphere adsorption matched experimental results where selenate was found to adsorb in outer sphere configuration on Al_2O_3.[18,25,72,73] The average interatomic distance of Se-O of outer-sphere SeO_4^{2-} adsorbed

on protonated Al_2O_3 found using my calculations (1.70 Å) closely matches the experimentally measured interatomic distance (1.64 Å) from EXAFS.[25,74] I analyzed the chemical interaction between the selenate and the surface using Crystal Orbital Hamilton Population (COHP) analysis. COHP analysis of the outer sphere SeO_4^{-2} configuration revealed that the selenate was only bound to the Al_2O_3 through hydrogen bonds (-ICOHP = 1.42 eV/bond to surface H's) and that selenate Os had very small orbital overlap with crystal's Al species (-ICOHP = 0.06 eV/bond). This was in contrast to SeO_4^{2-} in the inner sphere configuration on protonated Al_2O_3, where Al-OSe bond strength (-ICOHP =5eV/bond) was stronger than Al-OH_2bond strength (-ICOHP = -4 eV/bond). However, the Al-OSe bond strength was not enough to overcome the energy required to break hydrogen bonds between interfacial water (-ICOHP = 0.91 eV/bond). The strong bond strength (-ICOHP = -8.65 eV/bond) between Selenate's Se and O atoms in stable configurations confirmed that selenate reduction on the Al_2O_3 surface is strongly endothermic. At low pH, beyond the normal drinking water range, selenate is present in both semi and deprotonated state, and the surface dominated by protonated hydroxyl groups. Under these conditions, selenate was predicted to adsorb strongly in both inner and outer sphere configuration. Overall, I found that the most selenate was removed below pH 4, where > 98% of α-Al_2O_3 was covered with dissociated H_3O^+ molecules, which also matches experimental results (Figure 3.3d).[75]

There were clear relationships between the the system configurations and adsorption energies. The relative effects of system paramters on adsorption were: surface protonation > adsorption configuration ≈ protonation extent of selenate. The average adsorption energy increased by 4.41 eV from -3.15 eV exothermic for the protonated

surface to 1.26 eV endothermic for the neutral surface. This effect was at least 3.78 eV stronger than the other factors. The second most important factor in directing the adsorption energy was the adsorption configuration, where the average energy of BM, MM and outer sphere configurations were -0.63, -0.94 and -1.26 eV, respectively. The maximum difference in energy between averages of most stable configuration (outer sphere) and least stable configuration (Bidentate mononuclear, BM) was 0.63 eV, which was significantly less than effect of surface charge. Changing the protonation state of selenate resulted in the smallest change in the average adsorption energies: -0.86 eV, -0.60 eV and -1.38 eV for H_2SeO_4, $HSeO_4^-$ and SeO_4^{-2}, respectively, or 0.52 eV. Interestingly, the adsorption trend as a function of oxo-anion protonation extent was non-monotonic, unlike the other trends.

I calculated that the adsorption energy of selenate on the aluminum surface decreased as selenate loses its protons on neutral Al_2O_3. In fact, no fully deprotonated selenate was calculated to bind to the neutral surface exothermically. This finding is critical because only deprotonated selenate is present between pH 3-9.[76] On the protonated surface, the adsorption energy relations were not linear as a function of selenate protonation and configuration. In the BM configuration, the adsorption energy varied non-monotonically with energies of -3.82 eV, -4.46 eV, -4.17 eV for H_2SeO_4, $HSeO_4^-$ and SeO_4^{2-}, respectively. The opposite non-monotonic trend was observed in the MM configuration on protonated Al_2O_3, where the adsorption energy changed from -3.77 eV to -1.03 eV to -4.41 eV as selenate deprotonates.

I investigated the non-linear trends observed for inner sphere selenate adsorption on protonated surface using Bader analysis[77]. I calculated that the Se ion reduced from 6+ to a 4+ oxidation state upon adsorption in the MM H_2SeO_4, BM H_2SeO_4 and BM $HSeO_4^-$

configurations. This was consistent with the dissociation of one the four Se-O bonds seen in inner-sphere adsorption on protonated surface (Figure 3.6). These results also predict higher adsorption of selenite on protonated Al_2O_3 surface in inner-sphere configuration, which also matches the experimental results seen by Meher et. al. (2020),[37] Ji and Wang (2019)[78] and Yamani et. al. (2014).[75] Additionally, the density of states showed that the 4s orbitals of Se in the MM configuration decreased in energy and became occupied when the selenate was protonated, as seen in Figure 3.6d. This pronation dependent reduction explained the non-monotonic adsorption behavior of the selenate adsorption energy as a function of oxo-anion protonation.

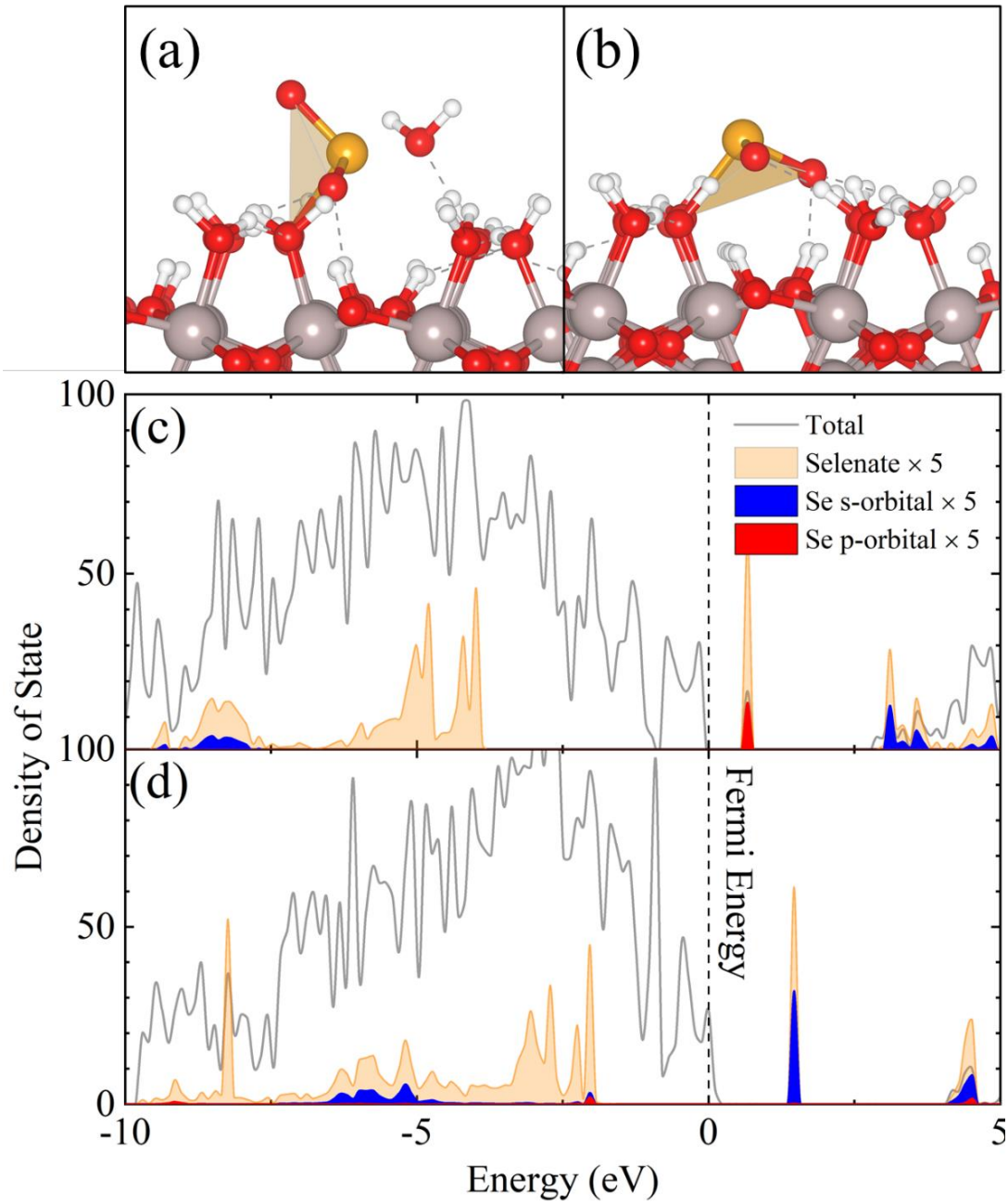

Figure 3.6: The geometry of (a) H_2SeO_4 in MM configuration (b) $HSeO_4^-$ in BM configuration on protonated Al_2O_3. and the Density of State plot for (c)SeO_4^{2-} and (d) H_2SeO_4 adsorbed on protonated Alumina Surface ($Al_2O_3.nH_3O^+$) in MM configuration. The grey, red, white, and orange spheres represent Al, O, H and Se atoms, respectively.

3.4.2 Effects of intrinsic factors on adsorption energy

I investigated the relationships between adsorption energies and the underlying physical changes by correlating the adsorption energies with electronic and geometric structural features (Table 3.2). These relationships could provide guidance in the search for new adsorbent materials which have higher adsorption capabilities based on their physical characteristics. All the physical changes considered belonged to one of the three categories: (1) interfacial water network changes, (2) alumina-selenate interaction and (3) selenate's bond strain. Category 1 was considered because the adsorption of selenate disrupted the uniform water matrix above the surface. This change was quantified by the difference of the number of intermolecular hydrogen bonds ($\Delta(H\cdot\cdot O)_{H\text{-}bond}$) and intra-molecular H-O covalent bonds ($\Delta(H\text{-}O)_{covalent}$) between water, selenate, and alumina before and after adsorption. A positive number indicates that additional bonds form after adsorption. Category 2, the alumina-selenate interaction, was quantified by calculating the adsorption energy of selenate on an alumina surface in the absence of explicit and implicit solvation (i.e., the anhydrous adsorption energy or vacuum adsorption energy) and the distance of selenium ion from alumina surface. The former - vacuum adsorption energy - is widely assumed to be the controlling factor and is commonly used for screening candidate adsorbents. Category 3, adsorption induced strain within the selenate anion, was quantified by change in Se-O bond lengths and O-Se-O bond angles.

The intrinsic factors were correlated with the adsorption energies, shown in Figure 3.7, and have the following relative impact on adsorption energy: interfacial water network changes > alumina-selenate interaction > selenate bond strain. Of the variables investigated, the change in number of interfacial hydrogen bonds ($\Delta(H\cdot\cdot O)_{H\text{-}bond}$) had the

strongest correlation with adsorption energy, R^2 = 0.81. Surprisingly, not only was the correlation between adsorption energy and anhydrous adsorption energy weak (R^2=0.57), but it was also anti-correlated. Configurations predicted to be exothermic from the anhydrous adsorption energy were predicted to be endothermic when solvation was properly accounted for, and vice versa. This anti-correlation has significant ramifications for materials design as this metric is commonly used for screening sorbents. The other factors had only a low coefficient of determination, R^2 < 0.50, and were not considered to directly predict/control the adsorption energy. Therefore, I discuss in detail below the effects of pH and configuration and their relationship with change in the interfacial water network.

Table 3.2: Adsorption Energy, change in hydrogen bonds and atomic distances.

Adsorbent species	Adsorption Configuration	Adsorption Energy (eV)	ΔOH bonds	ΔHO bonds	Se-Al distance	Se-O average bond length
Below Point of Zero Charge						
H_2SeO_4	Bidentate (BM)	-3.82	0	8	4.66	2.27*
	Monodentate (MM)	-3.77	1	4	3.72	2.11*
	Outer sphere	-0.22	0	2	5.76	1.69
$HSeO_4^-$	Bidentate (BM)	-4.46	1	9	3.59	2.25*
	Monodentate (MM)	-1.03	1	3	3.57	1.71
	Outer sphere	-1.87	0	6	4.39	1.68
SeO_4^{-2}	Bidentate (BM)	-4.17	0	5	3	1.69
	Monodentate (MM)	-4.41	1	5	3.38	1.68
	Outer sphere	-4.55	0	7	4.66	1.7
Above Point of Zero Charge						
H_2SeO_4	Bidentate (BM)	3.14	-1	-3	2.96	1.71
	Monodentate (MM)	0.73	0	-1	3.24	1.69
	Outer sphere	-1.2	0	1	4.53	1.69
$HSeO_4^-$	Bidentate (BM)	2.68	0	-2	2.81	1.68
	Monodentate (MM)	1.15	-1	2	3.47	1.68
	outer sphere	-0.3	-1	3	4.32	1.68
SeO_4^{-2}	Bidentate (BM)	2.78	0	-1	2.81	1.68
	Monodentate (MM)	1.61	-1	1	3.38	1.68
	outer sphere	0.35	-1	2	4.95	1.68

* denotes dissociated selenate upon adsorption.

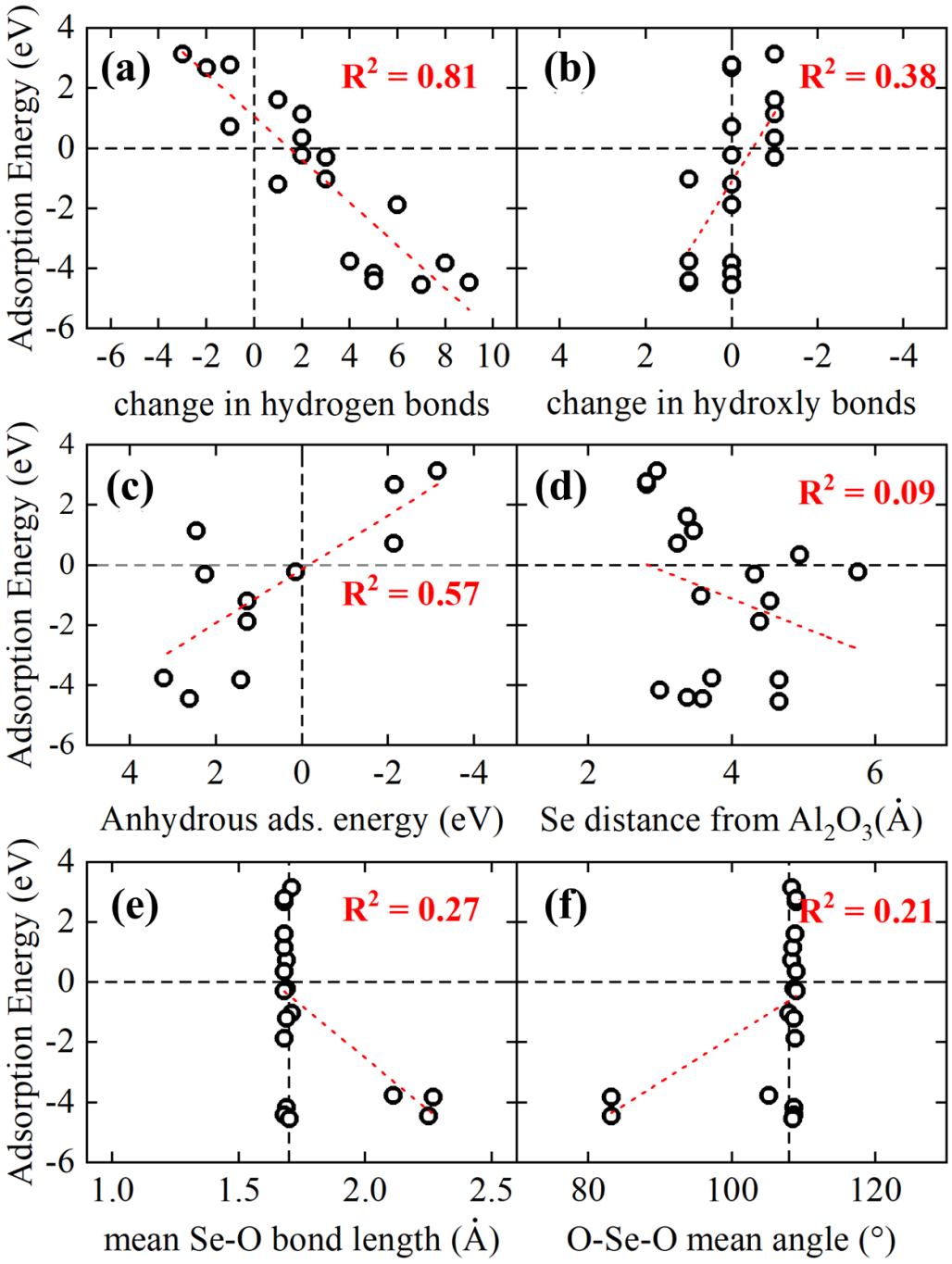

Figure 3.7: Effect of (a) Δ(H···O), (b) Δ(H-O), (c) anhydrous adsorption energy, (d) Se-Al distance, (e) mean Se-O bond length and (f) mean O-Se-O bond angle on adsorption energy.

3.4.2.1 Effect of Interfacial water network changes

The change in the bonding network of the water monolayer had the largest impact on the adsorption energy and was itself significantly controlled by protonation effects. Upon adsorption, the oxo-anion re-ordered the uniform water network, breaking the bonds between the adsorbed waters and replacing them with new water-selenate bonds. The interfacial water network consists of two types of bonds between oxygen and hydrogen atoms: strong covalent $(O\text{-}H)_{covalent}$ bonds within a single molecule with bond length < 1.2 Å[79] and weaker intermolecular hydrogen $(H\cdots O)_{H\text{-}bond}$ bonds with bond length between 1.2-2.1 Å[79]. As seen in Figure 3.7a and b, the change in intermolecular hydrogen bonds ($\Delta(H\cdots O)_{H\text{-}bond}$) had the strongest effect on the adsorption energy. Conversely, the change in the number of intra-molecular covalent ($\Delta(H\text{-}O)_{covalent}$) bonds did not correlate well with adsorption energies, R^2=0.38; however, the adsorption energy did exhibit stepped behavior in response to $\Delta(H\text{-}O)_{covalent}$, where a positive change in the number of intramolecular covalent ($\Delta(H\text{-}O)_{covalent}$ = +1) bonds resulted in exothermic adsorption and a negative change in the number of intra-molecular covalent bonds ($\Delta(H\text{-}O)_{covalent}$ = -1) resulted in endothermic energy. For systems with no change in the number of covalent bonds ($\Delta(H\text{-}O)_{covalent}$ = 0), the adsorption energy was directly related to change in hydrogen bonds in the system. The average energy for each step ($\Delta(H\text{-}O)_{covalent}$ = +1, 0 and -1) was -3.41, -1.07 and 1.33 eV respectively as represented by red dots in Figure 3.7b. The average adsorption energies correlated very well (R^2 = 0.99) with the number of covalent bonds made or broken.

The combined effect of interfacial water network change was calculated using the sum of $\Delta(H\cdots O)_{H\text{-}bond}$ and $\Delta(H\text{-}O)_{covalent}$ as inputs (Figure 3.8). The combined interfacial

water network changes (ΔHO_{net}) of intermolecular covalent and intramolecular hydrogen bonds slightly improved the relationship with adsorption energy. This finding suggested that both bonding types are important, but that the effects of H-bond dominate, likely due to the small change in the number of covalent bonds, and the fact that a change in the number of H-bonds was systematic with the change in the number of covalent bonds.

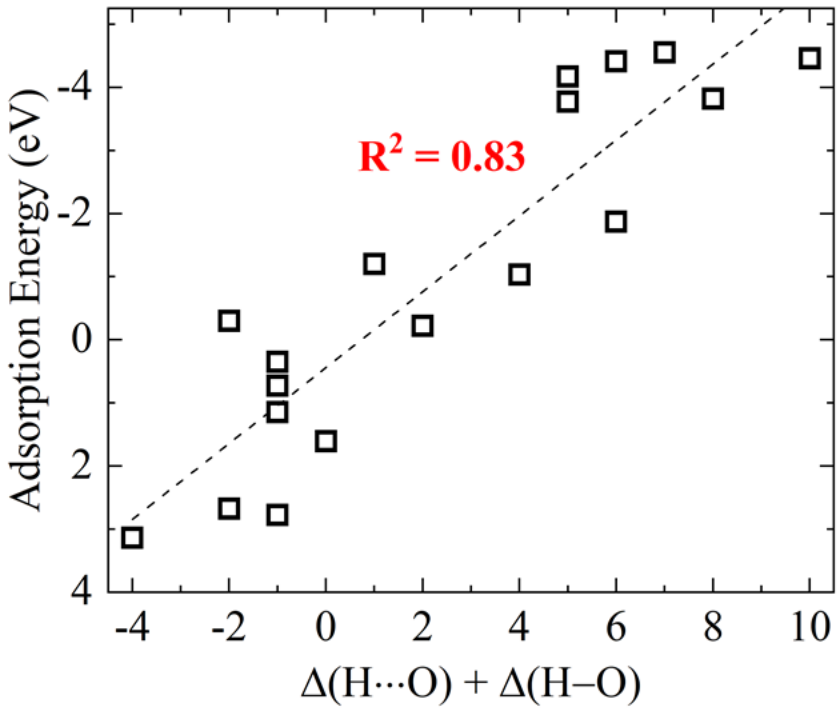

Figure 3.8: Sum of change of inter (H···O) and intra (H-O) bonds on adsorption energy.

The results of the ΔHO_{net} model agreed well with trends found between adsorption energy and configuration as a function protonation (Figure 3.5a). This agreement was because the number of H-bonds depend on the protonation states of the surface and selenate. On neutral [012] α-Al_2O_3 surface, the surface has equal numbers of hydrogen bonds $(H\cdots O)_{H\text{-bond}}$ and covalent H-O bond before adsorption. The bond types are evenly distributed between the two surface sites, OH1 and OH3. When selenate adsorbed in an inner sphere configuration, it displaced either one or two OH1 moieties, depending upon

configuration. In the fully protonated system, the selenate replaced a surface water OH1 group with a selenate OH, thus maintaining the number of hydrogen and oxygen on the metal oxide surface. However, in the semi and de-protonated inner-sphere configurations, the number of surface hydrogens was reduced, which decreased the overall number of surfaces inter and intra molecular hydrogen bonds, thus making adsorption more endothermic. In outer sphere adsorption on the neutral surface, the number of hydrogens remained unchanged. However, the number of oxygen atoms increased, which altered the orientation of protons, decreasing the number of H-bonds within the surface layer, and hence decreased the adsorption energy. On protonated Al_2O_3, the surface had 1.5 times more hydrogen atoms (some as protons) than surface oxygen atoms, as seen in Figure 3.2(e). The extra protons occupied sites between singly coordinated oxygen atoms and hydrogen bonded to triply coordinated oxygen, reducing the number of intramolecular hydrogen bonds on the surface before adsorption, as compared to the case on neutral Al_2O_3 surface. When selenate adsorbed in an inner-sphere configuration, it replaced H_2O1 with OH bonds, opening space for hydrogen bonding between selenate's O and the surrounding hydrogens. Upon de-protonation of selenate, the surface O to H ratio became closer 1, which increased the number of hydrogen bonds on the surface. Hence the adsorption was more exothermic because the adsorption configuration lost more protons from the surface. While the calculations reported here were only for the selenate-Al_2O_3 system, I hypothesize that similar arguments can be made for the high sensitivity of other oxo-anion-metal-oxide studies on pH such as selenate and selenite on graphene oxide,[80] selenite on mesoporous silica,[12] nitrite on Silicon dioxide[81] and Sulfate Adsorption on Al-Substituted Ferrihydrite [82] etc.

Even with the combined ΔHO_{net} model, the correlation was not perfect. For example, when H_2SeO_4 adsorbed in an outer sphere configuration on the Al_2O_3 surface, the number of hydrogen bonds added to the surface was +2 or +1, on the protonated or the neutral surface, respectively, with no change in the number of covalent bonds for either pH condition. The calculated adsorption energy was -0.22 eV and -1.22 eV on the protonated or the neutral surface respectively, which was the opposite behavior to what was expected from the correlations. In these cases, the average bond length of hydrogen bonds between selenate and water molecules on the neutral surface (1.75 Å) was smaller than the average bond length on protonated surface (1.92 Å). As the bond strength can be considered to be inversely proportional to bond length, adsorption energy of outer sphere H_2SeO_4 decreased as the average bond length increased. This demonstrates the fact that the strength, in addition to the number, of H-bonds contributes to the adsorption energetics.

The strong correlation between hydrogen bonding network and adsorptions energy also underlies the instabilities of selenate in bimolecular (MB and BB) configurations. In these configurations, the water molecules were singly coordinated with the alumina surface, and selenate adsorbed in a monodentate configuration replaced the singly coordinated Al-OH bond with an Al-O-Se bond. Bimolecular adsorption reduced the overall number of covalent OH and Al-O bonds, as a single Al-O-Se bond replaced two Al-OH bonds. The oxo-anion also broke the uniformity of the interfacial water layer on the surface, which required energy. Hence, the oxo-anion which was originally in a bimolecular configuration relaxed to a monomolecular configuration to maintain the symmetry of the water network, exposing surface Al atoms which then were able to re-bond with desorbed water.

3.4.2.2 Effect of Alumina and selenate interaction

The pioneering research into oxo-anion adsorption on metal oxide surfaces using density functional theory has generally focused on the interactions between the oxo-anion and metal-oxide,[83-85] as a logical hypothesis that this interaction should control the adsorption behavior. To isolate the significance of metal-oxide-oxo-anion binding strength in contributing to the adsorption energy, I calculated anhydrous adsorption energy of selenate over [012] alumina surface in vacuum, i.e., without explicit waters or implicit continuum solvent, and compared it to the adsorption energy calculated using the HSM. It is logical to think that there should be a strong relationship, linear or otherwise, between the two energies, however this was not the case. The relationship was in fact weakly anti-correlated. Critically, this suggested that oxo-anion adsorption on metal oxides should not be studied solely using un-solvated metal-oxide oxo-anion adsorption calculations because it resulted in both quantitative and qualitative errors. Also, no correlation existed between Se distance from α-Al_2O_3 surface with adsorption energy (Figure 3.7d).

3.5 Conclusion

In this work, I developed a surface adsorption model which accurately described selenate adsorption on Al_2O_3 and delineated the effects of experimentally indistinguishable factors such as oxo-anion configuration, protonation of oxo-anion and metal-oxide surface on adsorption energy of selenate on the α-Al_2O_3 (012) surface. This contribution demonstrates a computational framework for the accurate prediction of surface adsorption motif and pH dependances by 1) explicit inclusion of surface adsorbed water molecules with the PZC dependent protonation, 2) at least the inclusion of implicit solvation beyond

the first layer, 3) van der Waals's interactions, and 4) appropriate protonation state of the selenate molecule. Using this method, my predicted adsorption as a function of pH matches experimental data remarkably well, unlike small molecular cluster models or models used to studying only inner-sphere configurations.[41-47]

Most importantly, I identified, for the first time, that selenate adsorption on (012) α-Al_2O_3 is controlled by changes to the H-bonding network of surface water molecules. This finding arose from correlating adsorption energy with various chemo-physical quantities, which revealed that only the number and strength of hydrogen bonds between water molecules and the number of bonds between the waters and selenate were highly correlated with adsorption energy. Moreover, the adsorption energy behavior in the presence of water was anti-correlated with the adsorption energy in the absence of the solvent, giving rise to qualitative and quantitative errors in predicted adsorption behavior when using simplified anhydrous models. This finding is crucially important because many computational methods for screening sorbents, for selenate and other compounds, ignore surface solvation effects to increase computational speed, but now must be re-evaluated in the light of this work. Among the experimentally controllable factors, I found that the pH-controlled surface protonation has the most significant effect on the adsorption energy because it directly controls the surface H-bonding network through the number of H atoms available. This is in excellent agreement with experiments. These finding demonstrate the criticalities of including the solvation and pH effects on interfacial water layer in modelling adsorption behavior of oxo-anion on metal oxide surfaces. Overall, my findings suggest that surface water structures are the critical factor in designing highly active adsorbents for oxo-anion removal from drinking water treatment, at least for Al_2O_3 and probably for

similar materials. Therefore, materials with high points of zero charge, strong water dissociation, and high surface H concentrations should be sought for newly designed oxo-anion sorbents.

3.6 References

1. MacFarquhar, J. K.; Broussard, D. L.; Melstrom, P.; Hutchinson, R.; Wolkin, A.; Martin, C.; Burk, R. F.; Dunn, J. R.; Green, A. L.; Hammond, R.; Schaffner, W.; Jones, T. F., Acute selenium toxicity associated with a dietary supplement. Arch Intern Med 2010, 170, (3), 256-61.
2. Lenz, M.; Lens, P. N., The essential toxin: the changing perception of selenium in environmental sciences. Sci Total Environ 2009, 407, (12), 3620-33.
3. Fernández-Martínez, A.; Charlet, L., Selenium environmental cycling and bioavailability: a structural chemist point of view. Reviews in Environmental Science and Bio/Technology 2009, 8, (1), 81-110.
4. Neal, R. H.; Sposito, G., Selenate Adsorption on Alluvial Soils. Soil Science Society of America Journal 1989, 53, (1), 70-74.
5. Goh, K.-H.; Lim, T.-T., Geochemistry of inorganic arsenic and selenium in a tropical soil: effect of reaction time, pH, and competitive anions on arsenic and selenium adsorption. Chemosphere 2004, 55, (6), 849-859.
6. Simmons, D. B. D.; Wallschläger, D., A critical review of the biogeochemistry and ecotoxicology of selenium in lotic and lentic environments. Environmental Toxicology and Chemistry 2005, 24, (6), 1331-1343.
7. Rajan, S. S. S., ADSORPTION OF SELENITE, PHOSPHATE AND SULPHATE ON HYDROUS ALUMINA. Journal of Soil Science 1979, 30, (4), 709-718.
8. Ali, I.; Shrivastava, V., Recent advances in technologies for removal and recovery of selenium from (waste)water: A systematic review. Journal of Environmental Management 2021, 294, 112926.
9. Awual, M. R.; El-Safty, S. A.; Jyo, A., Removal of trace arsenic(V) and phosphate from water by a highly selective ligand exchange adsorbent. Journal of Environmental Sciences 2011, 23, (12), 1947-1954.
10. Ali, I., New Generation Adsorbents for Water Treatment. Chemical Reviews 2012, 112, (10), 5073-5091.
11. German, M. S.; Watkins, T. A.; Chowdhury, M.; Chatterjee, P.; Rahman, M.; Seingheng, H.; SenGupta, A. K., Evidence of economically sustainable village-scale microenterprises for arsenic remediation in developing countries. Environmental science & technology 2019, 53, (3), 1078-1086.
12. Awual, M. R.; Yaita, T.; Suzuki, S.; Shiwaku, H., Ultimate selenium(IV) monitoring and removal from water using a new class of organic ligand based composite adsorbent. Journal of Hazardous Materials 2015, 291, 111-119.
13. Rabiul Awual, M.; Munjur Hasan, M.; Ihara, T.; Yaita, T., Mesoporous silica based novel conjugate adsorbent for efficient selenium(IV) detection and removal from water. Microporous and Mesoporous Materials 2014, 197, 331-338.

14. Awual, M. R.; Hasan, M. M.; Khaleque, M. A., Efficient selenium(IV) detection and removal from water by tailor-made novel conjugate adsorbent. Sensors and Actuators B: Chemical 2015, 209, 194-202.
15. Johansson, C. L.; Paul, N. A.; de Nys, R.; Roberts, D. A., The complexity of biosorption treatments for oxyanions in a multi-element mine effluent. Journal of Environmental Management 2015, 151, 386-392.
16. Zhao, Q.; Huang, J.-C.; He, S.; Zhou, W., Enhancement of a constructed wetland water treatment system for selenium removal. Science of The Total Environment 2020, 714, 136741.
17. Awual, M. R.; Shenashen, M. A.; Yaita, T.; Shiwaku, H.; Jyo, A., Efficient arsenic(V) removal from water by ligand exchange fibrous adsorbent. Water Research 2012, 46, (17), 5541-5550.
18. Jordan, N.; Franzen, C.; Lützenkirchen, J.; Foerstendorf, H.; Hering, D.; Weiss, S.; Heim, K.; Brendler, V., Adsorption of selenium(vi) onto nano transition alumina. Environmental Science: Nano 2018, 5, (7), 1661-1669.
19. Holmes, A. B.; Gu, F. X., Emerging nanomaterials for the application of selenium removal for wastewater treatment. Environmental Science: Nano 2016, 3, (5), 982-996.
20. Yin, Y. B.; Guo, S. J.; Heck, K. N.; Clark, C. A.; Coonrod, C. L.; Wong, M. S., Treating Water by Degrading Oxyanions Using Metallic Nanostructures. Acs Sustain Chem Eng 2018, 6, (9), 11160-11175.
21. Pincus, L. N.; Rudel, H. E.; Petrović, P. V.; Gupta, S.; Westerhoff, P.; Muhich, C. L.; Zimmerman, J. B., Exploring the Mechanisms of Selectivity for Environmentally Significant Oxo-Anion Removal during Water Treatment: A Review of Common Competing Oxo-Anions and Tools for Quantifying Selective Adsorption. Environmental Science & Technology 2020, 54, (16), 9769-9790.
22. Goldberg, S., Modeling Selenate Adsorption Behavior on Oxides, Clay Minerals, and Soils Using the Triple Layer Model. Soil Science 2014, 179, 568 576.
23. Wang, L.; Shi, C.; Wang, L.; Pan, L.; Zhang, X.; Zou, J.-J., Rational design, synthesis, adsorption principles and applications of metal oxide adsorbents: a review. Nanoscale 2020, 12, (8), 4790-4815.
24. Jegadeesan, G.; Mondal, K.; Lalvani, S. B., Comparative study of selenite adsorption on carbon based adsorbents and activated alumina. Environmental Technology 2003, 24, (8), 1049-1059.
25. Peak, D., Adsorption mechanisms of selenium oxyanions at the aluminum oxide/water interface. J Colloid Interf Sci 2006, 303, (2), 337-345.
26. Su, T.; Guan, X.; Gu, G.; Wang, J., Adsorption characteristics of As(V), Se(IV), and V(V) onto activated alumina: Effects of pH, surface loading, and ionic strength. J Colloid Interf Sci 2008, 326, (2), 347-353.
27. Marjanovic, V.; Peric-Grujic, A.; Ristic, M.; Marinkovic, A.; Markovic, R.; Onjia, A.; Sljivic-Ivanovic, M., Selenate Adsorption from Water Using the Hydrous Iron Oxide-Impregnated Hybrid Polymer. Metals 2020, 10, (12).
28. Padungthon, S.; German, M.; Wiriyathamcharoen, S.; SenGupta, A. K., Polymeric anion exchanger supported hydrated Zr (IV) oxide nanoparticles: a reusable hybrid sorbent for selective trace arsenic removal. Reactive and Functional Polymers 2015, 93, 84-94.

29. Yang, Z.; Qian, J.; Shan, C.; Li, H.; Yin, Y.; Pan, B., Toward Selective Oxidation of Contaminants in Aqueous Systems. Environmental Science & Technology 2021, 55, (21), 14494-14514.
30. Rudel, H. E.; Lane, M. K. M.; Muhich, C. L.; Zimmerman, J. B., Toward Informed Design of Nanomaterials: A Mechanistic Analysis of Structure–Property–Function Relationships for Faceted Nanoscale Metal Oxides. ACS Nano 2020, 14, (12), 16472-16501.
31. Luo, J.; Yu, D.; Hristovski, K. D.; Fu, K.; Shen, Y.; Westerhoff, P.; Crittenden, J. C., Critical Review of Advances in Engineering Nanomaterial Adsorbents for Metal Removal and Recovery from Water: Mechanism Identification and Engineering Design. Environmental Science & Technology 2021, 55, (8), 4287-4304.
32. Chen, H.; Shepsko, C.; SenGupta, A. K., Use of a Novel Bio-Nano-IX Process to Remove SeO42– or Se(VI) from Contaminated Water in the Presence of Competing Sulfate (SO42–). ACS ES&T Water 2021, 1, (8), 1859-1867.
33. Peak, D.; Sparks, D. L., Mechanisms of Selenate Adsorption on Iron Oxides and Hydroxides. Environmental Science & Technology 2002, 36, (7), 1460-1466.
34. Han, J.; Kim, M.; Ro, H.-M., Factors modifying the structural configuration of oxyanions and organic acids adsorbed on iron (hydr)oxides in soils. A review. Environmental Chemistry Letters 2020, 18, (3), 631-662.
35. Villalobos, M.; Pérez-Gallegos, A., Goethite surface reactivity: A macroscopic investigation unifying proton, chromate, carbonate, and lead(II) adsorption. J Colloid Interf Sci 2008, 326, (2), 307-323.
36. Villalobos, M.; Cheney, M. A.; Alcaraz-Cienfuegos, J., Goethite surface reactivity: II. A microscopic site-density model that describes its surface area-normalized variability. J Colloid Interf Sci 2009, 336, (2), 412-422.
37. Meher, A. K.; Jadhav, A.; Labhsetwar, N.; Bansiwal, A., Simultaneous removal of selenite and selenate from drinking water using mesoporous activated alumina. Applied Water Science 2019, 10, (1), 10.
38. Youngran, J.; Fan, M.; Van Leeuwen, J.; Belczyk, J. F., Effect of competing solutes on arsenic(V) adsorption using iron and aluminum oxides. Journal of Environmental Sciences 2007, 19, (8), 910-919.
39. Lin, T.-F.; Wu, J.-K., Adsorption of Arsenite and Arsenate within Activated Alumina Grains: Equilibrium and Kinetics. Water Research 2001, 35, (8), 2049-2057.
40. Kubicki, J. D.; Kwon, K. D.; Paul, K. W.; Sparks, D. L., Surface complex structures modelled with quantum chemical calculations: carbonate, phosphate, sulphate, arsenate and arsenite. European Journal of Soil Science 2007, 58, (4), 932-944.
41. Shi, Q.; Yan, L.; Chan, T.; Jing, C., Arsenic Adsorption on Lanthanum-Impregnated Activated Alumina: Spectroscopic and DFT Study. ACS Applied Materials & Interfaces 2015, 7, (48), 26735-26741.
42. Paul, K. W.; Kubicki, J. D.; Sparks, D. L., Sulphate adsorption at the Fe (hydr)oxide–H2O interface: comparison of cluster and periodic slab DFT predictions. European Journal of Soil Science 2007, 58, (4), 978-988.
43. Wei, Z.; Luo, S.; Xiao, R.; Khalfin, R.; Semiat, R., Characterization and quantification of chromate adsorption by layered porous iron oxyhydroxide: An experimental and theoretical study. Journal of Hazardous Materials 2017, 338, 472-481.

44. Huang, X.; Hou, X.; Song, F.; Zhao, J.; Zhang, L., Facet-Dependent Cr(VI) Adsorption of Hematite Nanocrystals. Environ Sci Technol 2016, 50, (4), 1964-72.
45. Johnston, C. P.; Chrysochoou, M., Mechanisms of chromate adsorption on hematite. Geochimica et Cosmochimica Acta 2014, 138, 146-157.
46. Kubicki, J. D.; Paul, K. W.; Kabalan, L.; Zhu, Q.; Mrozik, M. K.; Aryanpour, M.; Pierre-Louis, A.-M.; Strongin, D. R., ATR–FTIR and Density Functional Theory Study of the Structures, Energetics, and Vibrational Spectra of Phosphate Adsorbed onto Goethite. Langmuir 2012, 28, (41), 14573-14587.
47. Sherman, D. M.; Randall, S. R., Surface complexation of arsenic(V) to iron(III) (hydr)oxides: structural mechanism from ab initio molecular geometries and EXAFS spectroscopy. Geochimica et Cosmochimica Acta 2003, 67, (22), 4223-4230.
48. Corum, K. W.; Abbaspour Tamijani, A.; Mason, S. E., Density Functional Theory Study of Arsenate Adsorption onto Alumina Surfaces. Minerals 2018, 8, (3).
49. Perdew, J. P.; Burke, K.; Ernzerhof, M., Generalized gradient approximation made simple. Phys Rev Lett 1996, 77, (18), 3865-3868.
50. Kresse, G.; Furthmüller, J., Efficient iterative schemes for ab initio total-energy calculations using a plane-wave basis set. Physical Review B 1996, 54, (16), 11169.
51. Kresse, G.; Furthmüller, J., Efficiency of ab-initio total energy calculations for metals and semiconductors using a plane-wave basis set. Computational Materials Science 1996, 6, (1), 15-50.
52. Kresse, G.; Joubert, D., From ultrasoft pseudopotentials to the projector augmented-wave method. Physical Review B 1999, 59, (3), 1758-1775.
53. Grimme, S.; Antony, J.; Ehrlich, S.; Krieg, H., A consistent and accurate ab initio parametrization of density functional dispersion correction (DFT-D) for the 94 elements H-Pu. J Chem Phys 2010, 132, (15), 154104.
54. Mathew, K.; Sundararaman, R.; Letchworth-Weaver, K.; Arias, T. A.; Hennig, R. G., Implicit solvation model for density-functional study of nanocrystal surfaces and reaction pathways. J Chem Phys 2014, 140, (8), 084106.
55. Kitayama, M.; Glaeser, A. M., The Wulff Shape of Alumina: III, Undoped Alumina. Journal of the American Ceramic Society 2002, 85, (3), 611-622.
56. Sun, W.; Ceder, G., A topological screening heuristic for low-energy, high-index surfaces. Surface Science 2018, 669, 50-56.
57. Peri, J. B., A Model for the Surface of γ-Alumina1. The Journal of Physical Chemistry 1965, 69, (1), 220-230.
58. Krukau, A. V.; Vydrov, O. A.; Izmaylov, A. F.; Scuseria, G. E., Influence of the exchange screening parameter on the performance of screened hybrid functionals. The Journal of Chemical Physics 2006, 125, (22), 224106.
59. Wang, V.; Xu, N.; Liu, J.-C.; Tang, G.; Geng, W.-T., VASPKIT: A user-friendly interface facilitating high-throughput computing and analysis using VASP code. Computer Physics Communications 2021, 267, 108033.
60. Nelson, R.; Ertural, C.; George, J.; Deringer, V. L.; Hautier, G.; Dronskowski, R., LOBSTER: Local orbital projections, atomic charges, and chemical-bonding analysis from projector-augmented-wave-based density-functional theory. Journal of Computational Chemistry 2020, 41, (21), 1931-1940.

61. Pinchon, D.; Hoggan, P. E., Rotation matrices for real spherical harmonics: general rotations of atomic orbitals in space-fixed axes. Journal of Physics A: Mathematical and Theoretical 2007, 40, (7), 1597-1610.
62. Momma, K.; Izumi, F., VESTA 3 for three-dimensional visualization of crystal, volumetric and morphology data. Journal of applied crystallography 2011, 44, (6), 1272-1276.
63. Bachrach, S. M., Microsolvation of Glycine: A DFT Study. The Journal of Physical Chemistry A 2008, 112, (16), 3722-3730.
64. Catalano, J. G.; Park, C.; Zhang, Z.; Fenter, P., Termination and Water Adsorption at the α-Al2O3 (012)−Aqueous Solution Interface. Langmuir 2006, 22, (10), 4668-4673.
65. Al-Abadleh, H. A.; Grassian, V. H., FT-IR Study of Water Adsorption on Aluminum Oxide Surfaces. Langmuir 2003, 19, (2), 341-347.
66. Sharma, V. K.; McDonald, T. J.; Sohn, M.; Anquandah, G. A. K.; Pettine, M.; Zboril, R., Biogeochemistry of selenium. A review. Environmental Chemistry Letters 2015, 13, (1), 49-58.
67. Santos, S.; Ungureanu, G.; Boaventura, R.; Botelho, C., Selenium contaminated waters: An overview of analytical methods, treatment options and recent advances in sorption methods. Sci Total Environ 2015, 521-522, 246-260.
68. Sung, J.; Zhang, L.; Tian, C.; Shen, Y. R.; Waychunas, G. A., Effect of pH on the Water/α-Al2O3 (1$\bar{1}$02) Interface Structure Studied by Sum-Frequency Vibrational Spectroscopy. The Journal of Physical Chemistry C 2011, 115, (28), 13887-13893.
69. Chelikowsky, J. R., 1.01 - Electrons in Semiconductors: Empirical and ab initio Pseudopotential Theories. In Comprehensive Semiconductor Science and Technology, Bhattacharya, P.; Fornari, R.; Kamimura, H., Eds. Elsevier: Amsterdam, 2011; pp 1-41.
70. Leung, K.; Criscenti, L. J., Lead and selenite adsorption at water–goethite interfaces from first principles. Journal of Physics: Condensed Matter 2017, 29, (36), 365101.
71. Åke Olin, B. N., Lars-Olof Öhman, Evgeniy Osadchii and Erik Rosén Chemical Thermodynamics of Selenium; OECD Nuclear Energy Agency.
72. Wijnja, H.; Schulthess, C. P., Vibrational Spectroscopy Study of Selenate and Sulfate Adsorption Mechanisms on Fe and Al (Hydr)oxide Surfaces. J Colloid Interf Sci 2000, 229, (1), 286-297.
73. Elzinga, E. J.; Tang, Y.; McDonald, J.; DeSisto, S.; Reeder, R. J., Macroscopic and spectroscopic characterization of selenate, selenite, and chromate adsorption at the solid–water interface of γ-Al2O3. J Colloid Interf Sci 2009, 340, (2), 153-159.
74. Ippolito, J. A.; Scheckel, K. G.; Barbarick, K. A., Selenium adsorption to aluminum-based water treatment residuals. J Colloid Interf Sci 2009, 338, (1), 48-55.
75. Yamani, J. S.; Lounsbury, A. W.; Zimmerman, J. B., Adsorption of selenite and selenate by nanocrystalline aluminum oxide, neat and impregnated in chitosan beads. Water Research 2014, 50, 373-381.
76. Torres, J.; Pintos, V.; Gonzatto, L.; Domínguez, S.; Kremer, C.; Kremer, E., Selenium chemical speciation in natural waters: Protonation and complexation behavior of selenite and selenate in the presence of environmentally relevant cations. Chemical Geology 2011, 288, (1), 32-38.
77. Yu, M.; Trinkle, D. R., Accurate and efficient algorithm for Bader charge integration. The Journal of Chemical Physics 2011, 134, (6), 064111.

78. Ji, Y.; Li, L.; Wang, Y.-t., Selenium removal by activated alumina in batch and continuous-flow reactors. Water Environment Research 2020, 92, (1), 51-59.
79. Legon, A. C.; Millen, D. J., Angular geometries and other properties of hydrogen-bonded dimers: a simple electrostatic interpretation of the success of the electron-pair model. Chemical Society Reviews 1987, 16, (0), 467-498.
80. Fu, Y.; Wang, J.; Liu, Q.; Zeng, H., Water-dispersible magnetic nanoparticle–graphene oxide composites for selenium removal. Carbon 2014, 77, 710-721.
81. Kamel, R. M.; Shahat, A.; Hegazy, W. H.; Khodier, E. M.; Awual, M. R., Efficient toxic nitrite monitoring and removal from aqueous media with ligand based conjugate materials. Journal of Molecular Liquids 2019, 285, 20-26.
82. Johnston, C. P.; Chrysochoou, M., Mechanisms of Chromate, Selenate, and Sulfate Adsorption on Al-Substituted Ferrihydrite: Implications for Ferrihydrite Surface Structure and Reactivity. Environmental Science & Technology 2016, 50, (7), 3589-3596.
83. Zhang, M.; He, G.; Pan, G., Binding mechanism of arsenate on rutile (110) and (001) planes studied using grazing-incidence EXAFS measurement and DFT calculation. Chemosphere 2015, 122, 199-205.
84. Kubicki, J. D.; Kabengi, N.; Chrysochoou, M.; Bompoti, N., Density functional theory modeling of chromate adsorption onto ferrihydrite nanoparticles. Geochemical Transactions 2018, 19, (1), 8.
85. Yan, L.; Song, J.; Chan, T.; Jing, C., Insights into Antimony Adsorption on (001) TiO2: XAFS and DFT Study. Environmental Science & Technology 2017, 51, (11), 6335-6341.

CHAPTER 4

UNDERSTANDING THE EFFECT OF SINGLE ATOM CATIONIC DEFECT SITES IN ALUMINA (012) SURFACE ON ALTERING SELENATE AND SULFATE ADSORPTION

4.1 Abstract

Adsorption is a promising under-the-sink selenate remediation technique for distributed water systems. Recently it was shown that adsorption induced water network re-arraignment control adsorption energetics on the α-Al_2O_3 (012) surface. Here, we aim to elucidate the relative importance of the water network effects and surface cation identity on controlling selenate and sulfate adsorption energy using density functional theory calculations. Density functional theory (DFT) calculations predicted the adsorption energies of selenate and sulfate on nine transition metal cations (Sc-Cu) and two alkali metal cations (Ga and In) in the α-Al_2O_3 (012) surface under simulated acidic and neutral pH conditions. We find that the water network effects had a larger impact on the adsorption energy than the cationic identity. However, cation identity secondarily controlled adsorption. Most cations decreased the adsorption energy weakening the overall performance, the larger Sc and In cations enabled inner-sphere adsorption in acidic conditions because they relaxed outward from the surface providing more space for adsorption. Additionally, only Ti induced Se selectivity over S by reducing the adsorbing selenate to selenite but not reducing the sulfate. Overall, this study indicates that tuning water network structure will likely have a larger impact than tuning cation-selenate interactions for increasing adsorbate effectiveness.

4.2 Introduction

Selenium is an essential micronutrient for all living beings; however, there is a narrow range between deficiency and toxicity.[1-3] Consumption of selenium above 400 µg/day causes nausea, diarrhea, tachycardia and gastrointestinal disturbances, and induces long-term effects like selenosis, hair loss, abnormal functioning of the nervous system, hepatotoxicity, etc.[4-6] Leaching of selenium from anthropogenic practices such as agriculture irrigation, run-off from mining sites, e-waste landfills and natural reservoirs can cause high Se concentrations in drinking water.[7-9] Once in the water, selenium oxidizes to its oxo-anion forms – selenate (Se(VI) or SeO_4^{2-}) or selenite (Se(IV) or $HSeO_3^-$), which are equally toxic to humans.[10-12] Therefore, water treatment methods are required to decrease Se levels to below the EPA limit of 0.05 mg/L water.[13]

Selenium removal methods include ion exchange, photocatalysis, coagulation, electrocoagulation, and bioremediation.[8,14] These methods, however, require expensive treatment plants, catalysts, chemical addition, or membranes and continuous management, which are not easily or economically accessible to small communities or private wells.[14] Conversely, adsorption based removal of selenium oxo-anions on low-cost materials can be easily implemented using under-the-sink installations for less than \$0.06/m^3 treated water.[15] Low-cost metal-oxide nanoparticles like hematite and alumina are preferred candidates as adsorbent materials because they are widely available in nature, safe to use in water remediation, and can be recovered again using chemical-, or thermal-regeneration.[16-19]

Aluminum oxide (Al_2O_3) in activated alumina and nanocrystalline particles forms are EPA approved for use as selenium adsorbents.[20-21] However, the adsorption capacity of alumina for selenate is 0.16-4.45 times lower than selenite,[22,23] which is problematic since selenate (Se(VI)) exists at higher concentrations than selenite in fresh water.[15,24-25] Moreover, the adsorption of oxo-anions on the alumina surface is sensitive to pH.[26-27] At pH 3, 1g of alumina in 200 ml solution adsorbs 100 % of 1.25 mM selenate from solution; however, the adsorption decreases to almost 0% when the pH is 9.[28] In-home operators cannot decrease the pH of drinking water below 6 for remediation purposes as it renders the water undrinkable;[29] additionally, although acidification, treatment, then neutralizing schemes are possible, they are too complex and expensive to implement in under-the-sink applications. Further, selenate adsorption must compete with less toxic sulphate species in the water, which occupies adsorption sites and thus decreases adsorption capacities.[18] For example, the adsorption capacity of aluminum oxide particles embedded in chitosan beads decreases from adsorbing 80% of the Se in water with 1 ppm selenate to less than 10% when 10 ppm of sulphate is present.[23] The decrease in performance arises because selenate and sulphate have similar structures and chemical properties, like pKa, and water typically has 2-1000 times higher S concentrations than Se.[15,18] Therefore, materials design strategies are needed to increase the affinity of Se for adsorption across a range of pH.[17,30-32]

In previous chapter, I examined the effects of solution pH and oxo-anion adsorption configuration on the adsorption of selenate on (012) α-Al_2O_3 surface using density functional theory calculations.[33] I found that the interaction between selenate and the surface water network is the major controller of selenate adsorption. At low pH, when the

surface is covered with excess H^+, the selenate induces the formation of additional hydrogen bonds within the water network, and hence has more exothermic adsorption energy. At high pH, the number of hydrogen bonds decreases when selenate adsorbs, which leads to endothermic adsorption. Moreover, selenate preferentially adsorbed in an outer-sphere configuration at low pH,[33] which explains the low selectivity of Al_2O_3 for selenate adsorption.[18,23] These findings beg two questions: 1) is the surface water network the sole controller of selenate adsorption on metal-oxide adsorbents?[34] and 2) can interactions between the oxo-anion and surface cations overcome the water network effects?[35-37] The importance of these questions is further highlighted by the recent work of Johnston and Chrysochoou who found that the adsorption mechanism of selenate and sulfate changes from inner-sphere to outer-sphere on naturally occurring Al substituted Fe (hydro)oxides at higher Al concentrations.[38] However, they did not discuss the cause of the changing motif or the adsorption energies when aluminum ions are substituted into ferrihydrites. Thus, if we are to design more selective and effective adsorbents, a delineation of the effects of water layers and cation identity effects is required.[39]

To isolate the role of the adsorbent cation, i.e., Al^{3+} in Al_2O_3, on adsorption without the confounding effects of various water networks, I used density functional theory (DFT) to calculate the adsorption energies of selenate on single atom substitutions into the (012) Al_2O_3 (X -Al_2O_3) (Figure 4.1). Specifically, I examine period 4 transition metals and group IIIA metal substitutions (X: Sc, Ti, V, Cr, Mn, Fe, Co, Ni, Cu, Ga and In). Past literature provides evidence that some of the transition metal cations (Fe, Co, Ni and Mn) can be substituted as dispersed ions in the α-phase Al_2O_3 at the Al:X ratio of 1.9993:0.0007 without changing the mechanical properties of the materials.[41] However, I ignored the

morphological variations that might occur due to the cationic substitutions to maintain a uniform water network on the surface. To understand the role of interaction between metal-ion and selenate on adsorption energy and mechanism, I compare the adsorption energy on the protonated and neutral surfaces in inner and outer sphere configuration to predict if the interaction between oxo-anion and cation overcomes the controlling effect of water network on the Al_2O_3 surface. I also compare the adsorption of selenate with sulphate to explore if X-Al_2O_3 can enable selective adsorption. Finally, I investigate the effect of atomic properties of adsorbent material on the adsorption of selenate and sulphate to delineate material properties that have the most significant correlations with the adsorption energy.

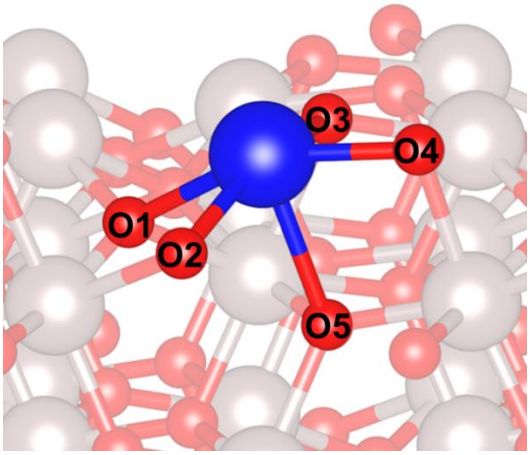

Figure 4.1: Bond distances used to calculate atomic radii. The blue, gray, and red spheres represent X, Al, and O respectively.

4.3 Methods

4.3.1 First-principle calculations

I performed Density Functional Theory (DFT) calculations in Vienna Ab initio Simulation Program (VASP)[41,42] using spin-polarized generalized gradient approximation functional (Perdew-Burke Ernzerhof - PBE)[43]. My previous work has shown that this method predicts energies that are in good agreement with the much more expensive HSE06 hybrid density functional, therefore the less expensive PBE functional is used.[33] Implicit solvent effects and non-local van der Waals (vdW) effects are accounted for by adding water dielectric constant in the polarizable continuum model (VASPsol module)[44] and DFT-D3 correction, based on the method of Grimme et. al[45]. The projected-augmented wave (PAW)[41,42] pseudopotentials used in calculations explicitly describe only valence orbitals 1s (H), 2s,2p (O), 3p,3d (Al, S), 3d,4s (Sc, Ti, V, Cr, Mn, Fe, Co, Ni, Cu), 3d,4s,4p (Ga, Se) and 4d,5s,5p (In) to reduce the computational cost associated with describing the core electrons.

The α-Al_2O_3 crystal was represented by the Al terminated (012) facet [46] slab supercell containing 2×2×1 primitive unit cells (α-$Al_{12}O_{18}$) separated by 45 Å polarized implicit solvent created using pymatgen[47,48]. The (012) facet is the largest constituent of gibbsite particles (47%) and has a low surface energy.[49,50] I obtained the crystal lattice constants for relaxed α-Al_2O_3 (a=b= 4.80Å, c=13.09Å, α=β=90° and γ=120°), which closely match previously published experimentally results (a=b= 4.76Å, c=12.99Å, α=β=90° and γ=120°).[51] The relaxed structure was used to construct the surface. The slab studied here is 13.5 Å thick and is comprised of 8 Al^{3+} layers, containing 4 cations (Figure

4.2). I fixed the position of bottom 4 Al^{3+} layers along with the oxygen to reduce the computational cost and preserve the bulk crystalline effects of Al_2O_3 nanoparticle. The adsorption energy difference of an example SeO_4^{2-} on an 8-layer thick slab and 10-layer thick slab is only 0.005 eV, which is well within chemical accuracy; thus, the less expensive 8-layer slab was used.

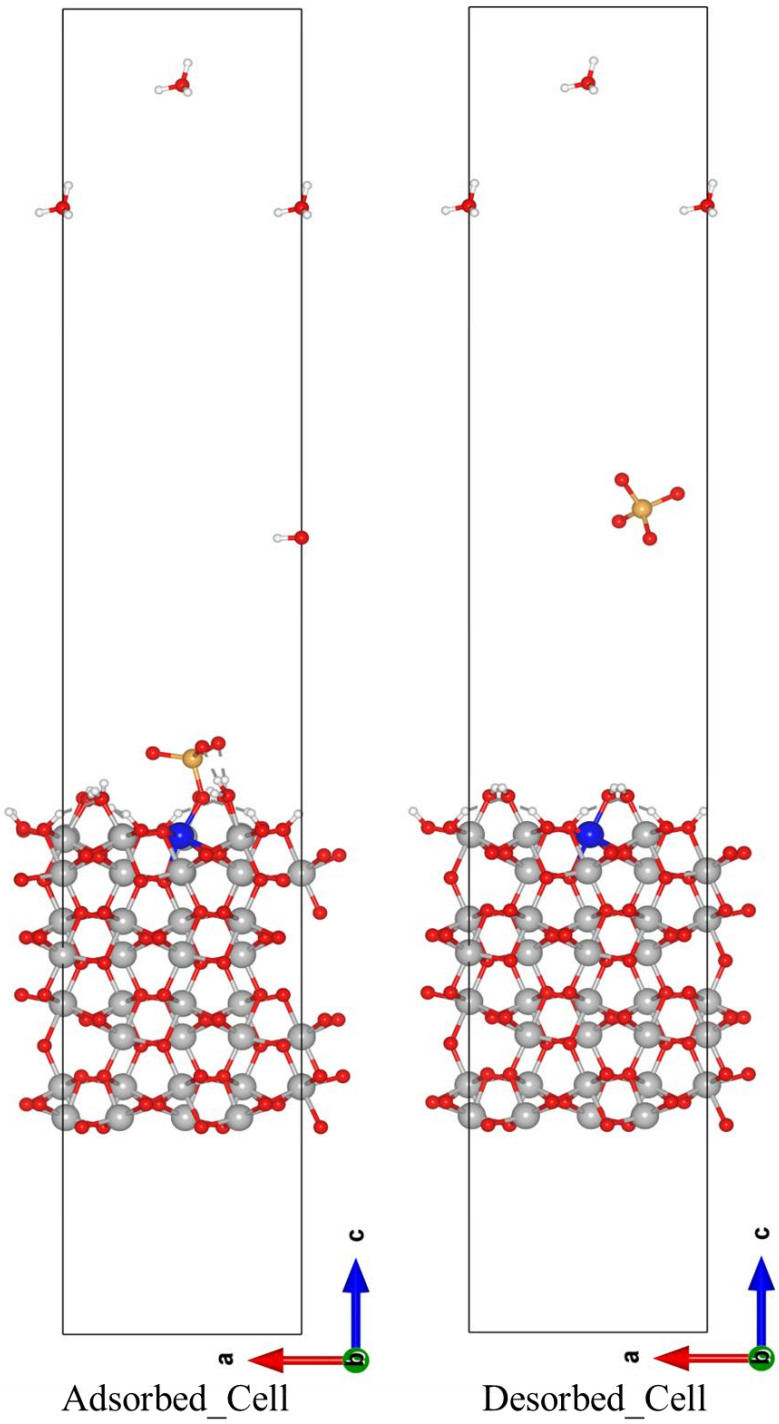

Figure 4.2: VASP simulation cell used for calculating the adsorption of selenate on (012) X-Al_2O_3 surface. Here X (represented by blue sphere) is the substituted cation. The grey, red, white and orange balls represent Al, O, H and Se atoms respectively. The desorbed species ($2\times H_3O^+$ and OH in Adsorbed_Cell, $2\times H_3O^+$ and SeO_4^{2-} in Desorbed_Cell) are suspended in vacuum with intermolecular distance of at least 6 Å, to represent a dilute limit and to minimize spurious Van der Waals interactions.

The surface was modeled by a hybrid explicit/implicit solvation. An explicit monolayer of dissociated water is added on the top surface of Al_2O_3 (one H_2O molecule per surface cation), as shown in figure 4.3(a), to mimic experimentally investigated interfacial water layer[46] in neutral environment to develop micro solvation model.[52] To model the surface below the point of zero charge, an additional proton was added to the dissociated hydroxyl group. In the vacuum above the explicit water, I included implicit solvation to complete the solvation model. My previous results showed that this hybrid model reproduced a full four layers of explicit water (Appendix A). Implicit continuum solvent space in my supercell was partially filled with desorbed selenate, water species and hydronium ions to retain charge parity upon adsorption. Intermolecular distances of at least 5 Å were maintained between desorbed species and surface to eliminate Van der Waals interactions between desorbed ions.[53]

Adsorption energies were calculated between supercells containing the same number of electrons and atoms using the hybrid solvent method (HSM), as outlined in my previous chapter (Figure 3.2).[33] In the HSM, I include an explicit water monolayer on the Al_2O_3 surface and implicit water dielectric effects between α-Al_2O_3 slabs to mimic the aqueous phase. Extra protons were added to the water monolayer as appropriate to represent the surface below the point of zero charge. The HSM is necessary to (1) include solvation effects on the surface, (2) compare adsorption energies of inner vs. outer sphere configurations, and (3) achieve experimental parity.

To avoid the high computational cost of large unit cells with implicit solvent and Van der Waals interactions, I initially calculated the geometries and energies of 11 different

adsorption configurations (5 inner-sphere and 6 outer-sphere) for each surface, i.e., substitution and protonation state, and sorbent, i.e., Se or S, at 350 eV cut off energy and 1×1×1 gamma point centered Monkhorst-Pack k-point mesh. For all in-depth analysis, I examined only the most exothermic geometries of the inner-sphere adsorption (IS) and outer-sphere adsorption (OS) configurations. These configurations were re-optimized at a higher 550 eV cut of energy and a finer 2×2×1 gamma point centered Monkhorst-Pack k-point mesh. The difference in adsorption energy between 350eV, 1×1×1 optimization and 550 eV, 2×2×1 was less than 0.05 eV, which is small compared to the adsorption energy difference in different configurations (> 0.4 eV). I found that there is only a 0.004 eV difference in adsorption energies calculated at 550 eV and 600 eV and only a 0.0005 eV difference between the 2×2×1 gamma-point centered Monkhorst-Pack k-point mesh and a finer 4×4×1 mesh grid; therefore, the less computationally expensive 550 eV and 2×2×1 mesh parameter were used. Atomic geometries were relaxed until total energies between two ionic steps were less than 0.001 eV.

4.3.2 Adsorption energy calculation

Supercells containing the single atom alloy substituted (X) metal-oxide surface ($X - Al_2O_3$), adsorbed water layer [54,55] ($(8 - y)OH^-.(n - z)H^+$, selenate (SeO_4^{2-}) and desorbed species ($2H_3O^+ + yOH^-.zH_{aq}^+$) were used to calculate adsorption energies. The adsorption energy is computed by subtracting the energy of desorbed_cell ($E_{desorbed\_cell}$)from the adsorbed_cell ($E_{adsorbed\_cell}$). The desorbed cell and adsorbed cell have the same number of atoms and electrons, as all desorbed species are explicitly included in solution regions of the supercell above the metal-oxide surface. Thus, all calculated energies arise from super cells containing exactly the same number of atoms and electrons. Example adsorbed_cell and desorbed_cell geometries are illustrated in Figure 4.2. In equations 4.1-4.3, the (.) between terms indicate bonded/adsorbed species and (+) indicates species that are separated by at least by 5 Å in the same supercell. I have previously validated this method for calculating adsorption energies using the bare Al_2O_3 surface by accurately reproducing adsorption isotherms.[33]

Table 4.1: Adsorbed and desorbed cell (eq 1) constituents for different configurations and protonation states used to calculate adsorption energies.

Configuration	Adsorbed_Cell	Desorbed_Cell	Number of atoms				
			Al	O	H	Se	X
Protonated Surface							
MM	$X-Al_2O_3.7H_2O.4H^+.SeO_4^{-2}+H_2O+2H_3O^+$	$X-Al_2O_3.8H_2O.4H^++SeO_4^{-2}+2H_3O^+$	63	110	26	1	1
BM	$X-Al_2O_3.7H_2O.4H^+.SeO_4^{-2}+H_2O+2H_3O^+$	$X-Al_2O_3.8H_2O.4H^++SeO_4^{-2}+2H_3O^+$	63	110	26	1	1
Outer	$X-Al_2O_3.8H_2O.4H^+.SeO_4^{-2}+2H_3O^+$	$X-Al_2O_3.8H_2O.4H^++SeO_4^{-2}+2H_3O^+$	63	110	26	1	1
Neutral Surface							
MM	$X-Al_2O_3.7H_2O.H^+.SeO_4^{-2}+OH^-+2H_3O^+$	$X-Al_2O_3.8H_2O+SeO_4^{-2}+2H_3O^+$	63	110	22	1	1
Outer	$X-Al_2O_3.8H_2O.SeO_4^{-2}+2H_3O^+$	$X-Al_2O_3.8H_2O+SeO_4^{-2}+2H_3O^+$	63	110	22	1	1

Details for all species present in adsorbed_cell and desorbed_cell for all configurations and protonation are listed in Table 4.1. I only computed adsorption energies of fully deprotonated oxo-anions (SeO_4^{2-} and SO_4^{2-}) as they are only species present at pH > 2, i.e., all environmentally relevant pHs.[56,57]

For a given configuration was calculated using eq. 4.1:

$$\Delta E = E_{adsorbed\_cell} - E_{desorbed_{cell}} \qquad eq.\ 4.1$$

Here $E_{adsorbed\_cell}$ is the energy of simulated cell containing adsorbed selenate.

$$E_{adsorbed\_cell} = E_{X-Al_2O_3.(8-y)OH^-.(n-z)H^+.SeO_4^{2-}+2H_3O^+_{aq}+yOH^-.zH^+_{aq}} \qquad eq.\ 4.2$$

And $E_{dedsorbed\_cell}$ is the energy of simulated cell containing desorbed selenate.

$$E_{desorbed\_cell} = E_{X-Al_2O_3.8OH^-.nH^+ + SeO_4^{2-}{}_{aq} + 2H_3O^+_{aq}} \quad eq.\ 4.3$$

The variable used in eq 4.2 and 4.3 change upon the adsorption configuration (y,z), surface protonation (n) and single atom (X) and values are listed in Table 4.2.

Table 4.2: Values of variables used in eq 4.2 and 4.3:

Factors		**Variables**	**Values**
Single atom impregnated on [012] α-Al_2O_3		X	Sc, Ti, V, Cr, Mn, Fe, Co, Ni, Cu, Ga, In
Surface protonation	Protonated surface (PS)	n	12
	Neutral Surface (NS)		8
Adsorption configuration	Bidentate Bimolecular (BB)	y	2
		z	2(PS), 0(NS)
	Monodentate Monomolecular (MM)	y	1
		z	1(PS),0(NS)
	Bidentate Monomolecular (BM)	y	1
		z	1(PS)
	Outer sphere (OS)	y	0
		z	0

In this work, I examine adsorption thermodynamics through adsorption energy lens and neglect entropic effects. However, given a drastic difference in enthalpic adsorption energy (on the order of -2 to 1 eV with ~0.5 eV difference between configurations), I expect the entropic effects will only slightly modify the thermodynamics as the entropy of water solvation is only ~ 0.1 eV.[58] Moreover, the substitution of one cation for another in the surface should not significantly affect the entropy of water on the surface, water desorption, or oxo-anion adsorption. Therefore, because this study focuses on understanding the effect

of cation on adsorption, I did not perform the computationally expensive entropic calculations.

Density of States (DOS), and charge density differences were calculated using vaspkit[59], and Crystal Orbital Overlap Populations (COOP) was calculated using LOBSTER[60,61] software. Crystal structure representations were obtained using VESTA.[62]

4.3.3 Ionic radius calculations

I calculated the atomic radii of the single atoms embedded in the Al_2O_3 surface by averaging the inter-atomic distance of the single atom with its coordinating surface O atoms (O1-O4) (Figure 4.1) and subtracting the ionic radii of O^{2-} (1.4 Å).[63] The atomic distance with sub-surface oxygen (O5) is not used to calculate atomic radii as this bond partially dissociated when the dispersed atom was much larger than Al and protruded out of the Al_2O_3 plane to reduce steric hindrance. I chose to use my calculated atomic radii rather than using literature values as ionic radii changes with their oxidation state.[63]

4.4 Results

I modeled the adsorption of selenate and sulphate on single atom substituted [012] Al_2O_3 (X-Al_2O_3) where I substituted one in every 8 Al atoms present on the surface to elucidate the effects of the cation on adsorption. Substitutions included Period 4 transition metal (Sc-Cu) and Group IIIA metals (Ga, In). I found that Ti, V, Mn, Fe, Co, Ni and Cu are spin polarized while Sc, Cr, Ga and In only have paired electrons. Only the lowest energy spin configurations are reported in this work.

I assume that the all substitutions are in the dilute limit, where secondary phase formation will not occur, to elucidate the relative effects of cation-selenate interaction and water network-selenate interactions. Experimental work has previously shown that Fe, Co, Ni and Mn can stability substituted at low Al: X ratios (1.9993:0.0007).[40] The fact that the cations are fully relaxed demonstrates that they are at least in a local minimum. Further, COOP analysis shows that the substitutions are strongly bond to their neighboring O anions (Figure 4.3). I do, however, note that In, Ga, Sc, Ti, V and Cr are expected to be more stable than the Mn, Fe, Co, Ni and Cu substitutions, as the former do not have anti-bonding character, while the later set does have some filled anti-bonding states.

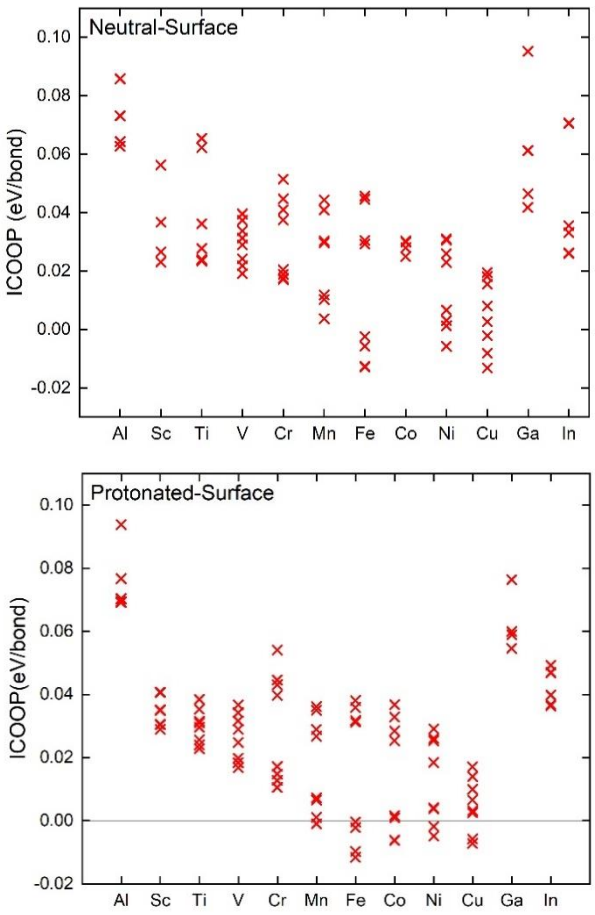

Figure 4.3: ICOOP of X-O bond up to the Fermi Energy used to understand the stability of metal-ion substitution. Negative ICOOP value indicated unstable bonds and positive ICOOP value indicated stable bonds.

Additionally, I note that several of the cations investigated here can adopt multiple oxidation states or have preferred oxidation states which differ from the +3 charge of Al. DOS analysis, Figure 4.4, show that Ti, V, Cr Mn, Fe, Co, and Ni induce mid-gap states localized on the cations, while Sc, Cu, Ga and In show slightly unfilled O 2p states. The missing O 2p state arise from the covalent nature of the metal-O bond, and the partial localization of the bonded electron on the cation. The charge localization is further quantified by Bader analysis in Table 4.3 and shows that the charge density on the neighboring Os' are modified by ~1.2-0.7 e^- depending on the substitution. However, even though the oxidation state of single atom substitution is not exactly +3, the electrons are still localized near single atoms on the neighboring O, and not transferred to the surface water network to form +4 or other oxidation state. This additional charge on the cations relative to Al, or the missing charge on the neighboring O atoms may alter the local point of zero charge, and thus protonation extent at a given system pH. Therefore, I examine both the protonated and neutral surface; I leave prediction of local protonation extents due to substitutions to future work.

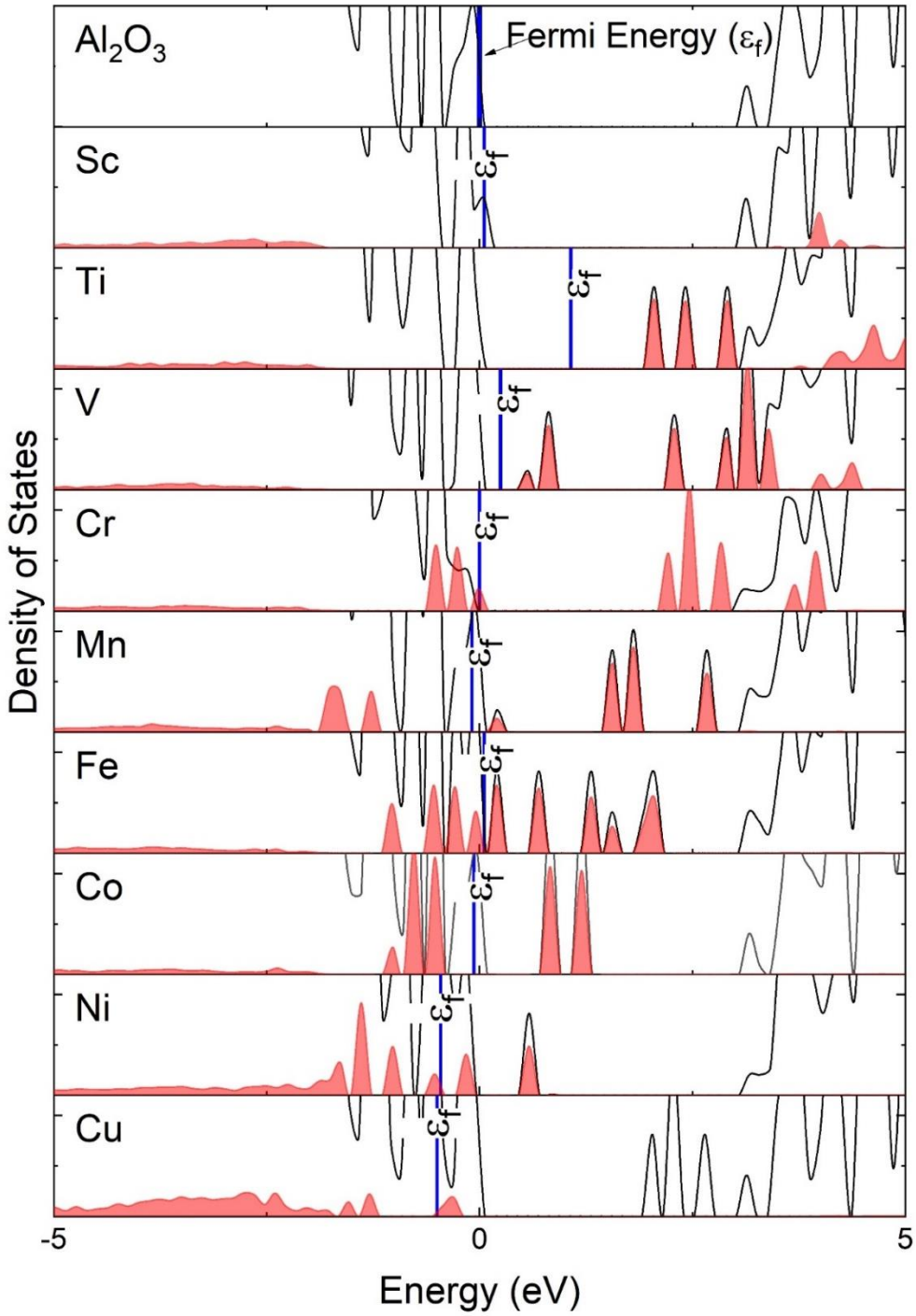

Figure 4.4: Density of states plot for neutral X-Al_2O_3, where X is transition metal substitution. The colored red area presents Density of state of X orbitals and black line presents total density of states on desorbed_cell.

Table 4.3: Bader charge on Single atom substitution before adsorption (desorbed_cell) in neutral and protonated surface.

	protonated Surface	Neutral surface
Al	2.5	2.5
Sc	1.8	1.8
Ti	1.7	1.7
V	1.7	1.7
Cr	1.6	1.6
Mn	1.6	1.6
Fe	1.6	1.6
Co	1.3	1.3
Ni	1.2	1.2
Cu	1.2	1.2
Ga	1.7	1.7
In	1.6	1.6

I calculated the adsorption energy of selenate on the neutral (pH >7.8) and protonated (pH <~5.5-6) Al_2O_3 surface, which are shown in Figure 4.5a-d. The neutral surface is covered by 8 dissociated water molecules ($Al_2O_3.8OH^-.8H^+$) before adsorption, while the protonated surface has 8 water molecules and 4 protons ($Al_2O_3.4H_2O.4OH^-.8H^+$). The 4 extra protons on the protonated surface bond with the original surface OH^- to form H_2O molecules. The protonated surface represents the system below the point of zero charge, 7.8 [28] for the (012) Al_2O_3 surface; at environmentally relevant conditions the surface may or may not be protonated, but the selenate and sulfate species are fully deprotonated. All charged supercells are compensated with background jellium charge; the large unit cells used here (~5600 $Å^3$) minimize the jellium charge in any location. The size effects of the jellium were validated in previous chapter.[33] I initially screened one mono-dentate monomolecular (MM), one bidentate molecular (BM) and three bi-dentate bimolecular (BB) inner sphere configurations, and six outer-sphere configurations (two

each of monodentate, bidentate and tridentate to the adsorbed waters). Exemplar MM, BM, BB, and OS adsorption configuration on Ga-Al_2O_3 are shown in Figure 4.5. I do not discuss BB adsorption energy as it was always significantly more endothermic than MM and BM adsorption energies (Table 4.4 and 4.5). The same preference for MM, BM and OS adsorption configurations exists for sulfate.

Table 4.4: Adsorption energies of SeO_4^{2-} on protonated X-Al_2O_3

protonated	**MM**	**BM**	**BB**	**Outer sphere**
	eV	**eV**	**eV**	**eV**
Al	-1.49		-0.32	-1.79
Sc	-1.27	-1.77	-0.57	-1.74
Ti	-1.58	-1.54	-1.02	-1.82
V	-1.51	-1.06	-0.57	-1.64
Cr	-1.53	-1.50	-0.34	-1.75
Mn	-0.89	-1.33	-0.24	-1.55
Fe	-1.54	-1.54*	-0.22	-1.48
Co	-1.17	-0.99*	-0.22	-1.42
Ni	-0.92	-0.74*	-0.21	-1.35
Cu	-0.96	-1.10*	-0.10	-1.37
Ga	-1.54	-1.53*	-0.50	-1.78
In		-1.83	-0.66	-1.74

*: relaxed into MM configuration

Table 4.5: Adsorption energies of SeO_4^{2-} on neutral X-Al_2O_3

Neutral	MM	BB	Outer sphere
	eV	eV	eV
Al	1.1	1.99	0.25
Sc	.84	2.03	0.45
Ti	.04	1.35	0.24
V	.88	1.33	0.42
Cr	1.03	1.35	0.48
Mn	.84	2.20	0.43
Fe	.98	2.17	0.50
Co	1.25	2.30	0.24
Ni	1.55	1.98	0.49
Cu	.95	2.12	0.44
Ga	1.12	3.12	0.44
In	1.06	3.09	0.48

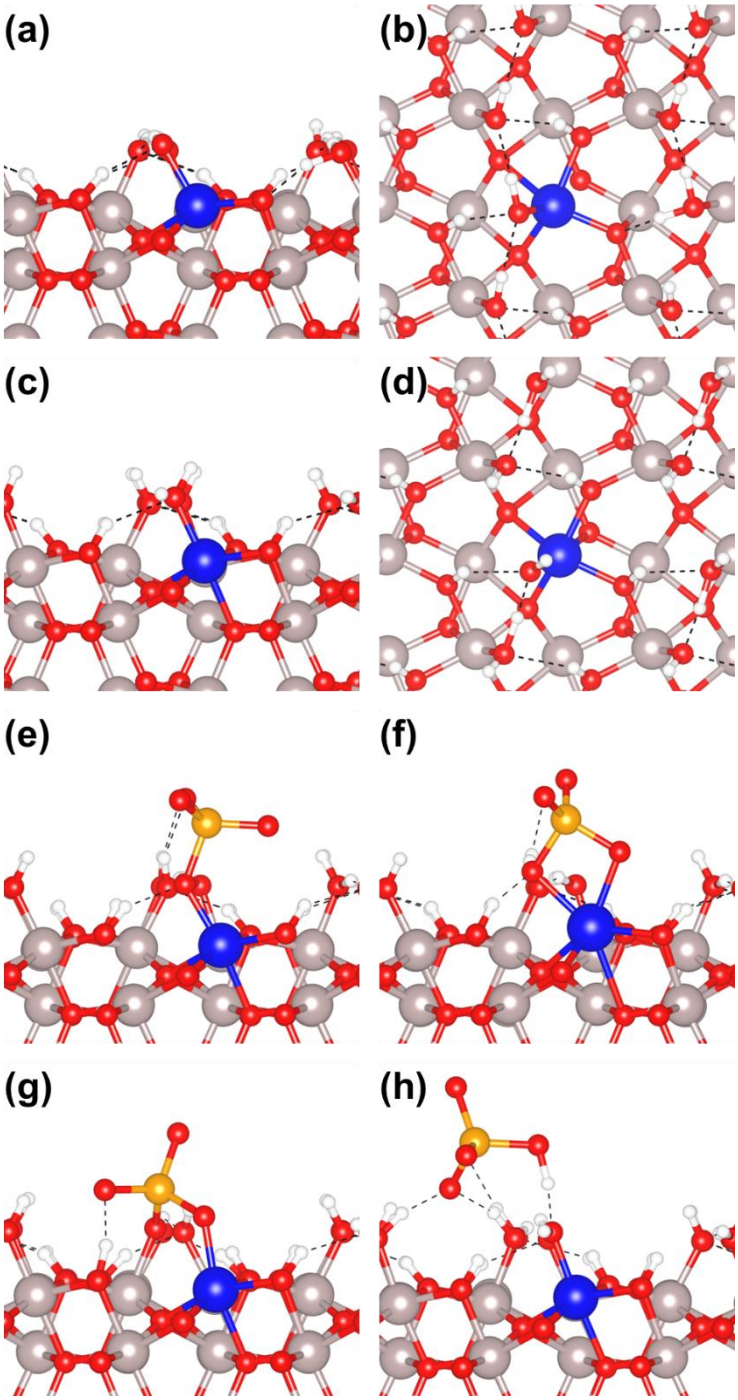

Figure 4.5: (012) X-Al_2O_3 where X (blue) is the impregnated single Atom (Ga- in figure) on surface in (a-b) neutral environment and (c-d) protonated environment. (a) and (c) are side view and (b) and (d) are top view of the neutral and protonated X-Al_2O_3 surface respectively. Side view of selenate (SeO_4^{2-}) adsorbed in (e) monodentate monomolecular (MM), (f) bidentate monomolecular (BM) (g) bidentate bimolecular (BB) and (c) outer sphere configuration (OS) on (012) α-Ga-Al_2O_3. The grey, orange, blue, red, white spheres represent Al, Se, Ga(X), O and H atoms, respectively.

4.4.1 Adsorption of selenate on single cation embedded in the [012] X-Al_2O_3

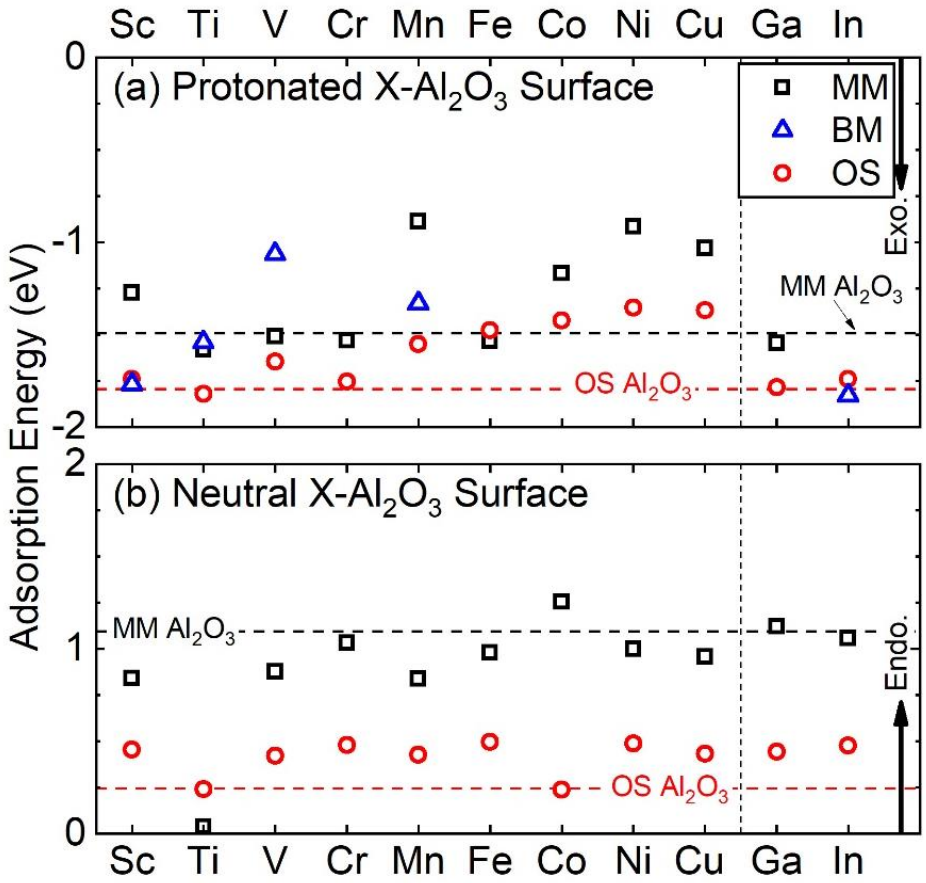

Figure 4.6: Adsorption of SeO_4^{2-} on (a) Protonated X-Al_2O_3 surface and (b) Neutral X-Al_2O_3 surface. The adsorption of selenate on [012] α-Al_2O_3 in MM, BM and outer sphere are depicted by dashed lines. BM on neutral surface relaxes in MM configuration and hence not added in (b).

I calculated the adsorption energy of selenate on X-Al_2O_3 as a function of adsorption motif and protonation state of the surface. The results, as summarized in Figure 4.6, show only the most exothermic configuration identified for the given system. I found that the adsorption of selenate was exothermic on protonated surface and endothermic on neutral surface for all X-Al_2O_3 surfaces. On the neutral surface, the adsorption energies remained similar in magnitude to the unsubstituted Al_2O_3 surface, and thus in most cases did not result in a reordering of the preferred binding motif. Some cations substitutions,

protonated In, Sc, Fe, and neutral Ti, altered the preferred binding from outer sphere to inner-sphere adsorption. However, the adsorption in most situations was less exothermic than on the unsubstituted Al_2O_3 surface, thus I saw no significant positive influence by adding dispersed single atoms. The monomolecular adsorption configurations (MM and BM), where selenate replaced one water molecule, was always more exothermic than bimolecular adsorption (BB), where two water molecules are replaced by single SeO_4^{2-} molecule. However, the adsorption energy did change in some cases by $< \pm 0.5$ eV from the unsubstituted [012] α-Al_2O_3 surface, usually destabilizing adsorption. In the rest of this section, I describe the behavior of adsorption trend across period 4 transition metal substituted and group IIIA metal substituted Al_2O_3 surface in (a) protonated and (b) neutral environments.

4.4.1.1 SeO_4^{2-} adsorption on the protonated X-Al_2O_3 (012) surface

On protonated X-Al_2O_3, I calculated that outer sphere adsorption energies range between -1.82 eV (Ti-Al_2O_3) and -1.32 eV (Cu-Al_2O_3) and monomolecular inner-sphere configurations range from -1.83 eV (In-Al_2O_3) to -0.96 eV (Cu-Al_2O_3). I categorize the substitutions elements into those which prefer the inner-sphere configuration (In, Sc and Fe) and those which prefer outer-sphere adsorption (Ti, V, Cr, Mn, Fe, Co, Cu, Ni and Ga). The inner-sphere configuration is the energetically favored structure on In-Al_2O_3 (BM, -1.83 eV), Sc-Al_2O_3 (BM, -1.77 eV), and Fe-Al_2O_3 (MM, -1.66 eV) as compared to outer-sphere adsorption.

Table 4.6: Ionic radii vs. Inner-sphere adsorption of selenate on protonated X-Al_2O_3 surface. The data is arranged in ascending order for ionic radius.

X	Ionic radius (Å)	Inner sphere adsorption energy (eV)	Preferred inner-sphere configuration
Al	0.51	-1.49	MM
Cr	0.58	-1.50	MM
Ga	0.59	-1.54	MM
Cu	0.62	-1.03	MM
V	0.62	-1.51	MM
Ni	0.63	-0.92	MM
Co	0.64	-1.17	MM
Fe	0.65	-1.54	MM
Ti	0.65	-1.58	MM
Mn	0.67	-1.33	BM
Sc	0.68	-1.77	BM
In	0.76	-1.83	BM

Adsorption of SeO_4^{2-} in the BM configuration on protonated In-Al_2O_3 (-1.83 eV) has the most exothermic energy across all configurations and surfaces, including unsubstituted Al_2O_3. I attribute the BM preference of In and Sc to distortions in its coordination at the surface. The ionic radii of the embedded In^{3+} (0.76 Å) and Sc^{3+} (0.68 Å) are substantially larger than that of their adjacent Al^{3+} (0.51 Å); and thus, In and Sc atoms protrude from the [012] Al_2O_3 surface, as shown in Figure 4.7, to minimize steric overlap with the in-plane O anions. I note that the ionic radii are calculated here using method described in section 4.2.3 and not from literature values. The extension outward also weakens the sub-surface X-O bond. From COOP analysis, I found that for Sc and In the O5-X bond strength (0.02 eV/bond for Sc and 0.03 eV/bond for In, labeled in Figure 4.1) is ~50% less than the average bond strength between surface O-X (O1-O4)(0.07 eV/bond for Sc and 0.09 eV/bond for In) and 6% less (0.15 eV/bond between O5-Al) than

the average bond strength for Al (0.16 eV/bond). The resulting undercoordination enables bidentate adsorption of selenate on Sc and In cations. The radius of In is so large, and thus so extended from the surface, that without the adsorbed water it is undercoordinated; consequently the MM configuration on In-Al_2O_3 is unstable and relaxes into BM configuration, providing a more complete coordination. The formation of the BM bond was verified through COOP analysis, which predicts two InO-Se bonds with strengths of 0.06 eV/bond.

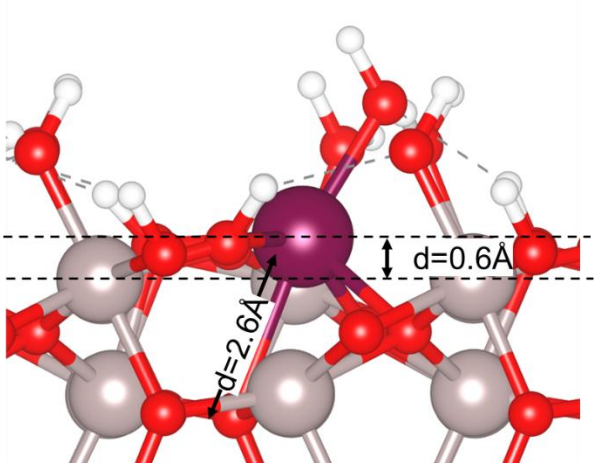

Figure 4.7: Protrusion of the In from the protonated Al_2O_3 surface before adsorption. The grey, purple, red, white spheres represent Al, In, O and H atoms, respectively.

Contrary to Sc and In, only the MM configuration of Fe-Al_2O_3 is more exothermic, by -0.41 eV, than the outer-sphere configuration. This configuration is -0.04 eV more exothermic than inner-sphere adsorption on unsubstituted Al_2O_3, but 0.32 eV less stable than outer sphere adsorption on Al_2O_3. The e^- density charge transfer between Al_2O_3 surface and selenate is similar when selenate adsorbs on Al_2O_3 and Fe-Al_2O_3. Therefore, the preferential adsorption of selenate on Fe-Al_2O_3 in the MM configuration is due to

weaker adsorption in the outer sphere configuration, rather than the Fe stabilizing inner-sphere selenate adsorption.

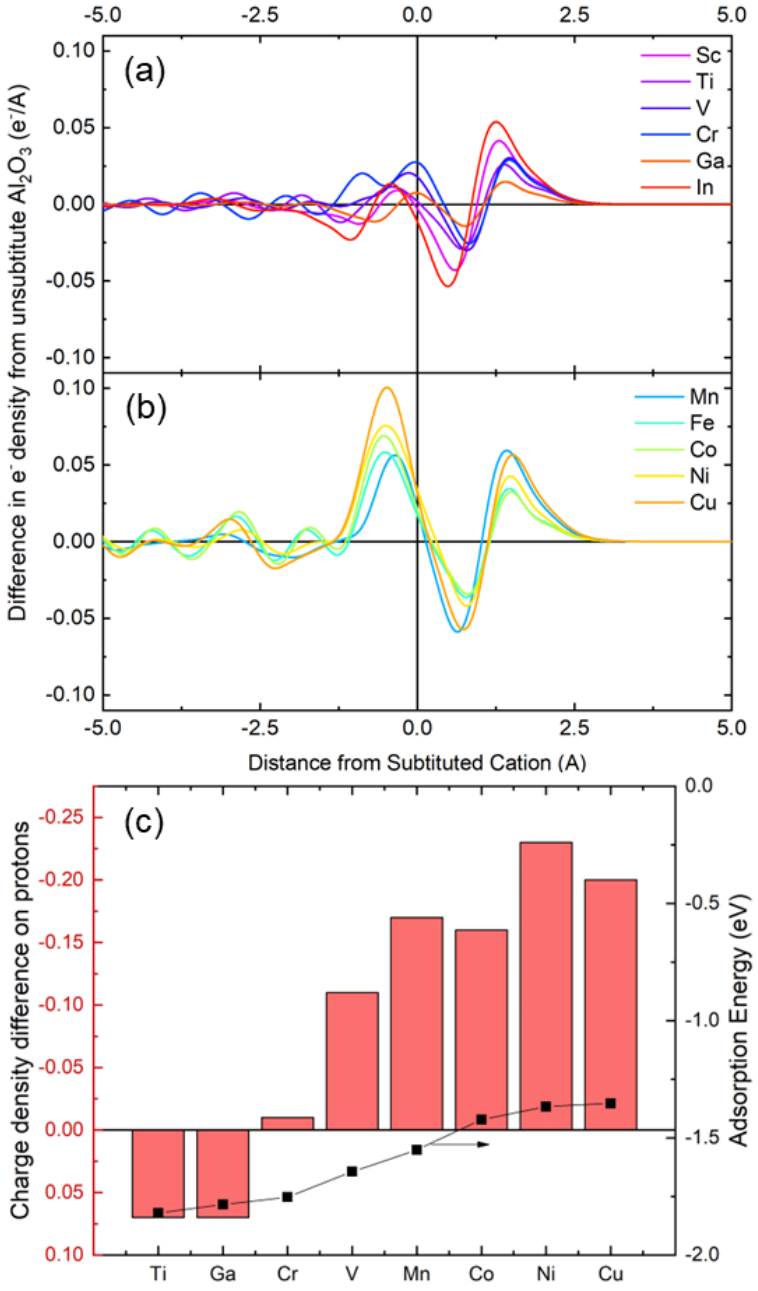

Figure 4.8: Difference in charge density on protonated X-Al_2O_3 relative to protonated unsubstituted Al_2O_3 before adsorption of selenate. (a) X: Sc, Ti, V, Cr, Ga, In and (b)X: Mn, Fe, Co, Ni, Cu. (c) Charge density difference between X-Al_2O_3 (X: *Ti, V, Cr, Mn, Co, Cu, Ni and Ga)* and unsubstituted Al_2O_3 vs. adsorption energy of selenate adsorption in outer-sphere.

Selenate adsorption at the Ti, V, Cr, Mn, Co, Cu, Ni and Ga sites maintain an outer sphere preference. In all cases except Ti the adsorption is less exothermic than unsubstituted Al_2O_3 (Figure 4.6). I note that the strong adsorption energy, which is on Ti-Al_2O_3, is only slightly (-0.03 eV) stronger than neat Al_2O_3. I attribute modification of outer-sphere adsorption energy to changes in the partial charges of the protons of the water layer. For all substitutions, additional charge density is localized near substituted cations as compared to unsubstituted Al_2O_3 (Figure 4.8(a-b)). Mn, Fe, Co, Cu and Ni induce the most charge localization, >0.05 $e^-/Å^2$, while Sc, Ti, V, Cr, Ga, and In induce the least. This localization weakens the HO-X bond for V, Cr, Mn, Fe, Co, Ni and Cu (0.05-0.02 eV/bond via COOP), as compared to higher bond strength of HO-X bond for unsubstituted Al_2O_3 (0.08 eV/bond) and other substitutions (0.10-0.07 eV/bond). Thus, more electron density accumulates on the protons of water molecules near V, Cr, Mn, Co, Cu and Ni substitutions as compared to unsubstituted Al_2O_3. The higher electron density, and thus reduced partial positive charge, decreases the coulombic attraction between the protons and the O of the selenate (Figure 4.8(c)). This weakening resulted in poorer adsorption energy of selenate on X-Al_2O_3 in outer-sphere adsorption. Conversely, in the case of Ti-Al_2O_3, Bader analysis indicates that the electron density is slightly lower (0.07 e^-) on the protons thus enabling slightly stronger hydrogen bonding and -0.03 eV stronger adsorption on Ti-Al_2O_3 as compared to unsubstituted Al_2O_3.

While outer-sphere adsorption is energetically preferred for Ti, V, Cr, Mn, Co, Cu, Ni and Ga, it was not necessarily the only stable configuration. Selenate adsorption was also dynamically stable in the MM configuration for Cr, Fe Co, Cu. Ni, Ga, while Ti, V, and Mn have stable MM and BM configurations. When the selenate was placed in a BM

configuration on Cr, Fe Co, Cu, Ni, it relaxed to a MM configuration. I attribute the ability to form BM configurations to the size of the substituted cation. The three BM binding cations, Mn, Ti and V which have atomic radii larger than 0.6 Å, (0.67 Å, 0.65 Å and 0.62 Å respectively) bind in BM configuration, while those with smaller radii do not (Table 4.6). In the BM configuration, the O-Se-O bond angle decreases (91°-99°) as compared to desorbed selenate (110°); which increases the strain on the oxo-anion. The adsorption of selenate in BM configuration needs to compensate for both the broken X-OH bond and increased strain of O-Se-O bond. For In and Sc, the net difference in bond strengths is positive (0.041 eV/bond (In) and 0.001 eV/bond (Sc)); while the net difference is negative for Ti (-0.014 eV/bond), V (-0.004 eV/bond) and Mn (-0.017 eV/bond). The altered bond strength enables stable BM configurations for Ti and Sc and less exothermic adsorption of selenate in BM for Mn, Ti, and V. I also observe that the protonation of adsorbed SeO_4^- changes to $HSeO_4^-$ (pulling H^+ from the surface) on Ti-Al_2O_3 and Ga-Al_2O_3 in outer-sphere configuration and Sc-Al_2O_3 and Mn-Al_2O_3 in monodentate configuration. However, this change does not show any effect on the adsorption energies.

4.4.1.2 SeO_4^{2-} adsorption on neutral metals substituted [012] X-Al_2O_3 surface

I calculate that selenate adsorption is endothermic on all neutral X-Al_2O_3 surfaces. The adsorption energies range between 0.24-0.48 eV in outer sphere configurations and 0.04-1.25 eV in MM configurations. Thus adsorption, in either MM or outer-sphere, is at best only -0.21 eV stronger than the unsubstituted α-Al_2O_3 (endothermic by 0.24 eV), but some substitutions destabilize adsorption to 0.50 eV. Ti-Al_2O_3 has the least endothermic adsorption energy (0.04 eV in its MM configuration) among all the neutral X-Al_2O_3 and

unsubstituted α-Al_2O_3 surfaces and is the only surface that prefers the MM configuration to outer-sphere adsorption. The adsorption energies in the outer sphere configuration on X-Al_2O_3 are either equal to (Ti, Co) or slightly more endothermic than (Sc, V, Cr, Mn, Fe, Ni, Cu, Ga, In) unsubstituted Al_2O_3. The adsorption of selenate in a monodentate configuration to all X-Al_2O_3 except Co-Al_2O_3 and Ga-Al_2O_3 is less endothermic than unsubstituted α-Al_2O_3. The Bidentate Monomolecular configuration is unstable on all neutral surfaces, and they relax to the monodentate monomolecular configuration. The selenate remains in fully de-protonated (SeO_4^{2-}) form upon adsorption on neutral X-Al_2O_3 in all configurations.

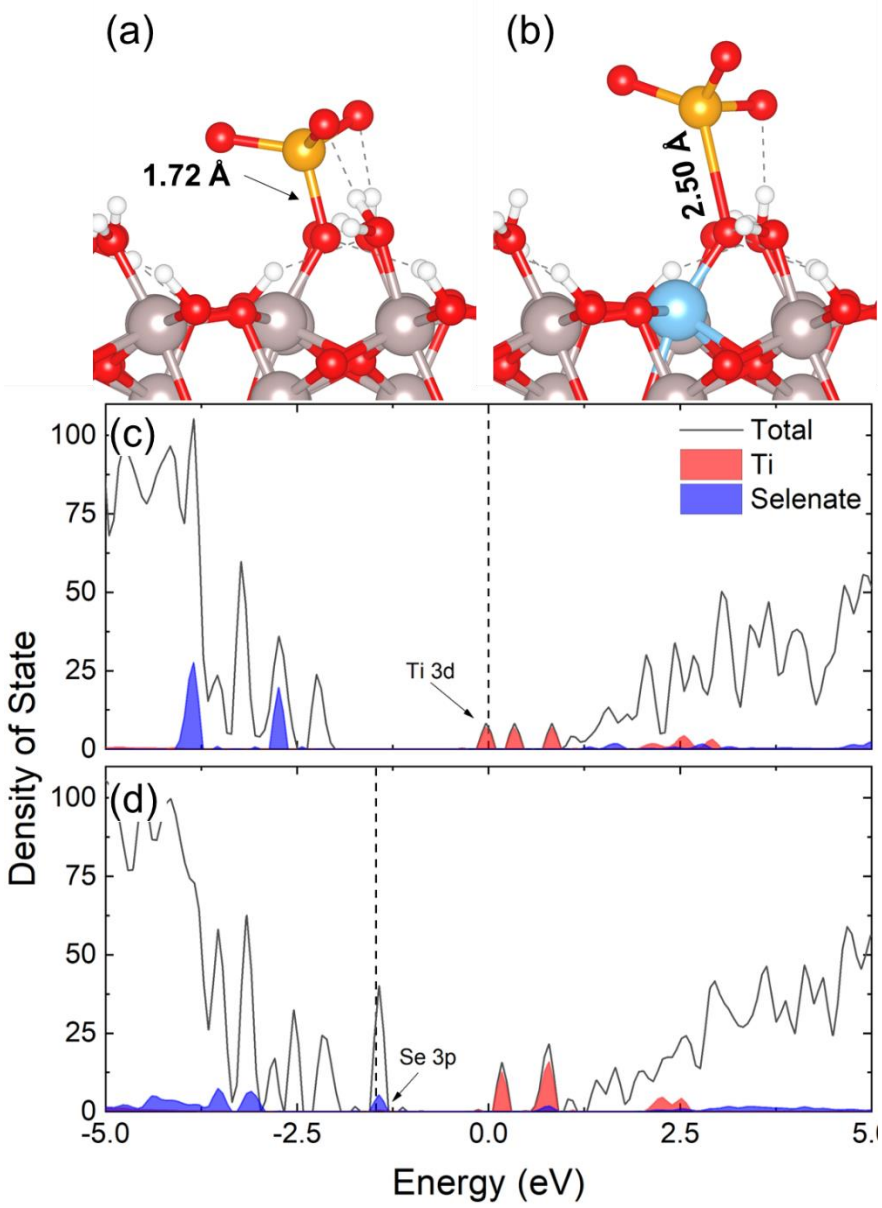

Figure 4.9: Selenate adsorption on neutral (a) Al_2O_3 and (b) Ti-Al_2O_3 in inner-sphere (MM) configuration. Density of State plots of Selenate on Ti-Al_2O_3 (c) before adsorption and (s) after adsorption. The grey, blue, dark grey, orange, red, white spheres represent Al, Ti, Ni, Se, O and H. atoms, respectively.

Neutral Ti-Al_2O_3 is the only surface structure that has a less endothermic adsorption energy in inner-sphere configuration than outer sphere configuration. From Bader analysis, I calculate that the Ti in Ti-Al_2O_3 transfers 0.18 e^- worth of electron density to the bonding O (Δe^- density = 0.16) of selenate. The remaining 0.02 e^- is distributed among the surface

OH^- ions. The transfer stretches the bond distance between the surface bonded O and Se to 2.5 Å from the ~1.7 Å between selenate's Se and the other O atoms. These bond changes suggest that the Se is only three-fold, rather than four-fold, quadrated after adsorption. Thus, the Ti cation acts to reduce selenate to selenite upon adsorption in neutral surface. The ability to reduce selenate arise from the instability of Ti in its +3-state which is present on the Al_2O_3 surface. Only after selenate adsorption, and the associated electron donation, does the Ti cation adopt its preferred +4 state.

Further electronic analysis supports the finding that Ti reduces the adsorbing selenate to selenite. The density of states (DOS) plot in Figure 4.9 shows that before adsorption, Ti induces mid-gap states 0.33 eV, 0.58 eV and 0.83 eV above the Fermi level. The highest mid-gap band is thus similar in energy to the valence band of selenate (1.08 eV above the Fermi level). Upon adsorption, the 3p orbital from Se ion is filled with the Ti 3d electron density, which now shifts to 0.04 eV above Fermi level (Figure 4.9(b)). Lastly, the reduction and Se-O bond cleavage is further verified by Crystal Orbital Overlap Population analysis (COOP), which shows presence of net anti-bonding orbital character (ICOOP = -0.0033 eV/bond) between TiO-Se bond after adsorption. The bond strength of Ti-OSe (ICOOP = 0.1038 eV/bond) after adsorption is also stronger than bond strength of Ti-OH (ICOOP = 0.0583 eV/bond) present before adsorption. This bond strengthening is not true for other surfaces, where the bond strength of X-OSe is always lower than the bond strength of X-OH. Thus, the formation of a strong, reducing Ti-O bond compensates for the water network disruption and H_2O dissociation upon selenate adsorption.

The adsorption of selenate in outer-sphere configuration results in adsorption energy on neutral X-Al_2O_3 is essentially equal to, or more endothermic than unsubstituted Al_2O_3. Additionally, the range in adsorption energies for outer-sphere adsorption on neutral X-Al_2O_3 surface is 0.26 eV which is the smallest of all the configurations. I attribute the narrower range to the indirect interactions between the selenate and the substitutional cations, via the water network which is only slightly modified by the cations. I found that the adsorption energies of selenate in outer sphere in Co-Al_2O_3 and Ti-Al_2O_3 (0.24 eV) is essentially the same as adsorption Al_2O_3 (0.25 eV). This is because the ionic radius of Co (1.94 Å) is the closest to ionic radii of Al (1.94 Å) on the neutral surface and thus the water network remains mostly undisturbed, while Ti is again unstable and donates 0.04 e^- to selenate upon adsorption. For other species, the ionic radius is larger than 1.99 Å which cause slight adjustments in water network, and hence decrease the adsorption energy. Measurements of the water network changes will be discussed in detail in Section 4.3.3.

Finally, I performed COOP analysis between the single atom substitutions and surface O's to (O1-O4, figure 4.1) to analyze the stability of metal substitution to confirm that the adsorption trends I observe are because of changes in surface properties and not due to poor stability of substitution cation (Figure 4.3). I found that the adsorption energies were not related to the stability of substitution on the Al_2O_3 surface. Mn, Fe, Co, Ni and Cu metal substitutions are less likely to be stable than other substitutions (In, Ga, Sc, Ti, V and Cr) as they have some filled anti-bonding orbitals before fermi energy (ICOOP < 0 eV/bond). However, the substitutions are stable enough and do not cause dramatic changes to the adsorption energies investigated here.

4.4.2 Adsorption energy of sulphate on single cation embedded in the [012] X-Al_2O_3

The adsorption behavior of sulfate on Al_2O_3 is very similar to that of selenate due to their similar geometric and electronic structures, and pKa's. The adsorption energies of SeO_4^{2-} and SO_4^{2-} on neutral and protonated X-Al_2O_3 in their most relaxed (exothermic) configurations are presented in Figure 4.10. The adsorption of these two species is essentially identical within methodological accuracy on the protonated unsubstituted Al_2O_3, having adsorption energies of -1.79 eV (SO_4^{2-}) and -1.79 eV (SeO_4^{2-}) in the favored outer sphere configuration. Their adsorption energies are very similar on neutral α-Al_2O_3 being 0.24 eV (SO_4^{2-}) and 0.25 eV (SeO_4^{2-}) which are both endothermic. Thus, because there is no meaningful thermodynamic preference for one ion or the other for the exothermic outer sphere binding, I do not predict Al_2O_3 to provide selenate selectivity.[64] This similarity in adsorption energy matches the experiments which shows no selectivity for selenate.

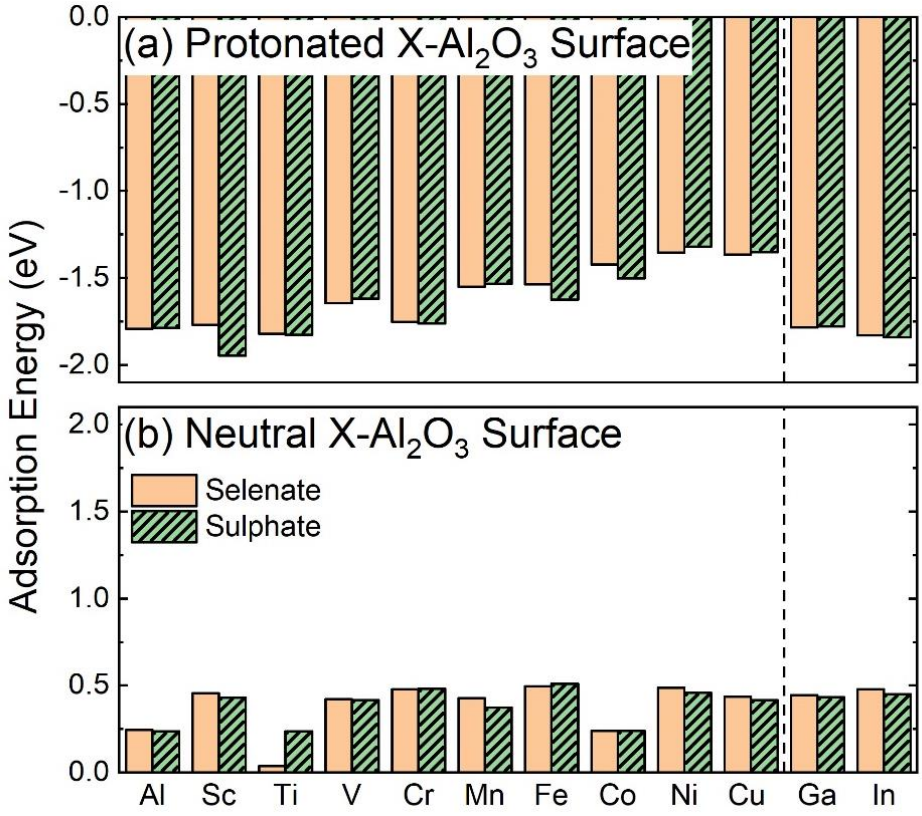

Figure 4.10: Adsorption of SeO_4^{2-} vs. SO_4^{2-} on (a) Protonated X-Al_2O_3 surface and (b) Neutral X-Al_2O_3 surface in the most exothermic configuration.

Ti is the only substitution which induces selectivity on the neutral surface. Ti stabilizes SeO_4^{2-} adsorption by 0.2 eV over SO_4^{2-}. All other substitutions only modified the adsorption energy of selenate by ±0.1 eV over sulfate, which is within the resolution of the computational method. The preference of Ti substitutions for Se over S arises from the slight differences in the electronic structures of Se and S and the position of the mid-gap states induced by Ti. On neutral Ti-Al_2O_3 selenate adsorption in the MM configuration was -1.06 eV more exothermic than unsubstituted Al_2O_3, because of the overlapping selenate and Ti orbitals, which cause selenate to reduce into selenite (Figure 4.9). Reduction does not, however, occur for sulphate as the valence bands of sulfate are 2.06 eV above Fermi level (Figure 4.11). This finding suggests that selective adsorption of selenate over sulfate

is possible when Se(VI) reduces to Se(IV) upon adsorption. However, the structures where Se(VI) reduce to Se(IV) are not the energetically favorable structures, and thus selectivity of Ti modified Al_2O_3 is unlikely to provide selectivity.

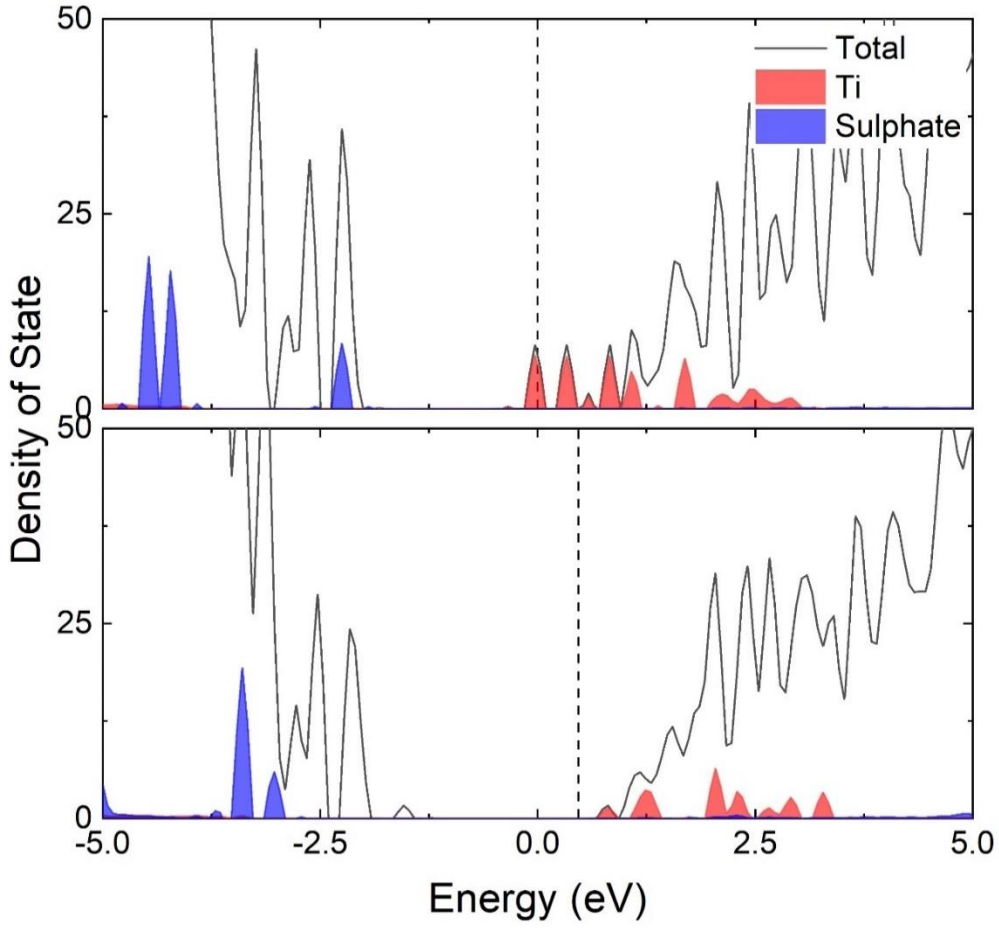

Figure 4.11: Density of State plots of Sulphate on Ti-Al_2O_3 (c) before adsorption and (s) after adsorption.

Both selenate and sulphate adsorb in BM configurations on the protonated Sc, V, Cr, Mn and Ti-Al_2O_3. Using Sc-Al_2O_3 as the exemplar, I calculate that it slightly prefers SO_4^{2-} adsorption by -0.18 eV. This preference arises because SO_4^{2-} has shorter O-S bonds (1.52 Å) than the O-Se of SeO_4^{2-}(1.70 Å). When the oxo-anions adsorb on Sc in BM configuration, O-Se-O bond angle decreases (93.25°) more than O-S-O bond angle

(98.53°) (Figure 4.12). This leads to lower bond strength of SeO bond (0.11 eV/bond) as compared to SO bond (0.13 eV/bond). Hence, I see a preferential adsorption of SO_4^{2-} on protonated Sc-Al_2O_3 as compared to SeO_4^{2-}. The same is accounted for the performance of the other cations and BM configurations (Table 4.7 & 4.8). This finding suggest size selective adsorption is possible, though not for selenate over sulfate, if we identify materials which adsorbs oxo-anions in inner-sphere bidentate configurations.

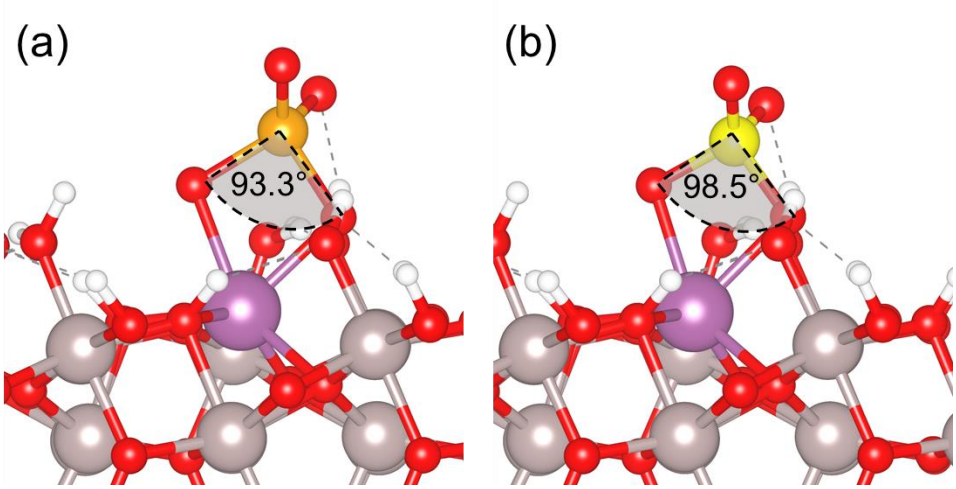

Figure 4.12: (a) Selenate and (b) Sulphate adsorption on protonated Sc-Al_2O_3 in inner-sphere (BM) configuration.

Table 4.7: Adsorption energies of SO_4^{2-} on protonated X-Al_2O_3

protonated	MM	BM	Outer sphere
	eV	eV	eV
Al	-1.55		-1.79
Sc	-1.29	-1.95	-1.76
Ti	-1.69	-1.72	-1.83
V	-1.52	-1.25	-1.62
Cr	-1.56	-1.60	-1.76
Mn	-0.98	-1.43	-1.53
Fe	-1.17	-1.62	-1.60
Co	-1.27	-1.33	-1.50
Ni	-0.89		-1.32
Cu	-0.88		-1.35
Ga	-1.61	-1.58	-1.78
In		-1.84	-1.77

Table 4.8: Adsorption energies of SO_4^{2-} on neutral X-Al_2O_3

Neutral	MM	Outer sphere
	eV	eV
Al	1.02	0.236
Sc	0.79	0.43
Ti	0.89	0.24
V	0.86	0.42
Cr	0.98	0.48
Mn	0.71	0.37
Fe	0.91	2.70
Co	1.23	0.24
Ni	0.88	0.46
Cu	0.92	0.42
Ga	1.12	0.43
In	1.02	0.45

4.4.3 Factors affecting the adsorption of SeO_4^{2-} and SO_4^{2-} on X-Al_2O_3

Lastly, I investigated mechanisms that control the adsorption energy of selenate and sulphate on X-Al_2O_3. In my previous chapter, I found that water network controls the adsorption of selenate on unsubstituted α-Al_2O_3.[33] The similar preference in adsorption motifs of the substituted and neat Al_2O_3, albeit with slightly modified energetics, suggests that the water network remains the primary director of adsorption thermodynamics, and that the substitutions only secondarily modify the energetics; I detail more concreate analysis which confirms this observation.

Table 4.9: List of variables considered for linear regression and PCA.

Variables	descriptors	label
Change in H-O covalent bonds	Δ#OH	a
Change in length of H-O covalent bonds	ΔOH_length	b
Change in HO bonds	Δ#HO	c
Change in length of OH bonds	ΔHO_length	d
Number of H-O covalent bonds	#OH	e
Length of H-O covalent bonds	OH_length	f
Number of HO bonds	#HO	g
Length of HO bonds	HO_length	h
Ionic radii of the single atom	Cation_size(X)	i
Electron density present on the single atom	Electron_den(X)	j
Electron density present on the oxo-anion cation	Electron_density(Oxo)	k

I examined 11 different variables which could control or describe the system as outlined in Table 4.9. Broadly, they consider the effect of water network, cation size and electron density, and configurations changes upon adsorption of selenate in the most exothermic configurations. I examined the water network effects by quantifying two types of water bonds, the number of intermolecular hydrogen bonds (#HO <1.2 Å)[65] and the

number of intra-molecular H-O covalent bonds (#OH ~ 1.2-2.5 Å)[65], along with surrogates for the bond strength, namely the average bond length of hydrogen bonds (HO_length) and H-O covalent (OH_length) bonds in the water network. The water network parameters depend on the substitutions because the position and charge of the cation slightly modifies the bond lengths of water networks on the surface. Moreover, on the surface, the selenate and sulfate both interact with surface hydroxyl groups. In some instances, oxo-anion upon adsorption on the surface takes up protons from the surface hydroxyl groups and changes the protonation of oxo-anion (Figure 4.13). This behavior is accounted for in my regression model and PCA analysis, where I include the change of surface water properties (including interaction of adsorbed selenate with water) as 4 separate variables. I also investigated the effects of cationic properties on adsorption of selenate such as ionic radii (size of X calculated using method mentioned in Section 4.2.3) and electron density present on the single atom imbedded in Al_2O_3 surface (Electron density(X), which was calculated using Bader analysis).

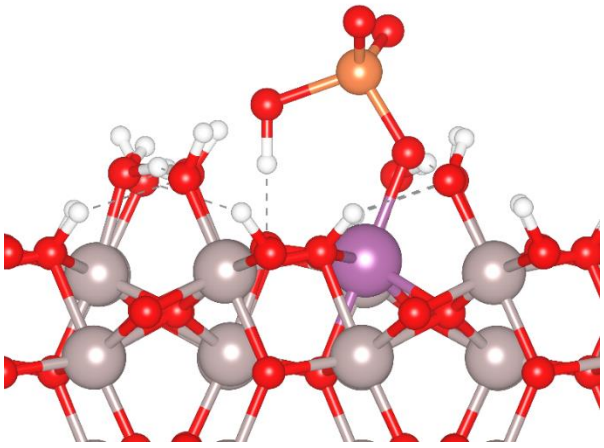

Figure 4.13: Selenate adsorption on protonated Sc-Al_2O_3 in inner-sphere (MM) configuration.

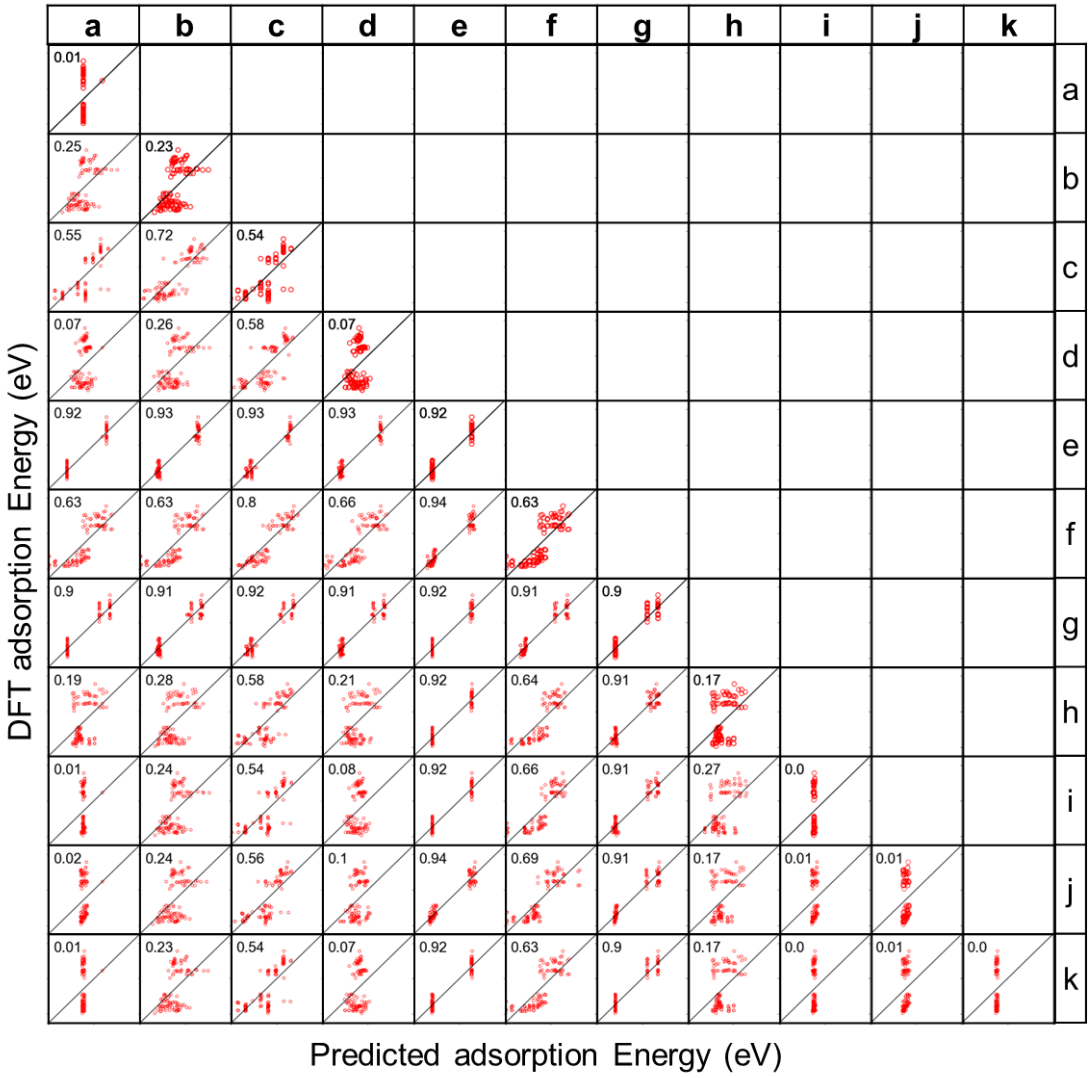

Figure 4.14: Performance of the predicted adsorption energy of SeO_4^{2-} and SO_4^{2-} adsorption on X-$Al_2O_3$from the linear regressions of one or two descriptors. A 1:1 line demonstrates the ideal prediction behavior. Diagonal elements are single variables (as outlined in Table 4.9) while off-diagonal plots show two component linear regression. The number in the corner is the r^2 value of the linear regression.

I find that the water network controls the adsorption behavior, as shown by the correlation plots in Figure 4.14 of the regression predicted energies and the DFT calculated energy. Linear regression of the adsorption energy with each of the 11 variables showed that the water network variables #OH and #HO have the highest correlation, achieving r^2 values of 0.92 and 0.90 respectively. Conversely, the cation descriptors only achieve a r^2

values of 0.00 and 0.01. I note, however, that the best performance based on r^2 shows highly clustered data points. In effect, these descriptors essentially determine the protonated and non-protonated surfaces. The water network variables which have a reasonable spread, i.e., OH_length and ΔOH, still present reasonably good correlations (0.63 and 0.54 respectively), particularly as compared to the cation descriptors. Thus, even though the cationic size affects OH_length, it is the water network variable which describes adsorption well, not the size. Only when cation size is combined with water network descriptors do reasonable correlations arise (achieving r^2 of 0.92); however, this is still not the best overall descriptor, which comes from the #OH and length (OH_length) of the water network (0.94).

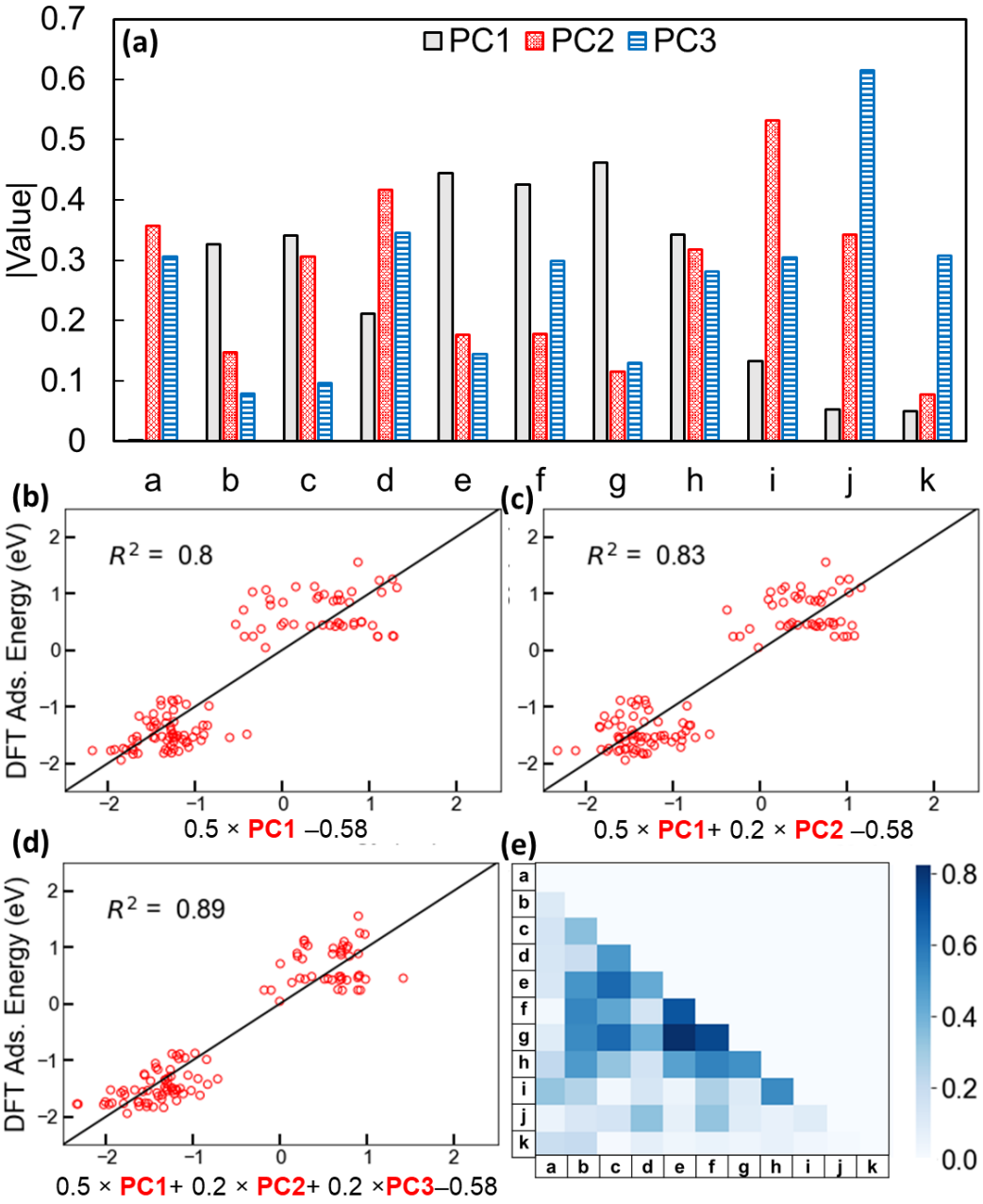

Figure 4.15: (a) Strength of each variable in 3 Principal Components. (b-d) Linear regression between Principal components and DFT calculated adsorption energy. (e) correlation plots between different variable specified in Table 4.9

To better understand the mechanistic properties that control the adsorption energies, I performed Principal Component Analysis (PCA) of the 11 variables described above to identify orthogonal variables for regression. Principal component (PC) 1 is mostly

composed of variables describing the water network and associated changes induced upon adoption (#HO (0.46), #OH (0.44) and Δ#HO (0.34)) and bond strength (OH_length (0.43) and ΔOH_length (0.33)), as shown in Figure 4.15a. I found that regressing the adsorption energy against PC1 achieved an r^2 value of 0.8. This r^2 value is lower than some of the single components because there is large spread in the data, and the data are no longer just classified by protonation of the surface. Thus, it represents a better fit. The addition of PC2, which is dominated by cation size (0.53), only improves the fit to an r^2 of 0.83. There is a modest correlation between cation size and the intra- and inter H-bond lengths (i.e.,0.5-0.1) as shown in Figure 4.15e. However, these length descriptors are more important in determining the adsorption energy as they appear prominently in PC1, which explains most of the adsorption energy. Thus, I attribute the cationic size effects to be only secondary, where the cation size modifies the water network and the modified water network controls the adsorption energy. Finally, PC 3 is mostly composed of the cation electron density descriptor (0.61) and improves the r^2 to 0.89. The minimal correlation between the charge density on the cation and bonding energy suggests that the charge interaction between the cation and selenate is small; additionally, this finding suggest my consideration of non-charged substitutions is valid for examining substitutional cationic effects. Additionally, only in PC 3 does the descriptor for SeO_4^{2-} or SeO_4^{2-} appear, and even there it contributes similarly (0.31) to other water network descriptors contributing to PC 3 (ΔHO_length, 0.35). The relegation of oxo-anion descriptor to a minor contributor suggests that finding adsorbates which rely on water networks to selectively remove selenate from water is challenging (Figure 4.16). This finding is consistent with the difficulty seen experimentally with identifying selective sorbents.

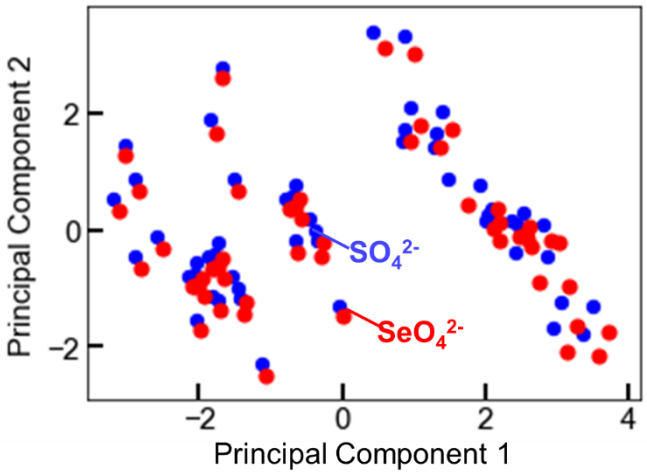

Figure 4.16: Principal Component Analysis of SeO_4^{2-} vs. SO_4^{2-} adsorption on X-Al_2O_3.

To further examine the relative importance of the water network and cation effects, I repeated the PCA including only the water or cationic descriptors, the results are shown in Figures 4.17 & 4.18. I find that the PC1-2 without the cationic descriptors fit the calculated values as well as the full set of descriptors, having r^2 values of 0.83 & 0.83 (1 & 2 PC's) and 0.8 &0.83 respectively. Conversely, the ion only descriptors were very poor in predicting the adsorption energies with r^2 values of 0.01. These results further support the conclusion that the cation affects adsorption only indirectly via modified water networks.

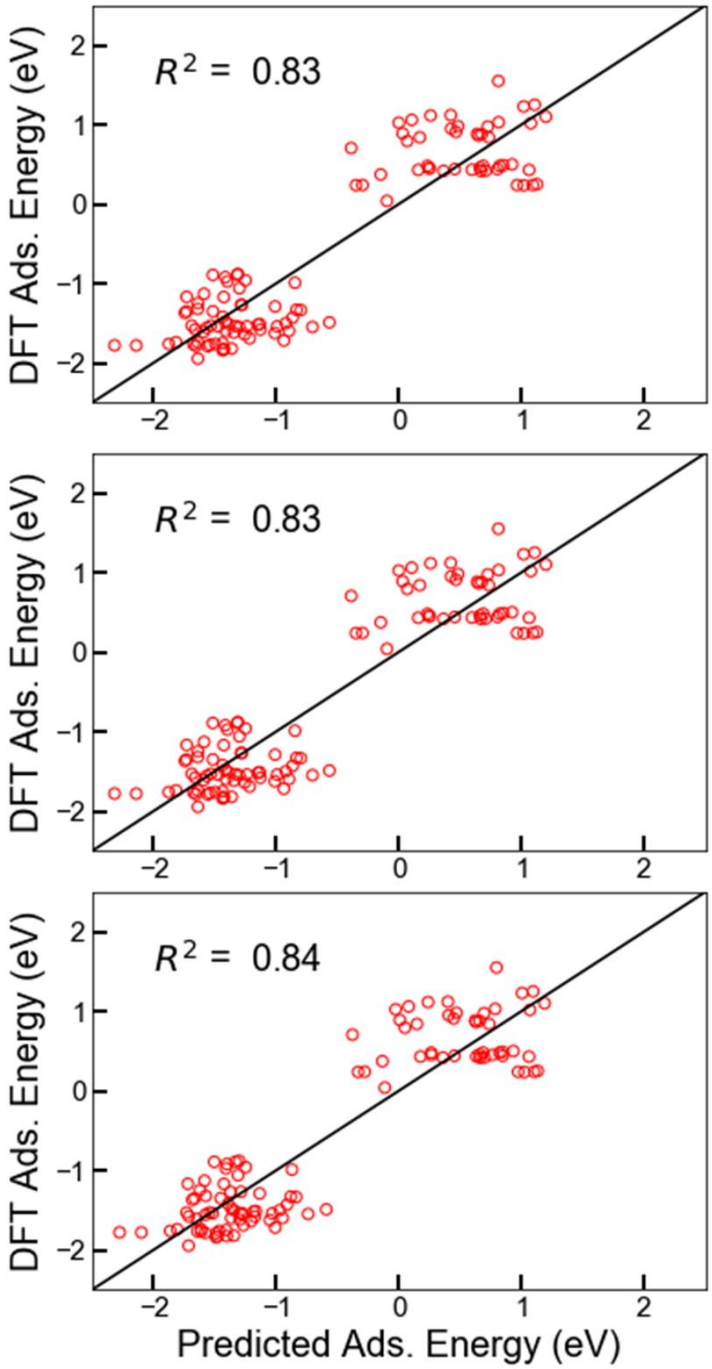

Figure 4.17: Linear regression between (a) PC1 and adsorption energy, (b) PC1 & PC2 and adsorption energy, (c) PC1, PC2, PC3 and adsorption energy with only water network variables (a-h from Table 4.9)

Predicted Ads. Energy = 0.50 PC1 + 0.07 PC2 + 0.06 PC3 -0.58

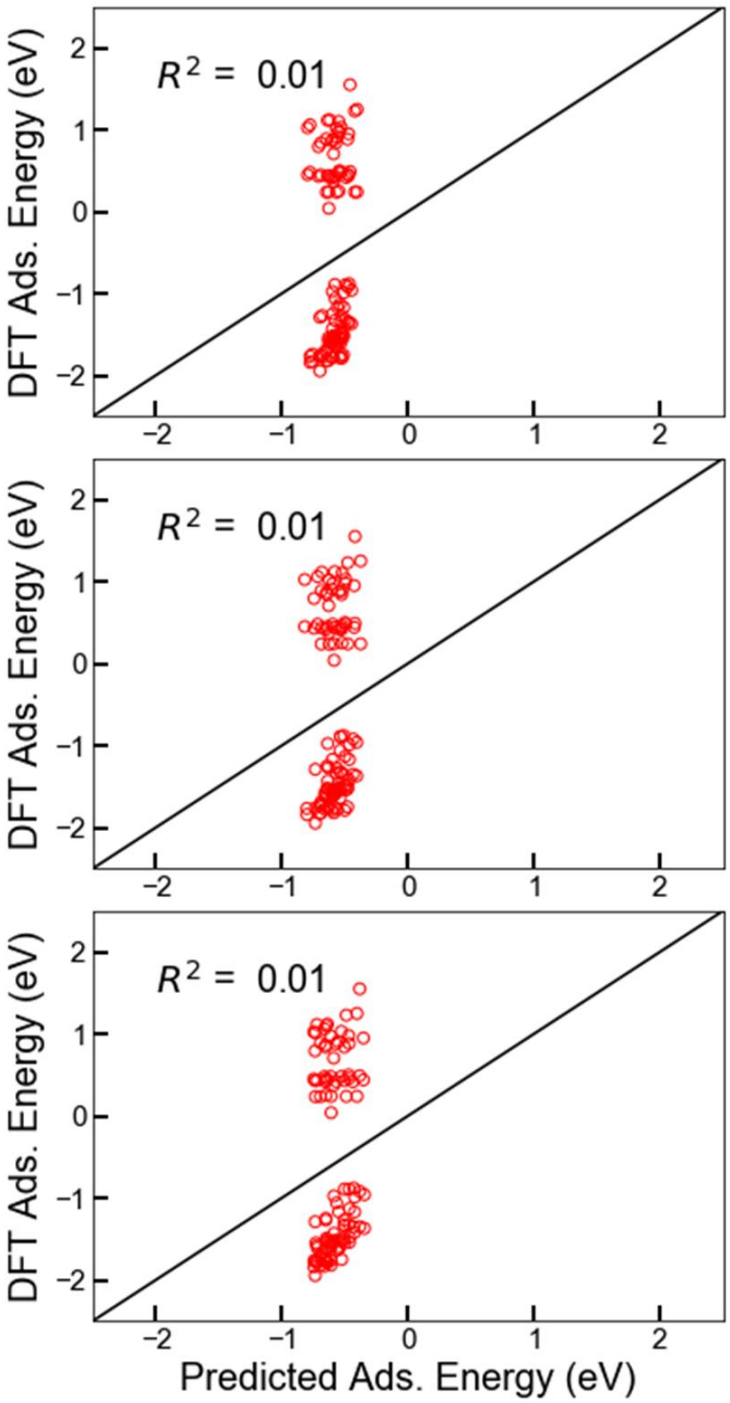

Figure 4.18: Linear regression between (a) PC1 and adsorption energy, (b) PC1 & PC2 and adsorption energy, (c) PC1, PC2, PC3 and adsorption energy with only cation effect variables (i-k from Table 4.9)

Predicted Ads. Energy = -0.08 PC1 -0.04 PC2 -0.06 PC3 -0.58

4.5 Conclusions

I investigated adsorption of selenate and sulphate on single cations embedded in the surface of (012) Al_2O_3 to delineate the effects of cation identity on adsorption without disturbing the water network on the surface. Overall, the addition of substitutional cations did not increase the adsorption of selenate or sulfate to the surface; only Sc, In and Ti increased the binding strength, albeit very slightly. I found that the water network exerts the strongest effect on adsorption energy of selenate, far greater than any correlation occurring between oxo-anion and cation. The adsorption of selenate on protonated surface is always exothermic and adsorption of selenate on neutral surface is always endothermic. I found that the size of cation embedded in protonated Al_2O_3 surface controlled the adsorption configuration of selenate through modifying the water network. Larger cations bind selenate in bidentate configuration as they break and weaken the sublayer X-O bonds. However, the bidentate adsorption comes with the added strain on oxo-anion as the bond angle decreases upon adsorption which destabilizes the adsorbate.

In terms of selectivity, I found that reducing cations, like Ti, favored selenate as its unoccupied bands are slightly lower in energy than those of sulfate, and thus are more easily occupied. Conversely, inner-sphere bidentate adsorption induces a slight preference towards sulphate as the angular strain experienced by sulfate is lower than selenate. I hypothesize that cations with ionic radii larger than In that might reverse the selectivity towards selenate. However, I cannot guarantee if the synthesis of such alloys or embedding of larger cations might be possible without changing the morphology of the adsorbent. Overall, I conclude that modifying and controlling the water network morphology on the surface provides the most promising path for developing highly active selenate sorbents.

Therefore, materials that retain extra protons on the surface around neutral pH ranges or materials where the water network is less rigid should be sought to improve adsorption technology for toxic oxo-anion removal.

4.6 References

1. Zhao, M.; Luo, T.; Zhao, Z.; Rong, H.; Zhao, G.; Lei, L., Food Chemistry of Selenium and Controversial Roles of Selenium in Affecting Blood Cholesterol Concentrations. Journal of Agricultural and Food Chemistry 2021, 69 (17), 4935-4945.
2. Fang, Y.; Catron, B.; Zhang, Y.; Zhao, L.; Caruso, J. a.; Hu, Q., Distribution and in Vitro Availability of Selenium in Selenium-Containing Storage Protein from Selenium-Enriched Rice Utilizing Optimized Extraction. Journal of Agricultural and Food Chemistry 2010, 58 (17), 9731-9738.
3. Fox, P. M.; LeDuc, D. L.; Hussein, H.; Lin, Z.-q.; Terry, N., Selenium Speciation in Soils and Plants. In Biogeochemistry of Environmentally Important Trace Elements, American Chemical Society: 2002; Vol. 835, pp 339-354.
4. Roman, M.; Jitaru, P.; Barbante, C., Selenium biochemistry and its role for human health. Metallomics 2013, 6 (1), 25-54.
5. R. Cardoso, B.; Hare, D. J.; Lind, M.; McLean, C. A.; Volitakis, I.; Laws, S. M.; Masters, C. L.; Bush, A. I.; Roberts, B. R., The APOE ε4 Allele Is Associated with Lower Selenium Levels in the Brain: Implications for Alzheimer's Disease. ACS Chemical Neuroscience 2017, 8 (7), 1459-1464.
6. Davis, T. Z.; Stegelmeier, B. L.; Hall, J. O., Analysis in Horse Hair as a Means of Evaluating Selenium Toxicoses and Long-Term Exposures. Journal of Agricultural and Food Chemistry 2014, 62 (30), 7393-7397.
7. Stillings, L. L.; Amacher, M. C., Chapter 17 Selenium attenuation in a wetland formed from mine drainage in the phosphoria formation, Southeast Idaho. In Handbook of Exploration and Environmental Geochemistry, Hein, J. R., Ed. Elsevier Science B.V.: 2004; Vol. 8, pp 467-482.
8. Stefaniak, J.; Dutta, A.; Verbinnen, B.; Shakya, M.; Rene, E. R., Selenium removal from mining and process wastewater: a systematic review of available technologies. Journal of Water Supply: Research and Technology-Aqua 2018, 67 (8), 903-918.
9. Luoma, S. N.; Presser, T. S., Emerging Opportunities in Management of Selenium Contamination. Environmental Science & Technology 2009, 43 (22), 8483-8487.
10. Olson, O. E., Selenium Toxicity in Animals with Emphasis on Man. Journal of the American College of Toxicology 1986, 5 (1), 45-70.
11. Séby, F.; Potin-Gautier, M.; Giffaut, E.; Borge, G.; Donard, O. F. X., A critical review of thermodynamic data for selenium species at 25°C. Chemical Geology 2001, 171 (3), 173-194.
12. Saunders, A. P., The Allotropic Forms of Selenium. The Journal of Physical Chemistry 1900, 4 (6), 423-513.
13. National Primary Drinking Water Regulations. https://www.epa.gov/ground-water-and-drinking-water/national-primary-drinking-water-regulations (accessed 10-27).

14. Ali, I.; Shrivastava, V., Recent advances in technologies for removal and recovery of selenium from (waste)water: A systematic review. Journal of Environmental Management 2021, 294, 112926.
15. Lenz, M.; Lens, P. N., The essential toxin: the changing perception of selenium in environmental sciences. Sci Total Environ 2009, 407 (12), 3620-33.
16. Wang, L.; Shi, C.; Wang, L.; Pan, L.; Zhang, X.; Zou, J.-J., Rational design, synthesis, adsorption principles and applications of metal oxide adsorbents: a review. Nanoscale 2020, 12 (8), 4790-4815.
17. Rudel, H. E.; Lane, M. K. M.; Muhich, C. L.; Zimmerman, J. B., Toward Informed Design of Nanomaterials: A Mechanistic Analysis of Structure–Property–Function Relationships for Faceted Nanoscale Metal Oxides. ACS Nano 2020, 14 (12), 16472-16501.
18. Pincus, L. N.; Rudel, H. E.; Petrović, P. V.; Gupta, S.; Westerhoff, P.; Muhich, C. L.; Zimmerman, J. B., Exploring the Mechanisms of Selectivity for Environmentally Significant Oxo-Anion Removal during Water Treatment: A Review of Common Competing Oxo-Anions and Tools for Quantifying Selective Adsorption. Environmental Science & Technology 2020, 54 (16), 9769-9790.
19. Ramadugu, S. K.; Mason, S. E., DFT Study of Antimony(V) Oxyanion Adsorption on α-Al2O3(1$\bar{1}$02). The Journal of Physical Chemistry C 2015, 119 (32), 18149-18159.
20. Trussell, R., A. Trussell, AND P. Kreft. SELENIUM REMOVAL FROM GROUND WATER USING ACTIVATED ALUMINA; EPA: 2002.
21. Trussell, R. R.; Trussell, A.; Kreft, P., Selenium removal from ground water using activated alumina. Municipal Environmental Research Laboratory, Office of Research and …: 1980; Vol. 1.
22. Ji, Y.; Li, L.; Wang, Y.-t., Selenium removal by activated alumina in batch and continuous-flow reactors. Water Environment Research 2020, 92 (1), 51-59.
23. Yamani, J. S.; Lounsbury, A. W.; Zimmerman, J. B., Adsorption of selenite and selenate by nanocrystalline aluminum oxide, neat and impregnated in chitosan beads. Water Research 2014, 50, 373-381.
24. Ugwuja, C. G.; Bayode, A. A.; Olorunnisola, D.; Unuabonah, E. I., Occurrence and Management of Selenium Oxyanions in Water. In Progress and Prospects in the Management of Oxyanion Polluted Aqua Systems, Oladoja, N. A.; Unuabonah, E. I., Eds. Springer International Publishing: Cham, 2021; pp 103-128.
25. Goldberg, S.; Lesch, S. M.; Suarez, D. L., Predicting selenite adsorption by soils using soil chemical parameters in the constant capacitance model. Geochimica et Cosmochimica Acta 2007, 71 (23), 5750-5762.
26. Su, T.; Guan, X.; Gu, G.; Wang, J., Adsorption characteristics of As(V), Se(IV), and V(V) onto activated alumina: Effects of pH, surface loading, and ionic strength. Journal of Colloid and Interface Science 2008, 326 (2), 347-353.
27. Wang, S.; Zeng, X.; Lin, J.; Yuan, Z.; Qu, S.; Zhang, B.; Pan, Y.; Chen, N.; Chen, W.; Jia, Y., Molecular Structure of Molybdate Adsorption on Goethite at pH 5–8: A Combined DFT + U, EXAFS, and Ab Initio XANES Study. The Journal of Physical Chemistry C 2021, 125 (40), 22052-22063.
28. Peak, D., Adsorption mechanisms of selenium oxyanions at the aluminum oxide/water interface. Journal of Colloid and Interface Science 2006, 303 (2), 337-345.

29. Hesham Mohamed Abdal-Salam Yehia, S. M. S., Drinking Water Treatment: pH Adjustment Using Natural Physical Field. Journal of Biosciences and Medicines 2021, 9 (6), 55-66.
30. He, G.; Zhang, M.; Pan, G., Influence of pH on Initial Concentration Effect of Arsenate Adsorption on TiO2 Surfaces: Thermodynamic, DFT, and EXAFS Interpretations. The Journal of Physical Chemistry C 2009, 113 (52), 21679-21686.
31. Chen, X.; Lam, K. F.; Zhang, Q.; Pan, B.; Arruebo, M.; Yeung, K. L., Synthesis of Highly Selective Magnetic Mesoporous Adsorbent. The Journal of Physical Chemistry C 2009, 113 (22), 9804-9813.
32. Wang, J.; Xie, L.; Li, S.; Wang, J.; Zhang, J.; Zeng, H., Probing the In Situ Redox Behavior of Selenium on a Pyrite Surface by Scanning Electrochemical Microscopy. The Journal of Physical Chemistry C 2021, 125 (5), 3018-3026.
33. Gupta, S.; Anh Nguyen, N.; Muhich, C. L., Surface water H-bonding network is key controller of selenate adsorption on [012] α-alumina: An Ab-initio study. Journal of Colloid and Interface Science 2022, 617, 136-146.
34. Le, H.-L. T.; Lazzari, R.; Goniakowski, J.; Cavallotti, R.; Chenot, S.; Noguera, C.; Jupille, J.; Koltsov, A.; Mataigne, J.-M., Tuning Adhesion at Metal/Oxide Interfaces by Surface Hydroxylation. The Journal of Physical Chemistry C 2017, 121 (21), 11464-11471.
35. Grassian, V. H., When Size Really Matters: Size-Dependent Properties and Surface Chemistry of Metal and Metal Oxide Nanoparticles in Gas and Liquid Phase Environments. The Journal of Physical Chemistry C 2008, 112 (47), 18303-18313.
36. Kunkel, C.; Viñes, F.; Illas, F., Surface Activity of Early Transition-Metal Oxycarbides: CO2 Adsorption Case Study. The Journal of Physical Chemistry C 2019, 123 (6), 3664-3671.
37. Peng, C.; Chen, J.; Hu, P.; Wang, H., Molecular Adsorption Kinetics: Nonlinear Entropy–Enthalpy Loss Quantified by Constrained AIMD and Insights into the Adsorption-Site Determination on Metal Oxides. The Journal of Physical Chemistry C 2021, 125 (20), 10974-10982.
38. Johnston, C. P.; Chrysochoou, M., Mechanisms of Chromate, Selenate, and Sulfate Adsorption on Al-Substituted Ferrihydrite: Implications for Ferrihydrite Surface Structure and Reactivity. Environmental Science & Technology 2016, 50 (7), 3589-3596.
39. Xu, H.; Zhang, R. Q.; Ng, A. M. C.; Djurišić, A. B.; Chan, H. T.; Chan, W. K.; Tong, S. Y., Splitting Water on Metal Oxide Surfaces. The Journal of Physical Chemistry C 2011, 115 (40), 19710-19715.
40. Li, C.; Ku, N.; Liu, Y.; Pan, J.; Chai, B.; Hu, F.; Kornecki, M.; Yan, Q.; Brennan, R.; Ren, S., Magnetically active transition metal cation-substituted alumina. Nanotechnology 2020, 31 (10), 105703.
41. Kresse, G.; Furthmüller, J., Efficient iterative schemes for ab initio total-energy calculations using a plane-wave basis set. Physical Review B 1996, 54 (16), 11169.
42. Kresse, G.; Furthmüller, J., Efficiency of ab-initio total energy calculations for metals and semiconductors using a plane-wave basis set. Computational Materials Science 1996, 6 (1), 15-50.
43. Perdew, J. P.; Burke, K.; Ernzerhof, M., Generalized gradient approximation made simple. Phys Rev Lett 1996, 77 (18), 3865-3868.

44. Mathew, K.; Sundararaman, R.; Letchworth-Weaver, K.; Arias, T. A.; Hennig, R. G., Implicit solvation model for density-functional study of nanocrystal surfaces and reaction pathways. J Chem Phys 2014, 140 (8), 084106.
45. Grimme, S.; Antony, J.; Ehrlich, S.; Krieg, H., A consistent and accurate ab initio parametrization of density functional dispersion correction (DFT-D) for the 94 elements H-Pu. J Chem Phys 2010, 132 (15), 154104.
46. Catalano, J. G.; Park, C.; Zhang, Z.; Fenter, P., Termination and Water Adsorption at the α-Al2O3 (012)−Aqueous Solution Interface. Langmuir 2006, 22 (10), 4668-4673.
47. Sun, W.; Ceder, G., Efficient creation and convergence of surface slabs. Surface Science 2013, 617, 53-59.
48. Ong, S. P.; Cholia, S.; Jain, A.; Brafman, M.; Gunter, D.; Ceder, G.; Persson, K. A., The Materials Application Programming Interface (API): A simple, flexible and efficient API for materials data based on REpresentational State Transfer (REST) principles. Computational Materials Science 2015, 97, 209-215.
49. Kitayama, M.; Glaeser, A. M., The Wulff Shape of Alumina: III, Undoped Alumina. Journal of the American Ceramic Society 2002, 85 (3), 611-622.
50. Sun, W.; Ceder, G., A topological screening heuristic for low-energy, high-index surfaces. Surface Science 2018, 669, 50-56.
51. Peri, J. B., A Model for the Surface of γ-Alumina1. The Journal of Physical Chemistry 1965, 69 (1), 220-230.
52. Bachrach, S. M., Microsolvation of Glycine: A DFT Study. The Journal of Physical Chemistry A 2008, 112 (16), 3722-3730.
53. Bondi, A., van der Waals Volumes and Radii. The Journal of Physical Chemistry 1964, 68 (3), 441-451.
54. Wang, R.; DelloStritto, M.; Remsing, R. C.; Carnevale, V.; Klein, M. L.; Borguet, E., Sodium Halide Adsorption and Water Structure at the α-Alumina(0001)/Water Interface. The Journal of Physical Chemistry C 2019, 123 (25), 15618-15628.
55. Lagauche, M.; Larmier, K.; Jolimaitre, E.; Barthelet, K.; Chizallet, C.; Favergeon, L.; Pijolat, M., Thermodynamic Characterization of the Hydroxyl Group on the γ-Alumina Surface by the Energy Distribution Function. The Journal of Physical Chemistry C 2017, 121 (31), 16770-16782.
56. Ullah, H.; Lun, L.; Rashid, A.; Zada, N.; Chen, B.; Shahab, A.; Li, P.; Ali, M. U.; Lin, S.; Wong, M. H., A critical analysis of sources, pollution, and remediation of selenium, an emerging contaminant. Environmental Geochemistry and Health 2022.
57. Casas, J. M.; Alvarez, F.; Cifuentes, L., Aqueous speciation of sulfuric acid–cupric sulfate solutions. Chemical Engineering Science 2000, 55 (24), 6223-6234.
58. Wang, B.; Li, C.; Xiangyu, J.; Zhu, T.; Zhang, J. Z. H., An Approach to Computing Solvent Reorganization Energy. Journal of Chemical Theory and Computation 2020, 16 (10), 6513-6519.
59. Wang, V.; Xu, N.; Liu, J.-C.; Tang, G.; Geng, W.-T., VASPKIT: A user-friendly interface facilitating high-throughput computing and analysis using VASP code. Computer Physics Communications 2021, 267, 108033.
60. Nelson, R.; Ertural, C.; George, J.; Deringer, V. L.; Hautier, G.; Dronskowski, R., LOBSTER: Local orbital projections, atomic charges, and chemical-bonding analysis

from projector-augmented-wave-based density-functional theory. Journal of Computational Chemistry 2020, 41 (21), 1931-1940.
61. Pinchon, D.; Hoggan, P. E., Rotation matrices for real spherical harmonics: general rotations of atomic orbitals in space-fixed axes. Journal of Physics A: Mathematical and Theoretical 2007, 40 (7), 1597-1610.
62. Momma, K.; Izumi, F., VESTA 3 for three-dimensional visualization of crystal, volumetric and morphology data. Journal of applied crystallography 2011, 44 (6), 1272-1276.
63. Shannon, R., Revised effective ionic radii and systematic studies of interatomic distances in halides and chalcogenides. Acta Crystallographica Section A 1976, 32 (5), 751-767.
64. Azizian, S.; Bashiri, H.; Iloukhani, H., Statistical Rate Theory Approach to Kinetics of Competitive Adsorption at the Solid/Solution Interface. The Journal of Physical Chemistry C 2008, 112 (27), 10251-10255.
65. Legon, A. C.; Millen, D. J., Angular geometries and other properties of hydrogen-bonded dimers: a simple electrostatic interpretation of the success of the electron-pair model. Chemical Society Reviews 1987, 16 (0), 467-498.

CHAPTER 5

FACET DEPENDENT ADSORPTION OF SELENATE, SELENITE AND ARSENATE ON HEMATITE SURFACES

5.1 Introduction

Arsenic and Selenium are naturally occurring elements found in sulfide minerals, sedimentary rocks, volcanic rocks and alkaline soils.[1,2] Dissolution of rocks in water or anthropogenic activities such as mining, industrial manufacturing, and agricultural practices have caused As and Se accumulation in water across United states, South America and South-East Asia.[3-6] Consumption of water with As concentration above 10 µg/L can cause skin lesions, skin cancer, bladder cancer, lung cancer, and other health effects.[7] Low levels of arsenic in drinking water is linked to cardiovascular disease, diabetes, and developmental effects in children.[8] Water rich in selenium (above 50 µg/L) causes hair and nail brittleness, skin rashes, and damage to the nervous system when consumed regularly.[9,10] In extreme cases, it can cause cirrhosis of the liver or pulmonary edema.[11] Therefore, the removal of high As and Se concentrations from drinking water is crucial.

As and Se dissolve in water in form of their oxo-anions (Arsenate or As(V), Selenate or Se(VI), and Selenite or Se(IV)).[11,12] Arsenide or As(III), another oxo-anion of As, oxidizes to As(V) under aerobic conditions.[13,14] Several remediation technologies like coagulation and filtration,[15,15] adsorption,[17,18] ion exchange,[19,20] and reverse osmosis[21] are commonly deployed to remove As and Se oxo-anions from water. Coagulation and filtration, ion exchange and reverse osmosis require large operation set-up, filter media, regeneration of resin and/or generate significant wastewater, and hence are not easily

accessible for under-the-sink, low-income, or low-water availability communities and well-based water systems.[22,23] Conversely, adsorption can be operated as an under-the-sink technology, which does not require high cost or extensive technical expertise to operate and does not produce wastewater streams.[24,25] Hence it is easily implemented in low-income and rural communities.[26]

Activated alumina, iron oxide-based materials like ferric hydroxide, hematite and goethite, activated carbon, zeolites, clay minerals and hybrid materials like polycyclic aromatic hydrocarbons (PAHs) modified with metal-oxide nanoparticles (or chitosan beads) are candidate adsorbent materials for adsorptive removal of Se and As oxo-anions.[17-19,21,27-29] Of these materials, metal-oxides like hematite and alumina are naturally abundant and currently approved adsorbents.[25] Moreover, hematite is stable and resistant to chemical degradation under wide range of pH conditions like high temperatures, acidic environments and ionic strengths, suitable for both batch and column adsorption methods.[23,30] Therefore hematite is an attractive sorbent for Se and As removal.

The hematite removal efficacy for As and Se oxo-anions depends upon water pH, oxo-anion concentration, the presence of competing non-toxic compounds such as sulphate and phosphate, and the physical structure of the hematite, i.e., size and surface facet.[18,31-36] Adsorption is more favorable under acidic conditions than neutral or alkaline ones.[37] I explained this phenomena in my previous chapters, where I found that change in water network on the metal-oxide surface by adsorption of excess protons in acidic conditions increase the hydrogen bonding upon oxo-anion adsorption, which increases the adsorption capacity.[32] The presence of competing species like phosphate and sulphate, which often occur in higher concentration in water and have chemically similar structures to oxo-

anions of As and Se, decreases the adsorption capacity because of non-competitive adsorption seen on the metal-oxide surface.[18]

Morphology effects direct adsorption through several mechanisms. Increasing the surface area by changing of adsorbent size directly increases the surface density of sites per mass, thus increase adsorption capacity. Tang et. al. (2011), demonstrated that synthesizing ultrafine iron oxide (α-Fe_2O_3) nanoparticles which has high specific surface area of ~162 m^2/g, removed 4.75 mg As(V)/ g α-Fe_2O_3.[38] The adsorption capacity is at least a 50% improvement over hematite powders commercially available at the time (specific surface area ~ 11.2 m^2/g).[38] However, after surface area effects have diminishing returns. In 2016, Lounsbury et. al. investigated the increase in adsorption capacity of Se oxo-anion on hematite nanoparticles at nanoscale by synthesizing nanoparticles with similar size and difference surface areas.[39] They found that specific surface area was not the key determinant factor at nanoscale but rather the number of reactive sites on the surface.[39] In 2019, Lounsbury et. al. found that for nano-hematite out of different factors such as size, shape and surface area, the crystal surface structure or facet of nanoparticle has strongest control over the adsorption extents for selenate and selenite adsorption.[40] Moreover, [012] facet promoted selenate adsorption more strongly over selenite adsorption.[40]

While these experimental studies provide insightful information on the adsorption capacity and efficiency of an adsorbent, they do not provide a complete understanding of the underlying mechanism of adsorption. Ab initio methods, like density functional theory (DFT) can provide useful information in understanding the adsorption mechanism of adsorbents and how it interacts with the adsorbate, including the nature of chemical

bonding, the geometry of the adsorption complex, and the energetics of the adsorption process.[29,33-35] For example, I found that the water network on the [012] Al_2O_3 surface has stronger control over the adsorption of selenate adsorption than the interaction between selenate with the Al_2O_3 surface without water layer in my previous chapter. Hence, selenate preferentially adsorbs in outer-sphere configuration through hydrogen bonds on the Al_2O_3 surface as compared to inner-sphere adsorption.[32] Moreover, DFT calculations can also help in predicting the adsorption capacity of an adsorbent and identifying the most favorable site properties for adsorption.[41] In chapter 4, I found that water network has stronger effect on adsorption that surface cationic species by calculating the adsorption energies of selenate on single atom cationic defect sites in Al_2O_3 (012) surface.

While I have investigated the effect of adsorbent cation and pH, it remains unknow if and how the water network on different facets controls the adsorption energies. Upon investigating the water network change on pH dependent Al_2O_3 surface for different protonation states, the data was still clustered into 2 groups – adsorption on protonated and neutral surface.[32] Moreover, the role of oxo-anion types on adsorption energy is still not completely understood. Therefore, in this study I calculate the adsorption energies of Se(VI) oxo-anion on [012] and [001] Fe_2O_3 surface to understand the role of different water network on adsorption energies. Similarly, I investigate the effect of properties of oxo-anion on the adsorption by calculating the adsorption energies of Se(IV), Se(VI) and As(IV) on [012] Fe_2O_3 surface.

5.2 Methods

5.2.1 Density Functional theory calculation parameters

I conducted periodic boundary condition DFT calculations using the Vienna Ab Initio Simulation Package (VASP) to calculate the adsorption energies of oxo-anion adsorption on hematite facets.[42,43] I employed the Perdew-Burke-Ernzerhof functional with a Hubbard correction (PBE+U).[44,45] The Hubbard onsite correction term U_{eff} was included on the Fe-d orbitals because the GGA functional does not adequately describe the strong electron correlation between Fe-d electrons.[46,47] A single point self-consistent field (SCF) study was conducted at different U values to calculate adsorption energies; the adsorption energies where compared with a reference adsorption energy calculated using HSE06 functional.[48] Based on these calculations, a U_{eff} of 5.15 eV best reproduced the HSE06 results. All calculations were conducted with spin polarization, several magnetic configurations were examined; the lowest energy spin configuration consisted of alternating double layers of spin-up and spin-down electrons perpendicular to c-axis, and thus this spin structure is used in the rest of this work. This finding is consistent with previous work.[49] I used projector augmented wave (PAW) pseudopotentials to eliminate the computational costs associated with calculating nonparticipating core electrons.[50,51] PAWs described the hydrogen 1s, oxygen 2s and 2p and iron, arsenic, and selenium 4s and 3d electrons explicitly. All calculations utilized a 350-eV plane-wave cutoff energy. I conducted calculations using a Γ-point centered 1 × 1 × 1 Monkhorst–Pack k-point mesh. Implicit solvent effects and non-local van der Waals (vdW) effects are accounted for by the polarizable continuum model (VASPsol module)[52] and DFT-D3 correction based on the method of Grimme et. al.[53] Atomic geometries were relaxed until total energies between

two ionic steps were less than 0.001 eV. Density of States (DOS) were calculated using vaspkit,[54] charge density differences using Bader analysis,[55] Crystal Orbital Overlap Populations (COOP) using lobster[56] and crystal structure representations were obtained using VESTA[57].

5.2.2 Water network on 2 terminations of [012] and [001] hematite facets

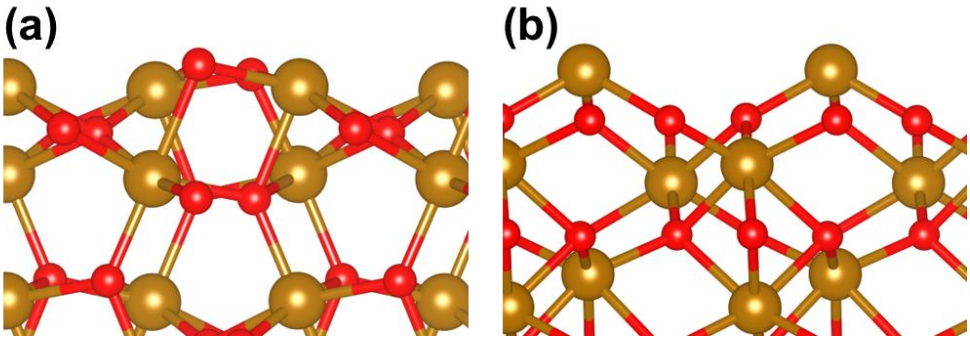

Figure 5.1: Hematite (a) [012] and (b) [001] facets. The brown, red spheres represent Fe, and O respectively.

The hematite [012] and [001] facets are shown in Figure 1. The slabs are composed of 24 and 32 structural units and have at least 8 layers of Fe2O3 with 8 and 4 surface Fe atoms exposed on [012] and [001] surface, respectively. The surface parameters are 10.81 × 10.81 Å, γ = 120° for the [001] and 10.02 × 10.97 Å, γ = 90.23° for [012]. The slabs are separated by at least 20 Å of vacuum space filled with implicit solvent. The entire slab was fully relaxed before freezing the cell shape and bottom four Fe^{+3} layers and their associated oxygen atoms for the adsorption energy calculations to reduce the computational cost and preserve the bulk crystalline structure of the Fe_2O_3 nanoparticle.

To simulate the solvated surface, I used a hybrid explicit/implicit solvation model (HSM). In the HSM, which I developed in the past study,[32] one layer of explicit water or hydroxyl groups are bound to the surface while the remain water is included via implicit water. Specifically, I added an explicit monolayer of dissociated water to the top surface

of Fe_2O_3 with one OH molecule per Fe-O bond broken due to surface formation to replicate the interfacial water layer under neutral conditions. I further constructed the interfacial water structure by sequentially adding protons and relaxing the surface, until a neutral surface was achieved (as shown in Figure 5.2).

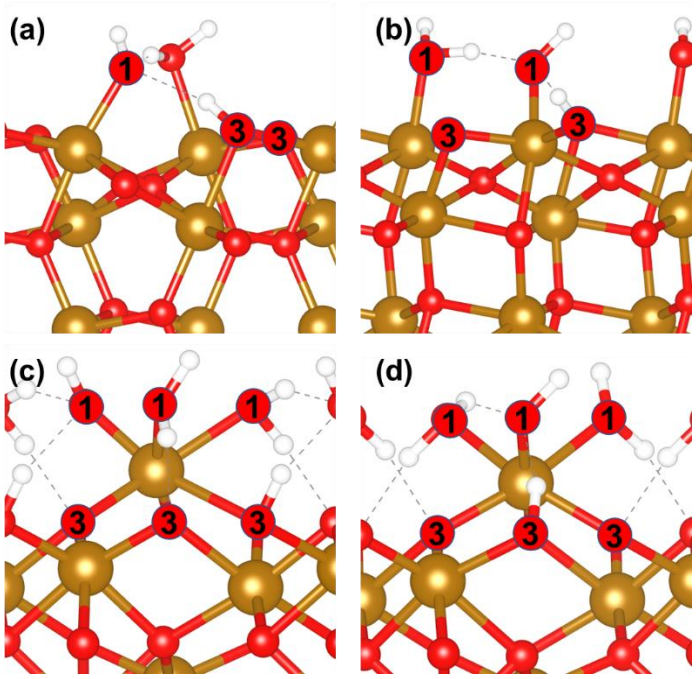

Figure 5.2: Water network on neutral hematite (a)-(b) [012], (c)-(d) [001] viewed perpendicular to x-direction (a,c) and y-direction (b,d). The number on top of surface O (1 or 3) represents number of Fe bonded to the respective O. The brown, red, and white spheres represent Fe, O, and H atoms respectively.

5.2.2.1 Constructing point of zero hematite surfaces using DFT calculations

I started with a hydroxyl bond capping every broken Fe-O bond of the surface of the hematite and then relaxing the surface (Figure 5.3(b)). Subsequently, a proton was added at surface hydroxyl groups and oxygen atoms (I-VI, Figure 5.3(b)), to find minimum energy (most stable) water network (Figure 5.3(c-e)). This step was repeated until there was an equal number of OH^- and H^+ on the surface. These structures, therefore, describe the hematite surface at the point of zero charge. The resulting surface water structure of [012] Fe_2O_3 surface found here is consistent with pervious literature,[58,59] thus suggesting

that the sequential H^+ addition and relaxation method produces realistic surface water structures.

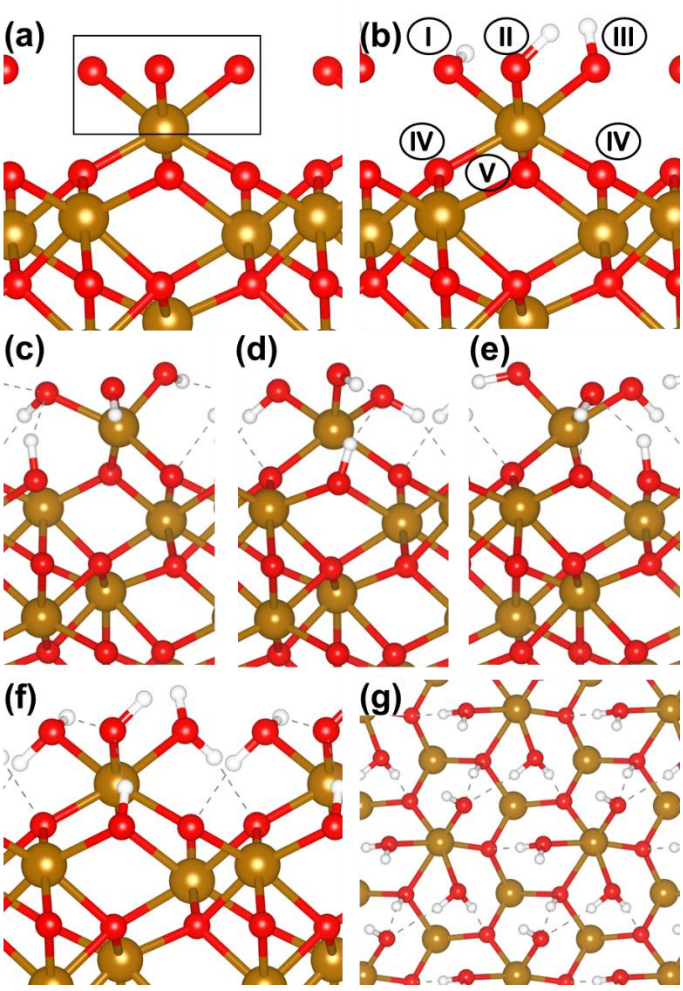

Figure 5.3: Methodology to build water network on top of hematite surface. (a) Hematite [001]- 1 facets with 3 broken Fe-O bonds (b) Hematite [001]- 1 facets with 3 hydroxyl group replacing Fe-O broken bonds. (I)-(VI) indicates potential sites to add H^+. (c)-(e) relaxed configurations with H^+ bond on sites (IV), (V) and (VI) respectively. (d) is the most stable configuration. This step is repeated 3 times to add 3 H^+ to neutralize the surface. (f) Side-view and (g) Top-view of hematite [001] facet with a single water layer at Point of Zero charge (neutral surface). The brown, red and white spheres represent Fe, O and H respectively.

5.2.3 Adsorption energy calculations

I calculate the adsorption energy of three oxo-anions, with four total protonation extents on the neutral hematite surfaces. The following oxo-anions are examined, deprotonated Se(VI) (SeO_4^{2-}), semi-protonated Se(IV) ($HSeO_3^-$) and two semi-protonated

As(V) ($H_2AsO_4^-$ and $HAsO_4^{2-}$) species. The protonation extents of Se(VI), Se(IV) and As(V) were selected based on the dominant species present in the pH range associated with drinking water, 6.5 to 8.[60-62] Adsorption of oxo-anions on hematite is calculated in inner- and outer-sphere configurations. The adsorption of oxo-anions in the inner-sphere configuration involves replacing surface OH^-/H_2O groups with oxo-anions. In the inner-sphere monodentate configuration (MM) one Fe—OH^-/H_2O group is replaced by a single Fe—OX (X: Se/As) bond. In the inner-sphere bidentate configuration (BM) two Fe—OH^-/H_2O groups are replaced by two Fe—OX bonds. In the outer-sphere configuration, the oxo-anion adsorbs to the surface by forming hydrogen bonds with surface water layer without displacing any Fe—OH^-/H_2O groups. The geometries of SeO_4^{2-} absorbed in inner-sphere monodentate, inner-sphere bidentate and outer-sphere configuration on the [001] and [012] hematite facets are shown in Figure 5.4. The number of possible inner-sphere and outer-sphere configurations depends upon the surface facet; all possible adsorption configurations are detailed in Table 5.1 and 5.2 for [001] and [012] surfaces, respectively.

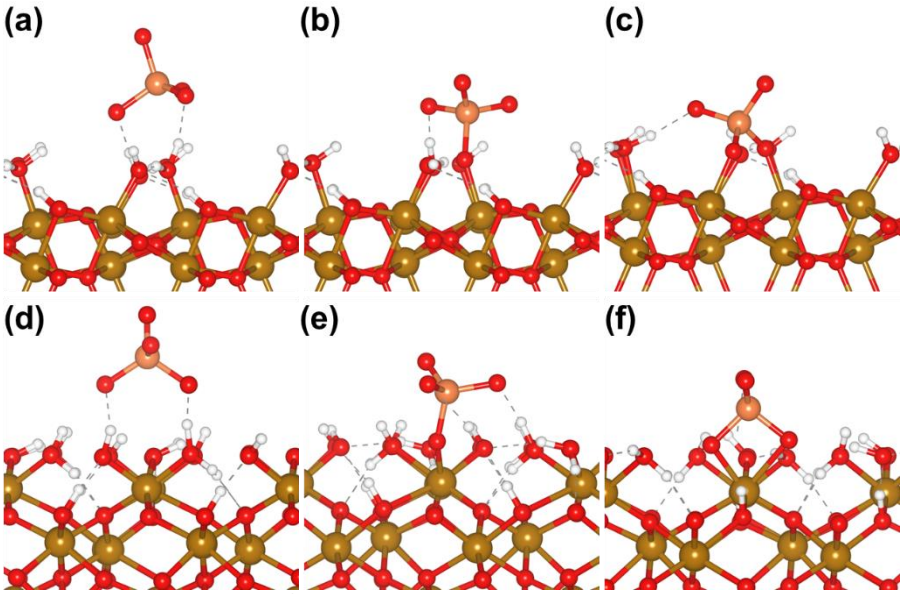

Figure 5.4: Adsorption of SeO_4^{2-} in (a) outer-sphere (OS), (b) inner-sphere monodentate (MM) and (c) inner-sphere bidentate (BM) configuration on [012] hematite facet. Adsorption of SeO_4^{2-} in (a) outer-sphere (OS), (b) inner-sphere monodentate (MM) and (c) inner-sphere bidentate (BM) configuration on [001] hematite facet. The brown, red, orange, and white spheres represent Fe, O, Se and H atoms respectively.

To appropriately account for solvation and prevent errors in energy calculations arising from the use of multiple charged super-cells, I calculate all adsorption energies based on super cells containing all adsorbed and desorbed species, as outlined in previous chapter.[32] Specifically, I calculate an adsorption energy by subtracting the energy of desorbed supercell (desorbed_cell), which contains the oxo-anion in the implicit solvent space above the slab, from adsorbed supercell (adsorbed_cell), where the oxo-anion is on the surface and all displaced water molecules reside in the implicit aqueous phase. The energies are calculated as outlined in equation 5.1. In these calculations, all species in the solution phase are separated by at least 4 Å. In the following equations, the (.) between terms indicates adsorbed species and (+) indicates species that are separated by implicitly solvated "vacuum" space.

$$\Delta E = E_{adsorbed\_cell} - E_{desorbed\_cell} \qquad eq.5.1$$

Here $E_{adsorbed\_cell}$ is the energy of simulated cell containing adsorbed selenate.

$$E_{adsorbed\_cell} = E_{Fe_2O_3\ .\ surface\ water.\ oxo-anion\ +counter\ ion+displace\ water} \quad eq.5.2$$

And $E_{dedsorbed\_cell}$ is the energy of simulated cell containing desorbed selenate.

$$E_{desorbed\_cell} = E_{Fe_2O_3\ .\ surface\ water\ +\ counter\ ion\ +oxo-anion} \quad eq.5.3$$

The number of adsorbed or desorbed waters, H_3O^+, and oxo-anions used in eq 5.2 and 5.3 change upon the adsorption configuration, facet, and oxo-anion and values are listed in Table 5.1 & 5.2.

Table 5.1: Species present in [001] hematite facet periodic cell and implicitly solvated "vacuum" space in adsorbed_cell and desorbed_cell in different configurations for SeO_4^{2-} .

Configuration		**Periodic slab**	**desorbed OH^-/H_2O/H_3O^+**		
SeO_4^{2-}					
Desorbed_cell		$Fe_{48}O_{72}.8H_2O.4\ H^+.4\ OH^-$	SeO_4^{2-}	$2H_3O^+$	
Adsorbed _cell	MM1	$Fe_{48}O_{72}.8H_2O.4H^+.3OH^-$ $.SeO_4^{2-}$	OH^-	$2H_3O^+$	
	MM2-MM3	$Fe_{48}O_{72}.7H_2O.4H^+.4OH^-$ $.SeO_4^{2-}$	H_2O	$2H_3O^+$	
	BM1	$Fe_{48}O_{72}.7H_2O.4H^+.3OH^-$ $.SeO_4^{2-}$	H_2O	$2H_3O^+$	OH^-
	BM2-BM3	$Fe_{48}O_{72}.6H_2O.4H^+.4OH^-$ $.SeO_4^{2-}$	$2H_2O$	$2H_3O^+$	
	OS1-OS3	$Fe_{48}O_{72}.8H_2O.4H^+.4OH^-$ $.SeO_4^{2-}$		$2H_3O^+$	

Table 5.2: Species present in [012] hematite facet periodic cell and implicitly solvated "vacuum" space in adsorbed_cell and desorbed_cell in different configurations for SeO_4^{2-}, $HSeO_3^-$, $HAsO_4^{2-}$ and $H_2AsO_4^-$.

Configuration		**Periodic slab**	**desorbed OH^-/H_2O/H_3O^+**		
SeO_4^{2-}					
Desorbed_cell		$Fe_{64}O_{96}.4H_2O.4H^+.4OH^-$	SeO_4^{2-}	$2H_3O^+$	
Adsorbed _cell	MM1	$Fe_{64}O_{96}.4H_2O.4H^+.3OH^-.SeO_4^{2-}$	OH^-	$2H_3O^+$	
	MM2	$Fe_{64}O_{96}.3H_2O.4H^+.4OH^-.SeO_4^{2-}$	H_2O	$2H_3O^+$	
	BM1-BM2	$Fe_{64}O_{96}.3H_2O.4H^+.3OH^-.SeO_4^{2-}$	H_2O	$2H_3O^+$	OH^-
	OS1-OS6	$Fe_{64}O_{96}.4H_2O.4H^+.4OH^-.SeO_4^{2-}$		$2H_3O^+$	
$HSeO_3^-$					
Desorbed_cell		$Fe_{64}O_{96}.4H_2O.4H^+.4OH^-$	$HSeO_3^-$	H_3O^+	H_2O
Adsorbed _cell	MM1	$Fe_{64}O_{96}.4H_2O.4H^+.3OH^-.HSeO_3^-$	OH^-	H_3O^+	H_2O
	MM2	$Fe_{64}O_{96}.3H_2O.4H^+.4OH^-.HSeO_3^-$		H_3O^+	$2H_2O$
	BM1-BM2	$Fe_{64}O_{96}.3H_2O.4H^+.3OH^-.HSeO_3^-$	$2H_2O$	OH^-	H_3O^+
	OS1-OS6	$Fe_{64}O_{96}.4H_2O.4H^+.4OH^-.HSeO_3^-$		H_3O^+	H_2O
$H_2AsO_4^-$					
Desorbed_cell		$Fe_{64}O_{96}.4H_2O.4\ H^+.4OH^-$	$H_2AsO_4^-$	H_3O^+	H_2O
Adsorbed _cell	MM1	$Fe_{64}O_{96}.4H_2O.4H^+.3OH^-.H_2AsO_4^-$	OH^-	H_3O^+	H_2O
	MM2	$Fe_{64}O_{96}.3H_2O.4H^+.4OH^-.H_2AsO_4^-$		H_3O^+	$2H_2O$
	BM1-BM2	$Fe_{64}O_{96}.3H_2O.4H^+.3OH^-.H_2AsO_4^-$	$2H_2O$	OH^-	H_3O^+
	OS1-OS6	$Fe_{64}O_{96}.4H_2O.4H^+.4OH^-.H_2AsO_4^-$		H_3O^+	H_2O
$HAsO_4^{2-}$					
Desorbed_cell		$Fe_{64}O_{96}.4H_2O.4\ H^+.4\ OH^-$	$HAsO_4^{2-}$	$2H_3O^+$	
Adsorbed _cell	MM1	$Fe_{64}O_{96}.4H_2O.4H^+.3OH^-.HAsO_4^{2-}$	OH^-	$2H_3O^+$	
	MM2	$Fe_{64}O_{96}.3H_2O.4H^+.4OH^-.HAsO_4^{2-}$	H_2O	$2H_3O^+$	
	BM1-BM2	$Fe_{64}O_{96}.3H_2O.4H^+.3OH^-.HAsO_4^{2-}$	H_2O	$2H_3O^+$	OH^-

	OS1-OS6	$Fe_{64}O_{96}.4H_2O.4H^+.4OH^-$ $.HAsO_4^{2-}$		$2H_3O^+$	

5.3 Results

I first analyzed the water network on two hematite surfaces under neutral conditions. Subsequently, I describe the adsorption of SeO_4^{2-} on the [012] and [001] hematite surfaces, elucidating the water network effect on adsorption energy. Lastly, I discuss the adsorption of SeO_4^{2-}, $HSeO_3^-$, $HAsO_4^{2-}$ and $H_2AsO_4^-$ on [012] hematite surface in MM, BM and OS configurations to investigate the effect of oxo-anion identity on the adsorption energies.

5.3.1 Water network on different termination of [001] and [012] hematite facets

Table 5.3: Water network parameters on hematite surface

	Fe_3OH	FeOH	$FeOH_2$	#O-H/Å^2	O-H length (Å)	#H—O/Å^2	H—O length (Å)
012	1	1	1	0.09	1.00	0.07	1.65
001	1	1	2	0.12	0.99	0.14	1.81

The water network on neutral hematite surfaces is shown in Figure 5.2. The hematite [001] surface has three broken Fe-O bonds per surface Fe atom, while the [012] surface has 2 broken bonds per surface Fe atom. The water density of the surface monolayer is greater on the [001] surface, one water per 8.4 Å^2, than on the [012] surface, one H_2O per 13.7 Å^2. The water molecules on both terminations partially dissociate. On the [012] surface, half of the water molecules are dissociated (OH^-/H^+), whereas on the [001] surface only one third of water molecules are in the dissociated form. The H^+ of the dissociated water molecules adsorbs on surface or surface-embedded triply coordinated O atoms (i.e., Fe_3O); these O^{2-} anions are labeled O3 in Figure 5.2 Therefore, the surfaces have different ratios of Fe_3OH and FeOH (or $FeOH_2$), and different surface water networks. The surface

water network comprises strong intramolecular covalent bonds within individual water molecules (O-H), characterized by bond lengths of less than 1.2 Å. There are also weaker intermolecular hydrogen bonds (H—O) with bond lengths ranging between 1.2 and 2.5 Å. The water network can be parameterized further into 4 components: (1) the number of covalent bonds (O-H) bonds present on the surface, (2) the average bond-length of covalent (O-H) bonds on the surface, (3) the number of weaker hydrogen bonds (H—O) present and (4) the average bond-length of hydrogen bond present on the surface. The water network parameters for hematite surfaces are presented in Table 5.3.

The [001] hematite facet has a much denser H-bonding water network than the [012] facet; the increased density arises from the additional H_2O molecule which binds per surface Fe atom on the 001 surface. As shown in Table 5.3, the number of O-H covalent bonds on the [012] surface is approximately 23% less than on the [001] surface (0.09 bonds per Å^2 and 0.12 bonds per Å^2, respectively). The decrease in the density of intermolecular bonds is even larger, where the [001] surface has ~0.14 H—O bonds/Å^2 while the [012] surface has approximately half as many, or ~0.07 /Å^2. Additionally, the O-H intramolecular bond length indicates that the [001] waters/hydroxyls are slightly stronger than on the [012] surface (0.99 and 1.00 Å, respectively). Counterintuitively, the less dense [012] surface has shorter H—O intermolecular hydrogen bond lengths (1.65 Å). The short length stems from the higher fraction of dissociated water molecules on the [012] surface and thus the dissociated protons are closer to the remaining hydroxyls and water forming a strong H-bond.

The water network found here on the [012] and [001] hematite surfaces is in close agreement with the past experimental and MD/AIMD studies perform to understand the

water-hematite interface. Most experimental studies support the presence of both H_2O and dissociated H_2O molecules on both the [001] and [012] surface.[59,63,64] The orientation of H_2O/OH molecules on [012] molecule found here matches noncontact atomic force microscopy results for H_2O/OH molecules found of [012] Fe_2O_3 surface by Jakub et. al. (2019).[59] The H—O bond lengths of 1.5 Å between $FeOH_2$ molecule and adjacent FeOH molecule and 1.8 Å between FeOH and Fe_3OH molecule are very slightly different than found by Jakub et. al. (2019)[59] (1.6 Å and 1.7 Å, respectively). Filippov et. al. (2022), also simulated the atomic surface concentration of water molecules (molecules/surface area) on [001] facet to be 13.66 nm^{-2} or one dissociated water molecule per 7.3 $Å^2$.[65] However, the water network on [001] facet remains ill- defined in literature, with several conflicting reports of the water network structure.[66-68] Since my method produced surface networks which matches the only well defied surfaces currently available, i.e. [012] facet, I consider it validated; additionally these findings may clarify the [001] surface water structure.

5.3.2 Adsorption of SeO_4^{2-} on hematite surfaces

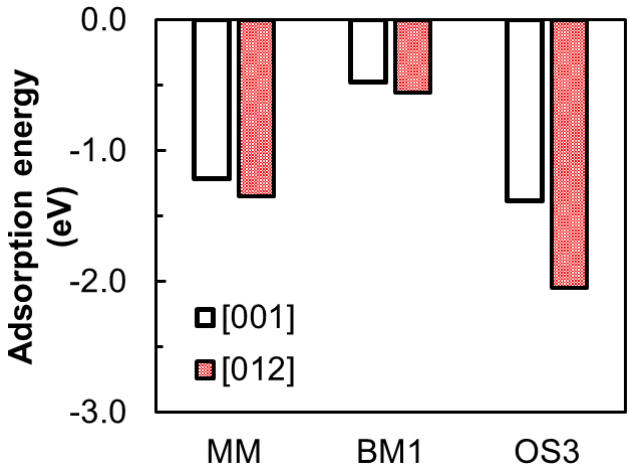

Figure 5.5: Adsorption on SeO_4^{2-} on [001] and [012] hematite facets.

I calculated the adsorption of selenate on neutral [012] and [001] surfaces, which are shown in Figure 5.5. I examined three bidentate, two monodentate and three outer-

sphere configurations on the [001] hematite surface and two bidentate, two monodentate and six outer-sphere configurations on the [012] hematite surface. Figure 5.5 shows the adsorption energy of the most stable MM, BM, and OS configurations. I found that the adsorption of SeO_4^{2-} is exothermic on both [012] and [001] Fe_2O_3 facets.

The outer sphere configuration had the most exothermic adsorption on [012] surface, followed by the MM and BM configurations with -2.05 eV, -1.34 eV and -0.54 eV adsorption energies, respectively. Although the MM and BM configurations are exothermic, the difference between outer-sphere and MM configuration energies is 0.71 eV. Using Boltzmann distribution, I predict that adsorption of selenate in MM configuration is 1.35×10^{-12} times as likely as the outer-sphere configuration. Therefore, I expect selenate to adsorb in outer-sphere configuration on [012] hematite surface under neutral conditions.

On the [001] Fe_2O_3 surface, the adsorption was also most exothermic in outer-sphere configuration followed by MM and BM with adsorption energy of -1.38 eV, -1.21 eV and -0.47 eV, respectively. The adsorption energy difference between OS and MM configuration was only 0.17 eV, which suggests approximately 14% of the adsorbed selenate will adsorb in inner-sphere configuration. Although no facet specific delineation of adsorption configuration has been reported in the literature, several studies have reported percentage of selenate adsorbs in inner sphere and outer-sphere configurations on neutral hematite nanoparticles with Johnston and Chrysochoou (2016) found 30% of SeO_4^{2-} adsorbed in inner-sphere configuration on Fe (hydr)oxides at pH 7. The finding of both structures matches my prediction, with the allowance that experiment did not determine

the surface terminations and thus relative [001] and [012] surface structures, which may account for the differences in inner-/outer-sphere partitioning.

Comparing adsorption behavior between the two facets, adsorption on the [012] facet is 0.67 eV more exothermic than the [001] facet. I predict that selenate will preferentially bind to the [012] surface of hematite nanoparticles containing both facets. Therefore, to increase inner-sphere adsorption, hematite nanoparticles with a higher percentage on [001] facets should be synthesized. However, to develop the more adsorbent material, a higher percentage of [012] hematite nanoparticle should be selected for selenate adsorption as it has the highest binding strength.

5.3.2.1 Effect of surface properties on adsorption of SeO_4^{2-} on hematite facets

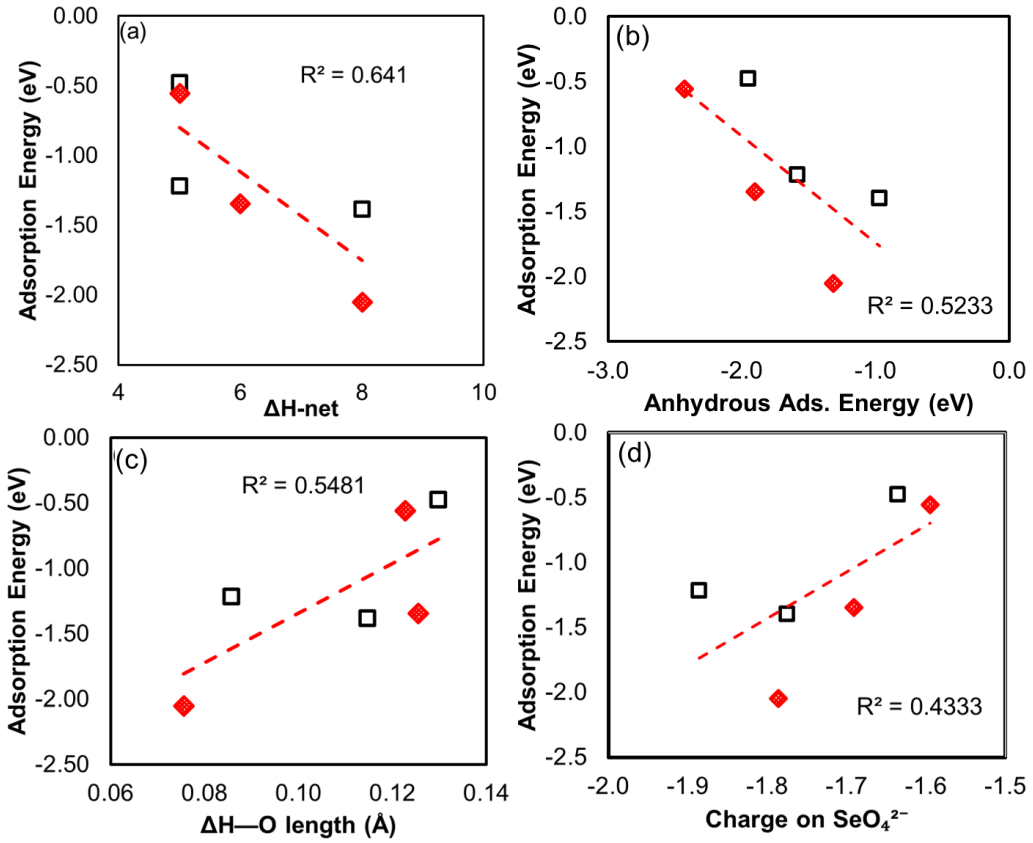

Figure 5.6: Effect of (a) change in intermolecular and intramolecular H-O bonds, (b) anhydrous adsorption energy, (c) change in H—O bond length, and (d) charge in SeO_4^{2-} on adsorption energies of SeO_4^{2-} on [001] and [012] Fe_2O_3 surfaces.

I investigated the effect of four properties on the facet dependent adsorption energies: (1) change in number of net intermolecular and intramolecular hydrogen bonds, (2) adsorption energy of selenate adsorbing on anhydrous hematite surface, (3) change in average H—O bond length present on the surface due to adsorption and (4) charge on SeO_4^{2-} after adsorbing on hematite surface. These characteristics were chosen to examine the degree to which different physical interactions might control adsorption, specifically: (1) changes to the water network upon adsorption, (2) direct SeO_4^{2-} interaction with the surface, (3) change in the intramolecular water forces, and (4) charge transfer, and thus

ionic/covalent bond formation. The relationships between the behavior characterizing factors and adsorption energy and a linear fit R^2 values are presented in Figure 5.6.

Amongst the different factors, those describing the water network correlate best with the calculated adsorption energies. The higher number of hydrogen bonds between oxo-anion and surface increases the adsorption energy exothermically. However, the water network is unlikely to be the only contributing factor, as R^2 is only 0.65. Additionally, the adsorption energy is an anti-correlated with selenate on the anhydrous surface. Thus, structures predicted to bind strongly without water networks actually bind weakly when considering the water.

These finding are consistent with the previous study of SeO_4^{2-} adsorption on the [012] Al_2O_3 surface which demonstrated that the water network controlled adsorption, and that anhydrous adsorption is inversely correlated with the solvated energies.[32] I note that the relationship between the change in the water network on different facets of hematite is weaker than on the [012] Al_2O_3 surface ($R^2 \sim 0.81$),[32] and thus there are additional factors which contribute to the binding strength. The change in H—O bond length has a slightly stronger correlation with adsorption energy than the charge on SeO_4^{2-}. On [001] and [012] surfaces, the average H—O bond length increases upon adsorbing SeO_4^{2-}. However, the average H—O bond length is 11.7% shorter on [012] surface as compared to [001] surface after adsorption. Since shorter H—O bond lengths correlate with stronger bonds, the overall adsorption on [012] surface is predicted to be stronger than adsorption on [001] surface in all the three configurations, which is what is found from the adsorption energies. On [012] surface, the H—O bond length is shorter for outer-sphere configurations (1.72 Å) than MM and BM configurations (1.77 and 1.77 Å). This combined with higher number

of bonds formed in the outer-sphere configuration leads to stronger bonding in outer-sphere than inner-sphere (MM/BM) configurations.

On [001], in the MM configuration, both the number of new bonds (5) and average H—O bond length increase (0.09 Å) are lower than outer-sphere adsorption (8, 0.11 Å, respectively). Since shorter bond lengths, i.e., stronger H—O bonds, are present on surface after selenate adsorption in MM configuration as compared to outer-sphere configuration, only a small difference in adsorption energy (0.18 eV) is observed between the two configurations. In BM configuration, the number of bond increase (5) is low and the average H—O bond length increase (0.13 Å) is high. Thus, the BM configuration is less exothermic than outer-sphere or MM adsorption. Hence, I have a lower number of weaker H-bonds on the surface, which leads to a much larger difference (0.92 eV) in adsorption energies in outer-sphere and BM configuration. Hence, the adsorption energy trends observed on different facets of hematite can correlated to surface H-network reconfiguration which includes the number of total intermolecular and intramolecular bonds, average H—O bond lengths and change in H—O bond length upon adsorption.

5.3.3 Adsorption of oxo-anions on [012] hematite surface

I also examiend the effect of oxoanion identity on the adsorption energetics on the [012] hematite surface. Given the stronger adsorption on the [012] surface, I restrict the remaining discussion to this surface. I considered Se(VI), Se(IV) and As(V). The DFT calculated adsorption energies on the neutral [012] Fe_2O_3 surface are presented in Figure 5.7. I found anion identity affects both the energies and structural preferences. Selenite adsorption is the most exothermic followed by arsenate and selenate adsorption with

energies of -2.46 eV, -2.30 eV and -2.05 eV respectively. The adsorption of doubly deprotonated Arsenate is more exothermic by 0.34 eV than singly deprotonated state ($H_2AsO_4^{2-}$) and I will, therefore, discuss the arsenate adsorption in its doubly deprotonated state ($HAsO_4^{2-}$).

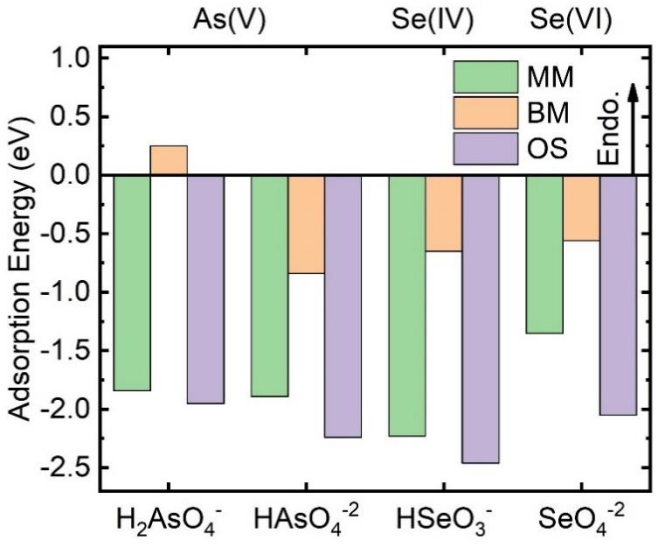

Figure 5.7: adsorption of Arsenate, selenite, and selenate on [012] hematite surface.

Outer sphere adsorption of all species is more exothermic than inner sphere configurations. The difference between outer-sphere and inner-sphere (MM/BM) adsorption is 0.40, 0.23 and 0.71 eV for $HAsO_4^{2-}$, $HSeO_3^{2-}$ and SeO_4^{2-} respectively. This means only 1.7×10^{-5} % of $HAsO_4^{2-}$, 1.5×10^{-2} % of $HSeO_3^{-}$ and 1.4×10^{-10} % of SeO_4^{2-} will adsorb in inner-sphere configuration. However, the difference between outer-sphere and inner-sphere configuration for $H_2AsO_4^{-}$ is only 0.11 eV, i.e., 1.19% $H_2AsO_4^{-}$ is expected to adsorb in inner-sphere configuration on [012] Fe_2O_3 facet.

5.3.3.1 Effect of oxo-anion and surface properties on adsorption energies

I compared the effect of different properties of oxo-anion and change in surface water network on adsorption energies. I did not examine the effect of anhydrous adsorption energy as it is anti-correlated to adsorption with water network. The results are shown in

Figure 5.8. I found that overall, the adsorption energies are not as strongly correlated to change in number of intermolecular and intramolecular H-O bonds. However, the water network still correlates to effect of configurational changes on adsorption energy (highest number of bonds corresponds to adsorption in outer-sphere and lowest number of bonds correspond to adsorption in BM configuration). The effect of oxo-anion species is not encapsulated with change in number of O-H bonds, change in length of O-H bonds, charge on oxo-anion or e^- transfer from oxo-anion to surface upon adsorption, as seen in figure 5.8.

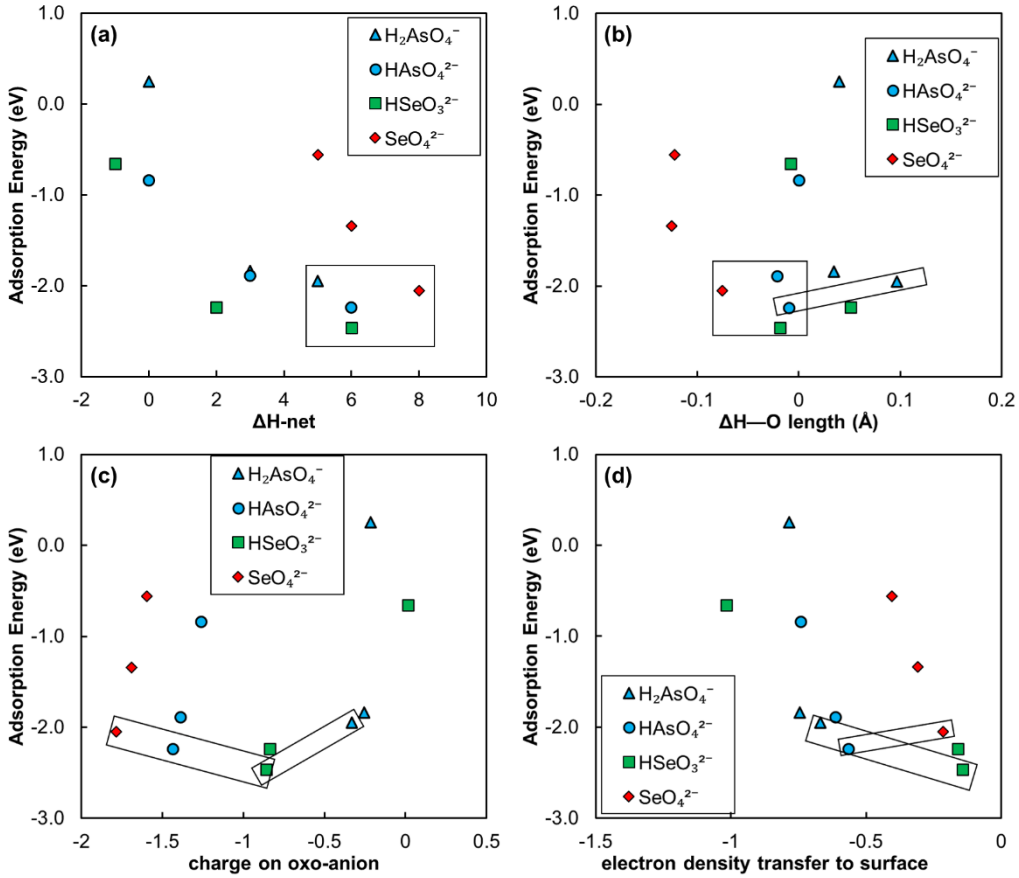

Figure 5.8: Effect of (a) change in intermolecular and intramolecular H-O bonds, (b) change in H—O bond length, (c) charge on oxo-anion and (d) electron transfer from oxo-anion to hematite surface on adsorption energies of Se(IV), Se(VI) and As(V) on [012] Fe_2O_3 surfaces. The boxed values indicate adsorption in outer-sphere configuration for the four oxo-anions.

I investigate the adsorption energy on [012] hematite surface by comparing the H-bond orientation upon adsorption in outer-sphere for the four oxo-anion in Figure 5.9. Even though SeO_4^{2-} has the highest number of new intermolecular H—O bonds, the orientation of three surface H^+ shifts towards oxo-anion which weakens the H—O bond network between the surface H_2O/OH molecules and hence decreases the adsorption energy. Upon $HSeO_3^-$ and $H_2AsO_4^{2-}$ adsorption, only two surface H^+ change their orientation, which effects only half of the H_2O/OH bond network on the surface. However, $HAsO_4^{2-}$ forms intermolecular O-H bonds where one of the surface H^+ and changes its orientation perpendicular to the surface (Figure 5.9(d)). Therefore, upon adsorption in outer-sphere, both change in H-bonds and protonation state effects the adsorption energy of $HAsO_4^{2-}$ on [012] hematite surface. Therefore, both the net change in number of intermolecular and intramolecular O-H bonds as well as orientational change in surface H^+ affect the adsorption energies of different oxo-anion on [012] hematite surface.

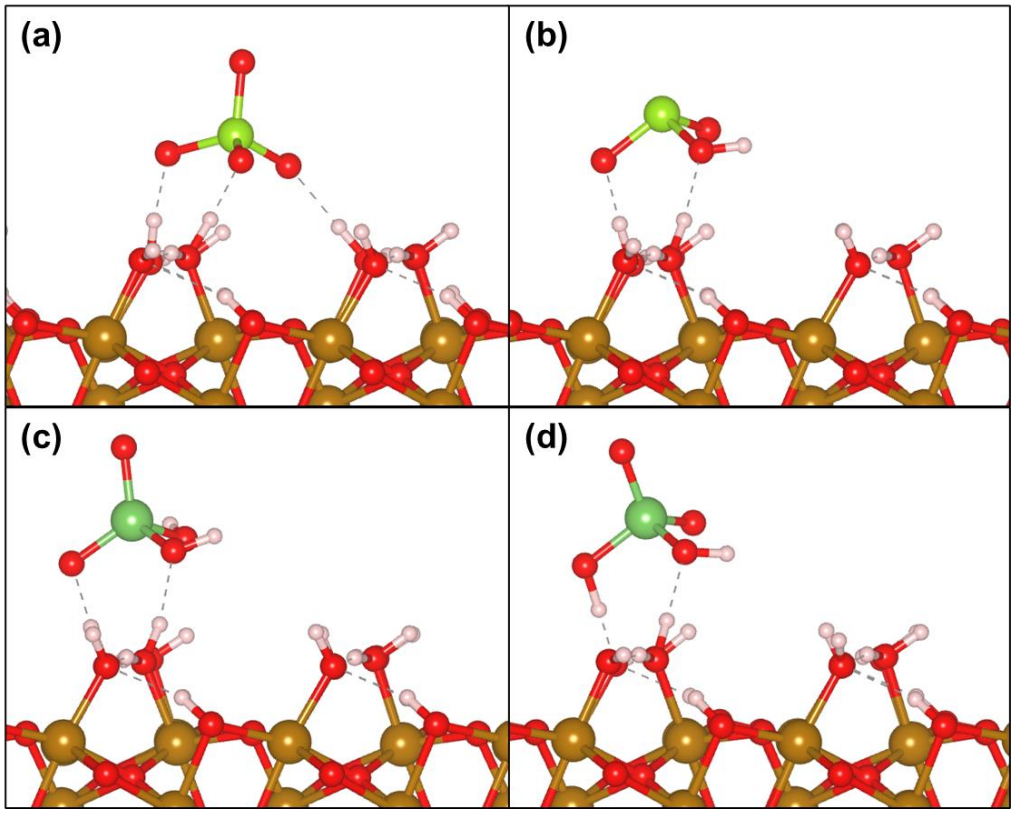

Figure 5.9: Water network on [012] hematite surface upon adsorption of (a) SeO_4^{2-}, (b) $HSeO_3^-$, (c) $H_2AsO_4^-$ and (d) $HAsO_4^{2-}$ in outer-sphere configuration.

5.4 Conclusion

I investigated the role of facet and oxo-anion properties on adsorption on hematite surface in neutral environment. Overall, I found that the SeO_4^{2-} adsorption on different hematite surface is affected by the change in water network due to adsorption. The adsorption is more exothermic on [012] Fe_2O_3 surface and occurs in outer-sphere configuration as a greater number of stronger intermolecular H—O bonds form upon selenate adsorption. However, on [001] surface higher percentage of selenate is expected to adsorb in inner-sphere configuration as the intermolecular H—O bonds on the [001] surface is weaker than [012] surface, and hence require lower energy to break. The adsorption of oxo-anions is also controlled by water network on [012] hematite surface. However, the additional effects like change in orientation of H^+ contribute towards change in adsorption energy for different oxo-anion adsorptions. In terms of selectivity, selenite has most exothermic adsorption on hematite surface and hence expected to be most selective as compared to Arsenate and Selenate adsorption. Overall, I conclude that the adsorption on hematite surface can occur at neutral surface and still significantly controlled by water network. However, I need to include more parameters like H^+ orientations to encapsulate the complete effect of change in water network on adsorption energies.

5.5 References

1. Fernández-Martínez, A.; Charlet, L., Selenium environmental cycling and bioavailability: a structural chemist point of view. Reviews in Environmental Science and Bio/Technology 2009, 8 (1), 81-110.
2. Distribution of Arsenic in the Environment. In Arsenic: Medical and Biologic Effects of Environmental Pollutants., Pollutants., N. R. C. U. C. o. M. a. B. E. o. E., Ed. National Academies Press (US): Washington (DC), 1977; Vol. 3.
3. Podgorski, J.; Berg, M., Global threat of arsenic in groundwater. Science 2020, 368 (6493), 845-850.

4. Ayotte, J. D.; Medalie, L.; Qi, S. L.; Backer, L. C.; Nolan, B. T., Estimating the High-Arsenic Domestic-Well Population in the Conterminous United States. Environmental Science & Technology 2017, 51 (21), 12443-12454.
5. Kaur, N.; Sharma, S.; Kaur, S.; Nayyar, H., Selenium in agriculture: a nutrient or contaminant for crops? Archives of Agronomy and Soil Science 2014, 60 (12), 1593-1624.
6. Jones, G. D.; Droz, B.; Greve, P.; Gottschalk, P.; Poffet, D.; McGrath, S. P.; Seneviratne, S. I.; Smith, P.; Winkel, L. H. E., Selenium deficiency risk predicted to increase under future climate change. Proceedings of the National Academy of Sciences 2017, 114 (11), 2848-2853.
7. Le, H.-L. T.; Lazzari, R.; Goniakowski, J.; Cavallotti, R.; Chenot, S.; Noguera, C.; Jupille, J.; Koltsov, A.; Mataigne, J.-M., Tuning Adhesion at Metal/Oxide Interfaces by Surface Hydroxylation. The Journal of Physical Chemistry C 2017, 121 (21), 11464-11471.
8. Cavanagh, J. B., EXPERIMENTAL AND CLINICAL NEUROTOXICOLOGY. Second edition. Brain 2000, 123 (12), 2571-2573.
9. Roman, M.; Jitaru, P.; Barbante, C., Selenium biochemistry and its role for human health. Metallomics 2013, 6 (1), 25-54.
10. R. Cardoso, B.; Hare, D. J.; Lind, M.; McLean, C. A.; Volitakis, I.; Laws, S. M.; Masters, C. L.; Bush, A. I.; Roberts, B. R., The APOE ε4 Allele Is Associated with Lower Selenium Levels in the Brain: Implications for Alzheimer's Disease. ACS Chemical Neuroscience 2017, 8 (7), 1459-1464.
11. Olson, O. E., Selenium Toxicity in Animals with Emphasis on Man. Journal of the American College of Toxicology 1986, 5 (1), 45-70.
12. Séby, F.; Potin-Gautier, M.; Giffaut, E.; Borge, G.; Donard, O. F. X., A critical review of thermodynamic data for selenium species at 25°C. Chemical Geology 2001, 171 (3), 173-194.
13. Taira, M.; Sakakibara, K.; Saeki, K.; Ohira, S.-I.; Toda, K., Determination of oxoanions and water-soluble species of arsenic, selenium, antimony, vanadium, and chromium eluted in water from airborne fine particles (PM2.5): effect of acid and transition metal content of particles on heavy metal elution. Environmental Science: Processes & Impacts 2020, 22 (7), 1514-1524.
14. Smedley, P. L.; Kinniburgh, D. G., A review of the source, behaviour and distribution of arsenic in natural waters. Applied Geochemistry 2002, 17 (5), 517-568.
15. Inam, M. A.; Khan, R.; Lee, K. H.; Wie, Y. M., Removal of Arsenic Oxyanions from Water by Ferric Chloride-Optimization of Process Conditions and Implications for Improving Coagulation Performance. Int J Environ Res Public Health 2021, 18 (18).
16. Hu, C.; Chen, Q.; Chen, G.; Liu, H.; Qu, J., Removal of Se(IV) and Se(VI) from drinking water by coagulation. Separation and Purification Technology 2015, 142, 65-70.
17. Rudel, H. E.; Lane, M. K. M.; Muhich, C. L.; Zimmerman, J. B., Toward Informed Design of Nanomaterials: A Mechanistic Analysis of Structure–Property–Function Relationships for Faceted Nanoscale Metal Oxides. ACS Nano 2020, 14 (12), 16472-16501.
18. Pincus, L. N.; Rudel, H. E.; Petrović, P. V.; Gupta, S.; Westerhoff, P.; Muhich, C. L.; Zimmerman, J. B., Exploring the Mechanisms of Selectivity for Environmentally Significant Oxo-Anion Removal during Water Treatment: A Review of Common

Competing Oxo-Anions and Tools for Quantifying Selective Adsorption. Environmental Science & Technology 2020, 54 (16), 9769-9790.
19. Bishayee, B.; Chatterjee, R. P.; Ruj, B.; Chakrabortty, S.; Nayak, J., Strategic management of nitrate pollution from contaminated water using viable adsorbents: An economic assessment-based review with possible policy suggestions. Journal of Environmental Management 2022, 303, 114081.
20. Li, P.; Damron, J. T.; Bryantsev, V. S.; Johnson, K. R.; Stamberga, D.; Mahurin, S. M.; Popovs, I.; Jansone-Popova, S., Guanidinium-Based Ionic Covalent-Organic Nanosheets for Sequestration of Cr(VI) and As(V) Oxoanions in Water. ACS Applied Nano Materials 2021, 4 (12), 13319-13328.
21. Stefaniak, J.; Dutta, A.; Verbinnen, B.; Shakya, M.; Rene, E. R., Selenium removal from mining and process wastewater: a systematic review of available technologies. Journal of Water Supply: Research and Technology-Aqua 2018, 67 (8), 903-918.
22. Sedlak, D. L., The Unintended Consequences of the Reverse Osmosis Revolution. Environmental Science & Technology 2019, 53 (8), 3999-4000.
23. Weidner, E.; Ciesielczyk, F. Removal of Hazardous Oxyanions from the Environment Using Metal-Oxide-Based Materials Materials [Online], 2019.
24. Ali, I.; Shrivastava, V., Recent advances in technologies for removal and recovery of selenium from (waste)water: A systematic review. Journal of Environmental Management 2021, 294, 112926.
25. Wang, L.; Shi, C.; Wang, L.; Pan, L.; Zhang, X.; Zou, J.-J., Rational design, synthesis, adsorption principles and applications of metal oxide adsorbents: a review. Nanoscale 2020, 12 (8), 4790-4815.
26. Nayak, D. C. Adsorption of oxy-anions of selenium and arsenic at oxide/water interfaces. M.S., University of Nevada, Reno, United States -- Nevada, 1995.
27. Yamani, J. S.; Lounsbury, A. W.; Zimmerman, J. B., Adsorption of selenite and selenate by nanocrystalline aluminum oxide, neat and impregnated in chitosan beads. Water Research 2014, 50, 373-381.
28. Suzuki, T. M.; Pacheco Tanaka, D. A.; Llosa Tanco, M. A.; Kanesato, M.; Yokoyama, T., Adsorption and removal of oxo-anions of arsenic and selenium on the zirconium(iv) loaded polymer resin functionalized with diethylenetriamine-N,N,N′,N′-polyacetic acid. Journal of Environmental Monitoring 2000, 2 (6), 550-555.
29. Kubicki, J. D.; Kwon, K. D.; Paul, K. W.; Sparks, D. L., Surface complex structures modelled with quantum chemical calculations: carbonate, phosphate, sulphate, arsenate and arsenite. European Journal of Soil Science 2007, 58 (4), 932-944.
30. Ma, Z.; Shan, C.; Liang, J.; Tong, M., Efficient adsorption of Selenium(IV) from water by hematite modified magnetic nanoparticles. Chemosphere 2018, 193, 134-141.
31. Hua, M.; Zhang, S.; Pan, B.; Zhang, W.; Lv, L.; Zhang, Q., Heavy metal removal from water/wastewater by nanosized metal oxides: A review. Journal of Hazardous Materials 2012, 211-212, 317-331.
32. Gupta, S.; Anh Nguyen, N.; Muhich, C. L., Surface water H-bonding network is key controller of selenate adsorption on [012] α-alumina: An Ab-initio study. Journal of Colloid and Interface Science 2022, 617, 136-146.

33. Wang, S.; Zeng, X.; Lin, J.; Yuan, Z.; Qu, S.; Zhang, B.; Pan, Y.; Chen, N.; Chen, W.; Jia, Y., Molecular Structure of Molybdate Adsorption on Goethite at pH 5–8: A Combined DFT + U, EXAFS, and Ab Initio XANES Study. The Journal of Physical Chemistry C 2021, 125 (40), 22052-22063.
34. He, G.; Zhang, M.; Pan, G., Influence of pH on Initial Concentration Effect of Arsenate Adsorption on TiO2 Surfaces: Thermodynamic, DFT, and EXAFS Interpretations. The Journal of Physical Chemistry C 2009, 113 (52), 21679-21686.
35. Ramadugu, S. K.; Mason, S. E., DFT Study of Antimony(V) Oxyanion Adsorption on α-Al2O3(1$\bar{1}$02). The Journal of Physical Chemistry C 2015, 119 (32), 18149-18159.
36. Su, T.; Guan, X.; Gu, G.; Wang, J., Adsorption characteristics of As(V), Se(IV), and V(V) onto activated alumina: Effects of pH, surface loading, and ionic strength. Journal of Colloid and Interface Science 2008, 326 (2), 347-353.
37. Börsig, N.; Scheinost, A. C.; Schild, D.; Neumann, T., Mechanisms of selenium removal by partially oxidized magnetite nanoparticles for wastewater remediation. Applied Geochemistry 2021, 132, 105062.
38. Tang, W.; Li, Q.; Gao, S.; Shang, J. K., Arsenic (III,V) removal from aqueous solution by ultrafine α-Fe2O3 nanoparticles synthesized from solvent thermal method. Journal of Hazardous Materials 2011, 192 (1), 131-138.
39. Lounsbury, A. W.; Yamani, J. S.; Johnston, C. P.; Larese-Casanova, P.; Zimmerman, J. B., The role of counter ions in nano-hematite synthesis: Implications for surface area and selenium adsorption capacity. Journal of Hazardous Materials 2016, 310, 117-124.
40. Lounsbury, A. W.; Wang, R.; Plata, D. L.; Billmyer, N.; Muhich, C.; Kanie, K.; Sugimoto, T.; Peak, D.; Zimmerman, J. B., Preferential adsorption of selenium oxyanions onto {1 1 0} and {0 1 2} nano-hematite facets. Journal of Colloid and Interface Science 2019, 537, 465-474.
41. Wang, Z.; Zhang, H.; Ren, J.; Lin, X.; Han, T.; Liu, J.; Li, J., Predicting adsorption ability of adsorbents at arbitrary sites for pollutants using deep transfer learning. npj Computational Materials 2021, 7 (1), 19.
42. Kresse, G.; Furthmüller, J., Efficient iterative schemes for ab initio total-energy calculations using a plane-wave basis set. Physical Review B 1996, 54 (16), 11169.
43. Kresse, G.; Furthmüller, J., Efficiency of ab-initio total energy calculations for metals and semiconductors using a plane-wave basis set. Computational Materials Science 1996, 6 (1), 15-50.
44. Perdew, J. P.; Burke, K.; Ernzerhof, M., Generalized gradient approximation made simple. Phys Rev Lett 1996, 77 (18), 3865-3868.
45. Hubbard, J.; Flowers, B. H., Electron correlations in narrow energy bands. II. The degenerate band case. Proceedings of the Royal Society of London. Series A. Mathematical and Physical Sciences 1964, 277 (1369), 237-259.
46. Dudarev, S. L.; Botton, G. A.; Savrasov, S. Y.; Humphreys, C. J.; Sutton, A. P., Electron-energy-loss spectra and the structural stability of nickel oxide: An LSDA+U study. Physical Review B 1998, 57 (3), 1505-1509.
47. Liechtenstein, A. I.; Anisimov, V. I.; Zaanen, J., Density-functional theory and strong interactions: Orbital ordering in Mott-Hubbard insulators. Physical Review B 1995, 52 (8), R5467-R5470.

48. Krukau, A. V.; Vydrov, O. A.; Izmaylov, A. F.; Scuseria, G. E., Influence of the exchange screening parameter on the performance of screened hybrid functionals. The Journal of Chemical Physics 2006, 125 (22), 224106.
49. Dzade, N. Y.; Roldan, A.; De Leeuw, N. H., A Density Functional Theory Study of the Adsorption of Benzene on Hematite (α-Fe2O3) Surfaces. Minerals 2014, 4 (1), 89-115.
50. Kresse, G.; Joubert, D., From ultrasoft pseudopotentials to the projector augmented-wave method. Physical Review B 1999, 59 (3), 1758-1775.
51. Blöchl, P. E., Projector augmented-wave method. Physical Review B 1994, 50 (24), 17953-17979.
52. Mathew, K.; Sundararaman, R.; Letchworth-Weaver, K.; Arias, T. A.; Hennig, R. G., Implicit solvation model for density-functional study of nanocrystal surfaces and reaction pathways. J Chem Phys 2014, 140 (8), 084106.
53. Grimme, S.; Antony, J.; Ehrlich, S.; Krieg, H., A consistent and accurate ab initio parametrization of density functional dispersion correction (DFT-D) for the 94 elements H-Pu. J Chem Phys 2010, 132 (15), 154104.
54. Wang, V.; Xu, N.; Liu, J.-C.; Tang, G.; Geng, W.-T., VASPKIT: A user-friendly interface facilitating high-throughput computing and analysis using VASP code. Computer Physics Communications 2021, 267, 108033.
55. Yu, M.; Trinkle, D. R., Accurate and efficient algorithm for Bader charge integration. The Journal of Chemical Physics 2011, 134 (6), 064111.
56. Nelson, R.; Ertural, C.; George, J.; Deringer, V. L.; Hautier, G.; Dronskowski, R., LOBSTER: Local orbital projections, atomic charges, and chemical-bonding analysis from projector-augmented-wave-based density-functional theory. Journal of Computational Chemistry 2020, 41 (21), 1931-1940.
57. Momma, K.; Izumi, F., VESTA 3 for three-dimensional visualization of crystal, volumetric and morphology data. Journal of applied crystallography 2011, 44 (6), 1272-1276.
58. Jakub, Z.; Meier, M.; Kraushofer, F.; Balajka, J.; Pavelec, J.; Schmid, M.; Franchini, C.; Diebold, U.; Parkinson, G. S., Rapid oxygen exchange between hematite and water vapor. Nature Communications 2021, 12 (1), 6488.
59. Jakub, Z.; Kraushofer, F.; Bichler, M.; Balajka, J.; Hulva, J.; Pavelec, J.; Sokolović, I.; Müllner, M.; Setvin, M.; Schmid, M.; Diebold, U.; Blaha, P.; Parkinson, G. S., Partially Dissociated Water Dimers at the Water–Hematite Interface. ACS Energy Letters 2019, 4 (2), 390-396.
60. Ullah, H.; Lun, L.; Rashid, A.; Zada, N.; Chen, B.; Shahab, A.; Li, P.; Ali, M. U.; Lin, S.; Wong, M. H., A critical analysis of sources, pollution, and remediation of selenium, an emerging contaminant. Environmental Geochemistry and Health 2022.
61. Sharma, V. K.; Sohn, M.; McDonald, T. J., Chapter 8 - Remediation of Selenium in Water: A Review. In Advances in Water Purification Techniques, Ahuja, S., Ed. Elsevier: 2019; pp 203-218.
62. Can, B. Z.; Boncukcuoglu, R.; Yilmaz, A. E.; Fil, B. A., Effect of some operational parameters on the arsenic removal by electrocoagulation using iron electrodes. Journal of Environmental Health Science and Engineering 2014, 12 (1), 95.

63. Guimarães, W. G.; de Lima, G. F.; Duarte, H. A., Comparative DFT study of the oxy(hydr)oxides of iron and aluminum – structural, electronic and surface properties. Surface Science 2021, 708, 121821.
64. Lahiri, N.; Song, D.; Zhang, X.; Huang, X.; Stoerzinger, K. A.; Carvalho, O. Q.; Adiga, P. P.; Blum, M.; Rosso, K. M., Interplay between Facets and Defects during the Dissociative and Molecular Adsorption of Water on Metal Oxide Surfaces. Journal of the American Chemical Society 2023, 145 (5), 2930-2940.
65. Filippov, L. O.; Silva, L. A.; Pereira, A. M.; Bastos, L. C.; Correia, J. C. G.; Silva, K.; Piçarra, A.; Foucaud, Y., Molecular models of hematite, goethite, kaolinite, and quartz: Surface terminations, ionic interactions, nano topography, and water coordination. Colloids and Surfaces A: Physicochemical and Engineering Aspects 2022, 650, 129585.
66. Futera, Z.; English, N. J., Water Breakup at Fe2O3–Hematite/Water Interfaces: Influence of External Electric Fields from Nonequilibrium Ab Initio Molecular Dynamics. The Journal of Physical Chemistry Letters 2021, 12 (29), 6818-6826.
67. Wang, R. B.; Hellman, A.; E., G.-R.; B., T.; M., M., Initial water adsorption on hematite (α-Fe2O3) (0001): A DFT + U study
Clays and oxide minerals as catalysts and nanocatalysts in Fenton-like reactions—A review. The Journal of Chemical Physics 2018, 148 (9), 094705.
68. Yamamoto, S.; Kendelewicz, T.; Newberg, J. T.; Ketteler, G.; Starr, D. E.; Mysak, E. R.; Andersson, K. J.; Ogasawara, H.; Bluhm, H.; Salmeron, M.; Brown, G. E., Jr.; Nilsson, A., Water Adsorption on α-Fe2O3(0001) at near Ambient Conditions. The Journal of Physical Chemistry C 2010, 114 (5), 2256-2266.

CHAPTER 6

ELECTROCHEMICAL RECYCLING N FROM WASTEWATER USING DISPERSED RU ATOM IN CU METAL CATALYST

6.1 Introduction

The constant recycling of nitrogen between earth, soil, water and atmosphere is essential for sustaining life on this planet. However, anthropogenic activities have disturbed the balance of this delicate cycle and depreciated environmental and human health.[1] Overuse of nitrate (NO_3^-) rich fertilizers to improve the crop yield have resulted in leaching of nitrate in our ground water. In aquatic ecosystem, excess nitrate causes "dead zone", which cannot support life forms due to lack of oxygen.[2] If nitrogen rich water is consumed by humans at concentrations higher than 10 mg/L, it can cause methemoglobinemia, or "blue baby syndrome", thyroid disease, fatigue, weight gain, hair loss, goiters and colon cancer.[3]

Nitrate remediation is an important step to re-balance the nitrogen cycle. Remediation methods such as ion exchange, reverse osmosis, electrodialysis and electro-capacitive ion capture can be used for filtering NO_3^- for water.[4,5] However, the product from these processes cannot be upcycled and require additional disposal steps. Electrocatalytic nitrate reduction (NO_3RR) has gained attention as a remediation process to rebuild a circular economy by reducing NO_3^- to NH_3.[6] The NH_3 can be reused again as crop fertilizers and industrial chemical and restore balance to nitrogen cycle. Currently, energy intensive Haber-Bosch process is used to produce NH_3 from atmospheric N_2 which contributes to >1% global CO_2 emissions.[7] In contrast to the Haber-Bosch process, NO_3RR can produce NH_3 at room temperature at low pressure condition, without chemical

reductants and using only renewable sources of electricity.[8] NO_3RR, however, is currently not commercially viable because of low selectivity towards NH_3 production, low activity of NO_3^- reduction and high cost of electrocatalysts like Ru.

NO_3RR reduces NO_3^- to NO_2^-, NO, N_2O, N_2, N_2H_2, NH_2OH or NH_3 or mixture of these species depending upon electrocatalyst, reduction potential and solution pH.[9] Moreover, the other side reactions with similar reduction potentials as compared to NO_3RR (0.69 V vs. reversible hydrogen electrode (RHE)) such as Hydrogen Evolution Reaction (HER) also occur on the catalytic surface.[10] HER suppresses NO_3RR due to presence of relatively lower concentration of NO_3^- (50-2000 ppm) as compared to H_2O and H_3O^+ molecules in wastewater. However, a commercial grade NO_3RR should have capability of delivering high current density (>1000mA/cm^2) and high NH_3 selectivity (>90%).[11]

Electrodes made of coinage metal (Cu, Ag, Au) and Platinoids (Ru, Rh, Ir, Pd and Pt) have been extensively researched as highly active and selective cathode surfaces for nitrate reduction respectively.[8,12] Specifically, the electrocatalytic reduction kinetics of nitrate to nitrite is highest on Cu surface, which is a critical rate limiting step towards production of NH_3.[6] Moreover, copper is sold only for $0.43 per mol of metal, which is a lot cheaper than other metals (Au, Ag, Pt, Pd).[10] However, the stability of Cu electrode is pH dependent and Cu cathode deactivates in alkaline medium and Cu^{+2} leaches into aqueous medium in acidic medium.[13,14] On the other hand, Platinoids metal electrodes selectively reduce NO_3^- to single product (NH_3 or N_2) , depending upon surface kinetics.[8] However, platinoid catalysts have low performance due to competitive HER reaction[15] and are expensive metals for NO_3^- remediation (> $800/mol).[10]

Metal alloys electrodes outcompetes single element electrodes in the activity and selectivity nitrate reduction.[8,16] Wang et. at. found that the NO_3RR activity of $Cu_{50}No_{50}$ alloys was 6-fold higher than Cu or Ni single metal electrode at 0V vs. RHE because of more favorable adsorption of NO_3^- on alloy surfaces.[17] Doping Cu with 2% Fe increased the catalytic current density to 55.6 mA/cm, 2.1 times higher than Cu material at -0.7 V vs. HER.[18] Yao et. al. (2021) developed copper phosphide on copper foam (Cu_3P/CF) electrode that was 98.01% selective towards N_2 production at -1.2 V vs. Ag/AgCl.[19] However, determining activity and selectivity of infinite probable mixtures of metal-metal alloys experimentally at different pH and potential is a daunting task.

Investigating nitrate reduction mechanism using density functional theory (DFT) propels material discovery for improved activity and selectivity of NO_3RR. In 2021, Wang et. al. synthesized 6 times more active $Pt_{63}Ru_{37}$ Carbon felt supported nanoparticle as compared to Pt nanoparticles based on initial screening done by Liu et. al. (2019) using DFT based microkinetic model on 8 transition metal electrocatalysts (Co, Cu, Rh, Pd, Pt, Ag, Au, and Fe).[11,20] However, both Pt and Ru are expensive minerals and therefore Pt_3Ru cannot considered as an economical NO_3RR solution. In a recent study by Chen et. al. (2022),[21] experimental results report 99% selective reduction of NO_3^- to NH_3 with 93% faradic efficiency and 1000 mA/cm^2 over Ru dispersed Cu nanowire catalyst (Figure 6.1), higher than pure Ru and Cu surfaces. However, determining the effect of single atom on the nitrate reduction mechanism is difficult to understand using experimental results.

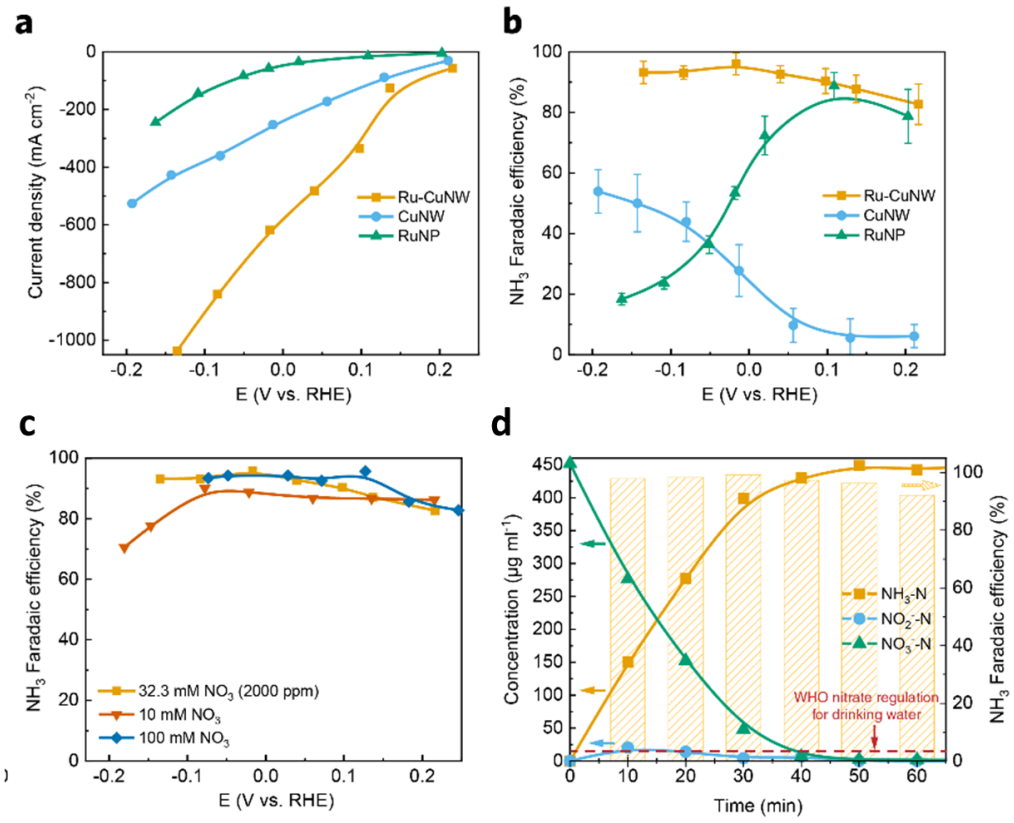

Figure 6.1: Experimental results from Feng-Yang Chen et. al.[21] "(a) I-V plots and (b) corresponding NH_3 Faradic efficiency (NH_3 FE) of Ru-CuNW (Ru-SAC), CuNW (Cu nanowire), and RuNP (Ru nanoparticle) in 1 M KOH and 2000 ppm NO_3^- electrolyte at different potential. (c) NH_3 FE of Ru-CuNW in 1 M KOH electrolyte with different concentration of NO_3^-. **(d)** Complete nitrate removal using Ru-CuNW with initial 1 M KOH and 2000 ppm NO_3^- (equals 451.6 μg ml^{-1} NO_3^-–N) electrolyte at 0 V versus RHE."

Therefore, in this work I investigated nitrate reduction on Ru single atom catalyst dispersed in Cu matrix (Ru-SAC) using density functional theory. The efficiency and selectivity on all the three catalysts are strongly related to pH and electrode potential of experimental conditions. Therefore, I developed a DFT based model to study the nitrate reduction and simultaneous hydrogen evolution reaction and other side reactions (figure

6.2) on Cu, Ru and Ru-SAC surface, to understand the effect of pH and potential on NO_3RR on all the three surfaces and the effect of Ru-SAC on nitrate activity and selectivity.

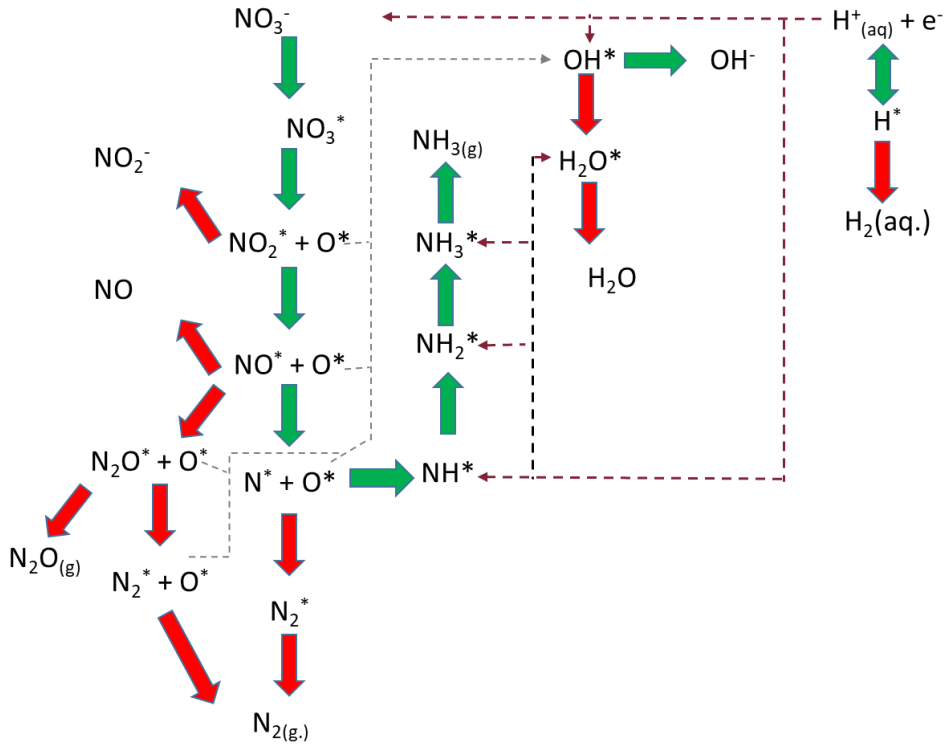

Figure 6.2: Mechanism of Nitrate reduction and other side reactions occurring over electrode surface.

6.2 Computational Methods

6.2.1 First-principle calculations

Periodic boundary condition density functional theory (DFT) calculations were performed using the Perdew-Burke-Ernzerhof (PBE) functional, as implemented in the Vienna Ab initio Simulation Package (VASP).[22-24] The wave function was constructed from a summation of plane waves with energies below 500 eV. There is less than a 0.01 eV difference in adsorption energies calculated at 500 eV and 600 eV cutoff energies. Projector-augmented wave (PAW) pseudopotentials[25] explicitly included the H 1s, O and N 2s 2p, Cu 4s 3d, and Ru 5s 4d electrons.

Cu and Ru-CuNW were represented by (111) terminated slabs consisting of 4x4x6 primitive units, while Ru was represented by a (001) terminated 4x4x6 slab. These surface terminations were chosen as they represent the low-energy surfaces.[26] Additionally, these crystal facets are equivalent since Ru is an HCP crystal structure whereas Cu is FCC (Figure 6.3). All slabs were separated by at least 12 Å of vacuum space to reduce spurious interactions between atomic layers. The Brillouin zone was sampled with an 8x8x1 Γ-point centered Monkhorst Pack mesh for each surface which showed only a 0.01 eV difference with a 10x10x1 mesh grid. All geometries were relaxed until forces were less than 1×10^{-3} eV/Å. Transition states for surface reactions were investigated using the climbing image nudged elastic band (NEB) method with at least five images per reaction until the residual forces were below 0.001 eV/Å.[27]

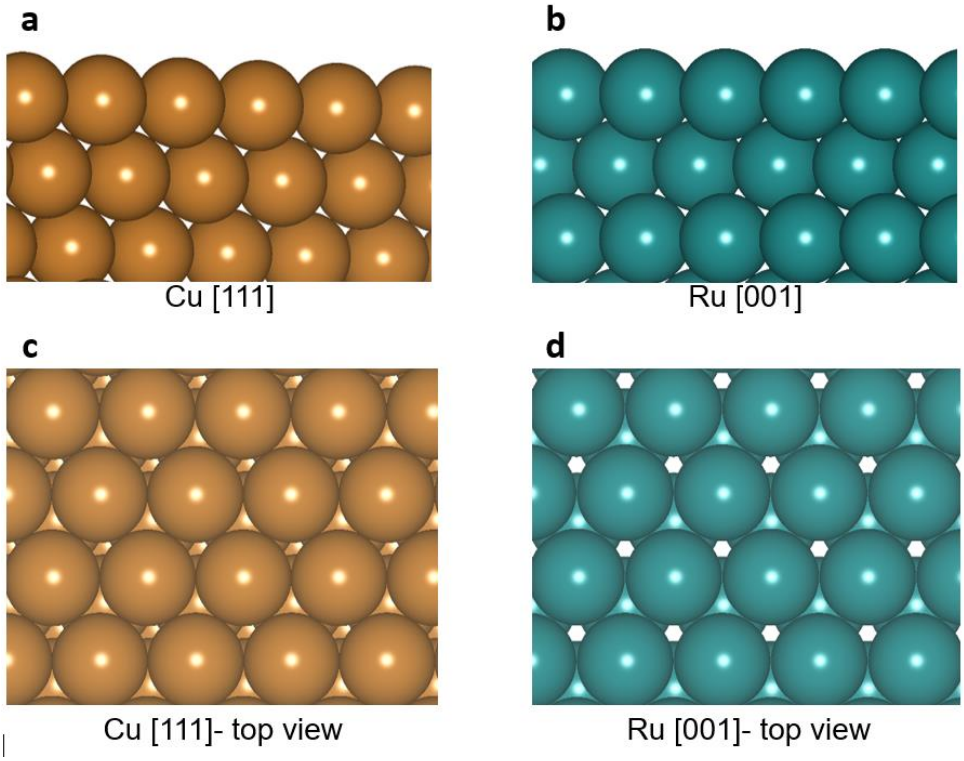

Figure 6.3: Side view (a,b) and top view (c,d) of Cu[111] and Ru[001] facet.

6.2.2 Energetics of pH and potential dependent reactions

I used Computational Hydrogen Electrode (CHE)[28] to include the voltage affects and calculate the Gibbs free energies of reaction involving electron transfer:

$$A + H^+ + e^- \rightarrow AH \qquad eq.6.1$$

The Gibbs free energy of proton-electron pair was determined by linear free energy dependence of electron energy at given potential:

$$G_{H^+} + G_{e^-} = \frac{1}{2} G_{H_2} - eU_{RHE} \qquad eq.\ 6.2$$

where U_{RHE} is applied potential with respect to the relative hydrogen electrode (RHE) and G_{H2} is the free energy of gaseous H_2.

The potential also affects the activation barriers of surface hydrogenation reactions (for e.g., $N^* + H^+ + e^- \rightarrow NH^*$). For hydrogenation reactions, the activation barriers are computed for using following reaction step and potential effects are included using Butler-Volmer formalism:

$$G(U^\circ) = G_{XH^*} - G_{X^*} - G_{H^+} - G_{e^-} \qquad eq.\ 6.3$$

$$G(U) = G(U^\circ) - \alpha ne(U - U^\circ) \qquad eq.\ 6.4$$

where n is number of electrons transferred and α is the portion of the electrons transferred at the transition state. Here I assumed α to be 0.5 as per the commonly accepted assumption that approximately half the electrons transfer at the transition state.[11]

For the adsorption and desorption of aqueous species is dependent of both reaction potential and pH of the solution. The thermodynamic cycles (Figure 6.4) are used to calculate the adsorption energies by using JANAF thermodynamic tables,[29] experimentally calculated solvation energies and pKa values obtained from CRC Handbook of Chemistry and Physics.[30] For example, the adsorption energy of NO_3^- is calculated using thermodynamic cycle as follows and outlined in equation 6.5-6.9:

$$NO_{3(l)}^- + * \rightarrow NO_3^* + e^- \qquad eq.6.5$$

$$\Delta G_{ads}(NO_3^-) = G_{NO_3^*} + G_{e^-} - G_{NO_{3(l)}^-} - G_* \qquad eq.6.6$$

$$\Delta G_{ads}(NO_3^-) = G_{NO_3^*} + [G_{H^+} + G_{e^-}] - \left[G_{NO_{3(l)}^-} + G_{H^+}\right] - G_* \qquad eq.6.7$$

$$\Delta G_{ads}(NO_3^-) = G_{NO_3^*} + \left[\frac{1}{2}G_{H_2} - eU_{RHE}\right] - \left[G_{HNO_3} - \Delta G_{vap} - \Delta G_{protonation}\right] - G_* eq.6.8$$

$\Delta G_{protonation}$ is the free energy of the association of NO_3^- in solution with a proton, and is calculated as

$$\Delta G_{protonation} = G^\circ - 2.303kT(pK_a - pH) \qquad eq.6.9$$

where k is the Boltzmann constant, T is the temperature, and pK_a is the experimental acid dissociation constant of HNO_3.[31]

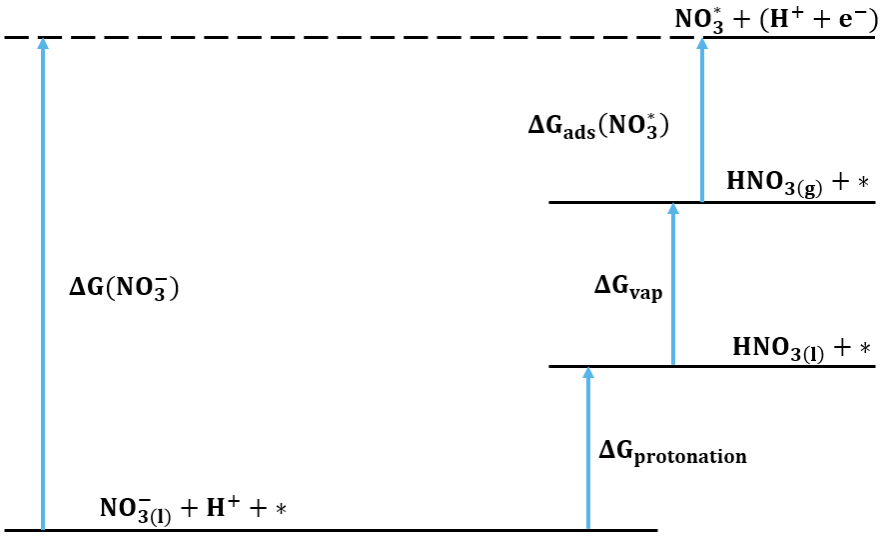

Figure 6.4: Thermodynamic cycle employed to account for free energy of protonation and solvation of NO_3, which enables calculation of overall free energy of NO_3^- adsorption.

pH also changes the proton donor for hydrogen evolution reaction and hydration step occurring over a cathode surface. At low pH, the aqueous solution will have surplus H_3O^+, which will donate H^+ to form H_2. This is considered here as acidic pathway for Hydrogen evolution reaction. Similarly, excess H^+ from the solution will be involved in nitrate reduction to form NH_3 and other products. The pathways for acidic reactions are as follows:

$$H^+ + e^- + * \rightarrow H^* \rightarrow \frac{1}{2} H_2 + * \qquad eq.\ 6.10$$

$$NO_3^- + 9H^+ + 8e^- \rightarrow NH_3 + 3\,H_2O \qquad E° = 0.88\,V\ vs\ RHE \qquad eq.\ 6.11$$

However, at high pH, H_2O becomes the biggest proton donor for hydrogen evolution reaction (by alkaline pathway) and hydration reactions:

$$H_2O + e^- + * \rightarrow H_2O^* + e^- \rightarrow H^* + OH^- \rightarrow \frac{1}{2} H_2 + OH^- + * \qquad eq.\ 6.12$$

$$NO_3^- + 6H_2O + 8e^- \rightarrow NH_3 + 9OH^- \qquad E° = 0.69\,V \quad vs.RHE \qquad eq.\ 6.13$$

6.3 Results and Discussion

6.3.1 Effect of pH and potential on NO_3^- reduction and HER

The NO_3^- adsorbs endothermically on Cu surface (+0.8 eV) at 0 pH, 0 V vs. RHE. The adsorption energy decreases by -0.1 eV/ (U V vs. RHE) (Figure 6.5). The adsorption energy also decreases as pH of the solution increases (E = E_0 - 0.13 × pH), where E_0 is adsorption energy at pH = 0. Therefore, the adsorption of NO_3^- is more exothermic at positive potential and high pH ranges.

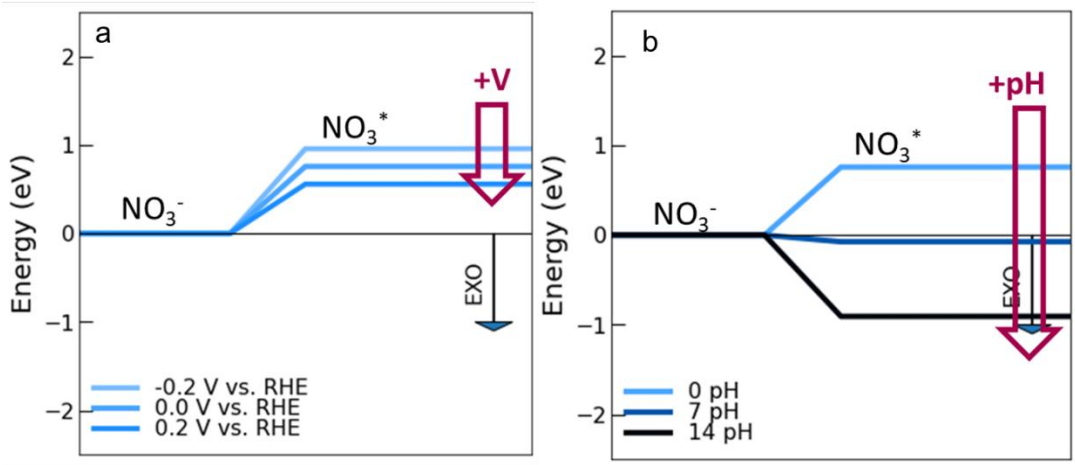

Figure 6.5: Adsorption of NO_3^- on Cu[111] surface as a function of (a) potential (V vs RHE) at pH = 0 (b) pH at 0V vs. RHE.

The activity of nitrate reduction depends upon adsorption of NO_3^- on the surface, competition from HER, dissociation energy required for first N-O bond scission (NO_3^* → NO_2^*). If NO_3^- does not adsorb exothermically or energy of HER pathway suppresses NO_3^- adsorption and dissociation, then the electrocatalyst will be a poor choice for nitrate reduction. The adsorption and dissociation NO_3^- on Ru and Cu surfaces is compared with

HER pathway at 0V vs. RHE and pH = 14 in Figure 6.6. NO_3^- adsorbs exothermically on both Cu and Ru surfaces. However, the adsorption is 0.75 eV more exothermic on Ru than Cu surface. The activation energy needed for first N-O bond scission is 0.2 eV higher than the energy required to desorb NO_3^* from the surface on Cu[111] surface. On Ru, NO_3^* desorption requires 0.55 eV higher energy than dissociation. Therefore, Ru is expected to have higher activity to reduce NO_3^- as compared to Cu surface. The H_2O adsorption is endothermic on Cu surface and requires no energy on Ru surface. Since H_2O is the main reactant for HER, competition from HER reaction is expected to be higher on Ru surface as compared to Cu surface. These results explain the high current density seen on Ru-nanoparticles as compared to Cu nanowire as in figure 6.1(a). The effect of pH on HER pathways vs. NO_3^- adsorption and dissociation on Ru-SAC are shown in Figure 6.6. HER via acidic pathway suppresses NO_3RR on Ru-SAC catalyst at 0 V vs. RHE and 0 pH. Similar results are seen on Cu and Ru surface. Increasing pH unfavorably affects the acidic HER pathway and hence makes the reaction endothermic. The nitrate adsorption, on the other hand, becomes exothermic as pH increases crossing over HER reaction pathway and becoming the dominant reaction of the cathode surface. The first step of HER alkaline pathway (H_2O adsorption) is not affected by pH or potential. In the following study, I only consider reaction occurring at high pH (pH = 14), as nitrate reduction dominates at high pH.

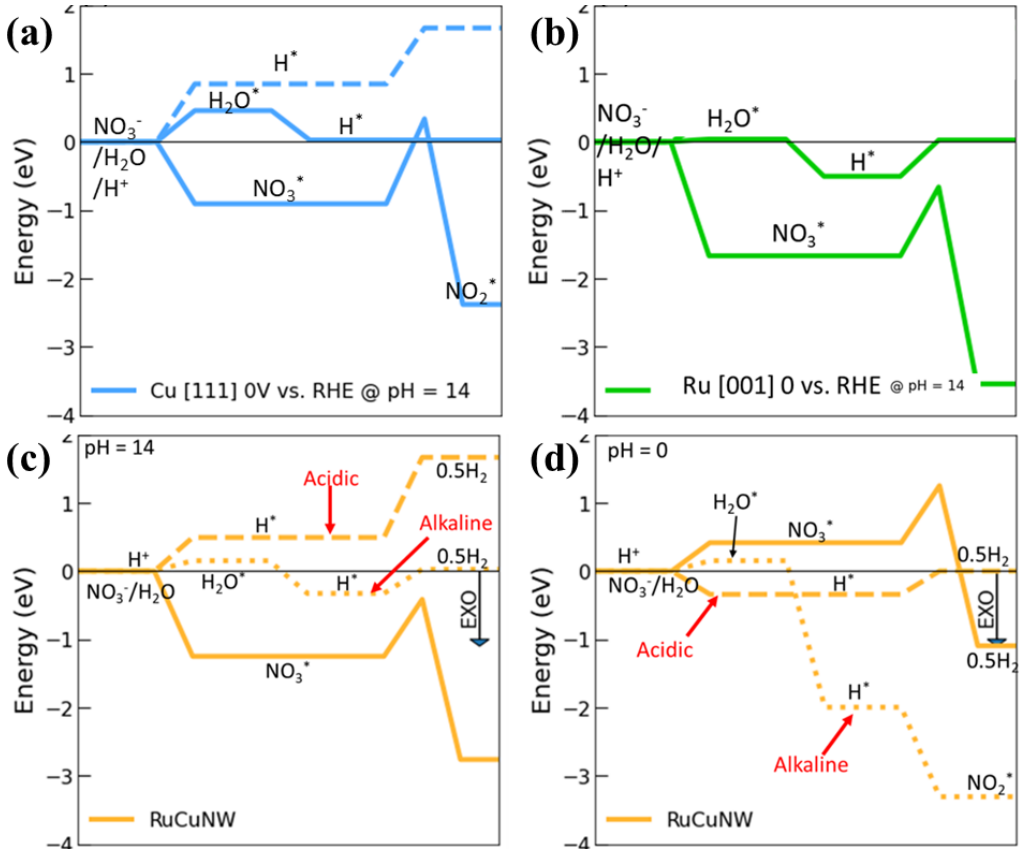

Figure 6.6: NO_3^- adsorption and reduction vs. HER on (a) Cu[111] and (b) Ru[001] via alkaline path at 0 V vs. RHE at pH =14. NO_3^- adsorption vs. HER on Ru-SAC via acidic and alkaline path at 0 V vs. RHE at (c) pH = 14 and (d) pH = 0.

6.3.2 Selectivity of Nitrate reduction on Cu[111], Ru[001] and Ru-SAC

I used DFT to calculate the minimum energy pathway NO_3RR as a function of potential (V vs. RHE) at pH = 14 to understand the factors contributing to the high selectivity over Ru-SAC compared to Cu and Ru single electrode surface. The NO_3RR reaction path on the electrode surface proceeds along the following path: (1) adsorption of NO_3^-, (2) deoxygenation of N-species, (3) hydrogenation on N-species and/or N-N bond formation and (4) desorption of reduced species. DFT calculations predict that NH_3 formation is the most favorable NO_3^- reaction pathway at the Ru site on Ru-SAC, because the activation barriers along the NH_3 path are much lower than the rate controlling barrier

for the other pathways (NO_2, NO, N_2O and N_2) (Figure 6.7). Ru-CuNW minimizes the HER as NO_3^- adsorption is 0.92 eV more favorable than H^+ adsorption at the Ru site and HER is unlikely to occur on the Cu sites due to endothermic adsorption (+0.09 eV) of H^+ on Cu sites, thus requiring very negative potentials for HER to occur (Figure 6.8). Although more negative potential increases the likelihood of NO_2^- desorption by reducing the desorption energy, the barrier for NO_2^- release remains higher than the NH_3 pathway until ~-0.9 V vs. RHE. The highly dispersed and isolated Ru active site additionally acts to restrict the NO_3RR to the Ru site due to high energy (0.39 eV) required for N^* to hop from Ru-Cu sites to Cu-Cu sites, thus minimizing N_2 formation with N atoms from other Ru sites. Overall, the combination of minimal HER, highly endothermic NO_2^- desorption and restricted movement of N^* species on the surface lead to high NH_3 selectivity for Ru-CuNW over a wide range of potentials.

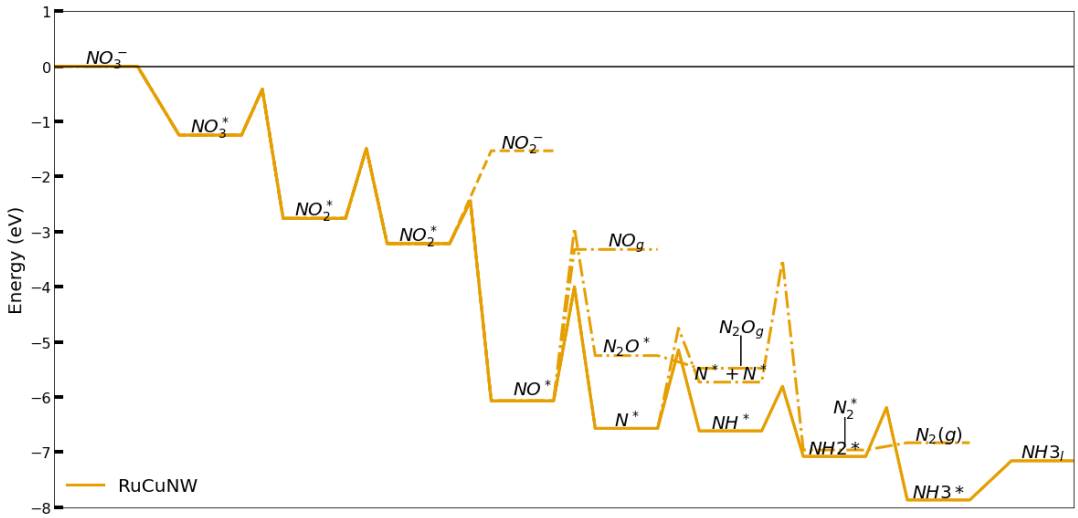

Figure 6.7: Energetics of NO_3^- reduction in NH_3, NO_2^-, NO, N_2O and N_2 on Ru-SAC at 0 V vs. RHE at pH = 14.

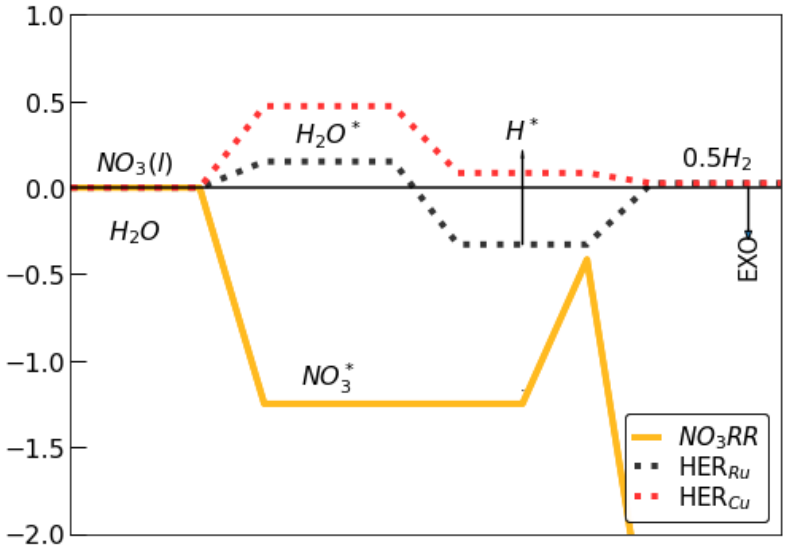

Figure 6.8: Nitrate adsorption vs. hydrogen evolution (via alkaline pathway) on Ru and Cu sites on Ru-CuNW at 0 V vs. RHE at pH = 14.

The poorer performance of CuNW compared to Ru-CuNW is attributed to the weaker adsorption of NO_3^-on the surface, poor ability to hydrogenate reduced N atoms, and the sensitivity of NH_3 versus NO_2^- path to the potential. First, the NO_3^- only weakly binds to the Cu surface and the activation barrier for decomposition to NO_2^* is ~0.02 eV higher than NO_3^- desorption at 0 V vs. RHE, thus it is expected that desorption is just as likely as further reaction (Figure 6.6). The NH_3 selectivity is highly sensitive to the slight changes in the relative stability of NO_2^--NO_2^*, NO_2^*-NO^*, and NO^*-N^* species caused by pH and potential reaction conditions (Figure 6.9) which contributes to the low selectivity at positive potentials. Moreover, H^* availability is very low because it is only available from H_2O reduction, and water adsorption is endothermic by 0.46 eV on CuNW, thus there is limited H^* for NH_3 formation. In addition to N^* hydrogenation, this also limits the HER for CuNW. These three obstacles indicate poor performance of CuNW for NH_3 production

and suggest that NO_2^- is the main expected product, which is in agreement with the experimental result.

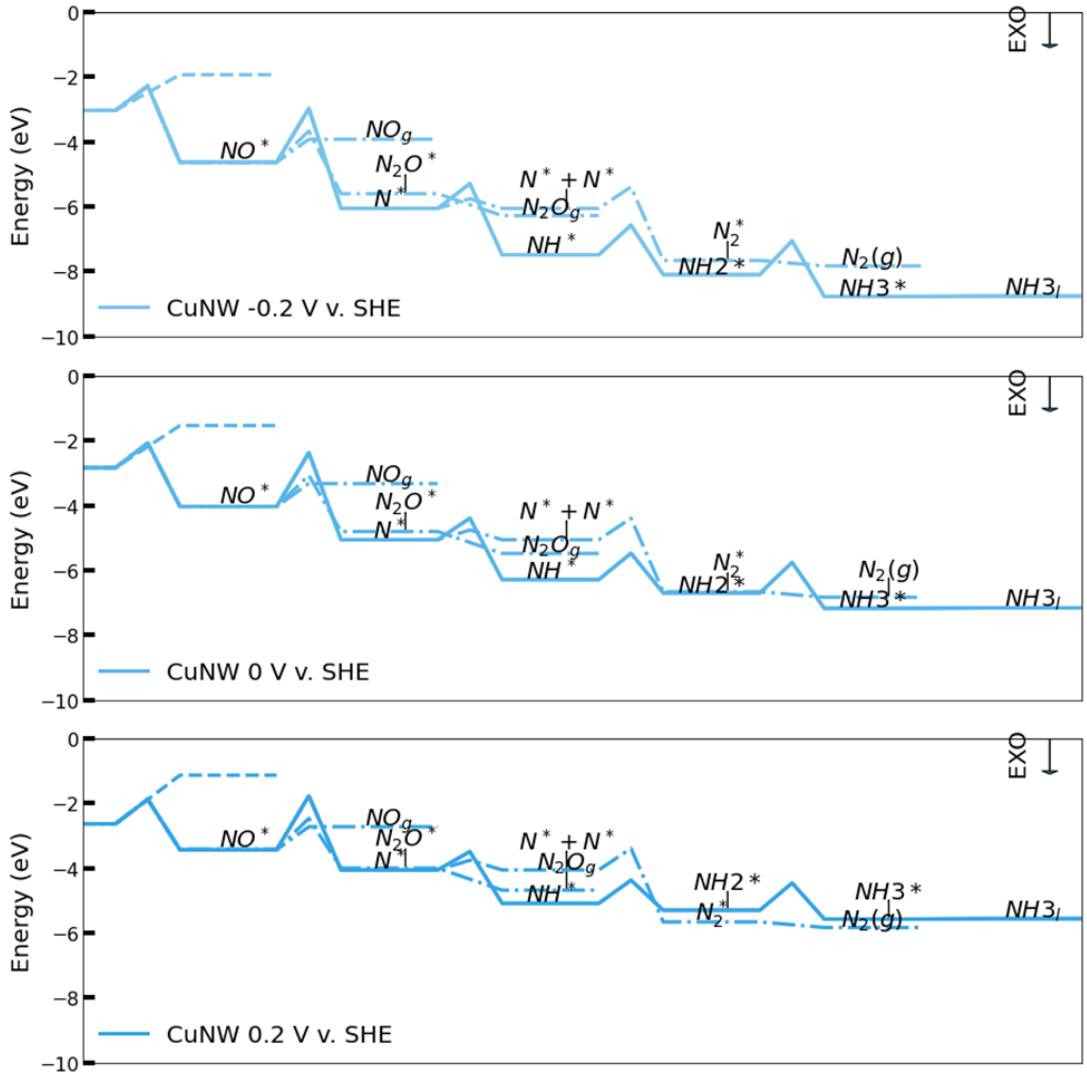

Figure 6.9: Energetics of NO_3^- reduction in NH_3, NO, N_2O and N_2 on Cu at pH = 14.

Unsurprisingly, the NO_3RR pathway on RuNP is similar to that on Ru-CuNW (Figure 6.10). However, there are higher number of active sites available for HER and lower energy requirements for the adsorption of H_2O molecule on RuNP as compared to Ru-CuNW (Fig. 6.6(d)), which increases the probability of H_2 formation and decreases NH_3 selectivity at negative potentials. Overall, RuNP is predicted to have lower NH_3 production at negative potential due to an increasing N^* hydrogenation activation barrier (Figure 6.11). In summary, these results explain why Ru-CuNW has a superior performance for NH_3 production via NO_3RR compared to CuNW and RuNP and highlight the importance of highly dispersed Ru in Cu matrix.

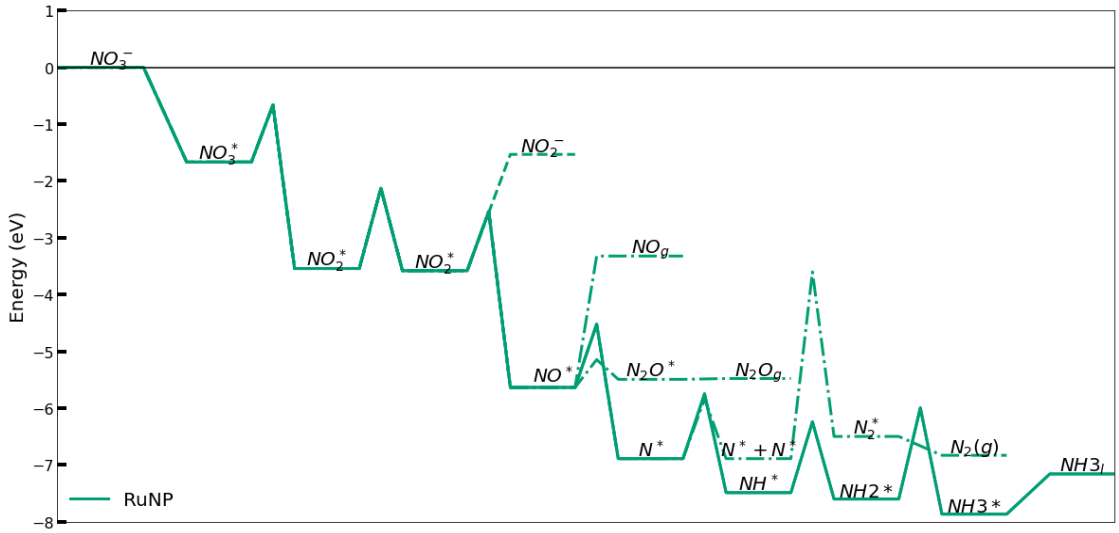

Figure 6.10: Energetics of NO_3^- reduction in NH_3, NO_2^-, NO, N_2O and N_2 on Ru at 0 V vs. RHE at pH = 14.

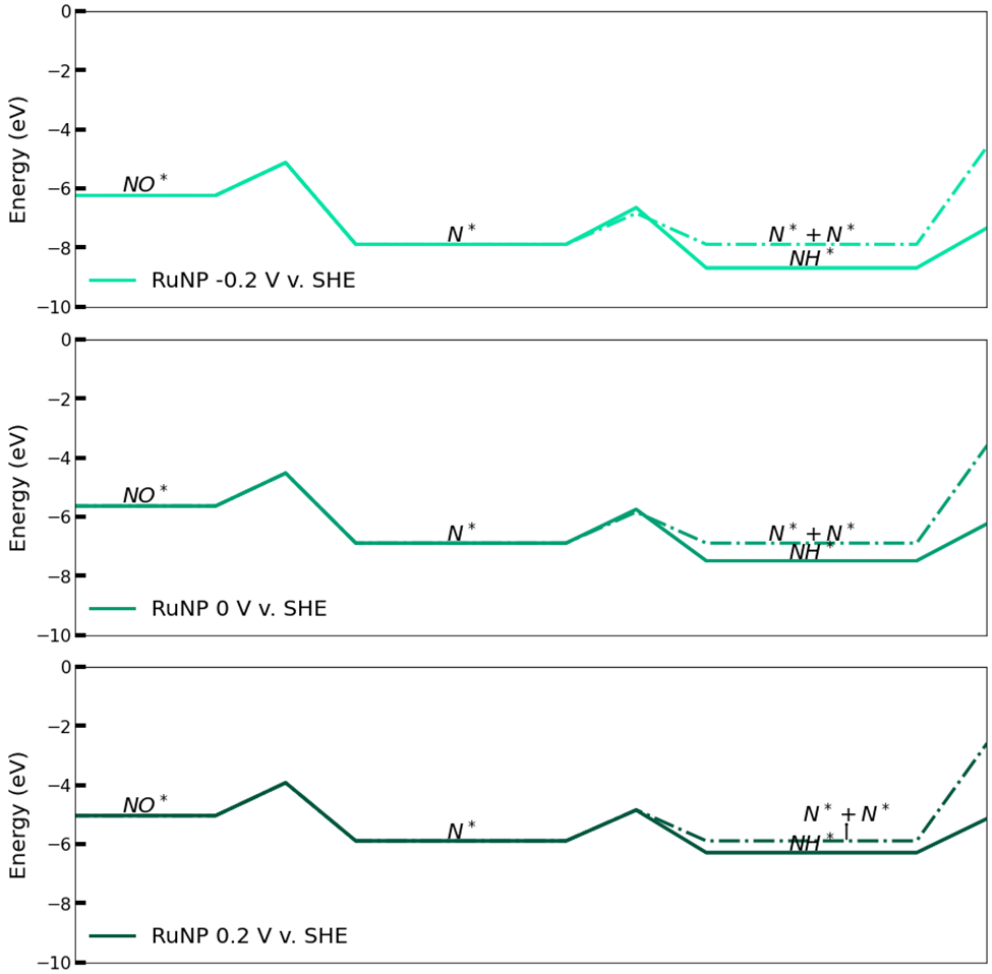

Figure 6.11: Energetics of N^* hopping *vs*. hydrogenation on RuNP at pH = 14.

6.4 Conclusion

In this work, I investigate electrocatalytic nitrate reduction mechanism on single metal electrode and single atom catalyst dispersed in metal matrix using DFT as a function of pH and potential. I found that pH has a stronger effect on the activity of nitrate reduction as increasing basicity of solution changes the HER pathway and proton donor. pH also controls the energy of adsorption and hydration steps of NO_3RR by controlling the concentration of H_3O^+ and H_2O ions in the solution. NO_3^- preferentially absorbs on the Cu, Ru and Ru-SAC surface as compared to H_2O at high pH. However, Ru is not the ideal catalyst because of the higher number of 'active' surface sites, which enables HER reaction. On Ru-SAC, Ru sites adsorb NO_3^- and Cu sites adsorb H_2O, which increases the selective reduction of NO_3^-, as Cu is poor electrode for HER reaction. The localization of nitrate species on Ru sites in Ru-SAC also preferentially favors selective reduction towards NH_3. On single metal surfaces, the potential has greater effect on selectivity of final product as it changes the activation barriers of nitrogen hydration steps.

6.5 References

1. Whiteman, L., Too Much of a Good Thing: Human Activities Overload Ecosystems with Nitrogen. The U.S. National Science Foundation: NSF news, 2010.
2. Michael F. Chislock, E. D., Rachel A. Zitomer, Alan E. Wilson, Eutrophication: Causes, Consequences, and Controls in Aquatic Ecosystems. Nature Education Knowledge 2013, 4 (4), 10.
3. Nitrate and Drinking Water from Private Wells. Centers for Disease Control and Prevention 2015.
4. Samatya, S.; Kabay, N.; Yüksel, Ü.; Arda, M.; Yüksel, M., Removal of nitrate from aqueous solution by nitrate selective ion exchange resins. Reactive and Functional Polymers 2006, 66 (11), 1206-1214.
5. Schoeman, J. J.; Steyn, A., Nitrate removal with reverse osmosis in a rural area in South Africa. Desalination 2003, 155 (1), 15-26.
6. Wang, Y.; Zhou, W.; Jia, R.; Yu, Y.; Zhang, B., Unveiling the Activity Origin of a Copper-based Electrocatalyst for Selective Nitrate Reduction to Ammonia. Angewandte Chemie International Edition 2020, 59 (13), 5350-5354.

7. Capdevila-Cortada, M., Electrifying the Haber–Bosch. Nature Catalysis 2019, 2 (12), 1055-1055.
8. Garcia-Segura, S.; Lanzarini-Lopes, M.; Hristovski, K.; Westerhoff, P., Electrocatalytic reduction of nitrate: Fundamentals to full-scale water treatment applications. Applied Catalysis B: Environmental 2018, 236, 546-568.
9. Pincus, L. N.; Rudel, H. E.; Petrović, P. V.; Gupta, S.; Westerhoff, P.; Muhich, C. L.; Zimmerman, J. B., Exploring the Mechanisms of Selectivity for Environmentally Significant Oxo-Anion Removal during Water Treatment: A Review of Common Competing Oxo-Anions and Tools for Quantifying Selective Adsorption. Environmental Science & Technology 2020, 54 (16), 9769-9790.
10. Wang, Z.; Richards, D.; Singh, N., Recent discoveries in the reaction mechanism of heterogeneous electrocatalytic nitrate reduction. Catalysis Science & Technology 2021, 11 (3), 705-725.
11. Liu, J.-X.; Richards, D.; Singh, N.; Goldsmith, B. R., Activity and Selectivity Trends in Electrocatalytic Nitrate Reduction on Transition Metals. ACS Catalysis 2019, 9 (8), 7052-7064.
12. Carvalho, O. Q.; Marks, R.; Nguyen, H. K. K.; Vitale-Sullivan, M. E.; Martinez, S. C.; Árnadóttir, L.; Stoerzinger, K. A., Role of Electronic Structure on Nitrate Reduction to Ammonium: A Periodic Journey. Journal of the American Chemical Society 2022, 144 (32), 14809-14818.
13. Speck, F. D.; Cherevko, S., Electrochemical copper dissolution: A benchmark for stable CO2 reduction on copper electrocatalysts. Electrochemistry Communications 2020, 115, 106739.
14. Paidar, M.; Roušar, I.; Bouzek, K., Electrochemical removal of nitrate ions in waste solutions after regeneration of ion exchange columns. Journal of Applied Electrochemistry 1999, 29 (5), 611-617.
15. Bae, S.-Y.; Mahmood, J.; Jeon, I.-Y.; Baek, J.-B., Recent advances in ruthenium-based electrocatalysts for the hydrogen evolution reaction. Nanoscale Horizons 2020, 5 (1), 43-56.
16. Gao, Q.; Pillai, H. S.; Huang, Y.; Liu, S.; Mu, Q.; Han, X.; Yan, Z.; Zhou, H.; He, Q.; Xin, H.; Zhu, H., Breaking adsorption-energy scaling limitations of electrocatalytic nitrate reduction on intermetallic CuPd nanocubes by machine-learned insights. Nature Communications 2022, 13 (1), 2338.
17. Wang, Y.; Xu, A.; Wang, Z.; Huang, L.; Li, J.; Li, F.; Wicks, J.; Luo, M.; Nam, D.-H.; Tan, C.-S.; Ding, Y.; Wu, J.; Lum, Y.; Dinh, C.-T.; Sinton, D.; Zheng, G.; Sargent, E. H., Enhanced Nitrate-to-Ammonia Activity on Copper–Nickel Alloys via Tuning of Intermediate Adsorption. Journal of the American Chemical Society 2020, 142 (12), 5702-5708.
18. Wang, C.; Liu, Z.; Hu, T.; Li, J.; Dong, L.; Du, F.; Li, C.; Guo, C., Metasequoia-like Nanocrystal of Iron-Doped Copper for Efficient Electrocatalytic Nitrate Reduction into Ammonia in Neutral Media. ChemSusChem 2021, 14 (8), 1825-1829.
19. Yao, F.; Jia, M.; Yang, Q.; Chen, F.; Zhong, Y.; Chen, S.; He, L.; Pi, Z.; Hou, K.; Wang, D.; Li, X., Highly selective electrochemical nitrate reduction using copper phosphide self-supported copper foam electrode: Performance, mechanism, and application. Water Research 2021, 193, 116881.

20. Wang, Z.; Ortiz, E. M.; Goldsmith, B. R.; Singh, N., Comparing electrocatalytic and thermocatalytic conversion of nitrate on platinum–ruthenium alloys. Catalysis Science & Technology 2021, 11 (21), 7098-7109.
21. Chen, F.-Y.; Wu, Z.-Y.; Gupta, S.; Rivera, D. J.; Lambeets, S. V.; Pecaut, S.; Kim, J. Y. T.; Zhu, P.; Finfrock, Y. Z.; Meira, D. M.; King, G.; Gao, G.; Xu, W.; Cullen, D. A.; Zhou, H.; Han, Y.; Perea, D. E.; Muhich, C. L.; Wang, H., Efficient conversion of low-concentration nitrate sources into ammonia on a Ru-dispersed Cu nanowire electrocatalyst. Nature Nanotechnology 2022, 17 (7), 759-767.
22. Kresse, G.; Furthmuller, J., Efficient iterative schemes for ab initio total-energy calculations using a plane-wave basis set. Phys Rev B 1996, 54 (16), 11169-11186.
23. Kresse, G.; Furthmüller, J., Efficiency of ab-initio total energy calculations for metals and semiconductors using a plane-wave basis set. Computational Materials Science 1996, 6 (1), 15-50.
24. Perdew, J. P.; Burke, K.; Ernzerhof, M., Generalized Gradient Approximation Made Simple. Phys. Rev. Lett. 1996, 77 (18), 3865-3868.
25. Kresse, G.; Joubert, D., From ultrasoft pseudopotentials to the projector augmented-wave method. Physical Review B 1999, 59 (3), 1758-1775.
26. Tran, R.; Xu, Z.; Radhakrishnan, B.; Winston, D.; Sun, W.; Persson, K. A.; Ong, S. P., Surface energies of elemental crystals. Scientific Data 2016, 3 (1), 160080.
27. Henkelman, G.; Uberuaga, B. P.; Jónsson, H., A climbing image nudged elastic band method for finding saddle points and minimum energy paths. The Journal of Chemical Physics 2000, 113 (22), 9901-9904.
28. Nørskov, J. K.; Rossmeisl, J.; Logadottir, A.; Lindqvist, L.; Kitchin, J. R.; Bligaard, T.; Jónsson, H., Origin of the Overpotential for Oxygen Reduction at a Fuel-Cell Cathode. The Journal of Physical Chemistry B 2004, 108 (46), 17886-17892.
29. Allison, T. C., NIST-JANAF Thermochemical Tables - SRD 13. National Institute of Standards and Technology 2013.
30. Lide, D. R., CRC handbook of chemistry and physics. CRC press: 2004; Vol. 85.
31. Levanov, A. V.; Isaikina, O. Y.; Lunin, V. V., Dissociation constant of nitric acid. Russ. J. Phys. Chem. A 2017, 91 (7), 1221-1228.

CHAPTER 7

ELECTROCHEMICAL VS. THERMOCHEMICAL NITRATE REDUCTION ON PD SINGLE ATOM SUBSTITUTED IN CU METAL

7.1 Introduction

Nitrate removal is important step is water remediation process due to high toxicity of nitrate to aquatic and terrestrial biodiversity.[1] Current technologies used in water treatment plants like ion-exchange and reverse-osmosis remove nitrate from drinking water by forming a secondary stream of concentrated wastewater.[1-5] The disposal of the waste stream is cumbersome and requires huge financial input to dispose.[2] Therefore, alternative nitrate remediation method to reduce nitrate into benign N_2 is currently explored as they do not form waste stream and help in maintaining a sustainable N-cycle present in nature.

Nitrate reduction reaction (NRR) on a metal catalyst surface is gaining interest as a water remediation method to remove nitrate from drinking water.[6] NRR reaction reduces NO_3^- into other nitrogen species like N_2, NH_3, NO_2^- and NO on the catalytic surface, depending upon the base metal and environmental conditions.[7,8] Palladium (Pd) metal has been heavily investigated for their efficiency as NRR catalysts as it forms N_2 as most selective product.[9] However, the first NO bond scission from NO_3 to NO_2 is rate limiting step on Pd surface.[9] Moreover, Pd is an expensive platinoid metal which cannot be used for developing a cost-effective water treatment process.[10] Cu, on the other hand, is inexpensive coinage metal that readily reduces NO_3^- on the surface in neutral and basic pH conditions.[11-13] However, the NRR on Cu surface is more selective towards equally toxic NO_2^- or HNOH products that need to be further removed from the drinking water.[10] Bimetallic Pd-Cu catalysts have shown to decrease reduction time of NO_3^- and increase the

N_2 selectivity of the surface.[14] However, they still use high percentages of Pd which is not suitable for water remediation process.

Nitrate reduction reactions requires a hydrogen source to remove the build of dissociated species from reduction steps (O^*) from the surface and improve the cyclability of the catalyst.[9] Moreover, hydrogen species combine with N-species to form meta-stable states with lower activation barriers. Thermochemical nitrate reduction (T-NRR) uses H_2 gas generated using H_2O gas splitting to provide hydrogen source required for NRR.[15] Whereas electrochemical nitrate reduction (E-NRR) uses direct electricity to split water or use protons in solutions are hydrogen source and provide electrons.[10] While both the reduction methods are studied in details, there are very few studies that compare the nitrate reduction activity on both T-NRR and E-NRR. In 2021, Wang et.al., experimentally evaluated T-NRR and E-NRR on Pd-Ru alloy nanoparticles.[15] They discovered similar activity and selectivity trends nitrate reduction as function of hydrogen and nitrate adsorption energies.[15] However, the pH of the reaction differentiated the reduction rate of the two processes.[15]

In recent study, my collaborators, Wu, Nazemi et. al. (2023) et. al., synthesized Pd single atom alloy in Cu surface (Pd-SAA) among a series of Pd-Cu bimetallic alloys and evaluated their performance for both T-NRR and E-NRR.[16] They found that the activity and selectivity for E-NRR was higher for nitrate reduction as compared to T-NRR. However, some experimental differences occur while performing T-NRR and E-NRR like pH, H_2 flow rate for T-NRR and potential of E-NRR makes it difficult to compare the two processes. Therefore, here I evaluate the mechanistic differences between T-NRR and E-NRR on Pd-SAA in Cu surface using density functional theory. First, I develop a method

of compare the H_2 flow rate in T-NRR with potential effects in E-NRR to have same energy scale for the two processes. This is used to plot reaction plots at the experimental conditions to investigate why E-NRR performs than T-NRR on Pd-SAA.

7.2 Density functional theory calculations.

Periodic boundary condition density functional theory (DFT) calculations were performed using the Perdew-Burke-Ernzerhof (PBE) functional, as implemented in the Vienna Ab initio Simulation Package (VASP).[17-19] The wave function was constructed from a summation of plane waves with energies up to 500 eV. Projector-augmented wave (PAW) pseudopotentials[20] explicitly included the H 1s, O and N 2s 2p, Cu 4s 3d, and Pd 5s 4d electrons. Cu nanoparticles were represented by a (111) terminated slab consisting of 4×4×5 primitive units. This surface termination was chosen, since it is the low-energy surface.[21] For representing Pd/Cu(1:100) particles, one surface Cu atom was substituted with Pd atom from Cu (111) slab. The slabs were separated by at least 12 Å of vacuum space to reduce spurious interactions between atomic layers. The Brillouin zone was sampled with an 8×8×1 Γ-point centered Monkhorst-Pack mesh for each surface. All geometries were relaxed until forces were less than 0.001 eV/Å. Transition states for surface reactions were calculated using the nudged elastic band (NEB)[22] method with five images per reaction. Geometric structure representations were generated using VESTA.[23]

I calculate the nitrate reduction in water using the proton coupled electron transfer (PCET) method, where the substrate reacts with H_2O/H^+ as well as an electron for both T-NRR and E-NRR. I used the PCET method because it dominates the hydrogenation pathway on metal clusters in the presence of protic solvents over direct hydrogenation,

where adsorbed H atoms react to form products.[24] The computational Hydrogen electrode (CHE) (Eq. 7.1) and Butler-Volmer formalism (Eq. 7.2) were used to account for potential effects on reaction energies and activation barriers, respectively:

$$G(U) = G(U^{\circ}) - n_e\,(U - U^{\circ}) \qquad eq.7.1$$

$$G(U) = G(U^{\circ}) - \alpha\, n_e\,(U - U^{\circ}) \qquad eq.7.2$$

where $G(U^{\circ})$ is the free energy at 0 V vs. SHE, U is the applied voltage, n_e is number of electrons transferred times charge of the electron. α in Eq. S7.2 is the portion of electrons transferred at the transition state, taken to be 0.5.

For T-NRR, I calculate the local potential near metal surface by inducing the so-called Open circuit potential (OCP); which is found using Nernst equation:

$$U = U^{\circ} + \frac{RT}{F}\ln\left(\frac{[H^{+}]}{P_{H_2}^{0.5}}\right) \qquad eq.7.3$$

where R, T and F are ideal gas constant, Temperate and Faradic constant, respectively. U° is the standard hydrogen electrode potential. $[H^{+}]$ and P_{H2} are the concentration of protons and pressure of H_2 gas during the reaction process. I use thermodynamic cycles to calculate the adsorption and desorption of charged species (NO_3^{-}, NO_2^{-}, OH^{-}), which include the entropic energies and solvation energies. Protonation energies in the thermodynamic cycles are modified using Eq. S11 to include the pH effects on the reactions:

$$\Delta G_{protonation} = G^{\circ} - 2.303kT(pK_a - pH) \qquad eq.7.4$$

Since pH also affects the major proton donor in the system, I have considered both H_3O^+ and H_2O as the proton source for T-NRR (pH =6) and E-NRR (pH =13) for the acidic and alkaline reaction pathways (Eq. S12 & S13):

$$H_3O^+ + X^* + e^- \rightarrow XH^* + H_2O \qquad (acidic\ path) \qquad eq.7.5$$

$$H_2O + X^* + e^- \rightarrow XH^* + OH^- \qquad (alkaline\ path) \qquad eq.7.6$$

For reactions (M-X → M + X) that do not involve proton transfer the reaction energies are calculated using eq:

$$E_{rec} = E_M + E_X - \left(E_{M-X} - E_{surface}\right) \qquad eq.7.7$$

And the activation energy is calculated using nudged elastic band (NEB) method with five images per reaction. The energy of most endothermic image is used to calculate activation barrier:

$$E_{act\ Energy} = \max(E_{M--X}) - E_{M-X} \qquad eq.7.8$$

7.3 Results

I performed DFT calculations to understand the reason behind the improved nitrate reduction activity and N_2 selectivity of $Pd/Cu_{(1:100)}$ SAA when switching from T-NRR to E-NRR. DFT predicts that NO_3^- adsorption is equally favorable on Pd_1 sites and on Cu NP sites of $Pd/Cu_{(1:100)}$. After adsorption to Pd_1 sites, NO_3^* (* denotes the adsorbed species) dissociates into NO_2^* then NO^* with activation barriers of 0.65 eV and 0.71 eV, respectively. After screening multiple competitive pathways, including H-assisted and non-H assisted deoxygenation, I found that under E-NRR, H-assisted NO deoxygenation is preferred and occurs by hydrogenation of NO^* to HNO^* followed by subsequent cleavage

of HNO^* to N^* and OH^-. After N^* forms, it preferentially migrates from the Pd_1 sites to the surrounding Cu NP matrix, where it either reacts with another N^* to form N_2 or with H to form NH^* and then follows the NH_3 pathway. The reaction map and main N reaction pathways for both T-NRR and E-NRR are shown in Figure 7.1.

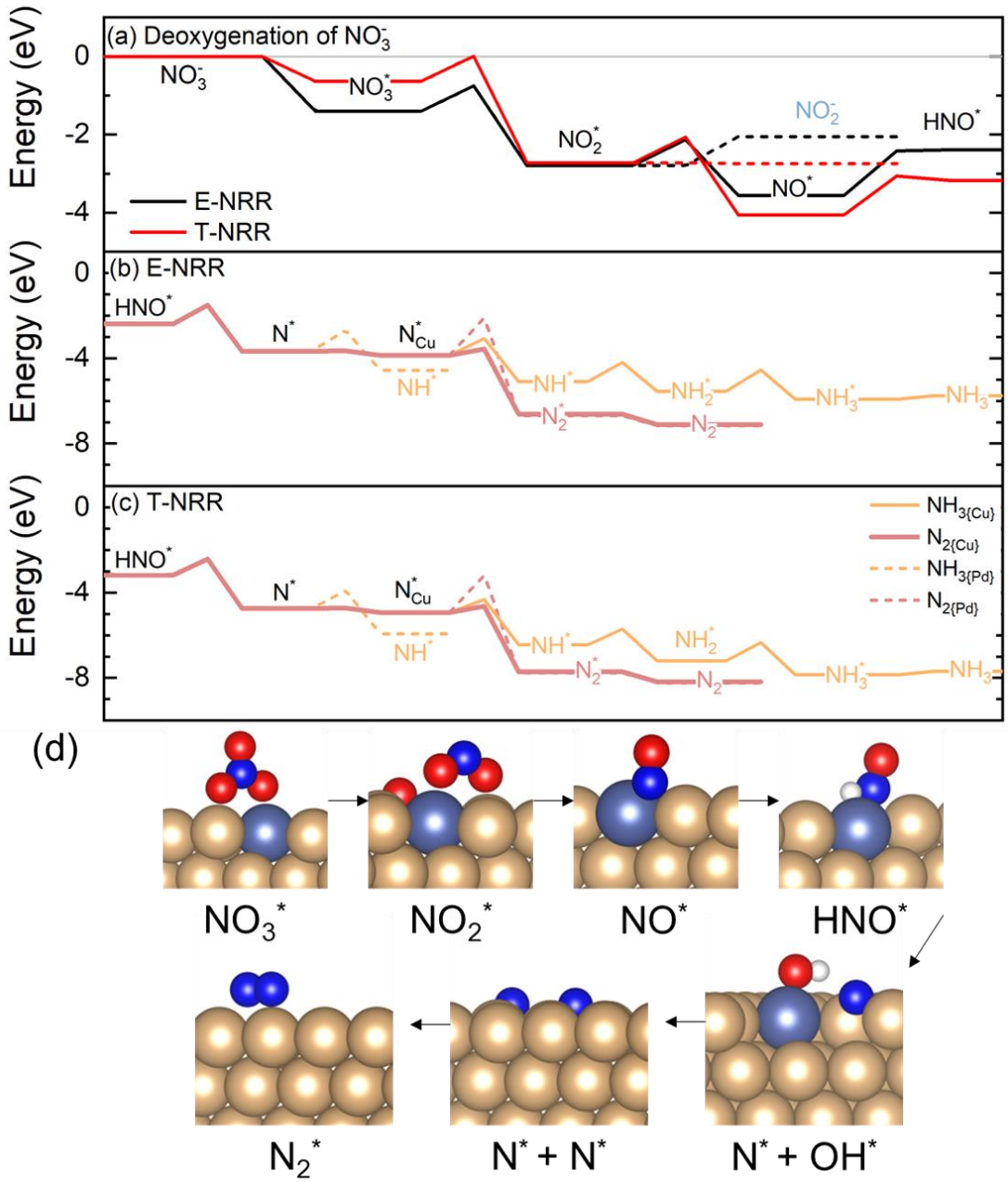

Figure 7.1. DFT calculations of (a) adsorption and deoxygenation of NO_3^- ($NO_3^- \rightarrow NO_3^*$, $NO_3^* \rightarrow NO_2^*$, $NO_2^* \rightarrow NO^*$, $NO^* \rightarrow HNO^*$) for T-NRR (red) and E-NRR (black) on the Pd_1 site of $Pd/Cu_{(1:100)}$ SAA. (b) HNO^* reduction on Pd_1 and Cu NP sites to N_2 and NH_3 for E-NRR at pH = 13 using H_2O as proton source. (b) HNO^* reduction on Pd_1 and Cu NP sites to N_2 and NH_3 for T-NRR at pH = 6 using H_3O^+ as proton source. (d) Meta-stable points along the minimum energy path for NO_3^- reduction to N_2. White, blue, red, golden, and blue-gray spheres correspond to H, N, O, Cu, and Pd atoms, respectively.

T-NRR and E-NRR operate under different pH with distinct proton sources (*i.e.*, H_2O or H_3O^+), which affects the activity and selectivity of NRR. DFT calculations demonstrate that the higher NO_3^- reduction activity of $Pd/Cu_{(1:100)}$ in E-NRR over T-NRR arises from higher NO_3^* stabilization (Figure 7.1a). Under E-NRR, the pH in the near surface region rises rapidly to pH 13, which increases the free energy of the dissolved NO_3^- by ~0.74 eV from the free energy at pH 6 of the T-NRR condition, and consequently stabilizes the adsorbed nitrate species. The increased stability of adsorbed NO_3^* and favorability of reaction under E-NRR condition means that NO_3^* dissociation (0.65 eV) is ~ 5.66×10^{12} times more likely than desorption (1.4 eV), and further surface reaction of the N species is favorable. Conversely, under T-NRR, NO_3^* desorption and dissociation are equally likely, with reaction energies of 0.66 eV and 0.65 eV, respectively. Thus, the adsorbed nitrate is just as possible to desorb into the solution as it is to dissociate under T-NRR conditions, hindering reaction progress.

DFT calculations also predict the higher N_2 selectivity of E-NRR *vs.* T-NRR for $Pd/Cu_{(1:100)}$ is because of lower NO_2^- desorption rates and lower N_2 barriers as compared to the NH_3 path (Figure 7.1b,c). Under E-NRR conditions, NO_2^- desorption and NO_2^* deoxygenation have roughly equivalent barriers (0.74 eV), which indicates equivalent reaction progression along each path. However, because the NO^* dissociation products are

highly stabilized compared to the desorbed NO_2^-, and because the barriers are essentially equivalent, the dissociated product is the more likely result over time. The preference for NO^* arises because desorbed NO_2^- could rapidly reabsorb without barrier and then decompose. Conversely, the acidic pH conditions of T-NRR stabilizes the desorption of NO_2^- by 0.12 eV/pH, making NO_2^- desorption slightly exothermic (-0.02 eV) at pH = 6, and likely than overcoming the 0.71 eV barrier for NO_2^* dissociation.

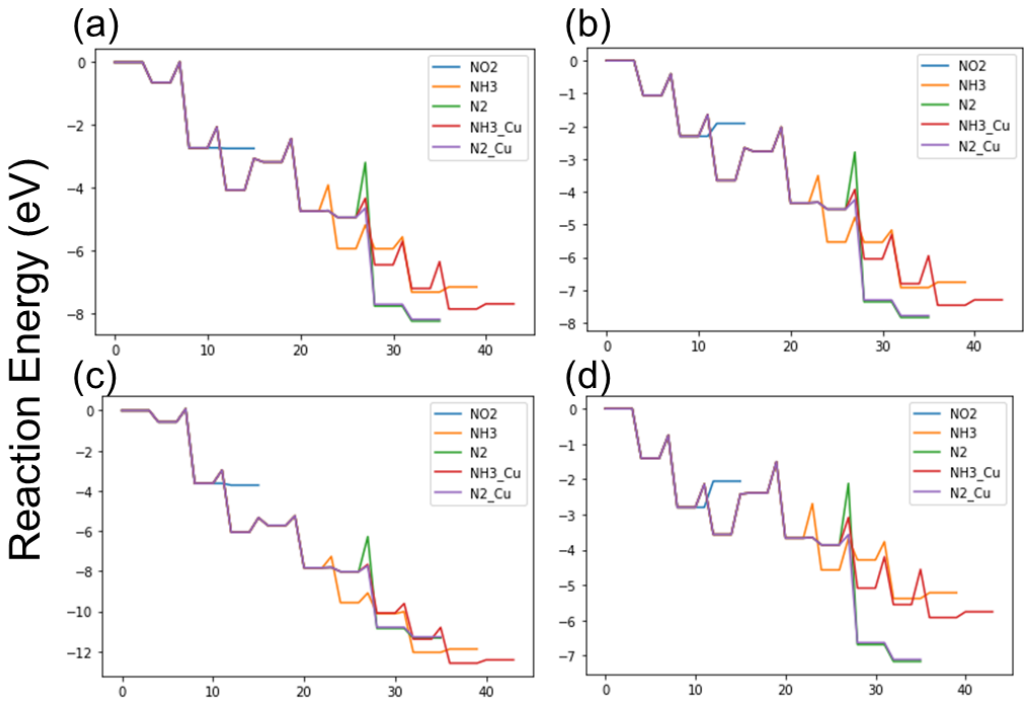

Figure 7.2. T-NRR on $Pd/Cu_{(1:100)}$ SAA: (a) at pH = 6 using H_3O^+ as proton donor; (b) at pH = 13 using H_3O^+ as proton donor. E-NRR on $Pd/Cu_{(1:100)}$ SAA: (c) at pH = 6 using H_2O as proton donor; (d) at pH = 13 using H_2O as proton donor. (conditions).

Moreover, the slightly acidic nature of the T-NRR pathway further reduces its selectivity to N_2 compared with alkaline E-NRR (Figure 7.2). Under both conditions, the reduced N^* hops preferentially to Cu sites (barrier of 0.02 eV) rather than remaining fixed

on the Pd and undergoing hydrogenation (barriers of 0.98 eV for E-NRR and 0.83 eV for T-NRR); taken with the entropic preference for delocalization the N-N and N-H reactions are expected to occur on Cu sites (Figure 7.1d). On the Cu sites, the N^*-N^* recombination has a 0.29 eV barrier which is 0.49 eV lower than hydrogenation for E-NRR; thus, DFT suggests a selective production of N_2 gas, in agreement with the experimental results. Moreover, the availability of H atoms from H_2 and H_3O^+, through decoupled electron/proton transfer, results in low activation barriers of hydrogenation steps under T-NRR by 0.29 eV (NH^* (0.60 eV), NH_2^* (0.74 eV), NH_3^* (0.85 eV) formation). Conversely, under E-NRR, only H_2O is available as the proton source, which provides fewer H atoms and increases the activation barrier of hydrogenation steps (NH^* (0.78 eV), NH_2^* (0.89 eV), NH_3^* (1.00 eV) formation). Overall, the higher pH, and H_2O as the only proton source contribute to the higher selectively towards N_2 of $Pd/Cu_{(1:100)}$ in E-NRR than in T-NRR.

7.4 Conclusion

In this chapter I investigated the thermochemical vs. electrochemical nitrate reduction reaction on Pd single atom alloy substituted in Cu surface. I used the equivalent near surface potential in thermochemical nitrate reduction using Open circuit potential Nernst equation, which is affected by H_2 pressure. I found that the activity and selectivity of the nitrate reduction depends upon the pH and potential of the surface rather than the electrochemical vs. thermochemical reduction pathway. During the electrochemical nitrate reduction, there is an increase in the pH of the solution as H_2O or H_3O^+ assistants nitrate reduction by donating a proton and forming OH^-. In thermochemical nitrate reduction, the OH^- formed continuous gets rebalanced by continuous pumping of H_2 gas.

I found that Pd single atom in Cu surfaces decreases the activation barrier for second NO bond scission, which improves the activity of nitrate reduction. Moreover, near Pd single atom, the NO^* hydrogenates and forms HNO^* and then N^* species which preferentially hops to Cu surface and combines with second N^* to form N_2. The electrochemical activity is higher on single atom catalysts due to high pH, which makes the NO_3^- adsorption more exothermic, and hence more likely to dissociate. In thermochemical nitrate reduction, where the pH is around 7, the nitrate reduction energy is same as nitrate dissociation energy and hence NRR has slow activity. Moreover, the NO_2^- desorption is strongly favored over dissociation at neutral pH. Therefore, higher activity can be achieved by fine tuning pH and potential of the reaction, irrespective of the reduction reaction set-up (thermochemical vs. electrochemical).

7.5 References

1. Huno, S. K. M.; Rene, E. R.; van Hullebusch, E. D.; Annachhatre, A. P., Nitrate removal from groundwater: a review of natural and engineered processes. Journal of Water Supply: Research and Technology-Aqua 2018, 67 (8), 885-902.
2. Ashok, V.; Hait, S., Remediation of nitrate-contaminated water by solid-phase denitrification process—a review. Environmental Science and Pollution Research 2015, 22 (11), 8075-8093.
3. Bishayee, B.; Chatterjee, R. P.; Ruj, B.; Chakrabortty, S.; Nayak, J., Strategic management of nitrate pollution from contaminated water using viable adsorbents: An economic assessment-based review with possible policy suggestions. Journal of Environmental Management 2022, 303, 114081.
4. Fewtrell, L., Drinking-Water Nitrate, Methemoglobinemia, and Global Burden of Disease: A Discussion. Environmental Health Perspectives 2004, 112 (14), 1371-1374.
5. Kapoor, A.; Viraraghavan, T., Nitrate Removal From Drinking Water—Review. Journal of Environmental Engineering 1997, 123 (4), 371-380.
6. Katsounaros, I.; Ipsakis, D.; Polatides, C.; Kyriacou, G., Efficient electrochemical reduction of nitrate to nitrogen on tin cathode at very high cathodic potentials. Electrochimica Acta 2006, 52 (3), 1329-1338.
7. Liu, J.-X.; Richards, D.; Singh, N.; Goldsmith, B. R., Activity and Selectivity Trends in Electrocatalytic Nitrate Reduction on Transition Metals. ACS Catalysis 2019, 9 (8), 7052-7064.

8. Min, B.; Gao, Q.; Yan, Z.; Han, X.; Hosmer, K.; Campbell, A.; Zhu, H., Powering the Remediation of the Nitrogen Cycle: Progress and Perspectives of Electrochemical Nitrate Reduction. Industrial & Engineering Chemistry Research 2021, 60 (41), 14635-14650.
9. Shin, H.; Jung, S.; Bae, S.; Lee, W.; Kim, H., Nitrite Reduction Mechanism on a Pd Surface. Environmental Science & Technology 2014, 48 (21), 12768-12774.
10. Wang, Z.; Richards, D.; Singh, N., Recent discoveries in the reaction mechanism of heterogeneous electrocatalytic nitrate reduction. Catalysis Science & Technology 2021, 11 (3), 705-725.
11. Hu, T.; Wang, C.; Wang, M.; Li, C. M.; Guo, C., Theoretical Insights into Superior Nitrate Reduction to Ammonia Performance of Copper Catalysts. ACS Catalysis 2021, 11 (23), 14417-14427.
12. Pérez-Gallent, E.; Figueiredo, M. C.; Katsounaros, I.; Koper, M. T. M., Electrocatalytic reduction of Nitrate on Copper single crystals in acidic and alkaline solutions. Electrochimica Acta 2017, 227, 77-84.
13. Wang, Y.; Qin, X.; Shao, M., First-principles mechanistic study on nitrate reduction reactions on copper surfaces: Effects of crystal facets and pH. Journal of Catalysis 2021, 400, 62-70.
14. Gao, Q.; Pillai, H. S.; Huang, Y.; Liu, S.; Mu, Q.; Han, X.; Yan, Z.; Zhou, H.; He, Q.; Xin, H.; Zhu, H., Breaking adsorption-energy scaling limitations of electrocatalytic nitrate reduction on intermetallic CuPd nanocubes by machine-learned insights. Nature Communications 2022, 13 (1), 2338.
15. Wang, Z.; Ortiz, E. M.; Goldsmith, B. R.; Singh, N., Comparing electrocatalytic and thermocatalytic conversion of nitrate on platinum–ruthenium alloys. Catalysis Science & Technology 2021, 11 (21), 7098-7109.
16. Xuanhao Wu, M. N., Srishti Gupta, Adam Chismar, Kiheon Hong, Hunter Jacobs, Wenqing Zhang, Kali Rigby, Tayler Hedtke, Qingxiao Wang, Eli Stavitski, Michael S. Wong, Christopher Muhich, and Jae-Hong Kim, Contrasting Capability of Single Atom Palladium for Thermocatalytic versus Electrocatalytic Nitrate Reduction Reaction. (unpublished).
17. Kresse, G.; Furthmüller, J., Efficient iterative schemes for ab initio total-energy calculations using a plane-wave basis set. Physical Review B 1996, 54 (16), 11169.
18. Kresse, G.; Furthmüller, J., Efficiency of ab-initio total energy calculations for metals and semiconductors using a plane-wave basis set. Computational Materials Science 1996, 6 (1), 15-50.
19. Perdew, J. P.; Burke, K.; Ernzerhof, M., Generalized gradient approximation made simple. Phys Rev Lett 1996, 77 (18), 3865-3868.
20. Kresse, G.; Joubert, D., From ultrasoft pseudopotentials to the projector augmented-wave method. Physical Review B 1999, 59 (3), 1758-1775.
21. Tran, R.; Xu, Z.; Radhakrishnan, B.; Winston, D.; Sun, W.; Persson, K. A.; Ong, S. P., Surface energies of elemental crystals. Scientific Data 2016, 3 (1), 160080.
22. Henkelman, G.; Jónsson, H., Improved tangent estimate in the nudged elastic band method for finding minimum energy paths and saddle points. The Journal of Chemical Physics 2000, 113 (22), 9978-9985.

23. Momma, K.; Izumi, F., VESTA 3 for three-dimensional visualization of crystal, volumetric and morphology data. Journal of applied crystallography 2011, 44 (6), 1272-1276.
24. Weinberg, D. R.; Gagliardi, C. J.; Hull, J. F.; Murphy, C. F.; Kent, C. A.; Westlake, B. C.; Paul, A.; Ess, D. H.; McCafferty, D. G.; Meyer, T. J., Proton-Coupled Electron Transfer. Chemical Reviews 2012, 112 (7), 4016-4093.

CHAPTER 8

ROLE OF SINGLE ATOM ON ACTIVITY AND SELECTIVITY OF ELECTROCHEMICAL NITRATE REDUCTION IN CU [111] SURFACE

8.1 Introduction

Anthropogenic activities including excessive fertilizer use, refuse dumps, animal feedlots, and septic tanks have disturbed the natural N-cycle and increased the concentration of nitrate in ground and water sources.[1,2] This excess nitrate causes so-called "dead zones" in aquatic ecosystems,[3] and renders the water undrinkable for humans and animals. For example, consumption of water with nitrate concentrations above 10 mg of N/ L is linked to methemologlobinemia, or "blue baby syndrome", thyroid disease, fatigue, weight gain, hair loss, goiters and colon cancer,[4-6]. Therefore, nitrate remediation is a necessary to improve ecosystem and human health.[7]

Nitrate remediation methods include adsorption, reduction through biological processes, ion exchange, membrane separations including reverse osmosis, and electrochemical nitrate reduction (NRR).[8-12] Electrochemical Nitrate reduction (NRR) is a particularly attractive remediation technology as it reduces nitrate (NO_3^-) to commercially useful (NH_3) or benign (N_2).[13,14] Moreover, it only requires electricity to operate, eliminating the need for chemical input or regular exchange of ion resins, adsorbents, or membranes and produces no biological waste.

Successful implementation of NRR depends on the development of a cost-effective electrocatalyst which is selective both to nitrate reduction, and the desired product, i.e., N_2 or NH_3, with no formation of more toxic NO_x species such as NO_2^-. Single metal electrocatalysts have been well studied for their NRR efficiency. The platinoid metals, Rh,

Ru, selectively reduce nitrate to NH_3 in acidic solutions. Pd selectively reduces NO_2^- to N_2 while Pt mainly forms NO and NH_3.[15,16] However, they are highly active towards the parasitic Hydrogen Evolution Reaction (HER), and thus result in low faradaic efficiencies at the low concentration of NO_3^{2-} (50-2000 ppm) in wastewater, are very expensive.[17-19] Conversely, Cu is relatively low cost and has the highest selectivity for nitrate reduction amongst the coinage metals in basic solution while suppressing HER,[20] but produces nitrite and hydroxylamine by products, which are more toxic that the original nitrate. Tin, bismuth can selectively reduce nitrate into N_2 but only at very high potential.[21,22] Moreover, the activity and selectivity are dependent on pH, potential and plane of the crystal planes. Bimetallic alloys have also been considered as alternative catalysts material for water remediation technologies as they provide dual active sites that enable high activity and selectivity towards nitrate reduction.[23] Bimetallic alloys of Pt-Ir, Pt-Sn, Pt-Ru, Pd-Cu, Au-Ag, Cu-Ni metal combinations have been synthesized and tested for nitrate reduction selectivity and activity.[24-27] Alloys provide bifunctional sites that improve the efficiency of different steps of reaction paths. For example, Pd-Cu alloys provide different sites to first reduce nitrate into nitrite and then convert nitrite into nitrogen gas.[28] Similarly, Fe/Cu and Ni/Cu showed more than double the activity for nitrate reduction and improved selectivity towards N_2 and NH_3 respectively.[24,29]

Recently, single atom alloy (SAA) catalysts have emerged as highly efficient electrocatalysts and which disrupt the energy scaling relations present on pure metallic and bimetallic catalytic surfaces.[17,28] For example, a NRR study by Calle-Vallejo et. al. (2013) on different ratios of Ag/Al bimetallic catalysts found that the peak activity of nitrate reduction occurs when Ag is present as single atom or 2 atoms on Au surface.[30] Similarly,

I recently showed that Ru in Cu SAA has high nitrate activity (93%) and selective towards NH_3 (99%) (Chen, Wu, Gupta et. al. (2022)).[31] Conversely, (Wu, Nazemi, Gupta, et. al. (2023)) Pd on Cu SAA resulted in high selectivity to N_2 and outperformed all examined Pd/Cu alloys.[32] While my recent work shows promise for the use of SAA for selective NRR, there is no clear understanding of how single atom alloys change the reaction pathways for nitrate reduction reaction. Moreover, the existing SAA catalysts literature still depends on platinoid metals. Thus, if we want to design more energetically and economically effective catalysts for NRR, a comprehensive examination is required which determines the governing mechanisms underpinning selectivity and activity single atoms under various operating conditions (i.e., potential and pH).

To understand the SAA mechanisms that govern the selectivity and activity of NRR, I use density functional theory (DFT) to calculate the nitrate reduction reaction pathway to the most stable products (NO_2^-, NH_3 and N_2) as expected from Frost-Ebsworth diagram.[33,1] I examine the competition between the nitrate reduction and hydrogen evolution reactions on nine single atom elements (Ti, Co, Ni, Mo, Ru, Pd, In, W, Pt and Au) representing a broad spectrum of chemical behavior embedded in the Cu (111) surface at neutral and basic (pH = 14) environmental conditions. I chose to examine the Cu base material because it is relatively inexpensive, highly conductive, and minimizes the hydrogen evolution reaction. I examine both the environmentally desired pH 7 condition and the basic condition because electrochemical reduction often increases the pH near the electrode during operation.[34] In this work I demonstrate that the d-band center of single atom site and N preference for Cu or single atom sites dictate the overall activity and

selectivity, respectively, and thus provide a mechanistic strategy for designing electrocatalysts for NRR.

8.2 Methods

8.2.1 First-principle calculations

I performed spin-polarized periodic boundary density functional theory (DFT) calculations using the Vienna Ab initio Simulation Package (VASP) to calculate the E-NRR pathway on various catalytic surfaces. The calculations were performed using Perdew-Burke-Ernzerhof (PBE) functional and constructed wave function summed of plane waves with energies below 350 eV. I found only 0.02 eV difference in adsorption energies calculated at 350 eV and 400 eV. This difference is small compared to the observed energetic trends, which are ~5 times higher or more, that dictate catalytic performance. Non-local van der Waals (vdW) interactions were accounted for through the DFT-D3 correction, based on the method of Grimme et. al.[35] To reduce computational cost, PAW pseudopotentials[36] were used that explicitly describe the 1s orbital of H, 2s and 2p orbitals of O & N, 3d, 4s and 4p orbitals of Ti, Fe, Ni & Cu, 4d, 5s and 5p orbitals of Mo, Ru, Pd & In, and 5d, 6s and 6p orbitals of Pt and Au atoms. The effect of implicit solvation is not included to limit the computational cost. The Cu (111) surface was chosen to model catalytic surface. The SAA was modeled by replacing a Cu atom with the desired element X, where X: Ti, W, In, Mo, Ni, Pt, Pd, Au. The Cu (111) surface was selected as it is the lowest energy crystal surface[37] and catalyzes the NRR at lower over potentials than other facets such as (100) in basic conditions.[20] Moreover, the Cu (111) has symmetric adsorption sites which simplifies DFT calculations. A supercell of 4×4×5 primitive cells (10.02×10.02×10.81 Å) compose the surface. This structure minimizes interactions

between the single atoms and adsorbents with their periodic images while remaining computationally tractable. All the slabs were separated by at least 10 Å of vacuum space to reduce spurious interactions between atomic layers. I calculated less than a 0.01 eV difference between a 10 Å and a 20 Å of vacuum space. Atomic geometries and system energies were calculated using a 6×6×1 gamma point centered Monkhorst-Pack k-point mesh, which showed only a 0.004 eV difference with a 8×8×1 mesh grid. Atomic geometries were relaxed until atomic energies changed by less than 0.001 eV in subsequent relaxation steps. Transition states for surface reactions were calculated using the nudged elastic band (NEB) method with at least five images per reaction until the residual forces were below 0.005 eV.[38] Density of States (DOS) were calculated using vaspkit[39], electronic charge density using Bader charge analysis[40] and Crystal Orbital Overlap Populations (COOP) was calculated using LOBSTER[41,42] software. Crystal structure representations were obtained using VESTA.[43]

8.2.2 Modelling Electrochemical Nitrate reduction

The NRR pathway includes adsorption and desorption of charged species and the hydrogenation of adsorbed species by proton coupled electron transfer (PCET).[44] The free energy of reactions involving ionic species cannot be calculated directly from DFT calculations in VASP, and periodic boundary condition calculations necessarily introduces a homogeneous background charge to maintain overall cell neutrality. This method introduces significant error in calculated energetics when using cells of different charge. Therefore, I calculate the DFT energies for neutral species and utilize Hess cycles and the computational hydrogen electrode to calculate reaction energies for charged ions.

The free energies of adsorption of ionic species including NO_3^-, NO_2^-, H^+ and OH^- (Appendix Table C.1, r1-r4) are calculated using thermodynamic Hess cycles; these cycles enable us to directly include the effects of entropy, solvation energy, protonation energy (including pH effects) and potential effects. My method is based on that of Calle-Vallejo et. al.[30] and Liu et. al. (2019)[17]. The free energy of anion A^- is calculated using eq. 8.1:

$$\Delta G_{ads}(A^-) = E_{A^*} + [G_{H^+} + G_{e^-}] - \left[G_{HA} - \Delta G_{sol} - \Delta G_{protonation}\right] - E_* \qquad eq.8.1$$

Where E_* and E_{A^*} are the DFT computed enthalpies of bare surface and A^* adsorbed surface, respectively. G_{H_2} and G_{HA} are the Gibbs free energies of desorbed species H_2 and HA, respectively, in the gas phase at 300 K, as calculated from eq. 8.2:

$$G_{HA} = E_{HA} - T\Delta S \qquad eq.8.2$$

where E_{HA} is the DFT computed energy of HA in the gas phase, T is the temperature (300 K) and ΔS is the entropic contributions to the free energy obtained using JANAF database.[45] The solvation energy and protonation energy are described in eq. 8.3 and 8.4, respectively:

$$\Delta G_{sol} = G_{HA(g)} - G_{HA(l)} \qquad eq.8.3$$

$$\Delta G_{protonation} = G_{A^-} + G_{H^+} - G_{HA(l)} - 2.303kT(pK_a - pH) \qquad eq.8.4$$

$G_{HA(g)}$ & $G_{HA(l)}$ are the free energies of HA molecule in gas and liquid phase respectively. The standard state (25° C, 100 kPa, 1mol/kg) energies of ion and neutral species in aqueous solution ($G_{HA(g)}$, $G_{A^-}, G_{H^+}, G_{HA(l)}$) are taken from the CHE handbook.[46] K_a is the acid dissociation constant for A^- anion.

I use the computational hydrogen electrode (CHE) to equate free energy of a proton-electron pair to the gaseous H_2 and electrode potential ($U_{RHE}\ vs.\ RHE$) in eq. 8.1:

$$2G_{OH^-} + G_{H_2} \leftrightarrow 2G_{e^-} + G_{H_2O} + 2U_{RHE} \qquad eq.\ 8.5$$

where RHE is Relative hydrogen potential.[47] More details on the Hess cycle for adsorption of ionic species can be found in chapter 6.[31]

I calculate reaction energy of hydrogenation steps ($A^* + H^* \rightarrow AH^*$) in nitrate reduction (Appendix C Table C.1, r8-r18) using the proton coupled electron transfer (PCET) method, where the substrate reacts with H_2O and an electron:[44]

$$\Delta E_{PCET} = E_{NH^*} + G_{OH^-} - E_{N^*} - G_{H_2O} - G_{e^-} \qquad eq.8.6$$

I used the PCET method because it dominates the hydrogenation pathway on metal clusters in the presence of protic solvents over direct hydrogenation, where adsorbed H atoms react to form products.[48] Under acidic conditions, H_3O^+ is the dominant hydrogen doner rather than H_2O in the CHE and PCET formalism. However, potential effects are referenced to the relative hydrogen electrode, not the standard hydrogen electrode (SHE), and thus the ΔE_{PCET} is independent of H_2O or H_3O^+ as the proton donor. I do note that the proton source concentration does change with pH and thus will affect the kinetics of the reaction pathways where the concentration of reactant species controls the rate of final product. However, that is beyond the score of this work and hence will not be considered further.

The activation barriers for hydrogenation reactions are calculated using Butler–Volmer formalism[49,50] to include the effect of potential on the activation energy:

$$G(U) = G(U^\circ) - \alpha\, n_e\, (U - U^\circ) \qquad eq.8.7$$

Where $G(U^{\circ})$ is the free energy at 0 V vs. RHE, U is the applied voltage, n_e is number of electrons transferred times charge of the electron. α is the fraction of the electrons transferred at the transition state, taken to be 0.5, as is commonly done.[49,50]

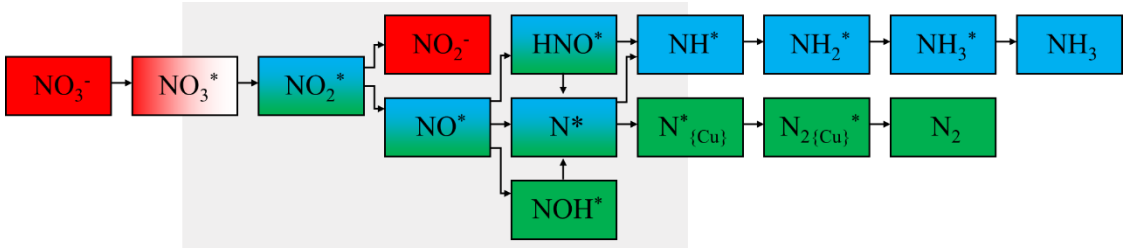

Figure 8.1: Direct reduction pathway of nitrate reducing into N_2, NH_3 and NO_2^- on single atom substitutions in Cu matrix. The red indicates non desirable species (NO_3^- and NO_2^-) and green and blue indicates desirable pathways into NH_3 and N_2. Selectivity determining activation barriers are calculated for reactions falling into grey shaded area.

8.3 Results

I investigated the electrochemical nitrate reduction pathway on neat and nine single-atom substitutions in (111) Cu surfaces to determine the mechanisms and properties directing NRR selectivity and activity. I first discuss the reaction on the neat Cu surface as a base case to understand the critical points that determine the activity and selectivity of nitrate reduction. I examined the NRR selectivity towards the three most thermodynamically stable products under standard conditions (N_2, NH_3 and NO_2^-) based on the Frost–Ebsworth diagram.[1] Figure 8.1 outlines the fundamental reaction mechanism studied in this work based on literature and my previous work.[31,51,52] The reaction pathway involves 18 elementary reactions, described in Table Appendix C.1. After summarizing the NRR behavior on Cu surface, I discuss how the single atoms change the reaction energetics and activation barriers of the critical steps controlling activity and selectivity. The eight transition metals (Ti, Mo, W, Ru, Ni, Pd, Pt, Au) and one post transition metal (In) were

selected to provide a large variation in the single atom properties, such as electron negativity, d-band structure, and atom size.

8.3.1 Nitrate reduction reaction pathways on Cu surface

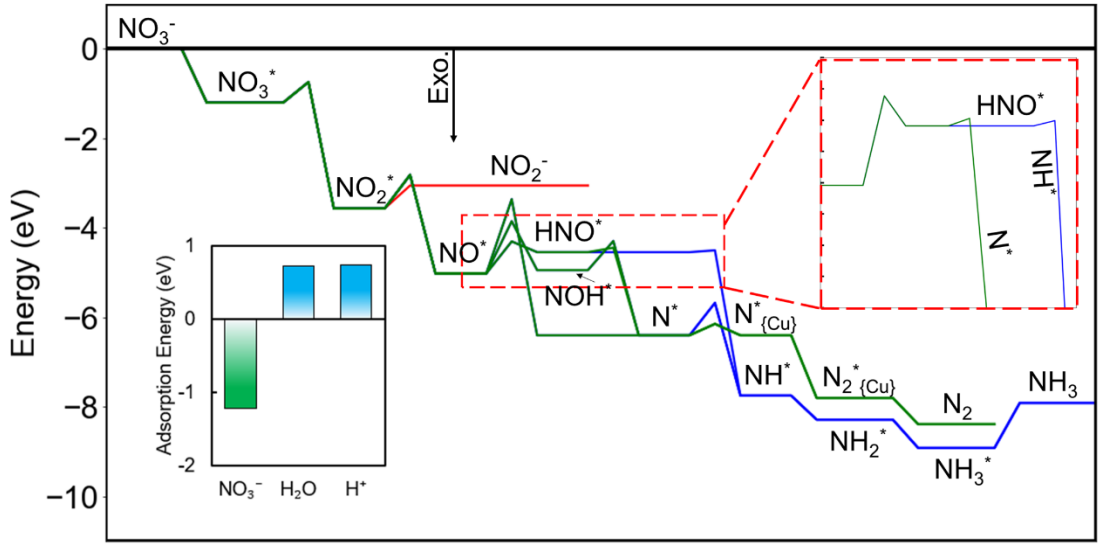

Figure 8.2: DFT calculated energy pathways for nitrate reduction to N_2, NH_3 and NO_2^- on Cu surface at pH = 14, 0 V vs. RHE. The red, blue and green indicates pathways leading to NO_2^-, NH_3 and N_2 respectively. Insert: (left) Adsorption energies of NRR and HER reactants (NRR: NO_3^-, HER: H_2O and H^+), (right) scale-up of HNO^* activation barrier to form N^*(green) and NH^*(blue).

NRR reaction occurs through the following general steps: (1) adsorption of NO_3^-, (2) deoxygenation of the N species, (3) hydrogenation of N-species and/or N-N bond formation and (4) desorption of the reduced species. Figure 8.2 depicts the minimum energy pathway on the Cu (111) electrode 0 V vs. RHE and pH = 14. NO_3^- exothermically adsorbs on the Cu surface (-1.21 eV) and dissociates with a low activation barrier (0.46 eV). The resulting O^* adatoms further reduce to form H_2O or OH^- and desorb. Under alkaline condition, OH^- forms when solvating H_2O or adsorbed H_2O molecules donate a proton to form 2 OH^- ions; at pH 14 and 0 V vs. RHE the calculated activation barrier of this reaction is 0.50 eV (Appendix Table C.1 eq. r19). The low activation barrier suggests that O^* will not accumulate on the surface and self-poison the NRR. Therefore, I predict

rapid electrochemical reduction of NO_3^- to NO_2^* on Cu under alkaline conditions, which is consistent with previous literature.[20]

After its formation, NO_2^* either desorbs to form the undesirable NO_2^- by-product or further dissociates. I calculate that the desorption is preferred, having a reaction energy of 0.51 eV compared to the 0.75 eV barrier for the second N-O bond scission. This preference is consistent with previous experimental and calculation results.[52] Although NO_2^- is predicted to be the major product, further deoxygenation is possible, either by direct reduction or reabsorption and reaction. The $NO_2^* \rightarrow NO^*$ is the rate determining step for additional reaction on neat Cu surface. The NO^* reduction product dictates the overall selectivity, where the formation of HNO^* leads to both NH_3 formation ($HNO^* \rightarrow NH^* \rightarrow NH_2^* \rightarrow NH_2^* \rightarrow NH_3^* \rightarrow NH_3$) and N_2 formation ($HNO^* \rightarrow N^* \rightarrow N_2^* \rightarrow N_2$). The former has a slightly lower maximum activation barrier (0.04 eV) than the latter (0.06 eV) and thus NH_3 and N_2 is predicted to be almost equally produce on Cu surface. In the previous chapter, the activation barriers for hydrogenation of NH^* to NH_2^* and NH_3 species and combination of N^* species to from N_2 are below 0.8 eV and thus do not control activity or selectivity; therefore, they are not considered in the remainder of this work.

The competing Hydrogen Evolution Reaction (HER) decreases electrochemical efficiency by consuming electrons and the reactants/intermediates can block active NRR sites. In HER, H_2O molecules or H^+ reduce to form H^* adatoms on the surface; subsequently two H^* recombine to form H_2 in the Volmer- Tafel route, or the H^* reacts with an available H^+ and electron to from H_2 in the Volmer-Heyrovsky route.[53] On Cu surface, H_2O and H^+ adsorption is endothermic (Figure 8.2(insert)), and hence HER minimally competes with NRR activity on Cu surface near 0 V vs. RHE. Moreover, the

activation barrier to dissociate H_2O on Cu surface is 0.98 eV, which further limits HER activity. This finding matches the experimental results of Farinazzo Bergamo Dias Martins et. al. (2019) who found that the Cu electrode to have low HER activity at pH ~13, due to highly hydrophobic nature of Cu surface.[54]

The activity and selectivity of Nitrogen Reduction Reaction (NRR) is also influenced by the pH and potential conditions of the reaction cell. At a pH of 14, when the potential of the electrode is -0.75 V vs. RHE the energy required to desorb NO_3^* (0.46 eV) is equal to the energy required to dissociate NO_3^* (0.46 eV), and therefore a significant decrease in NRR activity is expected at this potential and higher. At more positive potential than -0.75 v. RHE, dissociation is preferred. This prediction is in agreement with experiments by Pérez-Gallent et.al. (2017).[20] Conversely, increasing the potential above 0.5 V increases the activation and reaction energy of O* hydrogenation to > 1 eV. Thus, at positive potentials of 1.0 V and higher, I predict that excess oxygen accumulates on the surface blocking catalytic sites, and thereby preventing further NRR. As the pH of the solution decreases, the binding of NO_3^- to the Cu surface weakens until, at a pH of ~2 (and 0V vs. RHE) NO_3^- desorption (0.45 eV) is becomes favored over NO_3^* dissociation to NO_2^* and O^* (0.46 eV). Additionally, at pH lower than 2, H^+ adsorption becomes exothermic and competes with the NRR reaction. Overall, pH and potential change the NRR selectivity of the products by changing the activation barrier of hydrogenation reactions, where high pH and intermediate potentials (between -0.75 and 0.5 V) favors the desired NRR.

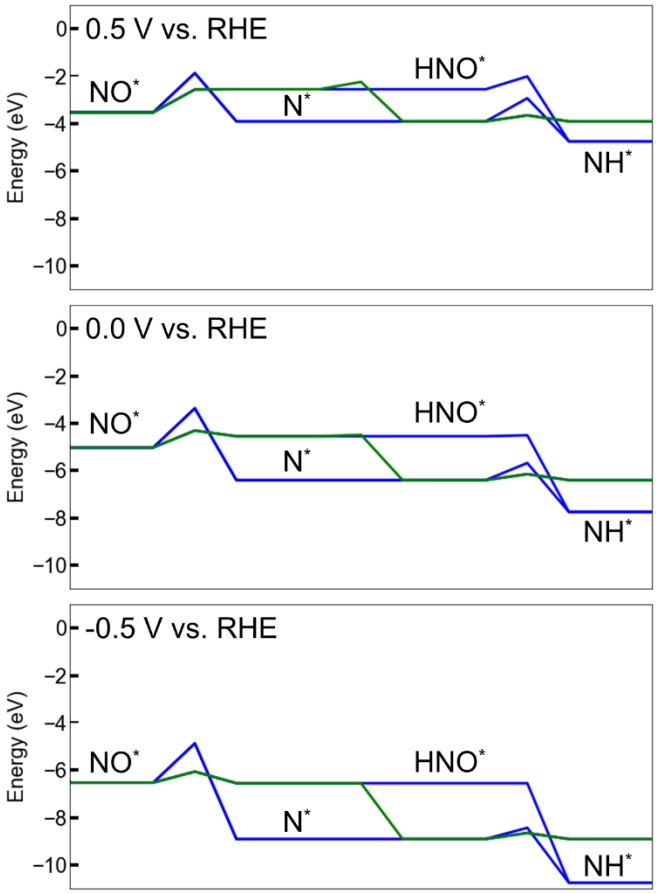

Figure 8.3: Energies of reaction steps involved in determining selectivity of NRR on Cu surface as a function of potential at pH 14.

Potential also affects the selectivity of NRR on Cu surface (Figure 8.3). At pH 14 and a potential 0.5 V vs. RHE, both the activation barriers for HNO^* reaction to HN^* and O* or N^* and OH^* molecules increase compared to the 0 V case. However, the activation barrier for HNO^* deoxygenation to NH^* is more sensitive to potential, increasing by 0.50 eV to 0.54 eV, whereas activation barrier for HNO^* splitting to N^* only increases by 0.25 eV to 0.31 eV. Therefore, the Cu surface will form a greater number of N^* species as compared to NH^*. Since the activation barrier of N^* hydrogenation to NH^* also increases by 0.25 eV to 0.97 eV, I predict a higher selectivity towards N_2 species as compared to NH_3. Conversely, at -0.5 V vs. RHE, the activation barriers for hydrogenation step (N^* to NH^*) and HNO^* deoxygenation step (HNO^* to HN^*) decrease by 0.25 eV. Moreover, the

NO_2^- desorption less endothermic at negative potentials. Hence, higher concentration of NO_2^- will desorb and N^* molecules will hydrogenate to form NH_3 as compared to N_2 at -0.5 V vs. RHE.

8.3.2 Overview of SAC activity

Here I examine the effect of adding a SAA into the Cu surface for the electrochemical NRR. Figure 8.4 shows the lowest energy MEP for each SAA and the base case Cu catalysts. The MEP for all SAA are displayed in Appendix Figures C.2 to C.10. The presence of the single atom provides new active sites, but also induces complexity, as reactive species are able to move between the SAA and the Cu surface. In general, the SAAs can be split into three categories, elements where the NRR occurs locally at the SAA site (Mo, Ru), elements where the NRR is on Cu (Pt, Au, In Ti, W), and those where the reactants switch reaction sites between the SAA and the Cu (Ni, Pd). Below, I examine the two major parts of the reaction network, nitrate deoxygenation and N^* reaction, within these categories. Although the Pt, Au, and In SAC sites are inactive due to the greater stability of N^*-species on the Cu surface, I briefly discuss them to examine correlations between the reaction energetics and elemental properties.

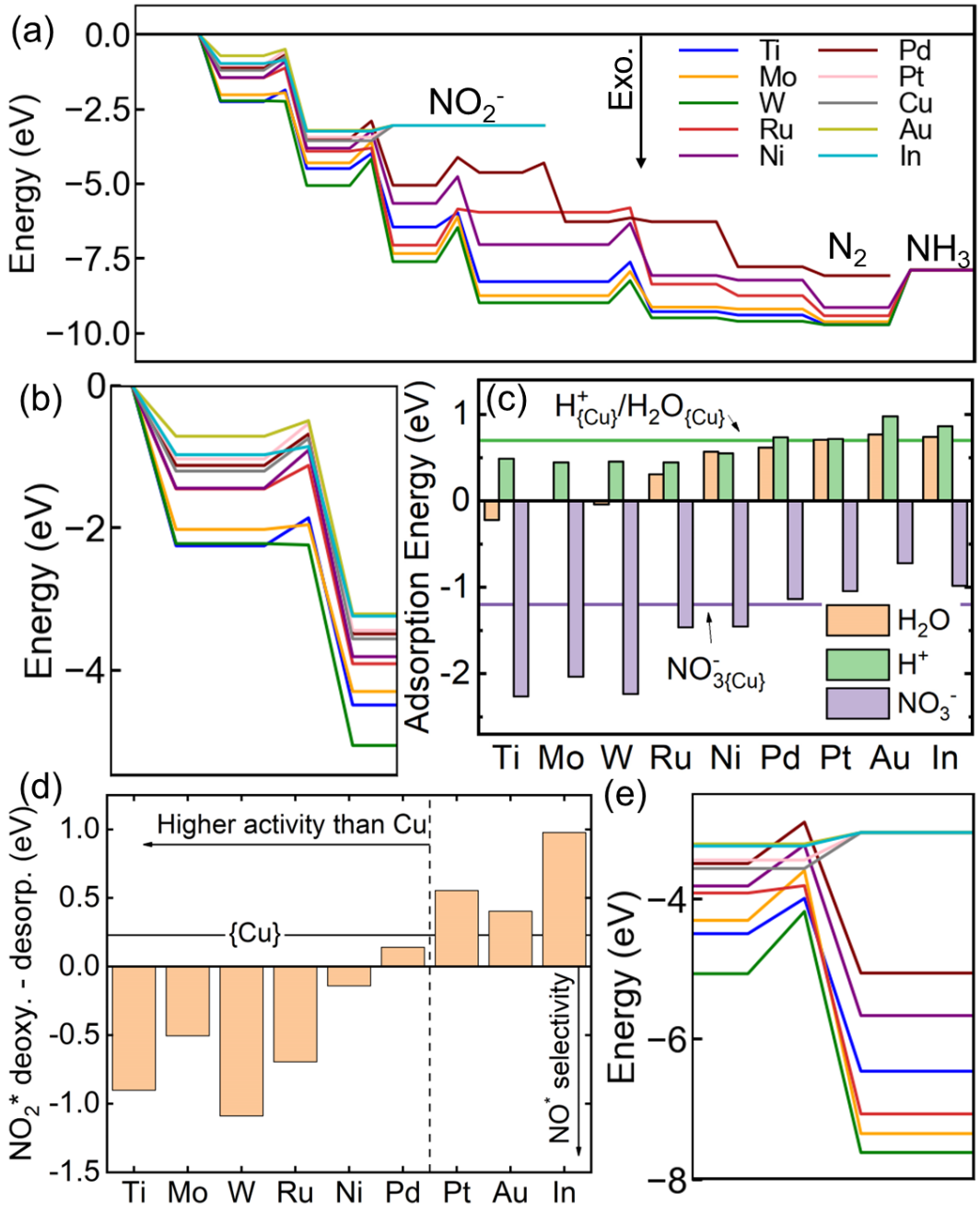

Figure 8.4: (a) Lowest energy MEP for each SAA and the base case Cu catalysts at pH = 14, 0 V vs. RHE. (b) NO_3^- adsorption and first N-O scission step for NO_3^* deoxygenation on SAA at pH = 14, 0 V vs. RHE. (c) adsorption energies of NO_3^- vs. HER reactants (H_2O and H^+) on SAA at pH=14, 0V vs. RHE. The solid lines indicate adsorption energies on base Cu surface. (d) NO_2^* deoxygenation – desorption energy of SAA at pH=14, 0V vs. RHE. (e) NO_2^- desorption and second N-O scission step for NO_2^* deoxygenation on SAA at pH = 14, 0 V vs. RHE.

8.3.2.1 Activity of nitrate deoxygenation on single atom catalysts sites

Efficient NRR sites are characterized by moderately strong NO_3^- adsorption and weak, or preferably no H_2O or H^+ adsorption, as they lead to HER. Additionally, the NO_3^* must subsequently reduce to NO_2^* rather than desorb. These requirements energetically correspond to exothermic nitrate adsorption, near zero or endothermic H_2O or H^+ adsorption, and a lower activation barrier for NO_3^* deoxygenation than desorption. Figure 8.4b provides the activation barrier first deoxygenation step and Figure 8.4c reports the adsorption energies for NO_3^-, H^+ and H_2O and. at pH = 14, 0 V vs. RHE.

I find that NO_3^- adsorption is exothermic and H^+ adsorption is endothermic on all the single atoms substitutions, while H_2O adsorption is endothermic for Ru, Mo, Ni, Pd, Pt, Au and In-SAA but slightly exothermic for Ti and W-SAA. These energies suggest that nitrate adsorption will dominate Mo, Ru, Ni, Pd, Pt, Au and In-SAA under basic conditions (pH = 14). Although Ti- and W-SAA have highly exothermic NO_3^- adsorption energies, H_2O also adsorbs exothermically and is present at much higher concentration in the aqueous environment; therefore, H_2O is likely to block these sites and lower the nitrate reduction rate. Thus, on Ti- and W-SAA, NRR can only occur on the Cu sites since H_2O does not bind to them. Further, NO_3^- adsorbs significantly more strongly on Cu than In and Au-SAA and therefore the initial NRR steps occur on Cu sites. The adsorption of NO_3^- on Ni, Pd, and Pt-SAA (-1.45 eV, -1.13 eV, -1.04 eV) are similar to that of the Cu single metal surface (-1.21 eV), and hence the active site for nitrate reduction may occur on either Cu metal surface or SAA.

Once bound to the electrocatalyst surface, I predict that all NO_3^* molecules reduce to NO_2^* because the reduction activation barrier is at least 0.50 eV lower than the

desorption energy of NO_3^* on all single atom substitutional sites at pH 14 and 0 V vs. RHE. The activity is predicted to be highest on Mo and Ru-SAA because NO_3^* localizes on these sites rather than Cu, and they have the lowest deoxygenation activation barrier. Although In, W, Ti, and Au-SAA have low activation barriers, NRR occurs on the Cu sites because of their strong preference for NO_3^* or the SAA sites are blocked by H_2O. Ni-, Pd-, and Pt-SAA will perform similarly to Cu sites because their activation barriers are similar (within 0.4 eV) and there is minimal preference for the SAA or Cu sites.

8.3.3 Effect of pH and potential on SAA deoxygenation activity

As with neat Cu, pH and potential alter the deoxygenation behavior on the SAA. Decreasing the pH and potential leads to less exothermic NO_3^- adsorption and more exothermic H^+ adsorption. Figure 8.5 displays the effect of pH and potential on the energetics and activation barriers of NO_3^- deoxygenation on the SAAs. Figure 8.5a demonstrates the effect of pH on the adsorption energies of NO_3, H^+ and H_2O on Cu and Ru-SAA. At pH below 6.5, H^+ adsorption becomes exothermic and therefore blocks NO_3 binding due to the relative concentrations, lowering the NRR efficiency. Conversely, this crossover does not happen until pH 1.6 for neat Cu. Figure 8.5(d) lists the pH where H_2O or H^+ adsorption becomes favorable for the various SAA. For Ti and W H_2O adsorption is exothermically even at pH 14. In decreasing pH order, H^+ adsorption becomes exothermic on Mo and Ru around pH 6.5, followed by Ni at pH 4.8, and Pd and Pt at pH 1.6 and 1.9 respectively. Neither H_2O nor H^+ exothermically adsorb to Au or In.

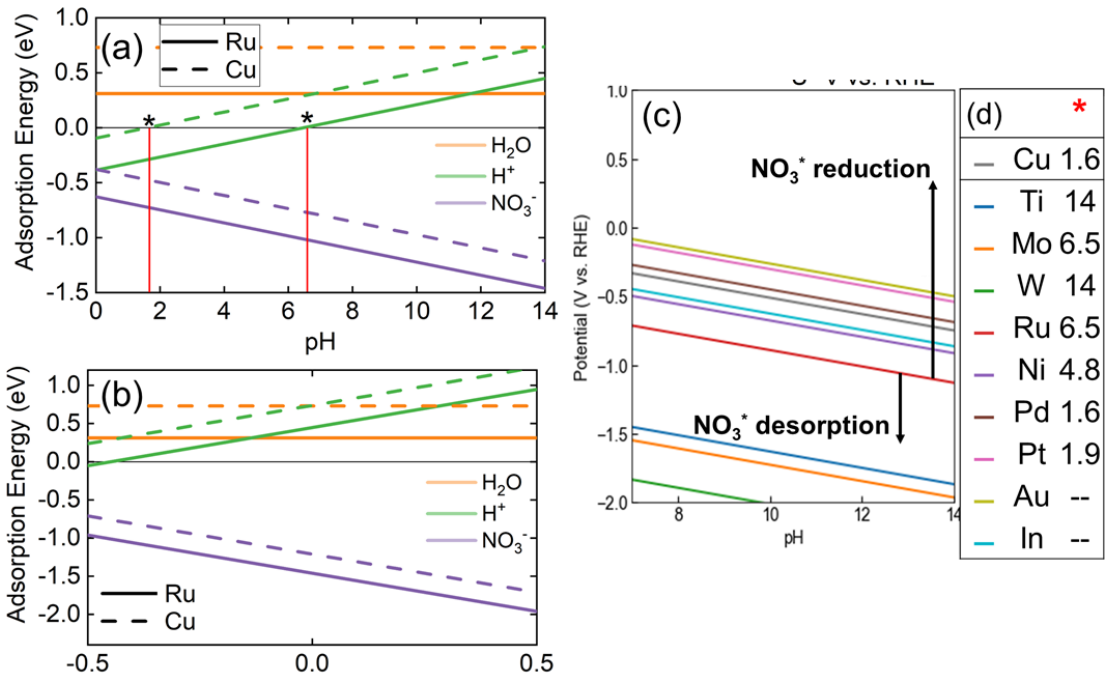

Figure 8.5: (a) pH dependent adsorption of NO_3^-, H^+ and H_2O at 0 V vs. RHE and (b) potential dependent adsorption of NO_3^-, H^+ and H_2O at pH 14 on Ru-SAA (solid) and Cu metal surface (dashed). (c) The NO_3^* desorption vs. reduction equilibrium lines on X-SAA on pourbaix diagram. (d) pH values for single atoms above which NO_3RR is favorable (*).

Figure 8.5b demonstrates the effect of potential on NO_3^-, H_2O and H^+ adsorption energies as a function of potential at pH 14. At potential < -0.45 V vs. RHE, H^+ adsorbs exothermically on the Ru surface and hence decreases NRR efficiency by blocking the SAA sites. This adsorption does not occur on Cu surface until -0.75 V vs. RHE. For other SAA, the adsorption H^+ is exothermic below -0.42 V, -0.55 V, -0.72 V, -0.74 V, -0.85 V and -0.98 V vs. RHE for Mo-, Ni-, Pt-, Pd-, In- and Au-SAA respectively. The adsorption of H_2O on Ti and W remains exothermic at all potential ranges.

The system pH and potential operating points also control the relative energetics of NO_3 deoxygenation and desorption. This relationship is shown in Figure 8.5(c). For example, Ru (red line in Figure 8.5(c)) preferentially catalyzes NO_3 reduction at pH 14 and a potential above -1.1 V vs. RHE, however at pH 7, the potential cannot exceed 0.71 V vs.

RHE. The slope of this relationship is the same across the SAAs, however the potential value changes depending on NO^* binding strength. In general, early transition metals catalyze deoxygenation even at stronger potentials than late transition metals and In.

8.3.4 Selectivity of NRR after NO_2 formation on single atom catalysts sites

Table 8.1: The most selective product, and site for minimum energy pathway on SAA in Cu surface.

SAA	Predicted product	Site for NRR (Cu/SAA or mixed)	Product if NO_3 deoxygenation on SAA
Cu	NO_2^-	-	-
Ti-SAA	NO_2^-	Cu	NH_3
Mo-SAA	NH_3	SAA	NH_3
W-SAA	NO_2^-	Cu	NH_3
Ru-SAA	NH_3	SAA	NH_3
Ni-SAA	NH_3	SAA	NH_3
Pd-SAA	N_2/ NO_2^-	mixed	N_2/NO_2^-
Pt-SAA	NO_2^-	Cu	NO_2^-
Au-SAA	NO_2^-	Cu	NO_2^-
In-SAA	NO_2^-	Cu	NO_2^-

After NO_2 forms, it can reduce to NH_3, N_2 or NO_2^- on the SAA or the Cu surface depending on the relative energetics and pH and potential (Table 8.1). Because of the diverging nature of the possible pathways, I will discuss the behavior of the SAA in groups based on their minimum energy pathway. I only calculated the activation barriers of the eight crucial selectivity determining steps of these pathways to avoid the high computational cost of examining low-barrier and/or non-reaction path directing steps, e.g., the addition of a second H* to NH_2^*. Due to the complexity of the reaction pathways and the single site nature of the SAA, I leave detailed predictions rates to future work dedicated to the detailed kinetic monte Carlo simulations needed to appropriately account for these interactions. The following analysis assumes a pH of 14 and a 0 V potential vs. RHE unless specifically stated otherwise.

Group 1- Mo-, Ru- and Ni-SAA

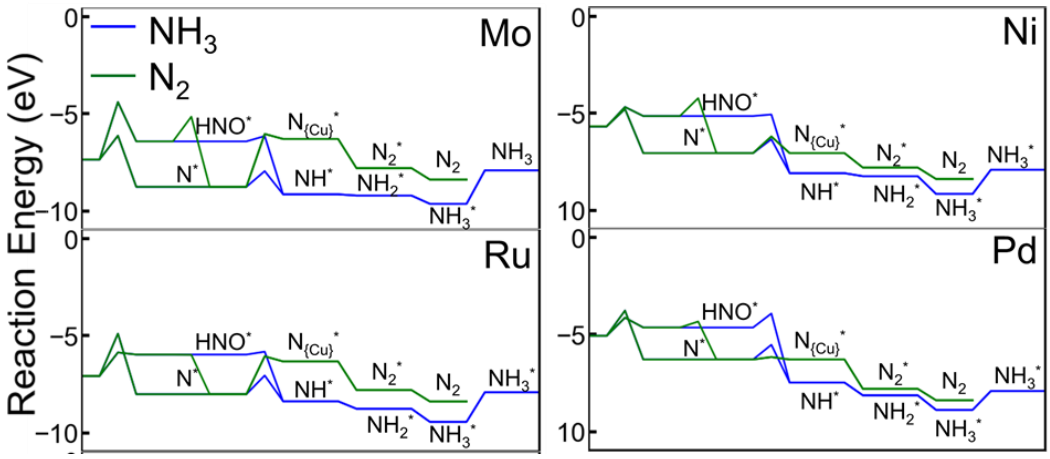

Figure 8.6: Reaction pathways effecting selectivity on Mo-, Ru-, Ni- and Pd-SAA towards NH_3 or N_2 formation at 0 V vs. RHE and pH 14.

Three SAA favor the production of NH_3, Mo, Ru and Ni. In all three cases, NO_3^* binds to the SAA and readily reduces to NO_2^*. There is a strong energetic preference for the NO_2^* to further reduce to NO^* rather than desorbing, with the N-O dissociation activation barriers being at least -0.18 eV lower in energy than desorption (Figure 8.4(d)). NO^* molecules on Mo- and Ni-SAA decompose directly to N^* and O^* adatom with barriers < 1.2 eV. The N^* and O^* atoms migrate to separate hollow sites adjacent to the SAA and are trapped there due to the 2.73 eV and 0.86 eV barrier on Mo- and Ni-SAA, respectively, to hop to Cu only hollow sites. From the hollow sites, the N^* and O^* undergo successive hydrogenations by PCET to for NH_3 and OH^- or H_2O, respectively. Because N^* and O^* are trapped, they cannot readily migrate to distant SAA or Cu sites and combine with other N^* containing species. The activation barrier for first hydrogenation, N^* to NH^* is 0.81 eV and 0.71 eV on Mo- and Ni-SAA, respectively. NO^* on Ru follows a slightly different pathway; it initially hydrogenated to from HNO^* rather than directly decomposing to N^* and O^*. The HNO^* then decomposes to NH^* and O^* before undergoing further

hydrogenation to NH_3 and OH^-/H_2O (Figure 8.6). Overall, Mo, Ru and Ni have a low NO_2^* decomposition barrier and strongly localize all resulting N^* species at the SAA; and thus, NRR I predict that Mo, Ru and Ni SAA are selective to NH_3.

Group 2 – Ti- and W-SAA

Although Ti- and W-SAA would localize N^*-species at the SAA site, they exothermically bind water which limits the access of the NO_3^- molecule to the SAA, minimizing NRR activity. Because NO_3^- adsorption is predicted to mostly occur on Cu, the Cu pathway is expected to dominate the performance, and thus NO_2^- is predicted to be the majority product at pH 14 and 0 V vs. RHE. However, when NO_3^* binds to Ti- and W-SAA, I predict that NH_3 is the preferred product. As shown in Appendix figure C.2 and C.4, these SAA elements follow the same pathway as Mo- and Ni-SAA, where NO_2^* decomposes to NO^* then N^* before hydrogenation to NH_3.

Group 3 – Pd-SAA

Pd-SAA has the most complex reaction pathway of the SAA investigated. The relative preference for N^*-species on the Pd or Cu is relatively small, meaning that reaction products rapidly exchange between the sites and the reaction pathway is highly branching. The binding energy and first N-O bond scission activation barrier of NO_3^* is similar on Pd-SAA and Cu, thus all sites are likely active during electrocatalytic NRR. On the Cu sites, NO_2^- desorption is highly preferred (0.24 eV) to further reduction; even if NO_2^- reabsorbs there is only a 0.009% chance for deoxygenation, given the Boltzmann distribution, and therefore NO_2^- is the main product. However, on the Pd-SAA site there is only a 0.14 eV preference for desorption compared to reduction, which corresponds to NO^* formation 0.45% of the time, according to the Boltzmann distribution. When the second N-O bond

does break, the reaction is exothermic by -1.56 eV, and there is minimal back reaction. I additionally note that the total activation barrier for NO_2^* deoxygenation is only 0.59 eV, which is expected to provide a relatively high flux through this metastable state to NO^*. Therefore, even though NO_2^* desorption is slightly favored, given sufficient time, the desorbed NO_2^- is predicted to reabsorb and continue along the NRR pathway.

Once NO^* is formed on the Pd SAA site, it preferentially hydrogenates to from HNO^* rather than decomposing to N^* and O^*. The HNO^* dissociates into N^* and OH^* rather than HN^* and O^*, with activation barriers of 0.02 eV and 0.72 eV respectively (Figure 8.6). In this step, HNO^* lays down from a vertical structure to the transition state where the H^* simultaneously transfers to the O^* while the N-O bond breaks. The transition state is stabilized by the Cu atoms onto which the O^* has partially attached. The resulting non-hydrogenated N^* migrates to the solvating Cu matrix. On both Pd-SAA and Cu sites, N-H bond formation has a large activation barrier of 0.76 eV and 0.72 eV, respectively, limiting the subsequent generation of NH_3. The N^* atom on the Cu surface combines with other N^* adatoms with a low 0.29 eV barrier. Overall, Pd SAA directs NRR towards the production of N_2 because NO_2^* deoxygenation is possible on Pd-SAA, the resulting HNO^* species strongly favors separate N^* and OH^* products, where the N^* migrates to Cu where it combines with other N^* atoms to from N_2 because the N^* hydrogenation activation barrier is high on Pd and Cu.

Group 4 – Pt-, Au and In-SAA.

I predict that Pt-, Au-, In-SAA preferentially form NO_2^-. Firstly, NO_3^- preferentially binds to Cu rather than these SAA, therefore NRR is not expected to occur on these sites. Even if NO_3^- were to bind to these sites, the activation barrier for the second N-O bond

scission (NO_2^* to NO^*) is at least 0.53 eV, 0.36 eV higher than NO_2^- desorption. In fact, NO_2^* deoxygenation has a higher activation barrier on these sites than the Cu matrix itself, further indicating that all NRR reaction would occur on the Cu. Given their expense and relative inactivity, it is unlikely that Pt-, Au-, and In-SAA should be used as SAA catalysts in Cu for NRR.

8.4 Discussion

I investigated the effect of SAA substitution on electronic structure of the surface and its correlation with adsorption energies, reaction energies and reaction pathways for transition states. The density of state plots of Cu surfaces substituted with single atom alloys is shown in Figure 8.7. I found that the d-band center of single atom substitution (ε_{d-SAA}) is higher than the fermi energy (ε_f) for early transition metals until Ru-SAA while it sits below ε_f for the late transition metals (Ni, Pd, Pt and Au). The d-band center effects the thermodynamic energetics and reaction pathways of NRR species near these single atom alloys. Carvalho et. al. (2022) found that d-band center of pure transition metal electrodes can predict NH_3 efficiency of NRR which was highest when d-band center approaches Fermi energy.[55] In this section, I investigate relationships between single atom properties and NRR energetics and activation pathways. Correlation between reaction energetics on In-SAA are not included here as In is not a transition metal, nor does it show strong NRR activity.

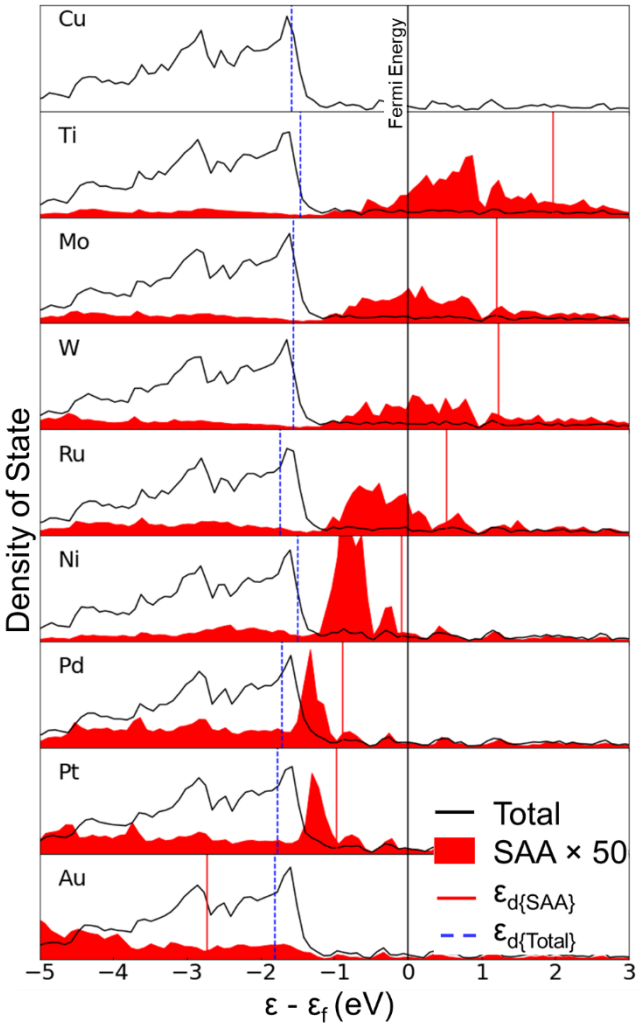

Figure 8.7: Density of state of transition atom substitutions in Cu [111] surface.

8.4.1 Effects of single atom properties on adsorption energies

As seen in section 8.3, the adsorption energies of NO_3^-, H_2O, and H^+ is more exothermic on early transition metals than on pure Cu and lower on later transition metals (Pt and Au). In Figure 8.8, I corelate the NO_3^-, H_2O, and H^+ adsorption energy trends as a function of d-band center of SAA. I find that adsorption energies are strongly related to the position of d-band center of substituted single atom relative to the fermi energy ($\varepsilon_{d-SAA} - \varepsilon_f$) ($R^2$ ~ 0.88-0.89). The NO_3^- adsorption is more sensitive to d-band center position than H_2O or H^+ having slopes of -0.34, -0.23 and -0.11, respectively. I also found that the

adsorption of NO_3^-, H_2O and H^+ adsorption on SAA sites occur in the same configurations as neat Cu. NO_3^-, H_2O and H^+ adsorb in bidentate bimolecular, top, and hollow sites, respectively (Figure 8.8(b-d)). This explains strong linear trends observed between adsorption energies and d-band centers of SAA.

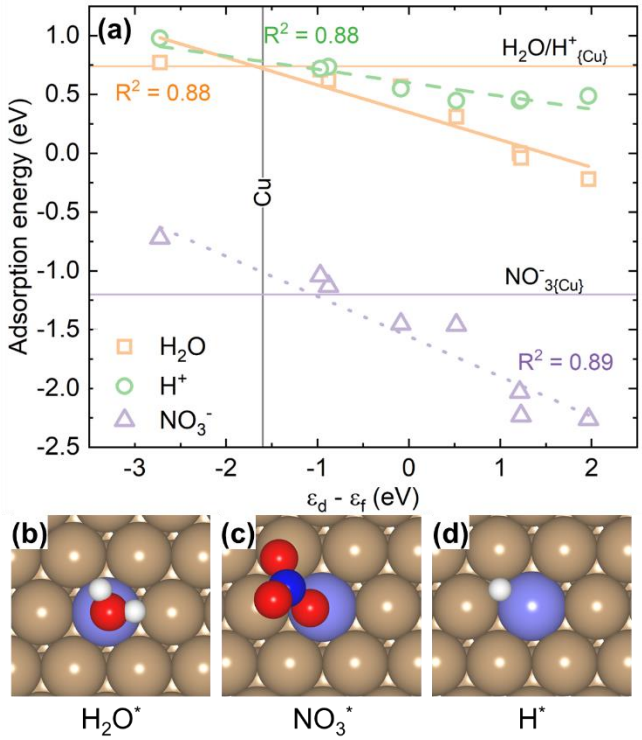

Figure 8.8: (a) Electrochemically measured adsorption energies of NO_3^-, H_2O and H^+ for on SAA as compared to the calculated shift of the d-band center of SAA ($\varepsilon_d - \varepsilon_f$). Relaxed configuration of H_2O (b), NO_3 (c) and H^+ (d) on Ru-SAA in Cu surface. White, blue, red, golden, and violet spheres correspond to H, N, O, Cu, and Ru, atoms, respectively.

I also observed higher adsorption energies for other meta-stable species and products of NRR and HER reactions (NO_2^-, NO, NH_3 and OH^-) on early transition metals alloys (Ti, Mo, W, Ru) as compared to late transition metals (Ni, Pd, Pt and Au). The linear relationships between d-band center and adsorption energies of OH^* and NO^* have higher residue error (R^2 ~ 0.69-0.72). This is because the NO^* adsorption configuration changes from hollow site for Ni-, Pd-, Pt-, and Au-SAA species to top site for Ti-, Mo-, W- and Ru-

SAA. Similarly, the OH^* adsorption configuration changes from hollow site for Ru-, Mo-, Ni-, Pd-, Pt-, and Au-SAA species to top site for Ti-, and W-SAA.

8.4.2 Effects of single atom properties on transition state activation pathways

From my calculations, I also found the SAA also changes the activation barriers energies and transition state configurations on the electrode surface. For the first N-O bond scission, I observe that on all SAA, NO_3^* binds to the surface in bidentate configuration via 2 O atoms, one bound to the SAA and the other on to a Cu atom (Figure 8.8(c)). However, Ti-, Mo-, W-, and Ru-SAA preferentially split the $N\text{-}O^*$ bond on top of SAA whereas the Ni-, Pd-, Pt-, and Au-SAA break the $N\text{-}O^*$ bond on top of neighboring Cu site, as exemplified in Figure 8.9. Thus, the activation energies calculated on SAA do not follow Brønsted−Evans−Polanyi (BEP) relation[56,57], which are often used to develop volcano plots and hence explore new catalytic systems. From Bader charge analysis I found that the SAA and neighboring Cu sites are slightly charged as compared to pure Cu surface. Ti-, Mo- and W- SAA donate some of their electron density to neighboring Cu atoms. I find that the electron density is slightly higher on O^* bonded on the SAA for Ti-, Mo-, W-, and Ru SAA, equal on Ni-SAA and higher on Pd-, Pt-, and Au-SAA, which preferentially splits with lower activation barrier as compared to the other bonded O^*.

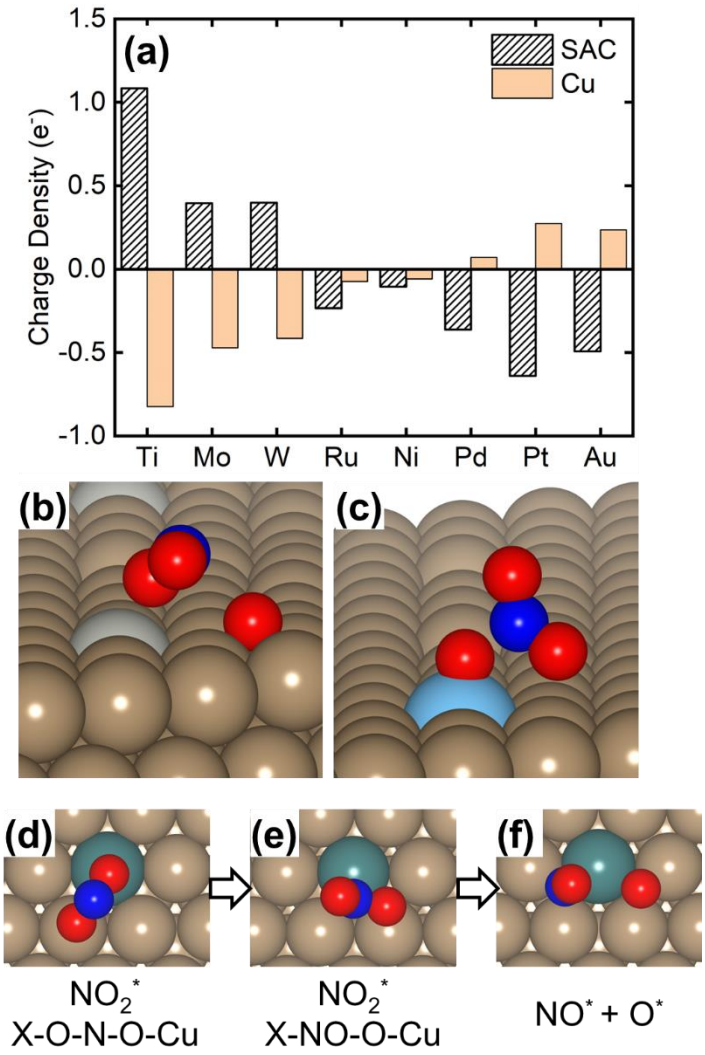

Figure 8.9: (a) Charge density on Single atom and neighboring Cu atom for SAA. Transition state (NO_2-O^*) for NO_3^* reduction on (b) Pd-SAA and (c) Ti-SAA. Reaction pathway of second NO bond session from (d) NO_2^* adsorption to (e) NO_2^* flip on the surface to (f) NO^* and O^* atoms on Ru-SAA. White, blue, red, golden, silver, teal and sky-blue spheres correspond to H, N, O, Cu, Pd, Ru and Ti atoms, respectively.

Different pathways for the same reaction do occur for other reaction steps. In the second N-O bond scission, the N-O bond splits on top of SAA; afterwards the NO_2^* flips from an X-O-N-O-Cu configuration to a X-NO-O-Cu configuration to bond N^* with the SAA (Figure 8.9(d-f)). The activation barrier depends upon both the energy needed to rotate the NO_2^* species on the surface and barrier to break N-O bond. For all but Ni-SAA, the energy required to break the N-O bond on the surface was higher than for NO_2^* rotation.

For Ti-, Mo-, W- and Ru-SAA the NO_2^* flips during NO_3^* dissociation step, which decreases the activation barrier of NO_2^* dissociation.

Similarly, the energy to hydrogenate NO^* is higher for early transition metals and Ni-SAA as compared to third NO^* bond session to N^* and O^* adatoms. The higher barrier arises because the H^* has to hop onto the top of SAA to hydrogenate NO^* species that are adsorbed on top of SAA on Ti-, Mo- and W-SAA rather than merely hopping to an adjacent hollow site where NO^* is adsorbed on Ru-, Pd-, Pt- and Au-SAA. These slight variations in relaxed configuration and energetics affect the activation barriers of critical reaction on SAA sites and change the minimum energy pathway on different SAA.

Finally, if the NO_2^* dissociates on the SAA site, all but Ru form N^* on the surface. The selectivity towards N_2 vs NH_3 on SAA sites depends upon N^* hopping energy vs. NH^* hydrogenation energy on Cu surface (Figure 8.10). This is different than what is observed on Cu electrode where NO^* hydrogenates to HNO^* which splits either in NH^* or N^*. Therefore, single atoms are preferentially better at achieving higher selectivity towards NH_3 as compared to Cu metal surface as they can isolate the reactants near the single atom sites, which limits their ability to bond with another N^* species to form N_2 (Figure 8.10). However, the selectivity towards N_2 will still depend upon the base surface, Cu in my case, as N^* can either combine with other N^* or hydrogenate on Cu sites, depending upon pH and potential conditions.

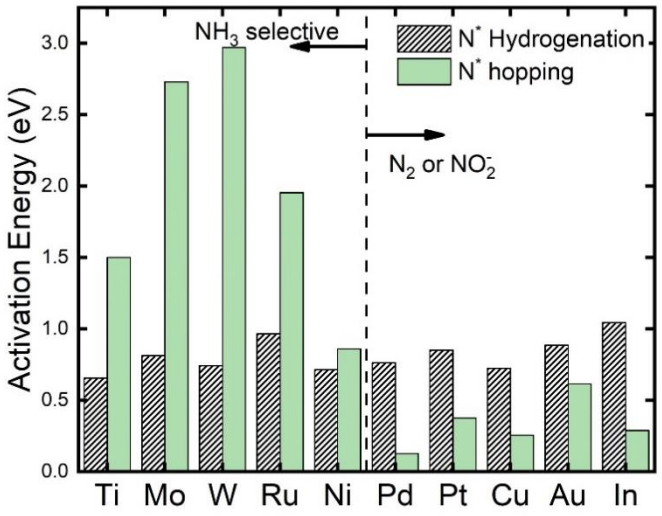

Figure 8.10: Activation energy for N^* hydrogenation vs. hopping to Cu sites on SAA at 0 V vs. RHE and pH 14.

8.5 Conclusion

I investigated the Nitrate reduction pathway activity and selectivity on single atom substitutions in Cu surface. I found that the energies along the nitrate reduction pathway are significantly controlled by the surface-active sites. The adsorption energies are strongly correlated to the d-band center of the single atom substitution. However, the activation barriers on single atoms do not follow simple scaling relationships as the reactions of some transition pathways occur on the single active sites and others occur on the adjacent Cu site, depending upon the reactant configuration, bond strength reactant with single atom site as compared to Cu site. The single atom, pH and potential also affects the activity of NRR and its competition with HER reaction. The adsorption of H_2O on Ti- and W-SAA is exothermic, which suggests poor NRR activity. The adsorption of NO_3 is weaker on Pt-, Au- and In-SAA as compared to Cu surface sites. Hence, it is unlikely that NRR will occur on substituted sites for Pt-, Au- and In-SAA.

I find that Mo-, Ru-, Ni- and Pd-SAA are less selective towards form NO_2^- as compared to Cu surface, as they decrease the activation barrier of NO_2^* deoxygenation.

The Mo-, Ru-, Ni-SAA will be selective towards NH_3. However, they adopt different pathways to NH formation. Ni-SAA has small differences between activation barrier of N^* hydrogenation and hopping. Hence, selectivity is predicted to be highly sensitive to the pH and potential conditions. Pd is the only substitution where NRR is expected to selectively reduce to N_2. The similarity in energies between the Cu and Pd/Ni sites suggest that NRR on Pd and Ni SAA are more sensitive to sensitive to potential and pH than the highly localized Mo-SAA and Ru-SAA. Overall, I conclude that single atom catalysts can be optimized to achieve higher selectivity towards NH_3 by tuning the relative binding strength of the SAA site to that of the solvating metal. However, achieving higher selectivity for N_2 with less expensive elements than Pd requires either changing the base metal or increasing the alloying concentration to achieve neighboring substitutionally active sites.

8.6 References

1. Garcia-Segura, S.; Lanzarini-Lopes, M.; Hristovski, K.; Westerhoff, P., Electrocatalytic reduction of nitrate: Fundamentals to full-scale water treatment applications. Applied Catalysis B: Environmental 2018, 236, 546-568.
2. Zhang, X.; Ward, B. B.; Sigman, D. M., Global Nitrogen Cycle: Critical Enzymes, Organisms, and Processes for Nitrogen Budgets and Dynamics. Chemical Reviews 2020, 120 (12), 5308-5351.
3. Serio, F.; Miglietta, P. P.; Lamastra, L.; Ficocelli, S.; Intini, F.; De Leo, F.; De Donno, A., Groundwater nitrate contamination and agricultural land use: A grey water footprint perspective in Southern Apulia Region (Italy). Science of The Total Environment 2018, 645, 1425-1431.
4. Fewtrell, L., Drinking-Water Nitrate, Methemoglobinemia, and Global Burden of Disease: A Discussion. Environmental Health Perspectives 2004, 112 (14), 1371-1374.
5. Rehman, H. U., Methemoglobinemia. West J Med 2001, 175 (3), 193-196.
6. Nitrate and Drinking Water from Private Wells. Centers for Disease Control and Prevention 2015.
7. Ashok, V.; Hait, S., Remediation of nitrate-contaminated water by solid-phase denitrification process—a review. Environmental Science and Pollution Research 2015, 22 (11), 8075-8093.
8. Koebke, K. J.; Pecoraro, V. L., Development of de Novo Copper Nitrite Reductases: Where We Are and Where We Need To Go. ACS Catalysis 2018, 8 (9), 8046-8057.

9. Rezvani, F.; Sarrafzadeh, M.-H.; Ebrahimi, S.; Oh, H.-M., Nitrate removal from drinking water with a focus on biological methods: a review. Environmental Science and Pollution Research 2019, 26 (2), 1124-1141.
10. Kapoor, A.; Viraraghavan, T., Nitrate Removal From Drinking Water—Review. Journal of Environmental Engineering 1997, 123 (4), 371-380.
11. Bishayee, B.; Chatterjee, R. P.; Ruj, B.; Chakrabortty, S.; Nayak, J., Strategic management of nitrate pollution from contaminated water using viable adsorbents: An economic assessment-based review with possible policy suggestions. Journal of Environmental Management 2022, 303, 114081.
12. Medford, A. J.; Hatzell, M. C., Photon-Driven Nitrogen Fixation: Current Progress, Thermodynamic Considerations, and Future Outlook. ACS Catalysis 2017, 7 (4), 2624-2643.
13. Radjenovic, J.; Sedlak, D. L., Challenges and Opportunities for Electrochemical Processes as Next-Generation Technologies for the Treatment of Contaminated Water. Environmental Science & Technology 2015, 49 (19), 11292-11302.
14. Min, B.; Gao, Q.; Yan, Z.; Han, X.; Hosmer, K.; Campbell, A.; Zhu, H., Powering the Remediation of the Nitrogen Cycle: Progress and Perspectives of Electrochemical Nitrate Reduction. Industrial & Engineering Chemistry Research 2021, 60 (41), 14635-14650.
15. Shin, H.; Jung, S.; Bae, S.; Lee, W.; Kim, H., Nitrite Reduction Mechanism on a Pd Surface. Environmental Science & Technology 2014, 48 (21), 12768-12774.
16. Dima, G. E.; Beltramo, G. L.; Koper, M. T. M., Nitrate reduction on single-crystal platinum electrodes. Electrochimica Acta 2005, 50 (21), 4318-4326.
17. Liu, J.-X.; Richards, D.; Singh, N.; Goldsmith, B. R., Activity and Selectivity Trends in Electrocatalytic Nitrate Reduction on Transition Metals. ACS Catalysis 2019, 9 (8), 7052-7064.
18. Bae, S.-Y.; Mahmood, J.; Jeon, I.-Y.; Baek, J.-B., Recent advances in ruthenium-based electrocatalysts for the hydrogen evolution reaction. Nanoscale Horizons 2020, 5 (1), 43-56.
19. Wang, Z.; Richards, D.; Singh, N., Recent discoveries in the reaction mechanism of heterogeneous electrocatalytic nitrate reduction. Catalysis Science & Technology 2021, 11 (3), 705-725.
20. Pérez-Gallent, E.; Figueiredo, M. C.; Katsounaros, I.; Koper, M. T. M., Electrocatalytic reduction of Nitrate on Copper single crystals in acidic and alkaline solutions. Electrochimica Acta 2017, 227, 77-84.
21. Dortsiou, M.; Kyriacou, G., Electrochemical reduction of nitrate on bismuth cathodes. Journal of Electroanalytical Chemistry 2009, 630 (1), 69-74.
22. Katsounaros, I.; Ipsakis, D.; Polatides, C.; Kyriacou, G., Efficient electrochemical reduction of nitrate to nitrogen on tin cathode at very high cathodic potentials. Electrochimica Acta 2006, 52 (3), 1329-1338.
23. Sanchis, I.; Diaz, E.; Pizarro, A. H.; Rodriguez, J. J.; Mohedano, A. F., Nitrate reduction with bimetallic catalysts. A stability-addressed overview. Separation and Purification Technology 2022, 290, 120750.
24. Wang, Y.; Xu, A.; Wang, Z.; Huang, L.; Li, J.; Li, F.; Wicks, J.; Luo, M.; Nam, D.-H.; Tan, C.-S.; Ding, Y.; Wu, J.; Lum, Y.; Dinh, C.-T.; Sinton, D.; Zheng, G.;

Sargent, E. H., Enhanced Nitrate-to-Ammonia Activity on Copper–Nickel Alloys via Tuning of Intermediate Adsorption. Journal of the American Chemical Society 2020, 142 (12), 5702-5708.
25. Santos, A. S. G. G.; Restivo, J.; Orge, C. A.; Pereira, M. F. R.; Soares, O. S. G. P., Influence of organic matter formed during oxidative processes in the catalytic reduction of nitrate. Journal of Environmental Chemical Engineering 2021, 9 (4), 105545.
26. Zhang, Y.; Chen, X.; Wang, W.; Yin, L.; Crittenden, J. C., Electrocatalytic nitrate reduction to ammonia on defective Au1Cu (111) single-atom alloys. Applied Catalysis B: Environmental 2022, 310, 121346.
27. Wang, Z.; Ortiz, E. M.; Goldsmith, B. R.; Singh, N., Comparing electrocatalytic and thermocatalytic conversion of nitrate on platinum–ruthenium alloys. Catalysis Science & Technology 2021, 11 (21), 7098-7109.
28. Gao, Q.; Pillai, H. S.; Huang, Y.; Liu, S.; Mu, Q.; Han, X.; Yan, Z.; Zhou, H.; He, Q.; Xin, H.; Zhu, H., Breaking adsorption-energy scaling limitations of electrocatalytic nitrate reduction on intermetallic CuPd nanocubes by machine-learned insights. Nature Communications 2022, 13 (1), 2338.
29. Zhang, Y.; Zhao, Y.; Chen, Z.; Wang, L.; Zhou, L.; Wu, P.; Wang, F.; Ou, P., Fe/Cu Composite Electrode Prepared by Electrodeposition and Its Excellent Behavior in Nitrate Electrochemical Removal. Journal of The Electrochemical Society 2018, 165 (9), E420.
30. Calle-Vallejo, F.; Huang, M.; Henry, J. B.; Koper, M. T. M.; Bandarenka, A. S., Theoretical design and experimental implementation of Ag/Au electrodes for the electrochemical reduction of nitrate. Physical Chemistry Chemical Physics 2013, 15 (9), 3196-3202.
31. Chen, F.-Y.; Wu, Z.-Y.; Gupta, S.; Rivera, D. J.; Lambeets, S. V.; Pecaut, S.; Kim, J. Y. T.; Zhu, P.; Finfrock, Y. Z.; Meira, D. M.; King, G.; Gao, G.; Xu, W.; Cullen, D. A.; Zhou, H.; Han, Y.; Perea, D. E.; Muhich, C. L.; Wang, H., Efficient conversion of low-concentration nitrate sources into ammonia on a Ru-dispersed Cu nanowire electrocatalyst. Nature Nanotechnology 2022, 17 (7), 759-767.
32. Xuanhao Wu, M. N., Srishti Gupta, Adam Chismar, Kiheon Hong, Hunter Jacobs, Wenqing Zhang, Kali Rigby, Tayler Hedtke, Qingxiao Wang, Eli Stavitski, Michael S. Wong, Christopher Muhich, and Jae-Hong Kim, Contrasting Capability of Single Atom Palladium for Thermocatalytic versus Electrocatalytic Nitrate Reduction Reaction. (unpublished).
33. Frost, A. A., Oxidation Potential-Free Energy Diagrams. Journal of the American Chemical Society 1951, 73 (6), 2680-2682.
34. Sun, J.; Garg, S.; Xie, J.; Zhang, C.; Waite, T. D., Electrochemical Reduction of Nitrate with Simultaneous Ammonia Recovery Using a Flow Cathode Reactor. Environmental Science & Technology 2022, 56 (23), 17298-17309.
35. Grimme, S.; Antony, J.; Ehrlich, S.; Krieg, H., A consistent and accurate ab initio parametrization of density functional dispersion correction (DFT-D) for the 94 elements H-Pu. J Chem Phys 2010, 132 (15), 154104.
36. Kresse, G.; Joubert, D., From ultrasoft pseudopotentials to the projector augmented-wave method. Physical Review B 1999, 59 (3), 1758-1775.

37. Tran, R.; Xu, Z.; Radhakrishnan, B.; Winston, D.; Sun, W.; Persson, K. A.; Ong, S. P., Surface energies of elemental crystals. Scientific Data 2016, 3 (1), 160080.
38. Henkelman, G.; Uberuaga, B. P.; Jónsson, H., A climbing image nudged elastic band method for finding saddle points and minimum energy paths. J. Chem. Phys. 2000, 113 (22), 9901-9904.
39. Wang, V.; Xu, N.; Liu, J.-C.; Tang, G.; Geng, W.-T., VASPKIT: A user-friendly interface facilitating high-throughput computing and analysis using VASP code. Computer Physics Communications 2021, 267, 108033.
40. Yu, M.; Trinkle, D. R., Accurate and efficient algorithm for Bader charge integration. The Journal of Chemical Physics 2011, 134 (6), 064111.
41. Nelson, R.; Ertural, C.; George, J.; Deringer, V. L.; Hautier, G.; Dronskowski, R., LOBSTER: Local orbital projections, atomic charges, and chemical-bonding analysis from projector-augmented-wave-based density-functional theory. Journal of Computational Chemistry 2020, 41 (21), 1931-1940.
42. Pinchon, D.; Hoggan, P. E., Rotation matrices for real spherical harmonics: general rotations of atomic orbitals in space-fixed axes. Journal of Physics A: Mathematical and Theoretical 2007, 40 (7), 1597-1610.
43. Momma, K.; Izumi, F., VESTA 3 for three-dimensional visualization of crystal, volumetric and morphology data. Journal of applied crystallography 2011, 44 (6), 1272-1276.
44. Koper, M. T. M., Volcano Activity Relationships for Proton-Coupled Electron Transfer Reactions in Electrocatalysis. Topics in Catalysis 2015, 58 (18), 1153-1158.
45. Allison, T. C., NIST-JANAF Thermochemical Tables - SRD 13. National Institute of Standards and Technology: 2013.
46. Handbook of Chemistry and Physics 103rd Edition. Internet Version 2021 ed.; Taylor & Francis Group,: 2022; Vol. 103.
47. Nørskov, J. K.; Rossmeisl, J.; Logadottir, A.; Lindqvist, L.; Kitchin, J. R.; Bligaard, T.; Jónsson, H., Origin of the Overpotential for Oxygen Reduction at a Fuel-Cell Cathode. The Journal of Physical Chemistry B 2004, 108 (46), 17886-17892.
48. Weinberg, D. R.; Gagliardi, C. J.; Hull, J. F.; Murphy, C. F.; Kent, C. A.; Westlake, B. C.; Paul, A.; Ess, D. H.; McCafferty, D. G.; Meyer, T. J., Proton-coupled electron transfer. Chem. Rev. 2012, 112 (7), 4016-4093.
49. Rostamikia, G.; Mendoza, A. J.; Hickner, M. A.; Janik, M. J., First-principles based microkinetic modeling of borohydride oxidation on a Au(111) electrode. Journal of Power Sources 2011, 196 (22), 9228-9237.
50. Nie, X.; Luo, W.; Janik, M. J.; Asthagiri, A., Reaction mechanisms of CO2 electrochemical reduction on Cu(111) determined with density functional theory. Journal of Catalysis 2014, 312, 108-122.
51. Hu, T.; Wang, C.; Wang, M.; Li, C. M.; Guo, C., Theoretical Insights into Superior Nitrate Reduction to Ammonia Performance of Copper Catalysts. ACS Catalysis 2021, 11 (23), 14417-14427.
52. Wang, Y.; Qin, X.; Shao, M., First-principles mechanistic study on nitrate reduction reactions on copper surfaces: Effects of crystal facets and pH. Journal of Catalysis 2021, 400, 62-70.

53. Lamoureux, P. S.; Singh, A. R.; Chan, K., pH Effects on Hydrogen Evolution and Oxidation over Pt(111): Insights from First-Principles. ACS Catalysis 2019, 9 (7), 6194-6201.
54. Farinazzo Bergamo Dias Martins, P.; Papa Lopes, P.; Ticianelli, E. A.; Stamenkovic, V. R.; Markovic, N. M.; Strmcnik, D., Hydrogen evolution reaction on copper: Promoting water dissociation by tuning the surface oxophilicity. Electrochemistry Communications 2019, 100, 30-33.
55. Carvalho, O. Q.; Marks, R.; Nguyen, H. K. K.; Vitale-Sullivan, M. E.; Martinez, S. C.; Árnadóttir, L.; Stoerzinger, K. A., Role of Electronic Structure on Nitrate Reduction to Ammonium: A Periodic Journey. Journal of the American Chemical Society 2022, 144 (32), 14809-14818.
56. Bronsted, J. N., Acid and Basic Catalysis. Chemical Reviews 1928, 5 (3), 231-338.
57. Evans, M. G.; Polanyi, M., Inertia and driving force of chemical reactions. Transactions of the Faraday Society 1938, 34 (0), 11-24.

CHAPTER 9

CONCLUSIONS AND RECOMMENDATIONS FOR FUTURE WORK

9.1 Conclusion

In my Ph.D., I investigated two water remediation processes - adsorption and catalytic reduction - using density functional theory. My focus was on understanding the surface mechanisms that control the adsorption of selenate on Al_2O_3 and Fe_2O_3, as well as the nitrate reduction reaction on the Cu surface and single atom in the Cu surface. The DFT-derived adsorption energies are validated against the experimental adsorption isotherms. The reaction pathway calculated using the DFT are also used to understand the trends observed in nitrate reduction experiments. This work highlights the critical steps in the adsorption and reaction mechanisms that dictate selectivity towards toxic oxo-anions, and how these mechanisms can be altered to achieve desirable outputs.

Overall, I concluded that the water network on metal-oxide surfaces controlled the adsorption of toxic oxo-anion and altering it is critical to find effective solutions to selective and efficient adsorption. This can be done by changing the facet of different metal-oxide of searching for alternative materials with non-uniform water structure on the surface. I also found that single coordinated H_2O molecules are easier to displace from the metal-oxide surface as compared to singly or triply coordinated OH ions. Therefore, materials that have excess protons near neutral pH can potentially provide better adsorption in inner-sphere configuration. For nitrate reduction, I found that even though the single atoms still follow the linear relationship for reaction energies, the BEP relationships between activation barriers and reaction energies are disruptive. The single atom catalysts (Mo, Ru and Ni) are more likely to be selective for NH_3 production as they can limit the

mobility of N^* adsorbed species as compared to N_2 formation. A more detailed summary and conclusion can be found in Chapters 3 to 8.

9.1.1 Understanding the effect of surface properties that controls Selenate adsorption on (012) α-Al_2O_3

In Chapter 3, the adsorption of selenate was investigated on the Al_2O_3 surface in the aqueous phase, as a function of adsorption configuration, surface protonation, and selenate ionization. A hybrid solvent model was developed to accurately compare the adsorption energies for charged oxo-anions in inner- and outer-sphere configurations. The adsorption energies derived from DFT were used to develop the adsorption isotherm as a function of pH, which matched the experimental results. Through correlations between surface properties and adsorption energies, the water network was found to control the adsorption of oxo-anions. I also discovered that adsorption energies calculated without the surface water molecules were anti-corelated to adsorption energies derived using hybrid solvent model, which means they cannot be used to predict adsorption energies.

9.1.2 Understanding the effect of single atom cationic defect sites in α-Al2O3 (012) surface on selenate and sulfate adsorption

In Chapter 4, I investigated the adsorption of selenate and sulfate on a single atom cationic defect in both protonated and neutral Al_2O_3 surfaces to isolate the role of the cation on adsorption energies. Using DFT calculations and the HSM model, eleven different single atoms were investigated to determine if change in cation can improve the adsorption efficiency. The surface water network still was found to control the oxo-anion adsorption and strongly outweighs direct cationic effects. However, cation substitutions do contribute by slightly altering the charge of surface protons and changing bond lengths, which then

modifies adsorption energies. Additionally, bulkier cations allowed the binding of selenate and sulfate in an inner-sphere bidentate configuration, rather than an outer-sphere configuration, by breaking the weaker sub-surface bond in acidic conditions. This study also showcases the ability of Ti^{+3} to selectively reduce selenate into selenite, and I believe this can be further explored where Ti^{+3} is more stable.

9.1.3 Adsorption of Se(VI), Se(IV) and As(V) oxo-anions on neutral (012) and (001) hematite surfaces

In Chapter 5, the effect of hematite facets and oxo-anions on adsorption energies are investigated using DFT. Initially, the neutral water network was calculated on [012] and [001] Fe_2O_3 surfaces using DFT calculations and compared it with experimental data. The adsorption trends of selenate on [012] and [001] hematite surfaces confirmed that the water network strongly controls adsorption energy. However, both the number of H-bonds and the average length of H-bonds control adsorption energies. Similarly, the changes in the water network control the configurational changes of selenate, selenite, and arsenate adsorption on the [012] Fe_2O_3 surface. However, the linear relationship between the water network and adsorption energy changes upon changing the oxo-anion, suggesting that the adsorption energy for different oxo-anions cannot be solely predicted by water network changes.

9.1.4 Electrochemical reduction of NO3- towards NH3 production using dispersed Ru single atom in Cu metal catalyst: an Ab-Initio Study

In Chapter 6, the nitrate reduction reaction mechanism was investigated on Cu, Ru, and Ru single atom substituted in Cu surface. The entropic, solvation and protonation effect on the adsorption of ionic species was included by using DFT energies of their neutral

counterparts and a Hess cycle. Computational Hydrogen Electrode model was used to include the experimental potential effects in calculating the adsorption energies, reactional energies, and activation barriers. The nitrate reduction activity on Cu surface was found to be poor due to lower exothermic adsorption of NO_3^- and higher reduction to NO_2^-. The nitrate reduction experienced higher competition from the Hydrogen evolution reaction on Ru surface. On Ru-SAC, the adsorption of water was found to be endothermic, and the adsorption of nitrate was found to be more exothermic than on Cu surface. Moreover, due to the localization of N^*-species near the Ru single atom, the selectivity towards NH_3 was found to be higher than on Ru surface.

9.1.5 Understanding electrochemical vs. thermochemical nitrate reduction on dispersed Pd-single atoms in Cu Metal Catalyst using density functional theory

In Chapter 7, I investigated the differences between thermochemical and electrochemical nitrate reduction on Pd-single atoms substituted in Cu surface. The H_2 pressure in the thermochemical process was equilibrated to find surface potential using open circuit potential. The main difference between electrochemical and thermochemical nitrate reduction is the pH of operation. In electrochemical nitrate reduction, the pH of the surface increases due to the generation of OH- ions, which improves the activity of nitrate reduction. In thermochemical reduction, the pH remains near neutral, resulting in weaker adsorption of NO_3^- reduction and a higher desorption of NO_2^-. In both mechanisms, on Pd-single atom, the generated N^* hops onto the Cu sites where they preferentially bind to other N^* species to form N_2.

9.1.6 Predicting the activity and selectivity of electrocatalytic and thermochemical nitrate reduction on single atom alloy in Cu surface

In Chapter 8, I investigated the nitrate reduction mechanism on nine single atom alloys substituted in Cu [111] surface as a function of pH and potential. Nitrate readily reduces to NO_2^- and absorbs the Cu surface. Increasing pH and potential decreases the ability of surface O^* to hydrogenate, thus poisoning the catalyst surface. Conversely, decreasing pH and potential makes the adsorption of nitrate less exothermic, leading to decreased activity of nitrate reduction. The Ti and W single atom alloys exothermically adsorb H_2O, which competes with nitrate reduction. Pt, Au, and In are not active sites as nitrate and other N-species prefer to adsorb on Cu sites. Mo, Ru, and Ni are selective towards nitrate reduction and selectively reduces to form NH_3. On Pd-SAA, N^*-species hop between Cu and Pd sites, finally forming N_2 on the Cu surface after dissociating NO_2^* and subsequently HNO^* to N^* on Pd site.

9.2 Recommendations for future work

The research conducted here provides a framework for studying adsorption in an aqueous environment and nitrate reduction reactions on single atom alloys as a function of pH and potential. These models or frameworks can be expanded to a variety of other systems and used to perform high-throughput calculations to identify more selective adsorbents and catalysts. Other potential research avenues are suggested below:

9.2.1 Adsorption of toxic oxo-anions

The selective adsorption of selenate on adsorbents is one of the most complex challenges due to its stable structure, particularly when studying its adsorption compared to sulfate. My work focused on understanding the fundamental mechanisms that control

adsorption energies. I used a process of elimination to determine that water network controls the adsorption of selenate. However, the role of oxo-anion chemical and physical properties has not been explored properly. To this end, I propose that the role of oxo-anion properties, such as cation species, oxo-anion size and protonation, bond lengths and angles, and charge on species, should be explored in more detail in future research.

Moreover, more avenues to find the water network structure on top of different metal-oxide surfaces in neutral and acidic environments should be explored using simple calculations, as they critically affect the adsorption energies. Performing adsorption studies on the wrong water network would lead to incorrect results. I also propose conducting a high-throughput investigation to calculate the absorption of different oxo-anions on multiple facets of metal-oxides using a hybrid solvent model. This extensive dataset should be used to find correlations between water network, oxo-anion and crystal lattice descriptors from Chapters 3-5, and adsorption energies.

The DFT calculated adsorption energies can be used to find the equilibrium constants to calculate the Point of Zero Charge (PZC) of the surface, as well as to develop adsorption isotherms as a function of pH and concentration. However, DFT does not calculate the repulsion forces and double-layer forces that also affect the adsorption isotherm. Therefore, it is still necessary to include another method of accounting for the repulsion forces and double-layer effects to develop more realistic adsorption isotherms.

From the studies performed in Chapters 3 and 4, I found that the adsorption is more exothermic below the point of zero charge on metal-oxide surfaces. Therefore, metal-oxides with high Point of Zero Charge, i.e., metal-oxides that are protonated in neutral

environments, should be explored for higher adsorption capacity under near-neutral water conditions.

Finally, I found that single atom Ti^{+3} was able to selectively reduce Selenate into selenite due to its location of d-band. I believe this can be explored further where Ti^{+3} is more stable to selectively reduce selenate.

9.2.2 Electrochemical nitrate reduction

Electrochemical nitrate reduction (NRR), powered by electricity from renewable resources, is a sustainable method of converting toxic nitrate into benign (N2) or value-added products (NH3). In my research I investigated higher activities of single atom substitution of precious metals (e.g., Pd and Ru) in inexpensive electrode (e.g. Cu) to increase the activity of NRR as compared to competitive HER reaction using density functional theory. I found a strong correlation between the b-band center and the trends in reaction and adsorption energies. However, the single atom catalyst surfaces do not follow BEP relationships as transition states do not occur in the same configuration on all the substitutions. The DFT calculation performed here can provide information for higher activity and selective, however, cannot inform the % of selectivity on single atom catalysts. Therefore, a thorough kinetic study using Monte-Carlo simulations is required to calculate the turnover frequency, study the build-up on different species over the surface and calculate the dynamic selectivity of NRR as a function of time for batch reactor.

Apart from Pd, Ru and Ni, Mo-single atom alloy in Cu is predicted to have high NRR activity and selectivity towards NH_3. I propose synthesizing the Mo-SAC in Cu surface as an alternative inexpensive catalyst. Moreover, since d-band center can inform about the activity of NRR, I propose performing a d-band center study to calculate

adsorption energies for single atom substitutions between Mo and Pd atoms to determine more substitutions for cheaper and more efficient NRR.

Even though single atom substitutions were clearly more efficient in selective reduction to NH_3, the reduction to N_2 was not nearly as selective as NH_3 on any researched single atom substitutions on Cu surface. However, if the substrate from Cu is replaced to other species that strongly favor N_2, higher selectivity towards N_2 gas can be achieved. Therefore, a study exploring the effect of substrate on activity and selectivity should be performed to discover more catalysts for higher N_2 selectivity.

Finally, one of the biggest barriers to performing DFT calculations is performing activation barrier calculations using NEBs. They are time consuming and require at least 5X number of computational nodes, which limits their use for high-throughput calculations. Moreover, this means informed decisions are needed regarding the limited reaction steps that are explored in detail to calculate the activation barriers. Therefore, machine learning-assisted NEB methods should be explored for faster calculations of activation barriers.

REFERENCES

A., B., A., S., N., K., M.-J., G., & J., J. (2007). Surface termination of hematite at environmental oxygen pressures: Experimental surface phase diagram. Phys. Rev. B, 75, 233406.

Åke Olin, B. N., Lars-Olof Öhman, Evgeniy Osadchii and Erik Rosén. Chemical Thermodynamics of Selenium. Retrieved from

Al-Abadleh, H. A., & Grassian, V. H. (2003). FT-IR Study of Water Adsorption on Aluminum Oxide Surfaces. Langmuir, 19(2), 341-347. doi:10.1021/la026208a

Ali, I. (2012). New Generation Adsorbents for Water Treatment. Chemical Reviews, 112(10), 5073-5091. doi:10.1021/cr300133d

Ali, I., & Shrivastava, V. (2021). Recent advances in technologies for removal and recovery of selenium from (waste)water: A systematic review. Journal of Environmental Management, 294, 112926. doi:https://doi.org/10.1016/j.jenvman.2021.112926

Allison, T. C. (2013). NIST-JANAF Thermochemical Tables - SRD 13. National Institute of Standards and Technology.

Alvarez, P. J. J., Chan, C. K., Elimelech, M., Halas, N. J., & Villagran, D. (2018). Emerging opportunities for nanotechnology to enhance water security. Nat Nanotechnol, 13(8), 634-641. doi:10.1038/s41565-018-0203-2

Ashok, V., & Hait, S. (2015). Remediation of nitrate-contaminated water by solid-phase denitrification process—a review. Environmental Science and Pollution Research, 22(11), 8075-8093. doi:10.1007/s11356-015-4334-9

Awual, M. R., El-Safty, S. A., & Jyo, A. (2011). Removal of trace arsenic(V) and phosphate from water by a highly selective ligand exchange adsorbent. Journal of Environmental Sciences, 23(12), 1947-1954. doi:https://doi.org/10.1016/S1001-0742(10)60645-6

Awual, M. R., Hasan, M. M., & Khaleque, M. A. (2015). Efficient selenium(IV) detection and removal from water by tailor-made novel conjugate adsorbent. Sensors and Actuators B: Chemical, 209, 194-202. doi:https://doi.org/10.1016/j.snb.2014.11.010

Awual, M. R., Shenashen, M. A., Yaita, T., Shiwaku, H., & Jyo, A. (2012). Efficient arsenic(V) removal from water by ligand exchange fibrous adsorbent. Water Research, 46(17), 5541-5550. doi:https://doi.org/10.1016/j.watres.2012.07.038

Awual, M. R., Yaita, T., Suzuki, S., & Shiwaku, H. (2015). Ultimate selenium(IV) monitoring and removal from water using a new class of organic ligand based

composite adsorbent. Journal of Hazardous Materials, 291, 111-119. doi:https://doi.org/10.1016/j.jhazmat.2015.02.066

Ayotte, J. D., Medalie, L., Qi, S. L., Backer, L. C., & Nolan, B. T. (2017). Estimating the High-Arsenic Domestic-Well Population in the Conterminous United States. Environmental Science & Technology, 51(21), 12443-12454. doi:10.1021/acs.est.7b02881

Azizian, S., Bashiri, H., & Iloukhani, H. (2008). Statistical Rate Theory Approach to Kinetics of Competitive Adsorption at the Solid/Solution Interface. The Journal of Physical Chemistry C, 112(27), 10251-10255. doi:10.1021/jp802278e

Bachrach, S. M. (2008). Microsolvation of Glycine: A DFT Study. The Journal of Physical Chemistry A, 112(16), 3722-3730. doi:10.1021/jp711048c

Bae, S.-Y., Mahmood, J., Jeon, I.-Y., & Baek, J.-B. (2020). Recent advances in ruthenium-based electrocatalysts for the hydrogen evolution reaction. Nanoscale Horizons, 5(1), 43-56. doi:10.1039/C9NH00485H

Bishayee, B., Chatterjee, R. P., Ruj, B., Chakrabortty, S., & Nayak, J. (2022). Strategic management of nitrate pollution from contaminated water using viable adsorbents: An economic assessment-based review with possible policy suggestions. Journal of Environmental Management, 303, 114081. doi:https://doi.org/10.1016/j.jenvman.2021.114081

Blöchl, P. E. (1994). Projector augmented-wave method. Physical Review B, 50(24), 17953-17979. doi:10.1103/PhysRevB.50.17953

Bondi, A. (1964). van der Waals Volumes and Radii. The Journal of Physical Chemistry, 68(3), 441-451. doi:10.1021/j100785a001

Borah, S. N., Sen, S., Sarma, H., & Pakshirajan, K. (2021). Biological Remediation of Selenium in Soil and Water. In Handbook of Assisted and Amendment: Enhanced Sustainable Remediation Technology (pp. 403-421).

Born, M., & Oppenheimer, R. (1927). Zur Quantentheorie der Molekeln. Annalen der Physik, 389(20), 457-484. doi:https://doi.org/10.1002/andp.19273892002

Börsig, N., Scheinost, A. C., Schild, D., & Neumann, T. (2021). Mechanisms of selenium removal by partially oxidized magnetite nanoparticles for wastewater remediation. Applied Geochemistry, 132, 105062. doi:https://doi.org/10.1016/j.apgeochem.2021.105062

Bratby, J. (2016). Coagulation and Flocculation in Water and Wastewater Treatment – Third Edition: IWA Publishing.

Bronsted, J. N. (1928). Acid and Basic Catalysis. Chemical Reviews, 5(3), 231-338. doi:10.1021/cr60019a001

Cai, J., Wei, Y., Cao, A., Huang, J., Jiang, Z., Lu, S., & Zang, S.-Q. (2022). Electrocatalytic nitrate-to-ammonia conversion with ~100% Faradaic efficiency via single-atom alloying. Applied Catalysis B: Environmental, 316, 121683. doi:https://doi.org/10.1016/j.apcatb.2022.121683

Calle-Vallejo, F., Huang, M., Henry, J. B., Koper, M. T. M., & Bandarenka, A. S. (2013). Theoretical design and experimental implementation of Ag/Au electrodes for the electrochemical reduction of nitrate. Physical Chemistry Chemical Physics, 15(9), 3196-3202. doi:10.1039/C2CP44620K

Can, B. Z., Boncukcuoglu, R., Yilmaz, A. E., & Fil, B. A. (2014). Effect of some operational parameters on the arsenic removal by electrocoagulation using iron electrodes. Journal of Environmental Health Science and Engineering, 12(1), 95. doi:10.1186/2052-336X-12-95

Capdevila-Cortada, M. (2019). Electrifying the Haber–Bosch. Nature Catalysis, 2(12), 1055-1055. doi:10.1038/s41929-019-0414-4

Carneiro, M. A., Pintor, A. M. A., Boaventura, R. A. R., & Botelho, C. M. S. (2021). Current Trends of Arsenic Adsorption in Continuous Mode: Literature Review and Future Perspectives. Sustainability, 13(3), 1186. Retrieved from https://www.mdpi.com/2071-1050/13/3/1186

Carvalho, O. Q., Marks, R., Nguyen, H. K. K., Vitale-Sullivan, M. E., Martinez, S. C., Árnadóttir, L., & Stoerzinger, K. A. (2022). Role of Electronic Structure on Nitrate Reduction to Ammonium: A Periodic Journey. Journal of the American Chemical Society, 144(32), 14809-14818. doi:10.1021/jacs.2c05673

Casas, J. M., Alvarez, F., & Cifuentes, L. (2000). Aqueous speciation of sulfuric acid–cupric sulfate solutions. Chemical Engineering Science, 55(24), 6223-6234. doi:https://doi.org/10.1016/S0009-2509(00)00421-8

Catalano, J. G., Park, C., Zhang, Z., & Fenter, P. (2006). Termination and Water Adsorption at the α-Al2O3 (012)−Aqueous Solution Interface. Langmuir, 22(10), 4668-4673. doi:10.1021/la060177s

Cavalca, L., Corsini, A., Zaccheo, P., Andreoni, V., & Muyzer, G. (2013). Microbial transformations of arsenic: perspectives for biological removal of arsenic from water. Future Microbiology, 8(6), 753-768. doi:10.2217/fmb.13.38

Cavanagh, J. B. (2000). EXPERIMENTAL AND CLINICAL NEUROTOXICOLOGY. Second edition. Brain, 123(12), 2571-2573. doi:10.1093/brain/123.12.2571

Chelikowsky, J. R. (2011). 1.01 - Electrons in Semiconductors: Empirical and ab initio Pseudopotential Theories. In P. Bhattacharya, R. Fornari, & H. Kamimura (Eds.), Comprehensive Semiconductor Science and Technology (pp. 1-41). Amsterdam: Elsevier.

Chen, F.-Y., Wu, Z.-Y., Gupta, S., Rivera, D. J., Lambeets, S. V., Pecaut, S., . . . Wang, H. (2022). Efficient conversion of low-concentration nitrate sources into ammonia on a Ru-dispersed Cu nanowire electrocatalyst. Nature Nanotechnology, 17(7), 759-767. doi:10.1038/s41565-022-01121-4

Chen, H., Shepsko, C., & SenGupta, A. K. (2021). Use of a Novel Bio-Nano-IX Process to Remove SeO42– or Se(VI) from Contaminated Water in the Presence of Competing Sulfate (SO42–). ACS ES&T Water, 1(8), 1859-1867. doi:10.1021/acsestwater.1c00126

Chen, X., Lam, K. F., Zhang, Q., Pan, B., Arruebo, M., & Yeung, K. L. (2009). Synthesis of Highly Selective Magnetic Mesoporous Adsorbent. The Journal of Physical Chemistry C, 113(22), 9804-9813. doi:10.1021/jp9018052

Chiter, F., Nguyen, V. B., Tarrat, N., Benoit, M., Tang, H., & Lacaze-Dufaure, C. (2016). Effect of van der Waals corrections on DFT-computed metallic surface properties. Materials Research Express, 3(4), 046501. doi:10.1088/2053-1591/3/4/046501

Corum, K. W., Abbaspour Tamijani, A., & Mason, S. E. (2018). Density Functional Theory Study of Arsenate Adsorption onto Alumina Surfaces. Minerals, 8(3). doi:10.3390/min8030091

Corum, K. W., & Mason, S. E. (2016). Using density functional theory to study shape-reactivity relationships in Keggin Al-nanoclusters. Water Research, 102, 413-420. doi:https://doi.org/10.1016/j.watres.2016.06.043

Cramer, C. J. (2017). Foundations of Molecular Orbital Theory. In Essentials of Computational Chemistry (Vol. 2nd, pp. 125-130): Wiley.

Davis, T. Z., Stegelmeier, B. L., & Hall, J. O. (2014). Analysis in Horse Hair as a Means of Evaluating Selenium Toxicoses and Long-Term Exposures. Journal of Agricultural and Food Chemistry, 62(30), 7393-7397. doi:10.1021/jf500861p

DeSimone, L. A., McMahon, P. B., & Rosen, M. R. (2015). The quality of our Nation's waters: Water quality in principal aquifers of the United States, 1991-2010 (1360). Retrieved from Reston, VA: http://pubs.er.usgs.gov/publication/cir1360

Dima, G. E., Beltramo, G. L., & Koper, M. T. M. (2005). Nitrate reduction on single-crystal platinum electrodes. Electrochimica Acta, 50(21), 4318-4326. doi:https://doi.org/10.1016/j.electacta.2005.02.093

Dion, M., Rydberg, H., Schröder, E., Langreth, D. C., & Lundqvist, B. I. (2004). Van der Waals Density Functional for General Geometries. Physical Review Letters, 92(24), 246401. doi:10.1103/PhysRevLett.92.246401

Dirac, P. A. M., & Fowler, R. H. (1929). Quantum mechanics of many-electron systems. Proceedings of the Royal Society of London. Series A, Containing Papers of a Mathematical and Physical Character, 123(792), 714-733. doi:10.1098/rspa.1929.0094

. Distribution of Arsenic in the Environment. (1977). In N. R. C. U. C. o. M. a. B. E. o. E. Pollutants. (Ed.), Arsenic: Medical and Biologic Effects of Environmental Pollutants. (Vol. 3). Washington (DC): National Academies Press (US).

Doane, T. A. (2017). The Abiotic Nitrogen Cycle. ACS Earth and Space Chemistry, 1(7), 411-421. doi:10.1021/acsearthspacechem.7b00059

Dortsiou, M., & Kyriacou, G. (2009). Electrochemical reduction of nitrate on bismuth cathodes. Journal of Electroanalytical Chemistry, 630(1), 69-74. doi:https://doi.org/10.1016/j.jelechem.2009.02.019

Dudarev, S. L., Botton, G. A., Savrasov, S. Y., Humphreys, C. J., & Sutton, A. P. (1998). Electron-energy-loss spectra and the structural stability of nickel oxide: An LSDA+U study. Physical Review B, 57(3), 1505-1509. doi:10.1103/PhysRevB.57.1505

Dzade, N. Y., Roldan, A., & De Leeuw, N. H. (2014). A Density Functional Theory Study of the Adsorption of Benzene on Hematite (α-Fe2O3) Surfaces. Minerals, 4(1), 89-115. Retrieved from https://www.mdpi.com/2075-163X/4/1/89

Elzinga, E. J., Tang, Y., McDonald, J., DeSisto, S., & Reeder, R. J. (2009). Macroscopic and spectroscopic characterization of selenate, selenite, and chromate adsorption at the solid–water interface of γ-Al2O3. Journal of Colloid and Interface Science, 340(2), 153-159. doi:https://doi.org/10.1016/j.jcis.2009.08.033

Evans, M. G., & Polanyi, M. (1938). Inertia and driving force of chemical reactions. Transactions of the Faraday Society, 34(0), 11-24. doi:10.1039/TF9383400011

Fang, Y., Catron, B., Zhang, Y., Zhao, L., Caruso, J. a., & Hu, Q. (2010). Distribution and in Vitro Availability of Selenium in Selenium-Containing Storage Protein from Selenium-Enriched Rice Utilizing Optimized Extraction. Journal of Agricultural and Food Chemistry, 58(17), 9731-9738. doi:10.1021/jf100934p

Farinazzo Bergamo Dias Martins, P., Papa Lopes, P., Ticianelli, E. A., Stamenkovic, V. R., Markovic, N. M., & Strmcnik, D. (2019). Hydrogen evolution reaction on copper: Promoting water dissociation by tuning the surface oxophilicity. Electrochemistry Communications, 100, 30-33. doi:https://doi.org/10.1016/j.elecom.2019.01.006

Fernández-Martínez, A., & Charlet, L. (2009). Selenium environmental cycling and bioavailability: a structural chemist point of view. Reviews in Environmental Science and Bio/Technology, 8(1), 81-110. doi:10.1007/s11157-009-9145-3

Fewtrell, L. (2004). Drinking-Water Nitrate, Methemoglobinemia, and Global Burden of Disease: A Discussion. Environmental Health Perspectives, 112(14), 1371-1374. doi:doi:10.1289/ehp.7216

Filippov, L. O., Silva, L. A., Pereira, A. M., Bastos, L. C., Correia, J. C. G., Silva, K., . . . Foucaud, Y. (2022). Molecular models of hematite, goethite, kaolinite, and quartz: Surface terminations, ionic interactions, nano topography, and water coordination. Colloids and Surfaces A: Physicochemical and Engineering Aspects, 650, 129585. doi:https://doi.org/10.1016/j.colsurfa.2022.129585

Fox, P. M., LeDuc, D. L., Hussein, H., Lin, Z.-q., & Terry, N. (2002). Selenium Speciation in Soils and Plants. In Biogeochemistry of Environmentally Important Trace Elements (Vol. 835, pp. 339-354): American Chemical Society.

Frost, A. A. (1951). Oxidation Potential-Free Energy Diagrams. Journal of the American Chemical Society, 73(6), 2680-2682. doi:10.1021/ja01150a074

Fu, Y., Wang, J., Liu, Q., & Zeng, H. (2014). Water-dispersible magnetic nanoparticle–graphene oxide composites for selenium removal. Carbon, 77, 710-721. doi:https://doi.org/10.1016/j.carbon.2014.05.076

Fu, Z.-J., Jiang, S.-K., Chao, X.-Y., Zhang, C.-X., Shi, Q., Wang, Z.-Y., . . . Sun, S.-P. (2022). Removing miscellaneous heavy metals by all-in-one ion exchange-nanofiltration membrane. Water Research, 222, 118888. doi:https://doi.org/10.1016/j.watres.2022.118888

Futera, Z., & English, N. J. (2021). Water Breakup at Fe2O3–Hematite/Water Interfaces: Influence of External Electric Fields from Nonequilibrium Ab Initio Molecular Dynamics. The Journal of Physical Chemistry Letters, 12(29), 6818-6826. doi:10.1021/acs.jpclett.1c01479

Gao, Q., Pillai, H. S., Huang, Y., Liu, S., Mu, Q., Han, X., . . . Zhu, H. (2022). Breaking adsorption-energy scaling limitations of electrocatalytic nitrate reduction on intermetallic CuPd nanocubes by machine-learned insights. Nature Communications, 13(1), 2338. doi:10.1038/s41467-022-29926-w

Garcia-Segura, S., Lanzarini-Lopes, M., Hristovski, K., & Westerhoff, P. (2018). Electrocatalytic reduction of nitrate: Fundamentals to full-scale water treatment applications. Applied Catalysis B: Environmental, 236, 546-568. doi:https://doi.org/10.1016/j.apcatb.2018.05.041

German, M. S., Watkins, T. A., Chowdhury, M., Chatterjee, P., Rahman, M., Seingheng, H., & SenGupta, A. K. (2019). Evidence of economically sustainable village-scale

microenterprises for arsenic remediation in developing countries. Environmental science & technology, 53(3), 1078-1086.

Goh, K.-H., & Lim, T.-T. (2004). Geochemistry of inorganic arsenic and selenium in a tropical soil: effect of reaction time, pH, and competitive anions on arsenic and selenium adsorption. Chemosphere, 55(6), 849-859. doi:https://doi.org/10.1016/j.chemosphere.2003.11.041

Goldberg, S. (2013). Modeling Selenite Adsorption Envelopes on Oxides, Clay Minerals, and Soils using the Triple Layer Model. Soil Science Society of America Journal, 77(1), 64-71. doi:https://doi.org/10.2136/sssaj2012.0205

Goldberg, S. (2014). Modeling Selenate Adsorption Behavior on Oxides, Clay Minerals, and Soils Using the Triple Layer Model. Soil Science, 179, 568 576.

Goldberg, S., Lesch, S. M., & Suarez, D. L. (2007). Predicting selenite adsorption by soils using soil chemical parameters in the constant capacitance model. Geochimica et Cosmochimica Acta, 71(23), 5750-5762. doi:https://doi.org/10.1016/j.gca.2007.04.036

Grassian, V. H. (2008). When Size Really Matters: Size-Dependent Properties and Surface Chemistry of Metal and Metal Oxide Nanoparticles in Gas and Liquid Phase Environments. The Journal of Physical Chemistry C, 112(47), 18303-18313. doi:10.1021/jp806073t

Grimme, S., Antony, J., Ehrlich, S., & Krieg, H. (2010). A consistent and accurate ab initio parametrization of density functional dispersion correction (DFT-D) for the 94 elements H-Pu. J Chem Phys, 132(15), 154104. doi:10.1063/1.3382344

Guimarães, W. G., de Lima, G. F., & Duarte, H. A. (2021). Comparative DFT study of the oxy(hydr)oxides of iron and aluminum – structural, electronic and surface properties. Surface Science, 708, 121821. doi:https://doi.org/10.1016/j.susc.2021.121821

Gupta, S., Anh Nguyen, N., & Muhich, C. L. (2022). Surface water H-bonding network is key controller of selenate adsorption on [012] α-alumina: An Ab-initio study. Journal of Colloid and Interface Science, 617, 136-146. doi:https://doi.org/10.1016/j.jcis.2022.02.128

Gupta, S., Chismar, A., & Muhich, C. L. (2023). Understanding the Effect of Single Atom Cationic Defect Sites in an Al2O3 (012) Surface on Altering Selenate and Sulfate Adsorption: An Ab Initio Study. The Journal of Physical Chemistry C. doi: https://doi.org/10.1021/acs.jpcc.3c00098

Han, J., Kim, M., & Ro, H.-M. (2020). Factors modifying the structural configuration of oxyanions and organic acids adsorbed on iron (hydr)oxides in soils. A review.

Environmental Chemistry Letters, 18(3), 631-662. doi:10.1007/s10311-020-00964-4

Handbook of Chemistry and Physics 103rd Edition. (2022). (M. J. D. Thomas J. Bruno, Alan J. Anderson, Judith N. Currano, Steve Freiman, Jeremy Garritano, Daryn Johnson, Ye Li , David R. Lide, David Martinsen, Leah Rae McEwen, Donna Wrublewski Ed. Internet Version 2021 ed. Vol. 103): Taylor & Francis Group,.

He, G., Zhang, M., & Pan, G. (2009). Influence of pH on Initial Concentration Effect of Arsenate Adsorption on TiO2 Surfaces: Thermodynamic, DFT, and EXAFS Interpretations. The Journal of Physical Chemistry C, 113(52), 21679-21686. doi:10.1021/jp906019e

Health, I. D. o. P. (2010). Nitrates In Drinking Water. Division of Environmental Health. Retrieved from http://www.idph.state.il.us/envhealth/factsheets/NitrateFS.htm

Henkelman, G., Uberuaga, B. P., & Jónsson, H. (2000). A climbing image nudged elastic band method for finding saddle points and minimum energy paths. The Journal of Chemical Physics, 113(22), 9901-9904. doi:10.1063/1.1329672

Hesham Mohamed Abdal-Salam Yehia, S. M. S. (2021). Drinking Water Treatment: pH Adjustment Using Natural Physical Field. Journal of Biosciences and Medicines, 9(6), 55-66.

Hohenberg, P., & Kohn, W. (1964). Inhomogeneous Electron Gas. Physical Review, 136(3B), B864-B871. doi:10.1103/PhysRev.136.B864

Holmes, A. B., & Gu, F. X. (2016). Emerging nanomaterials for the application of selenium removal for wastewater treatment. Environmental Science: Nano, 3(5), 982-996. doi:10.1039/C6EN00144K

Hu, C., Chen, Q., Chen, G., Liu, H., & Qu, J. (2015). Removal of Se(IV) and Se(VI) from drinking water by coagulation. Separation and Purification Technology, 142, 65-70. doi:https://doi.org/10.1016/j.seppur.2014.12.028

Hu, T., Wang, C., Wang, M., Li, C. M., & Guo, C. (2021). Theoretical Insights into Superior Nitrate Reduction to Ammonia Performance of Copper Catalysts. ACS Catalysis, 11(23), 14417-14427. doi:10.1021/acscatal.1c03666

Hua, M., Zhang, S., Pan, B., Zhang, W., Lv, L., & Zhang, Q. (2012). Heavy metal removal from water/wastewater by nanosized metal oxides: A review. Journal of Hazardous Materials, 211-212, 317-331. doi:https://doi.org/10.1016/j.jhazmat.2011.10.016

Huang, X., Hou, X., Song, F., Zhao, J., & Zhang, L. (2016). Facet-Dependent Cr(VI) Adsorption of Hematite Nanocrystals. Environ Sci Technol, 50(4), 1964-1972. doi:10.1021/acs.est.5b05111

Hubbard, J., & Flowers, B. H. (1964). Electron correlations in narrow energy bands. II. The degenerate band case. Proceedings of the Royal Society of London. Series A. Mathematical and Physical Sciences, 277(1369), 237-259. doi:doi:10.1098/rspa.1964.0019

Huno, S. K. M., Rene, E. R., van Hullebusch, E. D., & Annachhatre, A. P. (2018). Nitrate removal from groundwater: a review of natural and engineered processes. Journal of Water Supply: Research and Technology-Aqua, 67(8), 885-902. doi:10.2166/aqua.2018.194

Inam, M. A., Khan, R., Lee, K. H., & Wie, Y. M. (2021). Removal of Arsenic Oxyanions from Water by Ferric Chloride-Optimization of Process Conditions and Implications for Improving Coagulation Performance. Int J Environ Res Public Health, 18(18). doi:10.3390/ijerph18189812

Ippolito, J. A., Scheckel, K. G., & Barbarick, K. A. (2009). Selenium adsorption to aluminum-based water treatment residuals. Journal of Colloid and Interface Science, 338(1), 48-55. doi:https://doi.org/10.1016/j.jcis.2009.06.023

Ishikawa, S., Sekine, S., Miura, N., Suyama, K., Arihara, K., & Itoh, M. (2004). Removal of selenium and arsenic by animal biopolymers. Biol Trace Elem Res, 102(1-3), 113-127. doi:10.1385/bter:102:1-3:113

Jakub, Z., Kraushofer, F., Bichler, M., Balajka, J., Hulva, J., Pavelec, J., . . . Parkinson, G. S. (2019). Partially Dissociated Water Dimers at the Water–Hematite Interface. ACS Energy Letters, 4(2), 390-396. doi:10.1021/acsenergylett.8b02324

Jakub, Z., Meier, M., Kraushofer, F., Balajka, J., Pavelec, J., Schmid, M., . . . Parkinson, G. S. (2021). Rapid oxygen exchange between hematite and water vapor. Nature Communications, 12(1), 6488. doi:10.1038/s41467-021-26601-4

Jeffrey N. Grossman, A. E. G., Peter N. Schweitzer, Paul G. Schruben. (2008). National Geochemical Survey database (Database). Retrieved from https://mrdata.usgs.gov/geochem/method.php. (2004-1001). from U.S. Geological Survey https://mrdata.usgs.gov/geochem/method.php

Jegadeesan, G., Mondal, K., & Lalvani, S. B. (2003). Comparative study of selenite adsorption on carbon based adsorbents and activated alumina. Environmental Technology, 24(8), 1049-1059. doi:10.1080/09593330309385644

Ji, Y., Li, L., & Wang, Y.-t. (2020). Selenium removal by activated alumina in batch and continuous-flow reactors. Water Environment Research, 92(1), 51-59. doi:https://doi.org/10.1002/wer.1159

Johansson, C. L., Paul, N. A., de Nys, R., & Roberts, D. A. (2015). The complexity of biosorption treatments for oxyanions in a multi-element mine effluent. Journal of

Environmental Management, 151, 386-392. doi:https://doi.org/10.1016/j.jenvman.2014.11.031

Johnston, C. P., & Chrysochoou, M. (2014). Mechanisms of chromate adsorption on hematite. Geochimica et Cosmochimica Acta, 138, 146-157. doi:https://doi.org/10.1016/j.gca.2014.04.030

Johnston, C. P., & Chrysochoou, M. (2016). Mechanisms of Chromate, Selenate, and Sulfate Adsorption on Al-Substituted Ferrihydrite: Implications for Ferrihydrite Surface Structure and Reactivity. Environmental Science & Technology, 50(7), 3589-3596. doi:10.1021/acs.est.5b05529

Jones, G. D., Droz, B., Greve, P., Gottschalk, P., Poffet, D., McGrath, S. P., . . . Winkel, L. H. E. (2017). Selenium deficiency risk predicted to increase under future climate change. Proceedings of the National Academy of Sciences, 114(11), 2848-2853. doi:10.1073/pnas.1611576114

Jordan, N., Franzen, C., Lützenkirchen, J., Foerstendorf, H., Hering, D., Weiss, S., . . . Brendler, V. (2018). Adsorption of selenium(vi) onto nano transition alumina. Environmental Science: Nano, 5(7), 1661-1669. doi:10.1039/C8EN00293B

Kamel, R. M., Shahat, A., Hegazy, W. H., Khodier, E. M., & Awual, M. R. (2019). Efficient toxic nitrite monitoring and removal from aqueous media with ligand based conjugate materials. Journal of Molecular Liquids, 285, 20-26. doi:https://doi.org/10.1016/j.molliq.2019.04.060

Kapoor, A., & Viraraghavan, T. (1997). Nitrate Removal From Drinking Water—Review. Journal of Environmental Engineering, 123(4), 371-380. doi:doi:10.1061/(ASCE)0733-9372(1997)123:4(371)

Katsounaros, I., Ipsakis, D., Polatides, C., & Kyriacou, G. (2006). Efficient electrochemical reduction of nitrate to nitrogen on tin cathode at very high cathodic potentials. Electrochimica Acta, 52(3), 1329-1338. doi:https://doi.org/10.1016/j.electacta.2006.07.034

Katsoyiannis, I. A., & Zouboulis, A. I. (2004). Application of biological processes for the removal of arsenic from groundwaters. Water Research, 38(1), 17-26. doi:https://doi.org/10.1016/j.watres.2003.09.011

Kaur, N., Sharma, S., Kaur, S., & Nayyar, H. (2014). Selenium in agriculture: a nutrient or contaminant for crops? Archives of Agronomy and Soil Science, 60(12), 1593-1624. doi:10.1080/03650340.2014.918258

Kim, H., Choi, J.-M., & Goddard, W. A., III. (2012). Universal Correction of Density Functional Theory to Include London Dispersion (up to Lr, Element 103). The Journal of Physical Chemistry Letters, 3(3), 360-363. doi:10.1021/jz2016395

Kitayama, M., & Glaeser, A. M. (2002). The Wulff Shape of Alumina: III, Undoped Alumina. Journal of the American Ceramic Society, 85(3), 611-622. doi:10.1111/j.1151-2916.2002.tb00140.x

Klimeš, J., Bowler, D. R., & Michaelides, A. (2010). Chemical accuracy for the van der Waals density functional. Journal of Physics: Condensed Matter, 22(2), 022201. doi:10.1088/0953-8984/22/2/022201

Klimeš, J., Bowler, D. R., & Michaelides, A. (2011). Van der Waals density functionals applied to solids. Physical Review B, 83(19), 195131. doi:10.1103/PhysRevB.83.195131

Knobeloch, L., Salna, B., Hogan, A., Postle, J., & Anderson, H. (2000). Blue babies and nitrate-contaminated well water. Environmental Health Perspectives, 108(7), 675-678. doi:doi:10.1289/ehp.00108675

Koebke, K. J., & Pecoraro, V. L. (2018). Development of de Novo Copper Nitrite Reductases: Where We Are and Where We Need To Go. ACS Catalysis, 8(9), 8046-8057. doi:10.1021/acscatal.8b02153

Koper, M. T. M. (2015). Volcano Activity Relationships for Proton-Coupled Electron Transfer Reactions in Electrocatalysis. Topics in Catalysis, 58(18), 1153-1158. doi:10.1007/s11244-015-0489-3

Kreitler, C. W., & Jones, D. C. (1975). Natural Soil Nitrate: The Cause of the Nitrate Contamination of Ground Water in Runnels County, Texasa. Ground Water, 13, 53-62.

Kresse, G., & Furthmuller, J. (1996). Efficient iterative schemes for ab initio total-energy calculations using a plane-wave basis set. Physical Review B, 54(16), 11169-11186. doi:DOI 10.1103/PhysRevB.54.11169

Kresse, G., & Furthmüller, J. (1996). Efficiency of ab-initio total energy calculations for metals and semiconductors using a plane-wave basis set. Computational Materials Science, 6(1), 15-50. doi:10.1016/0927-0256(96)00008-0

Kresse, G., & Joubert, D. (1999). From ultrasoft pseudopotentials to the projector augmented-wave method. Physical Review B, 59(3), 1758-1775. doi:10.1103/PhysRevB.59.1758

Krukau, A. V., Vydrov, O. A., Izmaylov, A. F., & Scuseria, G. E. (2006). Influence of the exchange screening parameter on the performance of screened hybrid functionals. The Journal of Chemical Physics, 125(22), 224106. doi:10.1063/1.2404663

Kubicki, J. D., Kabengi, N., Chrysochoou, M., & Bompoti, N. (2018). Density functional theory modeling of chromate adsorption onto ferrihydrite nanoparticles. Geochemical Transactions, 19(1), 8. doi:10.1186/s12932-018-0053-8

Kubicki, J. D., Kwon, K. D., Paul, K. W., & Sparks, D. L. (2007). Surface complex structures modelled with quantum chemical calculations: carbonate, phosphate, sulphate, arsenate and arsenite. European Journal of Soil Science, 58(4), 932-944. doi:https://doi.org/10.1111/j.1365-2389.2007.00931.x

Kubicki, J. D., Paul, K. W., Kabalan, L., Zhu, Q., Mrozik, M. K., Aryanpour, M., . . . Strongin, D. R. (2012). ATR–FTIR and Density Functional Theory Study of the Structures, Energetics, and Vibrational Spectra of Phosphate Adsorbed onto Goethite. Langmuir, 28(41), 14573-14587. doi:10.1021/la303111a

Kunkel, C., Viñes, F., & Illas, F. (2019). Surface Activity of Early Transition-Metal Oxycarbides: CO2 Adsorption Case Study. The Journal of Physical Chemistry C, 123(6), 3664-3671. doi:10.1021/acs.jpcc.8b11942

Lagauche, M., Larmier, K., Jolimaitre, E., Barthelet, K., Chizallet, C., Favergeon, L., & Pijolat, M. (2017). Thermodynamic Characterization of the Hydroxyl Group on the γ-Alumina Surface by the Energy Distribution Function. The Journal of Physical Chemistry C, 121(31), 16770-16782. doi:10.1021/acs.jpcc.7b02498

Lahiri, N., Song, D., Zhang, X., Huang, X., Stoerzinger, K. A., Carvalho, O. Q., . . . Rosso, K. M. (2023). Interplay between Facets and Defects during the Dissociative and Molecular Adsorption of Water on Metal Oxide Surfaces. Journal of the American Chemical Society, 145(5), 2930-2940. doi:10.1021/jacs.2c11291

Lamoureux, P. S., Singh, A. R., & Chan, K. (2019). pH Effects on Hydrogen Evolution and Oxidation over Pt(111): Insights from First-Principles. ACS Catalysis, 9(7), 6194-6201. doi:10.1021/acscatal.9b00268

Le, H.-L. T., Lazzari, R., Goniakowski, J., Cavallotti, R., Chenot, S., Noguera, C., . . . Mataigne, J.-M. (2017). Tuning Adhesion at Metal/Oxide Interfaces by Surface Hydroxylation. The Journal of Physical Chemistry C, 121(21), 11464-11471. doi:10.1021/acs.jpcc.7b02456

Lee, K., Murray, É. D., Kong, L., Lundqvist, B. I., & Langreth, D. C. (2010). Higher-accuracy van der Waals density functional. Physical Review B, 82(8), 081101. doi:10.1103/PhysRevB.82.081101

Legon, A. C., & Millen, D. J. (1987). Angular geometries and other properties of hydrogen-bonded dimers: a simple electrostatic interpretation of the success of the electron-pair model. Chemical Society Reviews, 16(0), 467-498. doi:10.1039/CS9871600467

Lenz, M., & Lens, P. N. (2009). The essential toxin: the changing perception of selenium in environmental sciences. Sci Total Environ, 407(12), 3620-3633. doi:10.1016/j.scitotenv.2008.07.056

Leung, K., & Criscenti, L. J. (2017). Lead and selenite adsorption at water–goethite interfaces from first principles. Journal of Physics: Condensed Matter, 29(36), 365101. doi:10.1088/1361-648x/aa7e4f

Levanov, A. V., Isaikina, O. Y., & Lunin, V. V. (2017). Dissociation constant of nitric acid. Russian Journal of Physical Chemistry A, 91(7), 1221-1228. doi:10.1134/S0036024417070196

Li, C., Ku, N., Liu, Y., Pan, J., Chai, B., Hu, F., . . . Ren, S. (2020). Magnetically active transition metal cation-substituted alumina. Nanotechnology, 31(10), 105703. doi:10.1088/1361-6528/ab59fa

Li, J., Zhan, G., Yang, J., Quan, F., Mao, C., Liu, Y., . . . Yu, J. C. (2020). Efficient Ammonia Electrosynthesis from Nitrate on Strained Ruthenium Nanoclusters. Journal of the American Chemical Society, 142(15), 7036-7046. doi:10.1021/jacs.0c00418

Li, P., Damron, J. T., Bryantsev, V. S., Johnson, K. R., Stamberga, D., Mahurin, S. M., . . . Jansone-Popova, S. (2021). Guanidinium-Based Ionic Covalent-Organic Nanosheets for Sequestration of Cr(VI) and As(V) Oxoanions in Water. ACS Applied Nano Materials, 4(12), 13319-13328. doi:10.1021/acsanm.1c02845

Li, P., Jin, Z., Fang, Z., & Yu, G. (2021). A single-site iron catalyst with preoccupied active centers that achieves selective ammonia electrosynthesis from nitrate. Energy & Environmental Science, 14(6), 3522-3531. doi:10.1039/D1EE00545F

Li, Y., Zhang, L. A., Qin, Y., Chu, F., Kong, Y., Tao, Y., . . . Liu, M. (2018). Crystallinity Dependence of Ruthenium Nanocatalyst toward Hydrogen Evolution Reaction. ACS Catalysis, 8(7), 5714-5720. doi:10.1021/acscatal.8b01609

Lide, D. R. (2004). CRC handbook of chemistry and physics (Vol. 85): CRC press.

Liechtenstein, A. I., Anisimov, V. I., & Zaanen, J. (1995). Density-functional theory and strong interactions: Orbital ordering in Mott-Hubbard insulators. Physical Review B, 52(8), R5467-R5470. doi:10.1103/PhysRevB.52.R5467

Lim, K. T., Shukor, M. Y., & Wasoh, H. (2014). Physical, chemical, and biological methods for the removal of arsenic compounds. Biomed Res Int, 2014, 503784. doi:10.1155/2014/503784

Lin, T.-F., & Wu, J.-K. (2001). Adsorption of Arsenite and Arsenate within Activated Alumina Grains: Equilibrium and Kinetics. Water Research, 35(8), 2049-2057. doi:https://doi.org/10.1016/S0043-1354(00)00467-X

Liu, J.-X., Richards, D., Singh, N., & Goldsmith, B. R. (2019). Activity and Selectivity Trends in Electrocatalytic Nitrate Reduction on Transition Metals. ACS Catalysis, 9(8), 7052-7064. doi:10.1021/acscatal.9b02179

Lounsbury, A. W., Wang, R., Plata, D. L., Billmyer, N., Muhich, C., Kanie, K., . . . Zimmerman, J. B. (2019). Preferential adsorption of selenium oxyanions onto {110} and {012} nano-hematite facets. J Colloid Interface Sci, 537, 465-474. doi:10.1016/j.jcis.2018.11.018

Lounsbury, A. W., Yamani, J. S., Johnston, C. P., Larese-Casanova, P., & Zimmerman, J. B. (2016). The role of counter ions in nano-hematite synthesis: Implications for surface area and selenium adsorption capacity. Journal of Hazardous Materials, 310, 117-124. doi:https://doi.org/10.1016/j.jhazmat.2016.01.078

Luo, J., Yu, D., Hristovski, K. D., Fu, K., Shen, Y., Westerhoff, P., & Crittenden, J. C. (2021). Critical Review of Advances in Engineering Nanomaterial Adsorbents for Metal Removal and Recovery from Water: Mechanism Identification and Engineering Design. Environmental Science & Technology, 55(8), 4287-4304. doi:10.1021/acs.est.0c07936

Luoma, S. N., & Presser, T. S. (2009). Emerging Opportunities in Management of Selenium Contamination. Environmental Science & Technology, 43(22), 8483-8487. doi:10.1021/es900828h

Ma, Z., Shan, C., Liang, J., & Tong, M. (2018). Efficient adsorption of Selenium(IV) from water by hematite modified magnetic nanoparticles. Chemosphere, 193, 134-141. doi:https://doi.org/10.1016/j.chemosphere.2017.11.005

MacFarquhar, J. K., Broussard, D. L., Melstrom, P., Hutchinson, R., Wolkin, A., Martin, C., . . . Jones, T. F. (2010). Acute selenium toxicity associated with a dietary supplement. Arch Intern Med, 170(3), 256-261. doi:10.1001/archinternmed.2009.495

Marinho, B. A., Cristóvão, R. O., Boaventura, R. A. R., & Vilar, V. J. P. (2019). As(III) and Cr(VI) oxyanion removal from water by advanced oxidation/reduction processes—a review. Environmental Science and Pollution Research, 26(3), 2203-2227. doi:10.1007/s11356-018-3595-5

Marjanovic, V., Peric-Grujic, A., Ristic, M., Marinkovic, A., Markovic, R., Onjia, A., & Sljivic-Ivanovic, M. (2020). Selenate Adsorption from Water Using the Hydrous Iron Oxide-Impregnated Hybrid Polymer. Metals, 10(12). doi:10.3390/met10121630

Mathew, K., Sundararaman, R., Letchworth-Weaver, K., Arias, T. A., & Hennig, R. G. (2014). Implicit solvation model for density-functional study of nanocrystal surfaces and reaction pathways. J Chem Phys, 140(8), 084106. doi:10.1063/1.4865107

McBriarty, M. E., von Rudorff, G. F., Stubbs, J. E., Eng, P. J., Blumberger, J., & Rosso, K. M. (2017). Dynamic Stabilization of Metal Oxide–Water Interfaces. Journal of the American Chemical Society, 139(7), 2581-2584. doi:10.1021/jacs.6b13096

Medford, A. J., & Hatzell, M. C. (2017). Photon-Driven Nitrogen Fixation: Current Progress, Thermodynamic Considerations, and Future Outlook. ACS Catalysis, 7(4), 2624-2643. doi:10.1021/acscatal.7b00439

Meher, A. K., Jadhav, A., Labhsetwar, N., & Bansiwal, A. (2019). Simultaneous removal of selenite and selenate from drinking water using mesoporous activated alumina. Applied Water Science, 10(1), 10. doi:10.1007/s13201-019-1090-x

Michael F. Chislock, E. D., Rachel A. Zitomer, Alan E. Wilson. (2013). Eutrophication: Causes, Consequences, and Controls in Aquatic Ecosystems. Nature Education Knowledge, 4(4), 10.

Min, B., Gao, Q., Yan, Z., Han, X., Hosmer, K., Campbell, A., & Zhu, H. (2021). Powering the Remediation of the Nitrogen Cycle: Progress and Perspectives of Electrochemical Nitrate Reduction. Industrial & Engineering Chemistry Research, 60(41), 14635-14650. doi:10.1021/acs.iecr.1c03072

Momma, K., & Izumi, F. (2011). VESTA 3 for three-dimensional visualization of crystal, volumetric and morphology data. Journal of applied crystallography, 44(6), 1272-1276. doi:10.1107/S0021889811038970

Monkhorst, H. J., & Pack, J. D. (1976). Special points for Brillouin-zone integrations. Physical Review B, 13(12), 5188-5192. doi:10.1103/PhysRevB.13.5188

National Primary Drinking Water Regulations. (2022). Ground Water and Drinking Water. Retrieved from https://www.epa.gov/ground-water-and-drinking-water/national-primary-drinking-water-regulations

Nations, U. THE 17 GOALS. THE 17 GOALS. Retrieved from https://sdgs.un.org/goals

Nayak, D. C. (1995). Adsorption of oxy-anions of selenium and arsenic at oxide/water interfaces. (M.S.). University of Nevada, Reno, United States – Nevada. Dissertations & Theses Global database. (1377700)

Neal, R. H., & Sposito, G. (1989). Selenate Adsorption on Alluvial Soils. Soil Science Society of America Journal, 53(1), 70-74. doi:https://doi.org/10.2136/sssaj1989.03615995005300010013x

Nelson, R., Ertural, C., George, J., Deringer, V. L., Hautier, G., & Dronskowski, R. (2020). LOBSTER: Local orbital projections, atomic charges, and chemical-bonding analysis from projector-augmented-wave-based density-functional theory. Journal of Computational Chemistry, 41(21), 1931-1940. doi:https://doi.org/10.1002/jcc.26353

Nie, X., Luo, W., Janik, M. J., & Asthagiri, A. (2014). Reaction mechanisms of CO2 electrochemical reduction on Cu(111) determined with density functional theory. Journal of Catalysis, 312, 108-122. doi:https://doi.org/10.1016/j.jcat.2014.01.013

Nitrate and Drinking Water from Private Wells. (2015). Centers for Disease Control and Prevention.

Niu, H., Zhang, Z., Wang, X., Wan, X., Shao, C., & Guo, Y. (2021). Theoretical Insights into the Mechanism of Selective Nitrate-to-Ammonia Electroreduction on Single-Atom Catalysts. Advanced Functional Materials, 31(11), 2008533. doi:https://doi.org/10.1002/adfm.202008533

Nørskov, J. K., Rossmeisl, J., Logadottir, A., Lindqvist, L., Kitchin, J. R., Bligaard, T., & Jónsson, H. (2004). Origin of the Overpotential for Oxygen Reduction at a Fuel-Cell Cathode. The Journal of Physical Chemistry B, 108(46), 17886-17892. doi:10.1021/jp047349j

Olson, O. E. (1986). Selenium Toxicity in Animals with Emphasis on Man. Journal of the American College of Toxicology, 5(1), 45-70. doi:10.3109/10915818609140736

Ong, S. P., Cholia, S., Jain, A., Brafman, M., Gunter, D., Ceder, G., & Persson, K. A. (2015). The Materials Application Programming Interface (API): A simple, flexible and efficient API for materials data based on REpresentational State Transfer (REST) principles. Computational Materials Science, 97, 209-215. doi:https://doi.org/10.1016/j.commatsci.2014.10.037

Ortega, A., Oliva, I., Contreras, K. E., González, I., Cruz-Díaz, M. R., & Rivero, E. P. (2017). Arsenic removal from water by hybrid electro-regenerated anion exchange resin/electrodialysis process. Separation and Purification Technology, 184, 319-326. doi:https://doi.org/10.1016/j.seppur.2017.04.050

Padungthon, S., German, M., Wiriyathamcharoen, S., & SenGupta, A. K. (2015). Polymeric anion exchanger supported hydrated Zr (IV) oxide nanoparticles: a reusable hybrid sorbent for selective trace arsenic removal. Reactive and Functional Polymers, 93, 84-94.

Paidar, M., Roušar, I., & Bouzek, K. (1999). Electrochemical removal of nitrate ions in waste solutions after regeneration of ion exchange columns. Journal of Applied Electrochemistry, 29(5), 611-617. doi:10.1023/A:1026423218899

Patra, A., Bates, J. E., Sun, J., & Perdew, J. P. (2017). Properties of real metallic surfaces: Effects of density functional semilocality and van der Waals nonlocality. Proceedings of the National Academy of Sciences, 114(44), E9188-E9196. doi:doi:10.1073/pnas.1713320114

Paul, K. W., Kubicki, J. D., & Sparks, D. L. (2007). Sulphate adsorption at the Fe (hydr)oxide–H2O interface: comparison of cluster and periodic slab DFT predictions. European Journal of Soil Science, 58(4), 978-988. doi:10.1111/j.1365-2389.2007.00936.x

Peak, D. (2006). Adsorption mechanisms of selenium oxyanions at the aluminum oxide/water interface. Journal of Colloid and Interface Science, 303(2), 337-345. doi:https://doi.org/10.1016/j.jcis.2006.08.014

Peak, D., & Sparks, D. L. (2002). Mechanisms of Selenate Adsorption on Iron Oxides and Hydroxides. Environmental Science & Technology, 36(7), 1460-1466. doi:10.1021/es0156643

Peng, C., Chen, J., Hu, P., & Wang, H. (2021). Molecular Adsorption Kinetics: Nonlinear Entropy–Enthalpy Loss Quantified by Constrained AIMD and Insights into the Adsorption-Site Determination on Metal Oxides. The Journal of Physical Chemistry C, 125(20), 10974-10982. doi:10.1021/acs.jpcc.1c02537

Peng, H., Yang, Z.-H., Perdew, J. P., & Sun, J. (2016). Versatile van der Waals Density Functional Based on a Meta-Generalized Gradient Approximation. Physical Review X, 6(4), 041005. doi:10.1103/PhysRevX.6.041005

Pennino, M. J., Compton, J. E., & Leibowitz, S. G. (2017). Trends in Drinking Water Nitrate Violations Across the United States. Environmental Science & Technology, 51(22), 13450-13460. doi:10.1021/acs.est.7b04269

Perdew, J. P., Burke, K., & Ernzerhof, M. (1996). Generalized Gradient Approximation Made Simple. Physical Review Letters, 77(18), 3865-3868. doi:10.1103/PhysRevLett.77.3865

Perendija, J., Veličković, Z. S., Cvijetić, I., Lević, S., Marinković, A. D., Milošević, M., & Onjia, A. (2021). Bio-membrane based on modified cellulose, lignin, and tannic acid for cation and oxyanion removal: Experimental and theoretical study. Process Safety and Environmental Protection, 147, 609-625. doi:https://doi.org/10.1016/j.psep.2020.12.027

Pérez-Gallent, E., Figueiredo, M. C., Katsounaros, I., & Koper, M. T. M. (2017). Electrocatalytic reduction of Nitrate on Copper single crystals in acidic and alkaline solutions. Electrochimica Acta, 227, 77-84. doi:https://doi.org/10.1016/j.electacta.2016.12.147

Peri, J. B. (1965). A Model for the Surface of γ-Alumina1. The Journal of Physical Chemistry, 69(1), 220-230. doi:10.1021/j100885a033

Pinchon, D., & Hoggan, P. E. (2007). Rotation matrices for real spherical harmonics: general rotations of atomic orbitals in space-fixed axes. Journal of Physics A: Mathematical and Theoretical, 40(7), 1597-1610. doi:10.1088/1751-8113/40/7/011

Pincus, L. N., Rudel, H. E., Petrović, P. V., Gupta, S., Westerhoff, P., Muhich, C. L., & Zimmerman, J. B. (2020). Exploring the Mechanisms of Selectivity for Environmentally Significant Oxo-Anion Removal during Water Treatment: A

Review of Common Competing Oxo-Anions and Tools for Quantifying Selective Adsorption. Environmental Science & Technology, 54(16), 9769-9790. doi:10.1021/acs.est.0c01666

Plattes, M., Bertrand, A., Schmitt, B., Sinner, J., Verstraeten, F., & Welfring, J. (2007). Removal of tungsten oxyanions from industrial wastewater by precipitation, coagulation and flocculation processes. J Hazard Mater, 148(3), 613-615. doi:10.1016/j.jhazmat.2007.03.016

Podgorski, J., & Berg, M. (2020). Global threat of arsenic in groundwater. Science, 368(6493), 845-850. doi:doi:10.1126/science.aba1510

Poissier, A., Ganeshan, S., & Fernández-Serra, M. V. (2011). The role of hydrogen bonding in water–metal interactions. Physical Chemistry Chemical Physics, 13(8), 3375-3384. doi:10.1039/C0CP00994F

Progress towards the Sustainable Development Goals. (2021). Retrieved from High-level political forum on sustainable development, convened under the auspices of the Economic and Social Council: https://undocs.org/en/E/2021/58

R. Cardoso, B., Hare, D. J., Lind, M., McLean, C. A., Volitakis, I., Laws, S. M., . . . Roberts, B. R. (2017). The APOE ε4 Allele Is Associated with Lower Selenium Levels in the Brain: Implications for Alzheimer's Disease. ACS Chemical Neuroscience, 8(7), 1459-1464. doi:10.1021/acschemneuro.7b00014

Rabiul Awual, M., Munjur Hasan, M., Ihara, T., & Yaita, T. (2014). Mesoporous silica based novel conjugate adsorbent for efficient selenium(IV) detection and removal from water. Microporous and Mesoporous Materials, 197, 331-338. doi:https://doi.org/10.1016/j.micromeso.2014.07.005

Radjenovic, J., & Sedlak, D. L. (2015). Challenges and Opportunities for Electrochemical Processes as Next-Generation Technologies for the Treatment of Contaminated Water. Environmental Science & Technology, 49(19), 11292-11302. doi:10.1021/acs.est.5b02414

Rahman, K. Z., Wiessner, A., Kuschk, P., van Afferden, M., Mattusch, J., & Müller, R. A. (2014). Removal and fate of arsenic in the rhizosphere of Juncus effusus treating artificial wastewater in laboratory-scale constructed wetlands. Ecological Engineering, 69, 93-105. doi:https://doi.org/10.1016/j.ecoleng.2014.03.050

Rajan, S. S. S. (1979). ADSORPTION OF SELENITE, PHOSPHATE AND SULPHATE ON HYDROUS ALUMINA. Journal of Soil Science, 30(4), 709-718. doi:https://doi.org/10.1111/j.1365-2389.1979.tb01020.x

Ramadugu, S. K., & Mason, S. E. (2015). DFT Study of Antimony(V) Oxyanion Adsorption on α-Al2O3(1$\bar{1}$02). The Journal of Physical Chemistry C, 119(32), 18149-18159. doi:10.1021/acs.jpcc.5b02061

Ratnaike, R. N. (2003). Acute and chronic arsenic toxicity. Postgraduate Medical Journal, 79(933), 391-396. doi:10.1136/pmj.79.933.391

Rehman, H. U. (2001). Methemoglobinemia. The Western journal of medicine, 175(3), 193-196. doi:10.1136/ewjm.175.3.193

Rezvani, F., Sarrafzadeh, M.-H., Ebrahimi, S., & Oh, H.-M. (2019). Nitrate removal from drinking water with a focus on biological methods: a review. Environmental Science and Pollution Research, 26(2), 1124-1141. doi:10.1007/s11356-017-9185-0

Roman, M., Jitaru, P., & Barbante, C. (2013). Selenium biochemistry and its role for human health. Metallomics, 6(1), 25-54. doi:10.1039/c3mt00185g

Rostamikia, G., Mendoza, A. J., Hickner, M. A., & Janik, M. J. (2011). First-principles based microkinetic modeling of borohydride oxidation on a Au(111) electrode. Journal of Power Sources, 196(22), 9228-9237. doi:https://doi.org/10.1016/j.jpowsour.2011.07.042

Rudel, H. E., Lane, M. K. M., Muhich, C. L., & Zimmerman, J. B. (2020). Toward Informed Design of Nanomaterials: A Mechanistic Analysis of Structure–Property–Function Relationships for Faceted Nanoscale Metal Oxides. ACS Nano, 14(12), 16472-16501. doi:10.1021/acsnano.0c08356

Samatya, S., Kabay, N., Yüksel, Ü., Arda, M., & Yüksel, M. (2006). Removal of nitrate from aqueous solution by nitrate selective ion exchange resins. Reactive and Functional Polymers, 66(11), 1206-1214. doi:https://doi.org/10.1016/j.reactfunctpolym.2006.03.009

Sancha, A. M. (2006). Review of coagulation technology for removal of arsenic: case of Chile. J Health Popul Nutr, 24(3), 267-272.

Sanchis, I., Diaz, E., Pizarro, A. H., Rodriguez, J. J., & Mohedano, A. F. (2022). Nitrate reduction with bimetallic catalysts. A stability-addressed overview. Separation and Purification Technology, 290, 120750. doi:https://doi.org/10.1016/j.seppur.2022.120750

Santos, A. S. G. G., Restivo, J., Orge, C. A., Pereira, M. F. R., & Soares, O. S. G. P. (2021). Influence of organic matter formed during oxidative processes in the catalytic reduction of nitrate. Journal of Environmental Chemical Engineering, 9(4), 105545. doi:https://doi.org/10.1016/j.jece.2021.105545

Santos, S., Ungureanu, G., Boaventura, R., & Botelho, C. (2015). Selenium contaminated waters: An overview of analytical methods, treatment options and recent advances in sorption methods. Science of The Total Environment, 521-522, 246-260. doi:https://doi.org/10.1016/j.scitotenv.2015.03.107

Saunders, A. P. (1900). The Allotropic Forms of Selenium. The Journal of Physical Chemistry, 4(6), 423-513. doi:10.1021/j150024a001

Schoeman, J. J., & Steyn, A. (2003). Nitrate removal with reverse osmosis in a rural area in South Africa. Desalination, 155(1), 15-26. doi:https://doi.org/10.1016/S0011-9164(03)00235-2

Schröder, H., Creon, A., & Schwabe, T. (2015). Reformulation of the D3(Becke–Johnson) Dispersion Correction without Resorting to Higher than C6 Dispersion Coefficients. Journal of Chemical Theory and Computation, 11(7), 3163-3170. doi:10.1021/acs.jctc.5b00400

Séby, F., Potin-Gautier, M., Giffaut, E., Borge, G., & Donard, O. F. X. (2001). A critical review of thermodynamic data for selenium species at 25°C. Chemical Geology, 171(3), 173-194. doi:https://doi.org/10.1016/S0009-2541(00)00246-1

Sedlak, D. L. (2019). The Unintended Consequences of the Reverse Osmosis Revolution. Environmental Science & Technology, 53(8), 3999-4000. doi:10.1021/acs.est.9b01755

Serio, F., Miglietta, P. P., Lamastra, L., Ficocelli, S., Intini, F., De Leo, F., & De Donno, A. (2018). Groundwater nitrate contamination and agricultural land use: A grey water footprint perspective in Southern Apulia Region (Italy). Science of The Total Environment, 645, 1425-1431. doi:https://doi.org/10.1016/j.scitotenv.2018.07.241

Shannon, R. (1976). Revised effective ionic radii and systematic studies of interatomic distances in halides and chalcogenides. Acta Crystallographica Section A, 32(5), 751-767. doi:doi:10.1107/S0567739476001551

Sharma, V. K., McDonald, T. J., Sohn, M., Anquandah, G. A. K., Pettine, M., & Zboril, R. (2015). Biogeochemistry of selenium. A review. Environmental Chemistry Letters, 13(1), 49-58. doi:10.1007/s10311-014-0487-x

Sharma, V. K., Sohn, M., & McDonald, T. J. (2019). Chapter 8 - Remediation of Selenium in Water: A Review. In S. Ahuja (Ed.), Advances in Water Purification Techniques (pp. 203-218): Elsevier.

Sherman, D. M., & Randall, S. R. (2003). Surface complexation of arsenic(V) to iron(III) (hydr)oxides: structural mechanism from ab initio molecular geometries and EXAFS spectroscopy. Geochimica et Cosmochimica Acta, 67(22), 4223-4230. doi:https://doi.org/10.1016/S0016-7037(03)00237-0

Shi, Q., Yan, L., Chan, T., & Jing, C. (2015). Arsenic Adsorption on Lanthanum-Impregnated Activated Alumina: Spectroscopic and DFT Study. ACS Applied Materials & Interfaces, 7(48), 26735-26741. doi:10.1021/acsami.5b08730

Shin, H., Jung, S., Bae, S., Lee, W., & Kim, H. (2014). Nitrite Reduction Mechanism on a Pd Surface. Environmental Science & Technology, 48(21), 12768-12774. doi:10.1021/es503772x

Simmons, D. B. D., & Wallschläger, D. (2005). A critical review of the biogeochemistry and ecotoxicology of selenium in lotic and lentic environments. Environmental Toxicology and Chemistry, 24(6), 1331-1343. doi:https://doi.org/10.1897/04-176R.1

Smedley, P. L., & Kinniburgh, D. G. (2002). A review of the source, behaviour and distribution of arsenic in natural waters. Applied Geochemistry, 17(5), 517-568. doi:https://doi.org/10.1016/S0883-2927(02)00018-5

Song, B., Tian, Z., van der Weijden, R. D., Buisman, C. J. N., & Weijma, J. (2021). High-rate biological selenate reduction in a sequencing batch reactor for recovery of hexagonal selenium. Water Research, 193, 116855. doi:https://doi.org/10.1016/j.watres.2021.116855

Spalding, R. F., & Exner, M. E. (1993). Occurrence of Nitrate in Groundwater—A Review. Journal of Environmental Quality, 22(3), 392-402. doi:https://doi.org/10.2134/jeq1993.00472425002200030002x

Speck, F. D., & Cherevko, S. (2020). Electrochemical copper dissolution: A benchmark for stable CO2 reduction on copper electrocatalysts. Electrochemistry Communications, 115, 106739. doi:https://doi.org/10.1016/j.elecom.2020.106739

Staicu, L. C., van Hullebusch, E. D., Oturan, M. A., Ackerson, C. J., & Lens, P. N. (2015). Removal of colloidal biogenic selenium from wastewater. Chemosphere, 125, 130-138. doi:10.1016/j.chemosphere.2014.12.018

Stefaniak, J., Dutta, A., Verbinnen, B., Shakya, M., & Rene, E. R. (2018). Selenium removal from mining and process wastewater: a systematic review of available technologies. Journal of Water Supply: Research and Technology-Aqua, 67(8), 903-918. doi:10.2166/aqua.2018.109

Stillings, L. L., & Amacher, M. C. (2004). Chapter 17 Selenium attenuation in a wetland formed from mine drainage in the phosphoria formation, Southeast Idaho. In J. R. Hein (Ed.), Handbook of Exploration and Environmental Geochemistry (Vol. 8, pp. 467-482): Elsevier Science B.V.

Su, T., Guan, X., Gu, G., & Wang, J. (2008). Adsorption characteristics of As(V), Se(IV), and V(V) onto activated alumina: Effects of pH, surface loading, and ionic strength. Journal of Colloid and Interface Science, 326(2), 347-353. doi:https://doi.org/10.1016/j.jcis.2008.07.026

Sun, J., Garg, S., Xie, J., Zhang, C., & Waite, T. D. (2022). Electrochemical Reduction of Nitrate with Simultaneous Ammonia Recovery Using a Flow Cathode Reactor.

Environmental Science & Technology, 56(23), 17298-17309. doi:10.1021/acs.est.2c06033

Sun, W., & Ceder, G. (2013). Efficient creation and convergence of surface slabs. Surface Science, 617, 53-59. doi:https://doi.org/10.1016/j.susc.2013.05.016

Sun, W., & Ceder, G. (2018). A topological screening heuristic for low-energy, high-index surfaces. Surface Science, 669, 50-56. doi:https://doi.org/10.1016/j.susc.2017.11.007

Sung, J., Zhang, L., Tian, C., Shen, Y. R., & Waychunas, G. A. (2011). Effect of pH on the Water/α-Al2O3 (1$\bar{1}$02) Interface Structure Studied by Sum-Frequency Vibrational Spectroscopy. The Journal of Physical Chemistry C, 115(28), 13887-13893. doi:10.1021/jp2046596

Suzuki, T. M., Pacheco Tanaka, D. A., Llosa Tanco, M. A., Kanesato, M., & Yokoyama, T. (2000). Adsorption and removal of oxo-anions of arsenic and selenium on the zirconium(iv) loaded polymer resin functionalized with diethylenetriamine-N,N,N′,N′-polyacetic acid. Journal of Environmental Monitoring, 2(6), 550-555. doi:10.1039/B006738P

Taira, M., Sakakibara, K., Saeki, K., Ohira, S.-I., & Toda, K. (2020). Determination of oxoanions and water-soluble species of arsenic, selenium, antimony, vanadium, and chromium eluted in water from airborne fine particles (PM2.5): effect of acid and transition metal content of particles on heavy metal elution. Environmental Science: Processes & Impacts, 22(7), 1514-1524. doi:10.1039/D0EM00135J

Tang, W., Li, Q., Gao, S., & Shang, J. K. (2011). Arsenic (III,V) removal from aqueous solution by ultrafine α-Fe2O3 nanoparticles synthesized from solvent thermal method. Journal of Hazardous Materials, 192(1), 131-138. doi:https://doi.org/10.1016/j.jhazmat.2011.04.111

Tempio, J. S., & Zatz, J. L. (1980). Flocculation effect of xanthan gum in pharmaceutical suspensions. Journal of Pharmaceutical Sciences, 69(10), 1209-1214. doi:https://doi.org/10.1002/jps.2600691024

Torres, J., Pintos, V., Gonzatto, L., Domínguez, S., Kremer, C., & Kremer, E. (2011). Selenium chemical speciation in natural waters: Protonation and complexation behavior of selenite and selenate in the presence of environmentally relevant cations. Chemical Geology, 288(1), 32-38. doi:https://doi.org/10.1016/j.chemgeo.2011.06.015

Tran, R., Xu, Z., Radhakrishnan, B., Winston, D., Sun, W., Persson, K. A., & Ong, S. P. (2016). Surface energies of elemental crystals. Sci Data, 3, 160080. doi:10.1038/sdata.2016.80

Trussell, R., A. Trussell, AND P. Kreft. (2002). SELENIUM REMOVAL FROM GROUND WATER USING ACTIVATED ALUMINA. Retrieved from

Trussell, R. R., Trussell, A., & Kreft, P. (1980). Selenium removal from ground water using activated alumina (Vol. 1): Municipal Environmental Research Laboratory, Office of Research and ….

Ugwuja, C. G., Bayode, A. A., Olorunnisola, D., & Unuabonah, E. I. (2021). Occurrence and Management of Selenium Oxyanions in Water. In N. A. Oladoja & E. I. Unuabonah (Eds.), Progress and Prospects in the Management of Oxyanion Polluted Aqua Systems (pp. 103-128). Cham: Springer International Publishing.

Ullah, H., Lun, L., Rashid, A., Zada, N., Chen, B., Shahab, A., Wong, M. H. (2022). A critical analysis of sources, pollution, and remediation of selenium, an emerging contaminant. Environmental Geochemistry and Health. doi:10.1007/s10653-022-01354-1

Villalobos, M., Cheney, M. A., & Alcaraz-Cienfuegos, J. (2009). Goethite surface reactivity: II. A microscopic site-density model that describes its surface area-normalized variability. Journal of Colloid and Interface Science, 336(2), 412-422. doi:https://doi.org/10.1016/j.jcis.2009.04.052

Villalobos, M., & Pérez-Gallegos, A. (2008). Goethite surface reactivity: A macroscopic investigation unifying proton, chromate, carbonate, and lead(II) adsorption. Journal of Colloid and Interface Science, 326(2), 307-323. doi:https://doi.org/10.1016/j.jcis.2008.06.026

Wang, B., Li, C., Xiangyu, J., Zhu, T., & Zhang, J. Z. H. (2020). An Approach to Computing Solvent Reorganization Energy. Journal of Chemical Theory and Computation, 16(10), 6513-6519. doi:10.1021/acs.jctc.0c00672

Wang, C., Liu, Z., Hu, T., Li, J., Dong, L., Du, F., . . . Guo, C. (2021). Metasequoia-like Nanocrystal of Iron-Doped Copper for Efficient Electrocatalytic Nitrate Reduction into Ammonia in Neutral Media. ChemSusChem, 14(8), 1825-1829. doi:https://doi.org/10.1002/cssc.202100127

Wang, J., Xie, L., Li, S., Wang, J., Zhang, J., & Zeng, H. (2021). Probing the In Situ Redox Behavior of Selenium on a Pyrite Surface by Scanning Electrochemical Microscopy. The Journal of Physical Chemistry C, 125(5), 3018-3026. doi:10.1021/acs.jpcc.0c10333

Wang, L., Shi, C., Wang, L., Pan, L., Zhang, X., & Zou, J.-J. (2020). Rational design, synthesis, adsorption principles and applications of metal oxide adsorbents: a review. Nanoscale, 12(8), 4790-4815. doi:10.1039/C9NR09274A

Wang, R., DelloStritto, M., Remsing, R. C., Carnevale, V., Klein, M. L., & Borguet, E. (2019). Sodium Halide Adsorption and Water Structure at the α-

Alumina(0001)/Water Interface. The Journal of Physical Chemistry C, 123(25), 15618-15628. doi:10.1021/acs.jpcc.9b03054

Wang, R. B., Hellman, A., E., G.-R., B., T., & M., M. (2018). Initial water adsorption on hematite (α-Fe2O3) (0001): A DFT + U study

Clays and oxide minerals as catalysts and nanocatalysts in Fenton-like reactions—A review. The Journal of Chemical Physics, 148(9), 094705. doi:10.1063/1.5020358

Wang, S., Zeng, X., Lin, J., Yuan, Z., Qu, S., Zhang, B., . . . Jia, Y. (2021). Molecular Structure of Molybdate Adsorption on Goethite at pH 5–8: A Combined DFT + U, EXAFS, and Ab Initio XANES Study. The Journal of Physical Chemistry C, 125(40), 22052-22063. doi:10.1021/acs.jpcc.1c05497

Wang, V., Xu, N., Liu, J.-C., Tang, G., & Geng, W.-T. (2021). VASPKIT: A user-friendly interface facilitating high-throughput computing and analysis using VASP code. Computer Physics Communications, 267, 108033. doi:https://doi.org/10.1016/j.cpc.2021.108033

Wang, Y., Qin, X., & Shao, M. (2021). First-principles mechanistic study on nitrate reduction reactions on copper surfaces: Effects of crystal facets and pH. Journal of Catalysis, 400, 62-70. doi:https://doi.org/10.1016/j.jcat.2021.05.022

Wang, Y., Xu, A., Wang, Z., Huang, L., Li, J., Li, F., . . . Sargent, E. H. (2020). Enhanced Nitrate-to-Ammonia Activity on Copper–Nickel Alloys via Tuning of Intermediate Adsorption. Journal of the American Chemical Society, 142(12), 5702-5708. doi:10.1021/jacs.9b13347

Wang, Y., Zhou, W., Jia, R., Yu, Y., & Zhang, B. (2020). Unveiling the Activity Origin of a Copper-based Electrocatalyst for Selective Nitrate Reduction to Ammonia. Angewandte Chemie International Edition, 59(13), 5350-5354. doi:https://doi.org/10.1002/anie.201915992

Wang, Z., Ortiz, E. M., Goldsmith, B. R., & Singh, N. (2021). Comparing electrocatalytic and thermocatalytic conversion of nitrate on platinum–ruthenium alloys. Catalysis Science & Technology, 11(21), 7098-7109. doi:10.1039/D1CY01075A

Wang, Z., Richards, D., & Singh, N. (2021). Recent discoveries in the reaction mechanism of heterogeneous electrocatalytic nitrate reduction. Catalysis Science & Technology, 11(3), 705-725. doi:10.1039/D0CY02025G

Wang, Z., Zhang, H., Ren, J., Lin, X., Han, T., Liu, J., & Li, J. (2021). Predicting adsorption ability of adsorbents at arbitrary sites for pollutants using deep transfer learning. npj Computational Materials, 7(1), 19. doi:10.1038/s41524-021-00494-9

Ward, M. H., Jones, R. R., Brender, J. D., de Kok, T. M., Weyer, P. J., Nolan, B. T., . . . van Breda, S. G. (2018). Drinking Water Nitrate and Human Health: An Updated Review. Int J Environ Res Public Health, 15(7). doi:10.3390/ijerph15071557

Wei, Z., Luo, S., Xiao, R., Khalfin, R., & Semiat, R. (2017). Characterization and quantification of chromate adsorption by layered porous iron oxyhydroxide: An experimental and theoretical study. Journal of Hazardous Materials, 338, 472-481. doi:https://doi.org/10.1016/j.jhazmat.2017.06.001

Weidner, E., & Ciesielczyk, F. (2019). Removal of Hazardous Oxyanions from the Environment Using Metal-Oxide-Based Materials. Materials, 12(6). doi:10.3390/ma12060927

Weinberg, D. R., Gagliardi, C. J., Hull, J. F., Murphy, C. F., Kent, C. A., Westlake, B. C., . . . Meyer, T. J. (2012). Proton-Coupled Electron Transfer. Chemical Reviews, 112(7), 4016-4093. doi:10.1021/cr200177j

Weinberg, D. R., Gagliardi, C. J., Hull, J. F., Murphy, C. F., Kent, C. A., Westlake, B. C., . . . Meyer, T. J. (2012). Proton-coupled electron transfer. Chem. Rev., 112(7), 4016-4093.

Whiteman, L. (2010). Too Much of a Good Thing: Human Activities Overload Ecosystems with Nitrogen. In. NSF news: The U.S. National Science Foundation.

WHO, U. (2015). Progress on Sanitation and Drinking Water: 2015 Update and MDG Assessment. Retrieved from

Wijnja, H., & Schulthess, C. P. (2000). Vibrational Spectroscopy Study of Selenate and Sulfate Adsorption Mechanisms on Fe and Al (Hydr)oxide Surfaces. Journal of Colloid and Interface Science, 229(1), 286-297. doi:https://doi.org/10.1006/jcis.2000.6960

Xu, H., Zhang, R. Q., Ng, A. M. C., Djurišić, A. B., Chan, H. T., Chan, W. K., & Tong, S. Y. (2011). Splitting Water on Metal Oxide Surfaces. The Journal of Physical Chemistry C, 115(40), 19710-19715. doi:10.1021/jp2032884

Xu, T., & Catalano, J. G. (2018). Effects of Ionic Strength on Arsenate Adsorption at Aluminum Hydroxide–Water Interfaces. Soil Systems, 2(1), 1. Retrieved from https://www.mdpi.com/2571-8789/2/1/1

Xuanhao Wu, M. N., Srishti Gupta, Adam Chismar, Kiheon Hong, Hunter Jacobs, Wenqing Zhang, Kali Rigby, Tayler Hedtke, Qingxiao Wang, Eli Stavitski, Michael S. Wong, Christopher Muhich, and Jae-Hong Kim. Contrasting Capability of Single Atom Palladium for Thermocatalytic versus Electrocatalytic Nitrate Reduction Reaction. (unpublished).

Yamamoto, S., Kendelewicz, T., Newberg, J. T., Ketteler, G., Starr, D. E., Mysak, E. R., . . . Nilsson, A. (2010). Water Adsorption on α-Fe2O3(0001) at near Ambient Conditions. The Journal of Physical Chemistry C, 114(5), 2256-2266. doi:10.1021/jp909876t

Yamamura, S., & Amachi, S. (2014). Microbiology of inorganic arsenic: From metabolism to bioremediation. J Biosci Bioeng, 118(1), 1-9. doi:10.1016/j.jbiosc.2013.12.011

Yamani, J. S., Lounsbury, A. W., & Zimmerman, J. B. (2014). Adsorption of selenite and selenate by nanocrystalline aluminum oxide, neat and impregnated in chitosan beads. Water Research, 50, 373-381. doi:https://doi.org/10.1016/j.watres.2013.10.054

Yan, L., Song, J., Chan, T., & Jing, C. (2017). Insights into Antimony Adsorption on {001} TiO2: XAFS and DFT Study. Environmental Science & Technology, 51(11), 6335-6341. doi:10.1021/acs.est.7b00807

Yang, Z., Qian, J., Shan, C., Li, H., Yin, Y., & Pan, B. (2021). Toward Selective Oxidation of Contaminants in Aqueous Systems. Environmental Science & Technology, 55(21), 14494-14514. doi:10.1021/acs.est.1c05862

Yao, F., Jia, M., Yang, Q., Chen, F., Zhong, Y., Chen, S., . . . Li, X. (2021). Highly selective electrochemical nitrate reduction using copper phosphide self-supported copper foam electrode: Performance, mechanism, and application. Water Research, 193, 116881. doi:https://doi.org/10.1016/j.watres.2021.116881

Yin, Y. B., Guo, S. J., Heck, K. N., Clark, C. A., Coonrod, C. L., & Wong, M. S. (2018). Treating Water by Degrading Oxyanions Using Metallic Nanostructures. Acs Sustainable Chemistry & Engineering, 6(9), 11160-11175. doi:10.1021/acssuschemeng.8b02070

Youngran, J., Fan, M., Van Leeuwen, J., & Belczyk, J. F. (2007). Effect of competing solutes on arsenic(V) adsorption using iron and aluminum oxides. Journal of Environmental Sciences, 19(8), 910-919. doi:https://doi.org/10.1016/S1001-0742(07)60151-X

Yu, M., & Trinkle, D. R. (2011). Accurate and efficient algorithm for Bader charge integration. The Journal of Chemical Physics, 134(6), 064111. doi:10.1063/1.3553716

Zhang, M., He, G., & Pan, G. (2015). Binding mechanism of arsenate on rutile (110) and (001) planes studied using grazing-incidence EXAFS measurement and DFT calculation. Chemosphere, 122, 199-205. doi:10.1016/j.chemosphere.2014.11.053

Zhang, X., Ward, B. B., & Sigman, D. M. (2020). Global Nitrogen Cycle: Critical Enzymes, Organisms, and Processes for Nitrogen Budgets and Dynamics. Chemical Reviews, 120(12), 5308-5351. doi:10.1021/acs.chemrev.9b00613

Zhang, Y., Chen, X., Wang, W., Yin, L., & Crittenden, J. C. (2022). Electrocatalytic nitrate reduction to ammonia on defective Au1Cu (111) single-atom alloys. Applied Catalysis B: Environmental, 310, 121346. doi:https://doi.org/10.1016/j.apcatb.2022.121346

Zhang, Y., Zhao, Y., Chen, Z., Wang, L., Zhou, L., Wu, P., . . . Ou, P. (2018). Fe/Cu Composite Electrode Prepared by Electrodeposition and Its Excellent Behavior in Nitrate Electrochemical Removal. Journal of The Electrochemical Society, 165(9), E420. doi:10.1149/2.0081810jes

Zhao, M., Luo, T., Zhao, Z., Rong, H., Zhao, G., & Lei, L. (2021). Food Chemistry of Selenium and Controversial Roles of Selenium in Affecting Blood Cholesterol Concentrations. Journal of Agricultural and Food Chemistry, 69(17), 4935-4945. doi:10.1021/acs.jafc.1c00784

Zhao, Q., Huang, J.-C., He, S., & Zhou, W. (2020). Enhancement of a constructed wetland water treatment system for selenium removal. Science of The Total Environment, 714, 136741. doi:https://doi.org/10.1016/j.scitotenv.2020.136741

Zhou, B.-W., Zhang, H.-Z., Xu, Z.-L., & Tang, Y.-J. (2016). Interfacial polymerization on PES hollow fiber membranes using mixed diamines for nanofiltration removal of salts containing oxyanions and ferric ions. Desalination, 394, 176-184. doi:https://doi.org/10.1016/j.desal.2016.05.016

Zoroufchi Benis, K., McPhedran, K. N., & Soltan, J. (2022). Selenium removal from water using adsorbents: A critical review. Journal of Hazardous Materials, 424, 127603. doi:https://doi.org/10.1016/j.jhazmat.2021.127603

APPENDIX A

PROOF OF HYBRID SOLVENT MODEL FOR SELENATE ADSORPTION ON [012] ALUMINA SURFACE

Computational study of oxo-anion adsorption using multiple layers of water is, at minimum, cumbersome and expensive, and can lead to drastic changes in adsorption energy with even slight change in water orientation. Figure 1(b) shows that changing the number of water layers inconsistently changes the adsorption energy H_2SeO_4 on (012) α-Al_2O_3 because of the disordered water layers until multiple layers are employed. Ab initio molecular dynamics (AIMD) can be used to find the adsorption energy with explicit water layers by disordering the surrounding water layers over time. However, these are expensive calculations, and require significant computational power. Therefore, performing AIMD across several configurations and conditions for finding selective adsorbent material is not currently practical.

Hybrid Solvent Model (HSM) includes interfacial water effects at a modest computational cost. In the HSM, only the first highly ordered interfacial water layer is included explicitly (Figure A.1). The interfacial termination, O-Al distances, and orientation of water monolayer match previous computational work. The solvent effects beyond the first layer are considered by including a polarizable continuum dielectric in the vacuum layer (Figure A.2).

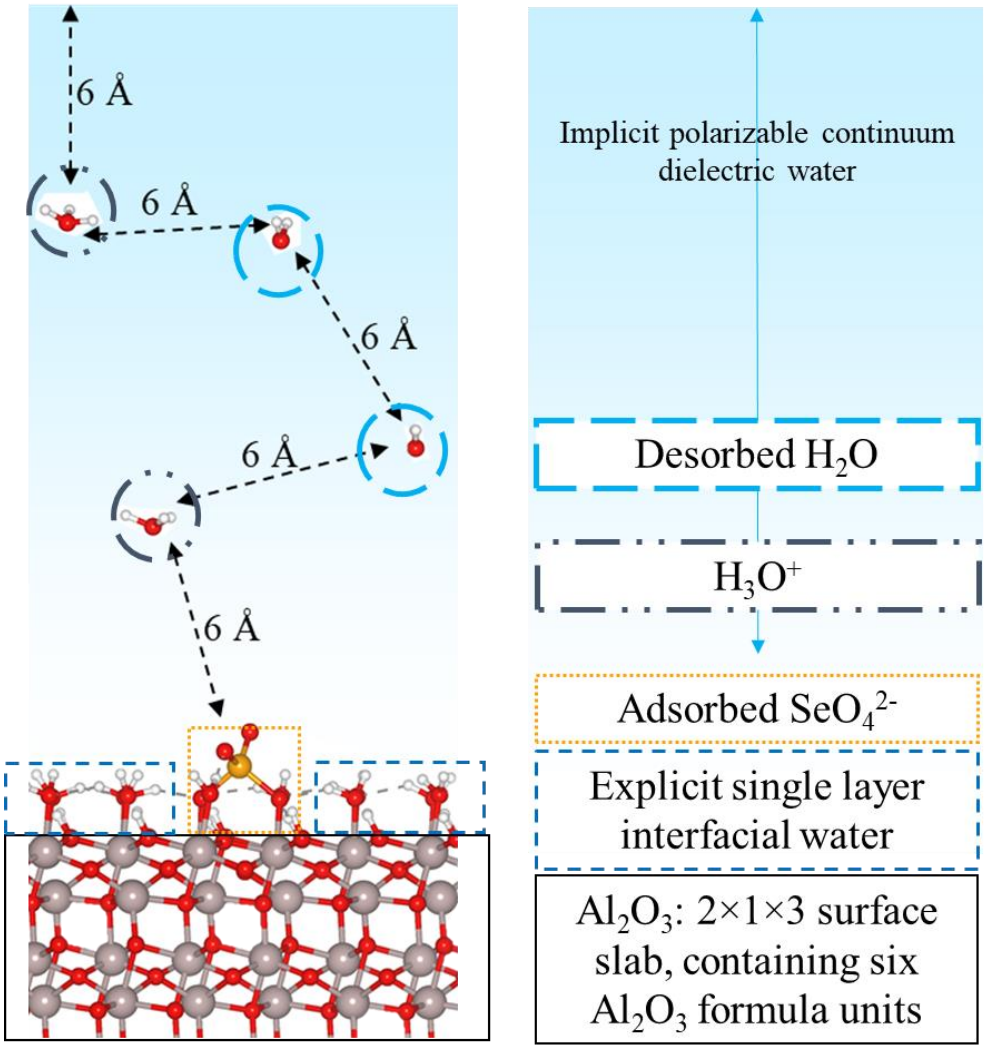

Figure A.1: Density Functional Theory simulation cell for calculating the adsorption of selenate on (012) Al_2O_3 surface. The cell integrates the Hybrid Solvent Model (HSM), where the surface is covered with single layer explicit solvent and vacuum space between metal-oxide lattice has polarizable continuum dielectric to include solvent effects. The desorbed water species are suspended in vacuum with intermolecular distance of at least 6 Å, to represent a dilute limit and to minimize spurious Van der Waals interactions. For Semi-protonated and de-protonated selenate, extra H_3O^+ are also added in the vacuum layer to maintain the neutrality of the simulation cell. The grey, red, white and orange balls represent Al, O, H and Se atoms respectively.

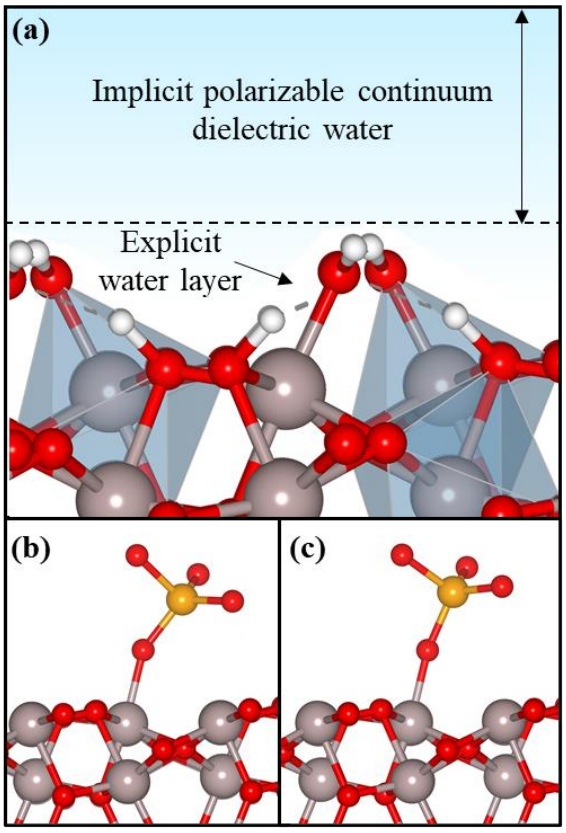

Figure A.2: (a) Hybrid Solvent Model demonstrating explicit interfacial water and implicit polarizable continuum dielectric. The relaxed H_2SeO_4 configuration on (b) fully solvated model (n=4) and (c) HSM with the waters removed for clarity. The gray, red, white, and orange spheres represent Al, O, H and Se atoms, respectively.

To test the validity of this model, I compared the H_2SeO_4 adsorption on (012) α-Al_2O_3 in vacuum, a single explicit layer (n=1), 4 explicit layers of solvent (n=4) and HSM (Figure A.3). The selenate-alumina bond strength (adsorption energy) and Se-Al bond distance were used as parameters for comparison (Table A.1).

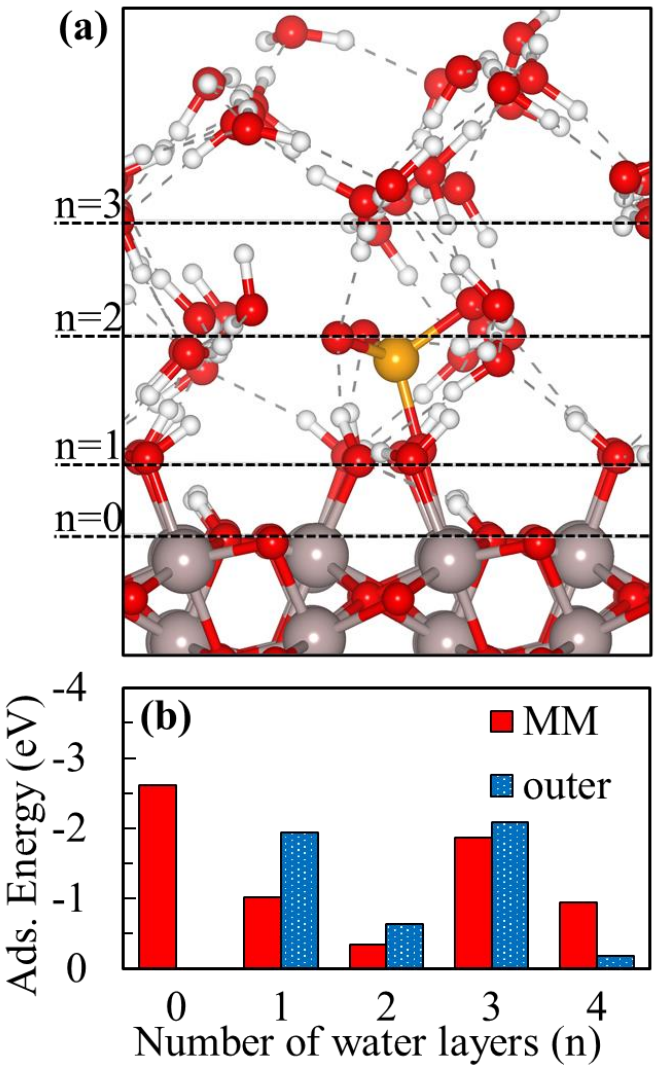

Figure A.3: (a) H_2SeO_4 adsorbed in on (012) Al_2O_3 surface with n = 4 water layers. Each layer contains 12 water molecules. (b) The adsorption energies of Monodentate Mononuclear (MM) and outer sphere selenate on Al_2O_3 surface with different water layers. The gray, red, white, and orange sphere represent Al, O, H, and Se atoms, respectively.

Table A.1: Calculated H_2SeO_4- α-Al_2O_3 adsorption energy and Se-Al bond length using different solvent models.

	H_2SeO_4-α-Al_2O_3 adsorption energy in vaccum (eV)*	**Se-Al bond length (Å)**
No solvent	-1.49	4.5
Single explicit water layer (n=1)	-0.22	4.6
Fully solvated system (n=4)	-0.47	4.9
HSM model	-0.42	5.0

Oxo-anion adsorption using HSM behaves similarly to four explicit layers of water, having similar adsorption energies (-0.47 and -0.42 eV respectively) and adsorption geometries (4.9 and 5Å Se-Al bond length respectively). Hence, the HSM provides quantitatively similar results to the significantly more expensive full solvation model.

APPENDIX B

REACTION ENERGIES OF NO3RR STEPS ON COPPER, RUTHENIUM AND RUTHENIUM-SAC IN COPPER SURFACE

Table B.1. Calculated reaction energy of elementary reactions involved in NO_3RR.

	CuNW	Ru-CuNW	RuNP
	eV	eV	eV
$NO_3^* \rightarrow NO_2^*$	-1.47	-1.51	-1.87
$NO_2^* \rightarrow NO^*$	-0.74	-2.39	-2.02
$NO^* \rightarrow N^*$	-0.57	-0.04	-1.21
$NH_3^* \rightarrow NH_{3(l)}$	0.01	0.71	0.71
$N^* \rightarrow N^*$	0.00	0.84	0.00
$N^* \rightarrow 0.5\ N_2^*$	-1.60	-1.23	0.39
$N_2^* \rightarrow N_{2(g)}$	-0.17	0.13	-0.33
$NO^* \rightarrow NO_{(g)}$	0.71	2.75	2.31
$NO^* \rightarrow N_2O^*$	-0.54	1.05	0.16
$N_2O^* \rightarrow N_2O_{(g)}$	-0.68	-0.23	0.01

Table B.2. Calculated activation energy of elementary reactions at 0 V *vs.* RHE involved in NO_3RR

	CuNW	Ru-CuNW	RuNP
	eV	eV	eV
$NO_3^* \rightarrow NO_2^*$	1.24	0.83	1.01
$O^* \rightarrow OH^-$	0.91	1.27	1.41
$NO_2^* \rightarrow NO^*$	0.76	0.78	1.04
$NO^* \rightarrow N^*$	1.66	2.07	1.11
$N^* \rightarrow NH^*$	0.67	1.42	1.14
$NH^* \rightarrow NH_2^*$	0.81	0.81	1.25
$NH_2^* \rightarrow NH_3^*$	0.94	0.89	1.60
$N^* \rightarrow N^*$	0.30	1.82	1.05
$N^* \rightarrow 0.5\ N_2^*$	0.67	2.22	3.29
$NO^* \rightarrow N_2O^*$	0.97	3.13	0.49

Table B.3: Calculated activation energy of all the hydrogenation elementary reactions in NO_3RR on Cu[111] involving electron transfer at various voltage vs. RHE

V	-0.20	-0.10	0.00	0.10	0.20
	eV	eV	eV	eV	eV

$NO_3^- \rightarrow NO_3^*$	-0.71	-0.81	-0.91	-1.01	-1.11
$O^* \rightarrow OH^-$	-0.85	-0.65	-0.45	-0.25	-0.05
$NO_2^* \rightarrow NO_2^-$	1.10	1.20	1.30	1.40	1.50
$N^* \rightarrow NH^*$	-1.43	-1.33	-1.23	-1.13	-1.03
$NH^* \rightarrow NH_2^*$	-0.61	-0.51	-0.41	-0.31	-0.21
$NH_2^* \rightarrow NH_3^*$	-0.67	-0.57	-0.47	-0.37	-0.27

Table B.4: Calculated activation energy of all the hydrogenation elementary reactions in NO_3RR on Ru[001] involving electron transfer at various voltage vs. RHE

V	-0.20	-0.10	0.00	0.10	0.20
	eV	eV	eV	eV	eV
$NO_3^- \rightarrow NO_3^*$	-1.47	-1.57	-1.67	-1.77	-1.87
$O^* \rightarrow OH^-$	-0.44	-0.24	-0.04	0.16	0.36
$NO_2^* \rightarrow NO_2^-$	1.85	1.95	2.05	2.15	2.25
$N^* \rightarrow NH^*$	-0.80	-0.70	-0.60	-0.50	-0.40
$NH^* \rightarrow NH_2^*$	-0.31	-0.21	-0.11	-0.01	0.09
$NH_2^* \rightarrow NH_3^*$	-0.47	-0.37	-0.27	-0.17	-0.07

Table B.5: Calculated activation energy of all the hydrogenation elementary reactions in NO_3RR on Ru- SAC in Cu[111] involving electron transfer at various voltage vs. RHE

V	-0.20	-0.10	0.00	0.10	0.20
	eV	eV	eV	eV	eV
$NO_3^- \rightarrow NO_3^*$	-1.05	-1.15	-1.25	-1.35	-1.45
$O^* \rightarrow OH^-$	-0.86	-0.66	-0.46	-0.26	-0.06
$NO_2^* \rightarrow NO_2^-$	1.48	1.58	1.68	1.78	1.88
$N^* \rightarrow NH^*$	-0.25	-0.15	-0.05	0.05	0.15
$NH^* \rightarrow NH_2^*$	-0.66	-0.56	-0.46	-0.36	-0.26
$NH_2^* \rightarrow NH_3^*$	-0.99	-0.89	-0.79	-0.69	-0.59

APPENDIX C

REACTION PATHWAYS AND TABLES OF NRR STEPS ON SINGLE ATOM SUBSTITUTED IN COPPER [111] SURFACE

Table C.1: Gibbs Free energy formulas for NRR reaction steps

Reaction steps	Energies	Eq. Number
$NO_3^- + * \rightarrow NO_3^* + e^-$	$\Delta G_{ads}(NO_3^-) = G_{NO_3^*} + \left[\frac{1}{2}G_{H_2} - eU_{RHE}\right] - \left[G_{HNO_3} - \Delta G_{sol} - \Delta G_{protonation}\right] - G_*$	r1
$NO_2^- + * \rightarrow NO_2^* + e^-$	$\Delta G_{ads}(NO_2^-) = G_{NO_2^*} + \left[\frac{1}{2}G_{H_2} - eU_{RHE}\right] - \left[G_{HNO_2} - \Delta G_{sol} - \Delta G_{protonation}\right] - G_*$	r2
$H^+ + e^- + * \leftrightarrow H^* \leftrightarrow 0.5\,H_2 + *$	$\Delta G_{ads}(H^*) = G_{H^*} - \left[\frac{1}{2}G_{H_2} - eU_{RHE} - 2.303\,RTpH\right] - G_*$	r3
$OH^- + * \rightarrow OH^* + e^-$	$\Delta G_{ads}(OH^-) = G_{OH^*} + \left[\frac{1}{2}G_{H_2} - eU_{RHE}\right] - \left[G_{H_2O} - \Delta G_{sol} - \Delta G_{protonation}\right] - G_*$	r4
$H_2O + * \rightarrow H_2O^*$	$\Delta G_{ads}(H_2O) = G_{H_2O^*} - \left[G_{H_2O} - \Delta G_{sol}\right] - G_*$	r5
$N_2 + * \rightarrow N_2^*$	$\Delta G_{ads}(N_2) = G_{N_2^*} - G_{N_2} - G_*$	r6
$NH_3 + * \rightarrow NH_3^*$	$\Delta G_{ads}(NH_3) = G_{NH_3^*} - G_{NH_3} - G_*$	r7
$NO_3^* + H_2O + 2e^- \rightarrow NO_2^* + 2OH^-$	$\Delta E = E_{NO_2^*} + 2 \times G_{OH^-} - E_{NO_3^*} - G_{H_2O} - 2 \times G_{e^-}$	r8
$NO_2^* + H_2O + 2e^- \rightarrow NO^* + 2OH^-$	$\Delta E = E_{NO^*} + 2 \times G_{OH^-} - E_{NO_2^*} - G_{H_2O} - 2 \times G_{e^-}$	r9
$NO^* + H_2O + 2e^- \rightarrow N^* + 2OH^-$	$\Delta E = E_{N^*} + 2 \times G_{OH^-} - E_{NO^*} - G_{H_2O} - 2 \times G_{e^-}$	r10
$N^* + H_2O + e^- \rightarrow NH^* + OH^-$	$\Delta E = E_{NH^*} + G_{OH^-} - E_{N^*} - G_{H_2O} - G_{e^-}$	r11
$NH^* + H_2O + e^- \rightarrow NH_2^* + OH^-$	$\Delta E = E_{NH_2^*} + G_{OH^-} - E_{NH^*} - G_{H_2O} - G_{e^-}$	r12
$NH_2^* + H_2O + e^- \rightarrow NH_3^* + OH^-$	$\Delta E = E_{NH_2{}^*} + G_{OH^-} - E_{NH^*} - G_{H_2O} - G_{e^-}$	r13
$NO^* + H_2O + e^- \rightarrow HNO^* + OH^-$	$\Delta E = E_{HNO^*} + G_{OH^-} -$	

Table C.2: Reactions for which activation barriers are calculated.

Activation barriers	Equation Numer.
$NO_3^* \rightarrow NO_2^* + O^*$	a1
$NO_2^* \rightarrow NO^* + O^*$	a2
$NO^* \rightarrow N^* + O^*$	a3
$N^* + H^* \rightarrow NH^*$	a4
$NH^* + H^* \rightarrow NH_2^*$	a5
$NH_2^* + H^* \rightarrow NH_3^*$	a6
$NO^* + H^* \rightarrow HNO^*$	a7
$NO^* + H^* \rightarrow NOH^*$	a8
$HNO^* \rightarrow NH^* + O^*$	a9
$HNO^* \rightarrow N^* + OH^*$	a10

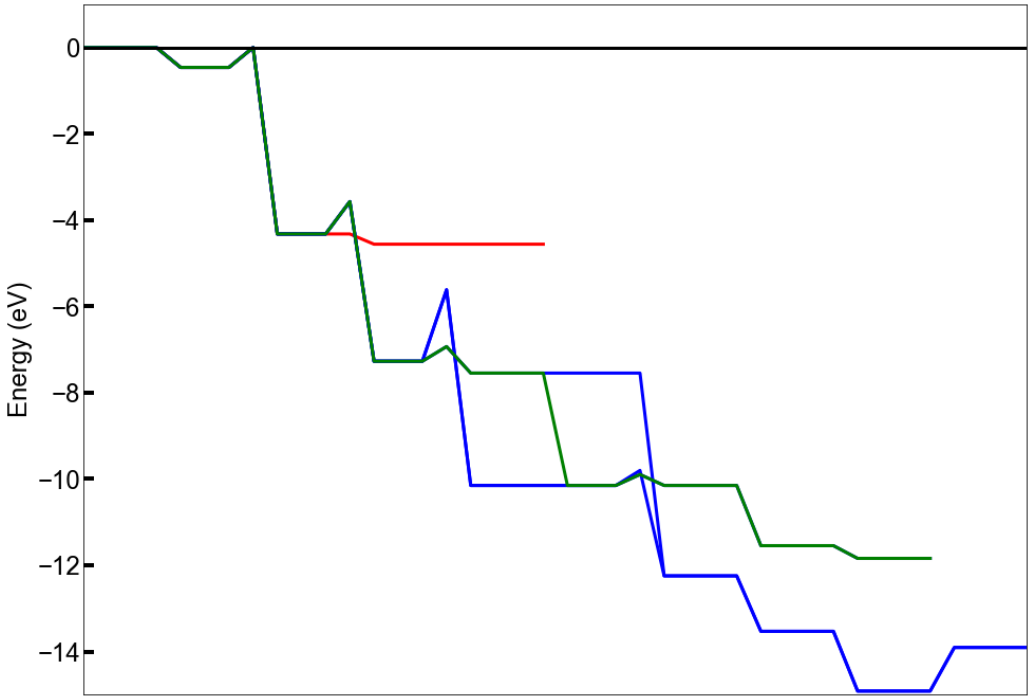

Figure C.1: NRR on Cu surface at -0.75 V vs. RHE at pH 14. The red, blue and green indicates pathways leading to NO_2^-, NH_3 and N_2 respectively.

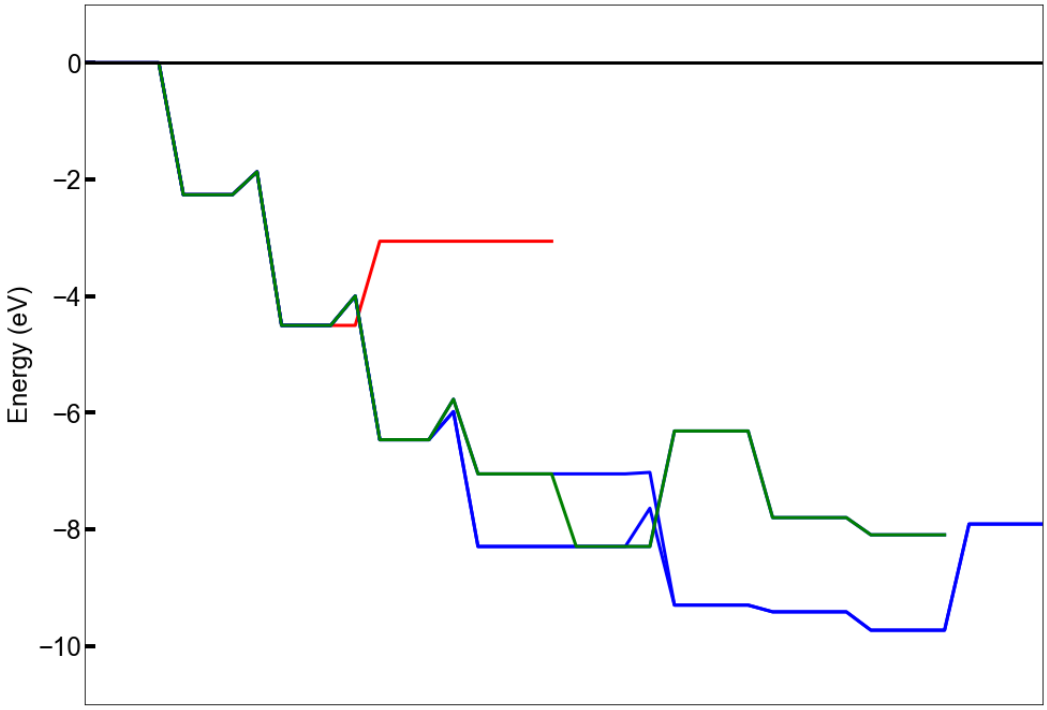

Figure C.2: NRR on Ti-SAA surface at 0 V vs. RHE at pH 14. The red, blue and green indicates pathways leading to NO_2^-, NH_3 and N_2 respectively.

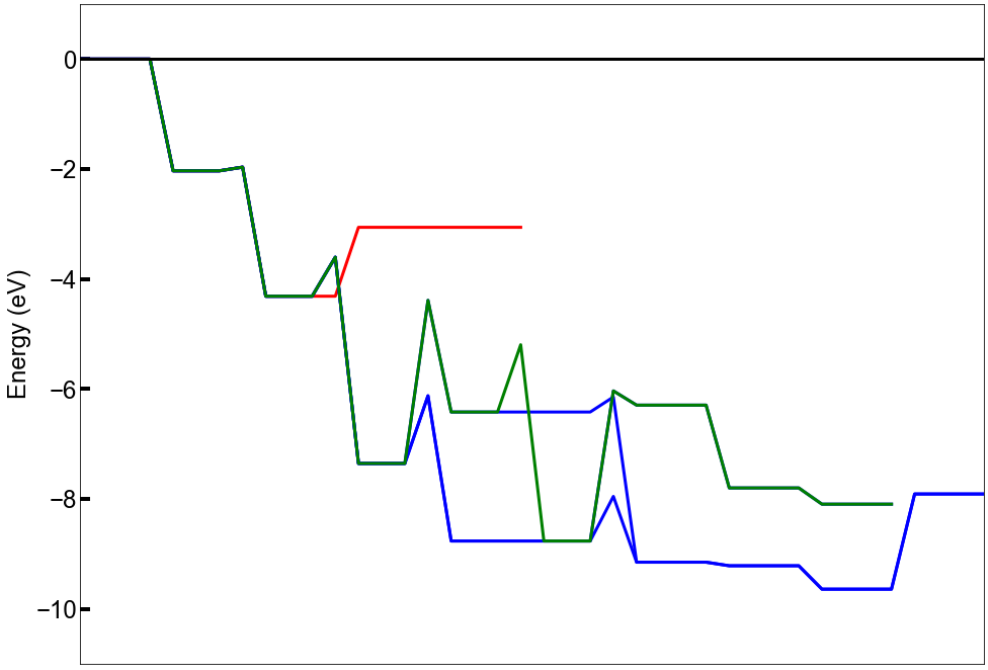

Figure C.3: NRR on Mo-SAA surface at 0 V vs. RHE at pH 14. The red, blue and green indicates pathways leading to NO_2^-, NH_3 and N_2 respectively.

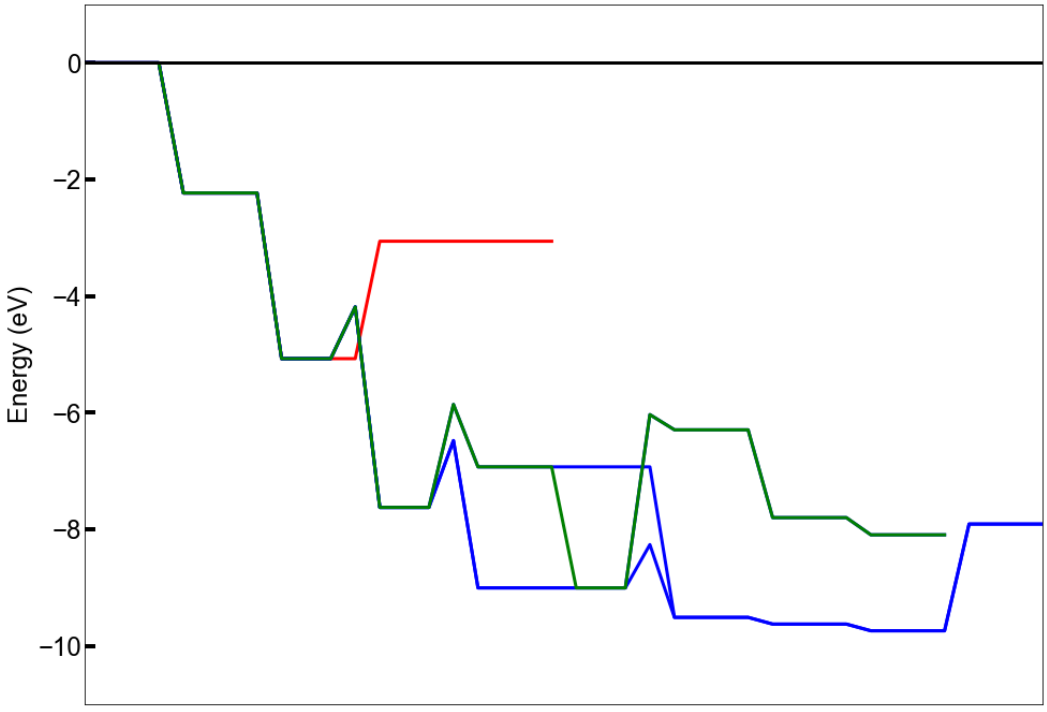

Figure C.4: NRR on W-SAA surface at 0 V vs. RHE at pH 14. The red, blue and green indicates pathways leading to NO_2^-, NH_3 and N_2 respectively.

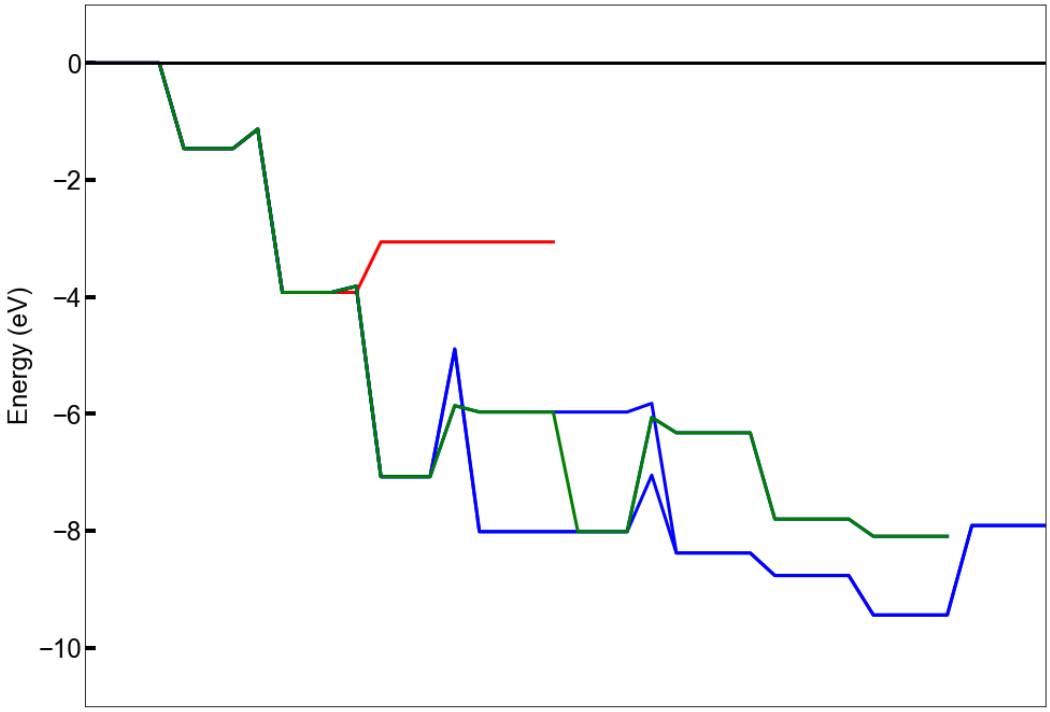

Figure C.5: NRR on Ru-SAA surface at 0 V vs. RHE at pH 14. The red, blue and green indicates pathways leading to NO_2^-, NH_3 and N_2 respectively.

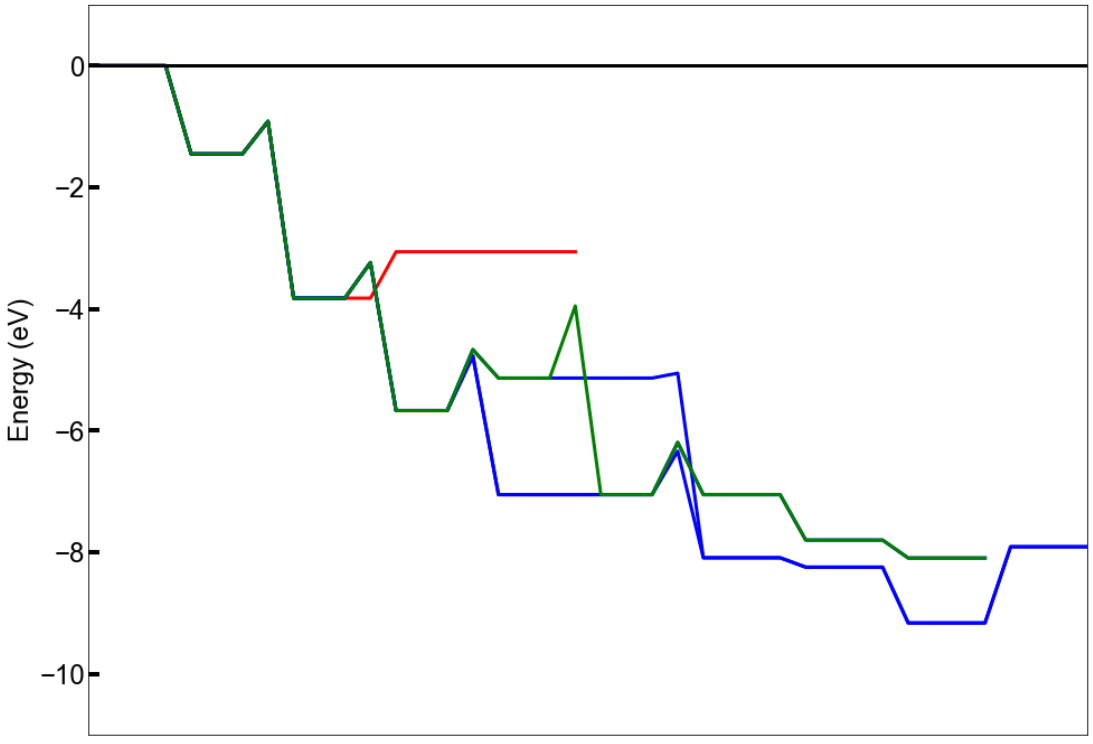

Figure C.6: NRR on Ni-SAA surface at 0 V vs. RHE at pH 14. The red, blue and green indicates pathways leading to NO_2^-, NH_3 and N_2 respectively.

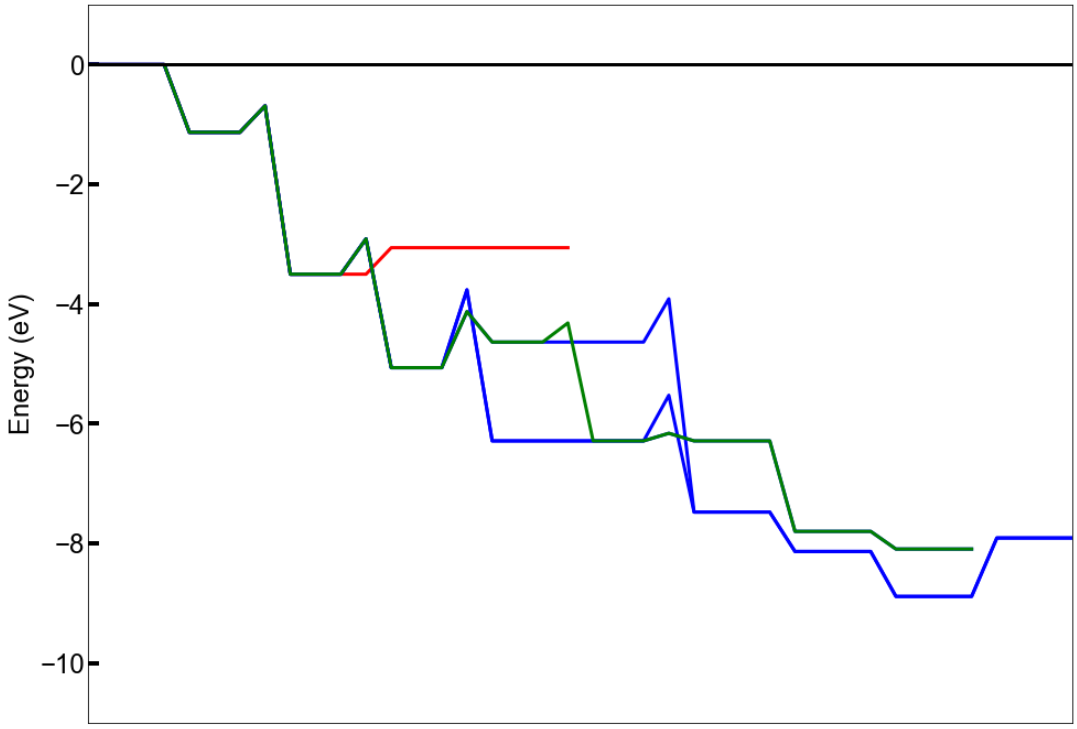

Figure C.7: NRR on Pd-SAA surface at 0 V vs. RHE at pH 14. The red, blue and green indicates pathways leading to NO_2^-, NH_3 and N_2 respectively.

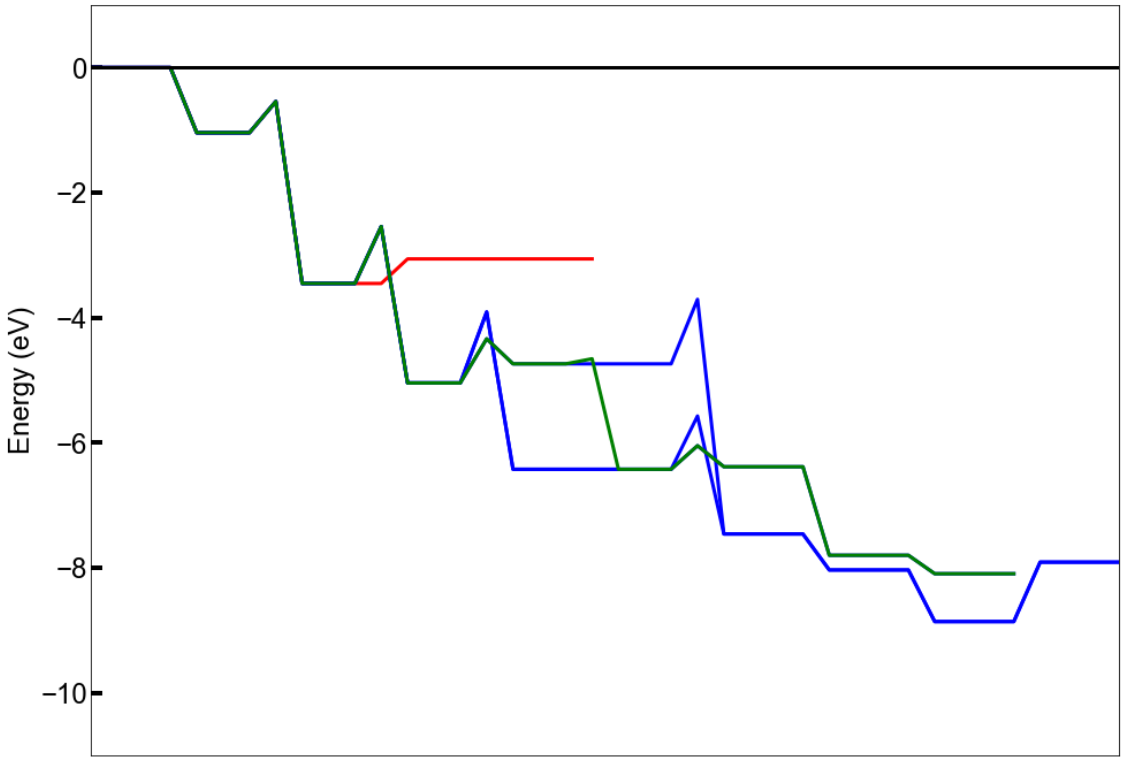

Figure C.8: NRR on Pt-SAA surface at 0 V vs. RHE at pH 14. The red, blue and green indicates pathways leading to NO_2^-, NH_3 and N_2 respectively.

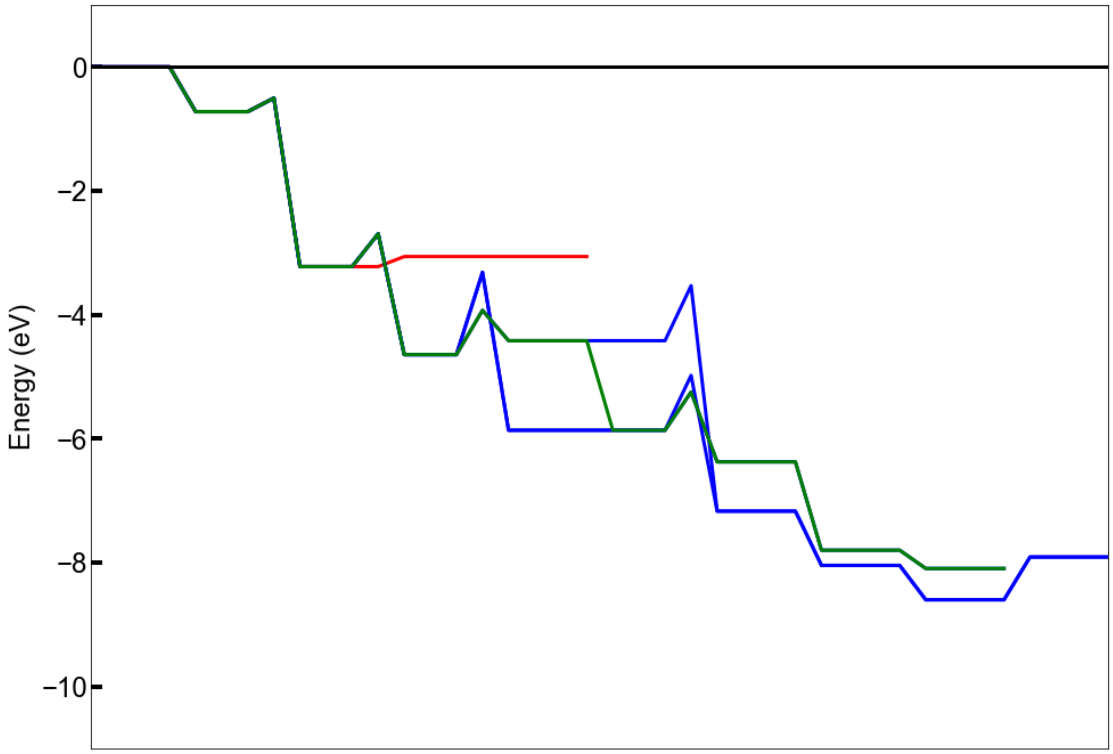

Figure C.9: NRR on Au-SAA surface at 0 V vs. RHE at pH 14. The red, blue and green indicates pathways leading to NO_2^-, NH_3 and N_2 respectively.

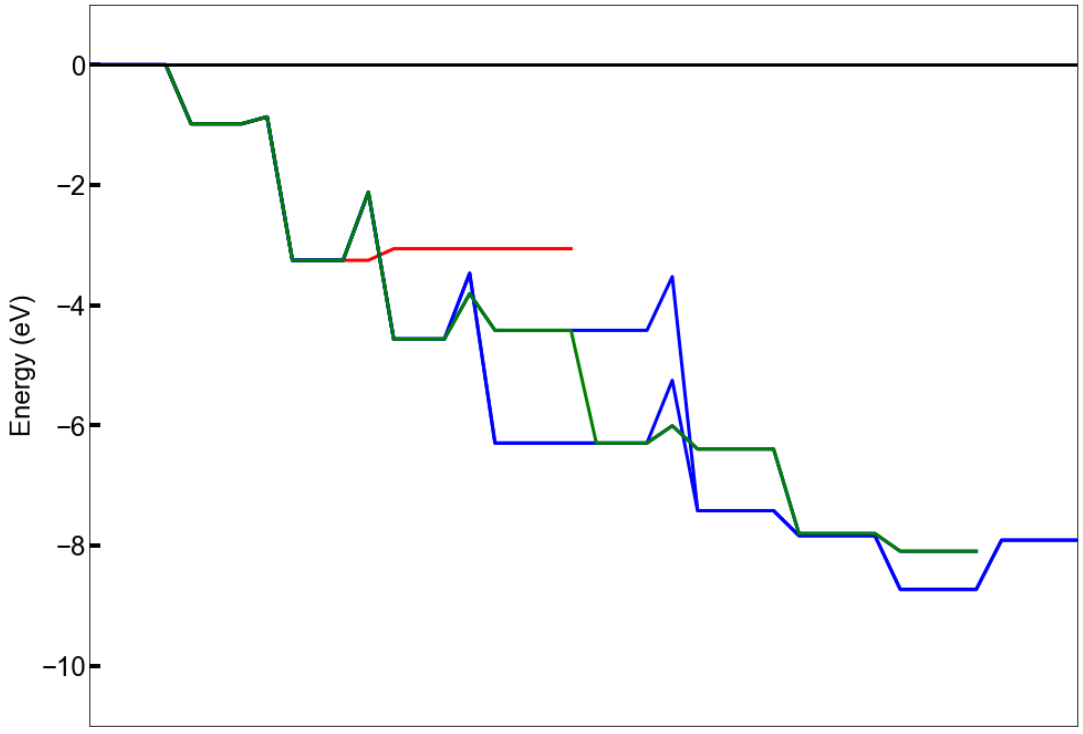

Figure C.10: NRR on In-SAA surface at 0 V vs. RHE at pH 14. The red, blue and green indicates pathways leading to NO_2^-, NH_3 and N_2 respectively.

APPENDIX D

STATEMENT OF INCORPORATED PUBLICATIONS

Chapter 3 has been published in Journal of Colloid and Interface Science (Gupta et al., 2022). Chapter 4 has been published in The Journal of Physical Chemistry C (Gupta et al., 2023). I, Srishti Gupta, affirm that I am the principal author and that all subsequent coauthors (Ngan Anh Nguyen, Adam Chismar and Christopher L Muhich) approve the addition of these publications in my dissertation. I also received permissions from the Nature Nanotechnology to use the figures from the published article (Chen et. al., 2022) in which I was the co-first author in Chapter 6.